



THÈSE

En vue de l'obtention du

DOCTORAT DE L'UNIVERSITÉ DE TOULOUSE

Délivré par : *l'Institut Supérieur de l'Aéronautique et de l'Espace (ISAE-SUPAERO)*

Présentée et soutenue le 14/02/2023 par :

CORENTIN LUBEIGT

**Traitement du Signal pour la Télédétection par GNSS
(Signal Processing for GNSS Reflectometry)**

JURY

NABIL EL KORSO	Président
FABIO DOVIS	Rapporteur
GUILLAUME GINOLHAC	Rapporteur
ESTEL CARDELLACH	Examinatrice
LAURENT LESTARQUIT	Encadrant
LORENZO ORTEGA	Encadrant
JORDI VILÀ-VALLS	Co-Directeur de thèse
ÉRIC CHAUMETTE	Directeur de thèse

École doctorale et spécialité :

MITT : Informatique et Télécommunications

Unité de Recherche :

TéSA : Laboratoire de Télécommunications Spatiales et Aéronautiques

ISAE-DEOS NaviRReS : Navigation Radar and Remote Sensing

Directeur(s) de Thèse :

Éric CHAUMETTE et Jordi VILÀ-VALLS

Rapporteurs :

Fabio DOVIS et Guillaume GINOLHAC

Remerciements

Le contenu rassemblé dans ce document n'est bien entendu pas le résultat de mon seul travail mais le fruit d'une série de rencontres et de discussions. Je me lance donc dans la longue énumération de ces rencontres qui, soyez-en sûrs, ne sera jamais assez complète.

Il semble naturel de commencer par les personnes qui ont validé le travail réalisé au cours de ces trois dernières années : merci donc à Fabio Dovis et Guillaume Ginolhac pour le sacrifice de leurs vacances de fin d'année au service de la science. Fabio, je regrette que tu n'aies pas pu venir le jour de la soutenance, je me faisais une joie de te rencontrer. Guillaume, nous nous sommes croisés déjà plusieurs fois et c'est un plaisir d'avoir échangé avec toi à chacun de ces moments. Merci également à Nabil El Korso pour avoir présidé le jury, ton exemplaire de ce manuscrit a été retrouvé par un agent SNCF à la maintenance de Châtillon, j'ai l'impression qu'il te le garde (ça a dû l'intéresser). Merci enfin à Estel Cardellach, d'avoir fait le trajet en van anglais depuis Barcelone, nous nous connaissons par ailleurs, c'est pourquoi je reviens vers toi plus loin dans ces remerciements.

Je passe alors à mon encadrement de thèse : merci Eric Chaumette pour ta passion de la recherche. C'est en t'écoutant parler de ton propre directeur de thèse que j'ai réalisé le lien particulier qui nous unissait. J'espère pouvoir aussi développer un tel lien dans de futures expériences professionnelles. Merci à Jordi Vilà-Valls pour ta vision catalane de la recherche, c'est très instructif de te voir travailler et tout aussi instructif de te voir ne pas travailler, il faudra qu'on retourne à la montagne un de ces quatre ! Merci à Lorenzo Ortega, tu as été la personne la plus proche de mes travaux. On aura compris beaucoup de choses ensemble rien qu'en discutant au téléphone ou dans le bureau. J'espère que ta première expérience en tant qu'encadrant t'a plu, personnellement ma première expérience en tant que doctorant s'est bien passée. Un jour, je suis sûr qu'on pourra discuter dans une autre langue que le français ou l'anglais, donne-moi juste un peu de temps. Enfin merci à Laurent Lestarquit pour tes tentatives de nous ramener sur Terre, vers une recherche plus appliquée. Je sais bien que tout n'a pas été fait comme tu l'imaginais, mais personnellement, j'ai le sentiment d'avoir réussi à un peu intégrer ta vision dans cette thèse en essayant de pousser pour travailler sur les données et en allant rencontrer les personnalités du domaine.

Je remercie maintenant tous ceux que j'appelle les satellites : ce sont ces personnes qui ont fait avancer mes travaux par de courtes mais riches interventions. Merci à Gustavo Vallejo-Garcia pour ta patience face à des responsables de stage qui ne parlaient que de bornes, merci aussi d'avoir partagé ta culture mexicaine ! Merci à Benoit Priot pour ta grande expérience sur le traitement de données réelles ainsi que ton précieux logiciel qui m'a accompagné tout au long de la thèse. Merci aussi à François Vincent pour ton génie et ta recherche pragmatique. J'espère avoir l'occasion de travailler avec toi à nouveau ! Pour les satellites CNES, je remercie Jean-Louis Mazens et François-Xavier Marmet pour le bon temps passé à Gruissan. Je garde de ces deux journées un excellent souvenir ensoleillé. Merci enfin aux satellites barcelonais : Estel Cardellach et Weiqiang Li, qui m'ont accueilli pendant quatre mois à l'ICE et qui

m'ont véritablement accordé du temps. J'ai beaucoup appris lors de ce séjour et j'espère avoir l'occasion de vous recroiser pour continuer ce qui a été commencé ou bien traiter de nouveaux problèmes.

Une petite phrase pour formellement remercier les grands acteurs financiers de cette thèse : l'ISAE Supaero, le CNES et, d'une autre manière, le laboratoire TéSA. Nous ne pouvons rien faire sans argent, c'est comme ça. Merci d'avoir payé mon beurre ainsi que l'intéressante recherche qui a résulté de cette thèse.

Ce qui nous conduit à des remerciements moins formels et moins directement liés au travail de thèse en tant que tel mais plutôt à l'environnement de travail et à la sympathique compagnie que j'ai pu trouver là où j'ai travaillé. Un grand merci donc à tous les membres de TéSA, que ce soit les nouveaux, les permanents, les anciens qui sont partis et les très anciens (coucou mich-mich), je ne saurais le répéter assez, mais j'ai passé trois belles années de thèse (malgré la crise sanitaire) en compagnie de stagiaires, de doctorants, de chercheurs, de collègues, d'amis. L'ambiance est saine et bonne et c'est grâce à tout le monde. C'est en particulier grâce à toi Corinne Mailhes qui assumes complètement ton rôle de garante du bien-être de l'employé. Ta gestion maternelle du laboratoire peut parfois faire sourire l'hautain ou râler l'indépendant mais tout le monde doit se rendre compte qu'elle permet à tous de se sentir bien au travail et c'est quelque chose que je n'ai jamais vu ailleurs (du haut de ma grande expérience car il est vrai que j'ai déjà pas mal roulé ma bosse). Merci aussi aux collègues de l'ISAE, enseignants-chercheurs, doctorants et post-doctorants, avec qui j'ai pu échanger sur divers sujets à travers des repas d'équipe, des journées de doctorants du DEOS ou des BE.

C'est votre tour les amis ! C'est aussi grâce à vous si j'arrive jusqu'ici, car j'ai toujours été bien entouré pour me changer les idées, randonner, skier, squasher et trinquer. Alors voilà, merci aux toulousains : Wiwi, Jojo, Aymeline Loïc, Loïc, Pinch, Quentin, Louis, Sido, Alex, Caro, Lucas et j'en oublie. Merci aux non-toulousains (je vous aime quand même) : Henry, Tits, Clément, Paul, Wince, Marc, Eric, Amédée, Tatou, Maxou, Elie et j'en oublie. Merci aussi à ces amis qu'on voit un temps et qu'on sait qu'on gardera toujours malgré la distance : Charles, Clem, Harald et j'en oublie. Merci enfin à Gabex : Gabriel, Alexandre, je n'ai pas toujours eu le bon choix de mots pour parler de vous, et pourtant vous êtes là depuis toujours, vous avez traversé continents et océans pour que l'on puisse se retrouver. Le temps passé avec vous est du temps précieux et c'est bien ça que je veux vous dire. Vous êtes le meilleur d'entre nous, rien n'est plus vrai.

Je vous remercie mes chers parents pour votre soutien et votre exemple. Pour vos conseils et votre patience. Quand je rentre à la maison, c'est-à-dire chez vous, je redeviens un enfant, je cours dans l'escalier et je traîne toute la journée. Je me demande ce que vous ressentez quand vous entrez chez moi ? Merci pour tout. Emma et Ludo, vous êtes grande sœur et grand frère. C'est ainsi que je vous ai toujours vu et je me suis construit en sachant que vous étiez devant, en voici juste deux exemples : merci Emma d'avoir débarrassé le chemin de la prépa, puis de l'école d'ingé, puis de la thèse, c'est plus simple quand on sait à quoi s'attendre ! Merci Ludo d'avoir ouvert la porte de l'Asie et le goût du voyage. C'est avec tristesse que je t'ai vu partir pour ton île, mais ça a rendu possible, voire évident, des voyages qui m'ont

permis et me permettront de te retrouver.

Enfin, Fanny. Comme aurait pu dire Alain à Dalida, tu es celle qui nomme les couleurs de l'arc-en-ciel que j'ai dans le cœur. Mais comme tu n'es pas caramels, bonbons et chocolats, laisse-moi juste te dire merci d'avoir été là tout au long de ces années, merci d'être revenue à Toulouse où nous avons fait notre nid aux Tomettes, merci pour tous les moments passés ensemble, sur le toit de Toulouse, sur le toit Corse, sur le toit des Pyrénées (ou presque), sur le toit des Etats-Unis ! Notre randonnée est loin d'être terminée alors allons ensemble chercher le prochain toit.

Résumé

La réflectométrie par système de navigation par satellite, ou GNSS-R, est l'étude des signaux de géolocalisation réfléchis sur la surface de la Terre. Ces signaux dits d'opportunité, souvent perçus comme des nuisances pour le bon fonctionnement des récepteurs de navigation, sont en fait une source d'information sur la nature et la position de la surface de réflexion. Suivant la plateforme sur laquelle se situe le récepteur (par exemple, station sol, avion) et la surface de réflexion (par exemple, mer agitée, lac), le signal réfléchi présente des déformations plus ou moins faciles à modéliser, et les approches pour en estimer les paramètres d'intérêt varient.

Ce travail de thèse repart du problème du multitrajet lors d'une navigation en milieu contraint. Celui-ci peut être modélisé comme un problème d'estimation à deux sources, où la source principale est le signal d'intérêt et la source secondaire est une unique réflexion de ce même signal. En fonction du scénario et des ressources à disposition, il est possible i) d'estimer les paramètres d'intérêt (retard, Doppler, amplitude et phase) des deux sources, ou bien ii) de n'estimer que les termes d'une seule source, au risque d'obtenir des estimations biaisées par la présence du signal parasite. Dans tous les cas il est nécessaire de maîtriser les performances atteignables pour ces problèmes d'estimation. Pour cela des outils de la théorie de l'estimation, tels que la borne de Cramér-Rao (BCR) peuvent être utilisés. Dans le cadre de cette thèse, la BCR a été calculée pour le cas d'un modèle bien spécifié (deux sources) et d'un modèle mal spécifié (une source). Ces bornes ont été comparées aux performances de différents estimateurs afin d'obtenir une caractérisation théorique du problème.

Cela a permis d'établir un cadre mathématique qui s'applique au problème du GNSS-R proche du sol, pour lequel le signal réfléchi est peu déformé par la surface de réflexion. Dans ce cas, les signaux direct et réfléchi sont très proches en temps, ce qui conduit à des interférences entre eux et à une dégradation des performances. Les techniques de GNSS-R existantes, mal adaptées au cas proche du sol, ont alors été comparées à la BCR et à deux approches : i) une approximation du critère de vraisemblance dans le cas où les deux sources sont temporellement très proches et ii) une application d'estimateurs à deux sources pour éliminer l'interférence. Cette partie sur la réflectométrie proche du sol s'appuie sur les données d'une campagne de mesure organisée par le CNES (Toulouse, France).

Le problème se modifie progressivement lorsque l'élévation du satellite augmente : la réflexion, jusqu'alors supposée cohérente devient lentement non-cohérente car sensible à la rugosité de la surface. La détection automatique de cette transition (c'est à dire, de cohérent à non-cohérent) est capitale pour de futures missions satellite. La cohérence d'une réflexion s'observe principalement sur la différence de phase entre les signaux réfléchi et direct. Ainsi une étude statistique de séries temporelles de cette grandeur permet de construire des tests en fonction de la gaussianité de cette série ou de sa régularité. Les tests proposés ont été appliqués à des données fournies par l'IEEC (Barcelone, Espagne).

Enfin, pour des cas où la surface de réflexion déforme le signal de manière significative, il est nécessaire de travailler sur un modèle de signal plus adapté. L'approche envisagée dans

cette thèse est de considérer le signal réfléchi comme la convolution du signal émis et de la réponse impulsionnelle de la surface de réflexion. Cette modélisation s'accompagne du calcul de la BCR correspondante, ainsi que de l'implémentation de l'algorithme du maximum de vraisemblance. La question de la détermination de la taille de la réponse impulsionnelle, c'est-à-dire du nombre de points nécessaires pour la décrire est alors traitée à l'aide de différents tests statistiques. Les résultats obtenus par simulation montrent le potentiel de cette nouvelle approche.

Mots clés: traitement du signal; GNSS; GNSS-R; télédétection; estimation; Borne de Cramér-Rao.

Abstract

Global Navigation Satellite Systems (GNSS) Reflectometry, or GNSS-R, is the study of GNSS signals reflected from the Earth's surface. These so-called signals of opportunity, usually seen as a nuisance in standard navigation applications, contain meaningful information on the nature and relative position of the reflecting surface. Depending on the receiver platform (e.g., ground-based, airplane, satellite) and the reflecting surface itself (e.g., rough sea, lake), the reflected signal, more or less distorted, is difficult to model, and the corresponding methods to estimate the signal parameters of interest may vary.

This thesis starts from the navigation multipath problem in harsh environments, which can be seen as a dual source estimation problem where the main source is the signal of interest, and the secondary one is a single reflection of the main source. Depending on the scenario and the resources at hand, it is possible i) to estimate the parameters of interest (i.e., time-delay, Doppler frequency, amplitude and phase) of both sources, or ii) to estimate only one source's parameters, although these estimates may be biased because of the interfering source. Either way, it is necessary to know the achievable performance for these estimation problems. For this purpose, tools from the estimation theory, such as the Cramér-Rao bound (CRB), can be used. In this thesis a CRB expression was derived for the properly specified case (dual source), and the misspecified one (single source). These bounds were compared to the performance obtained with different estimators, in order to theoretically characterize the problem at hand.

This study allowed to establish a clear mathematical framework that also fits the ground-based GNSS-R problem, for which the reflected signal is little distorted by the reflecting surface. In this case, the direct and reflected signals are close in time, which inevitably leads to interference, or crosstalk, and then to a clear performance degradation. Standard GNSS-R techniques, which do not perform well in this ground-based scenario, were compared to the CRB and two proposed approaches: i) a Taylor approximation of the dual source likelihood criterion when both sources are very close in time, and ii) a dual source estimation strategy to reduce or cancel the crosstalk. This part on ground-based GNSS-R was supported by a real data set, obtained from a data collection campaign organized by CNES (Toulouse, France).

The problem changes slowly when the satellite elevation increases: the reflection, assumed coherent so far, turns non-coherent because of the reflecting surface roughness. The automatic detection of this transition (i.e., from coherent to non-coherent) is of great interest for future satellite missions. Reflection coherence is mainly observed by looking at the relative phase between the reflected and direct signals. Consequently, a statistical study of phase difference time series allowed to build tests that depend on the time series Gaussianity or regularity. The proposed tests were applied to a data set provided by the IEEC (Barcelona, Spain).

Finally, for scenarios where the reflecting surface distorts the signal significantly, it is necessary to adapt the signal model. The approach proposed in this thesis is to consider the received signal as a convolution between the transmitted signal and the reflecting surface

impulse response. This signal model goes with the derivation of the corresponding CRB and the implementation of the maximum likelihood estimator. The question of the impulse response size determination, that is, the determination of the number of pulses required to describe the impulse response, was also tackled based on hypothesis tests. Simulation results show the potential of this approach.

Key words: signal processing; GNSS; GNSS-R; remote sensing; estimation; Cramér-Rao bound.

Contents

Introduction	1
1 Concepts and Tools: From Estimation Theory to GNSS-R	7
1.1 Introduction	8
1.2 Background on Deterministic Estimation Theory	9
1.3 Global Navigation Satellite Systems	17
1.4 The Multipath Problem	28
1.5 GNSS Reflectometry	35
1.6 Conclusion	42
2 Multipath Effect and Its Impact on Positioning Performance	45
2.1 Introduction	46
2.2 MPEE for Different Multipath Mitigation Techniques	51
2.3 Joint Delay-Doppler Estimation Performance in a Dual Source Context	53
2.4 A Metric for Multipath-Robust Signal Design and Analysis	64
2.5 Misspecified Cramér-Rao Bounds in Multipath Scenarios	73
2.6 Conclusion	82
3 Ground-Based GNSS-R	83
3.1 Introduction	84
3.2 Gruissan Data Campaign	88
3.3 Crosstalk Characterization	103
3.4 Approximate Maximum Likelihood for Narrowband GNSS Signals	112
3.5 Performance on Simulated Data	120
3.6 Altimetry Using Wideband GNSS Signals	122
3.7 Conclusion	128
4 Towards Diffuse Scattering	131
4.1 Introduction	132
4.2 Coherence Analysis	135
4.3 Impulse Response Estimation	145
4.4 Impulse Response Size Determination: A Detection Problem	155
4.5 Conclusion	162
Conclusion and Perspectives	163
A Fourier Transform Relations	167
B Matrices Relations	169

B.1	Block Matrix inversion Lemma	169
B.2	Details on Orthogonal Projectors Upon Subspaces of a Vector Subspace	169
C	Details on the Derivation of the Dual Source Model Fisher Information Matrix	173
C.1	Derivation Based on the Slepian-Bangs Formulas	173
C.2	Derivation Based on Orthogonal Projection	180
D	Details on the Derivation of the Misspecified Cramér Rao Bounds	183
E	Details on the Computation of the Approximate Maximum Likelihood Estimator	191
E.1	Details on the Taylor Approximation of c and β_1 Functions	191
E.2	Details on the Taylor Approximation of the Likelihood Criterion	194
F	Details on the Derivation of the Impulse Response Model Fisher Information Matrix	197
F.1	Real and Imaginary Parts Parameterization	197
F.2	Amplitude and Phase Parameterization	199
F.3	Derivation of the Integral Terms	199
G	Details on the Impulse Response Size Determination Problem	203
G.1	Details on the Global MSE for Under- and Overshooting Cases	203
G.2	P + next Correlation Coefficient	204
G.3	Chung and Mecklenbräuker Likelihood Ratio Distribution Derivation	205
	Bibliography	207

List of Figures

1	Graphical summary of the thesis.	3
1.1	Example of the CRE algorithm for the estimation of the time-delay of two sources. (a) is the single source likelihood term of the first iteration (the expected shapes should be symmetric). (b) is the three consecutive steps where the blue curves are associated to one source and the orange curves are associated to the other. The final curves, marked with the vertical black lines, are symmetric as expected.	15
1.2	Example of the APE algorithm for the estimation of the time-delay of two sources. (a) is the dual source likelihood function to be maximized and (b) is a contour plot of the same function with the stair-shaped trajectory of the APE algorithm iterative steps.	15
1.3	General Principle of GNSS.	19
1.4	Quasi-orthogonality property of a PRN sequence. (a) is the ACF of GPS PRN 1 and (b) is the CCF of the same PRN with GPS PRN 2.	20
1.5	Layered structure of a GNSS signal.	20
1.6	GPS signals power spectral density for all three bands: (a) is L1 band, (b) is L2 and (c) is L5.	23
1.7	GALILEO signals power spectral density for all three bands: (a) is E1 band, (b) is E5 and (c) is E6.	25
1.8	Example of ambiguity function in two cases, (a) the PRN tested is present in the received signal and (b) the PRN tested is not present in the received signal.	26
1.9	Example of the Early-minus-Late tracking architecture. (a) presents a scenario where the prompt is too early, and (b) presents the opposite scenario where it is too late.	26
1.10	50 realizations of a noisy signal in presence of noise. (a) presents the corresponding cross-correlation functions and (b) presents the histogram of the estimated time-delays for the 50 realizations and for 5000 realizations.	27
1.11	Ground multipath scenario and path separation prediction thanks to geometry consideration.	29
1.12	Example of PDP with the direct signal, near echoes and far echoes.	30

1.13	Multipath effect on the cross-correlation function between the single-multipath-corrupted signal and a clean replica of a GPS L1 C/A signal. (a) shows the auto-correlation function (without multipath), (b) shows the cross-correlation when the single multipath is in-phase with the LOS ($\Delta\phi = 0$), (c) is when the single multipath is in quadrature ($\Delta\phi = \pi/2$) and (d) is when it is out-of-phase ($\Delta\phi = \pi$). RF front-end bandwidth is equal to 4 MHz in green and 24 MHz in red, excess delay is equal to 0.25 L1 C/A chips and MDR equal to 0.1.	31
1.14	MPEE applied to a E-L architecture (a) with different spacing for a GPS L1 C/A signal and (b) with a fixed spacing for different signals: GPS L1 C/A and GALILEO E1B. Front-end filter bandwidth set to 24 MHz, MDR = 0.1 and integration time $T_I = 4$ ms.	34
1.15	Typical spaceborne GNSS-R geometry.	36
1.16	Example of non-coherent integration effect with integration time set to (a) 1 ms, (b) 10 ms, (c) 100 ms and (d) 1 s. Extracted from Gleason <i>et al.</i> 2005 [Gle05].	38
1.17	Example of delay-Doppler mapping. On the left, horizontal black lines are iso-Doppler lines and green ellipses are iso-delay lines. Each cell can be associated to a cell of the DDM. Extracted from Zavorotny <i>et al.</i> 2014 [Zav14].	39
1.18	Example of complex waveform and the effect of surface wind speed on the trailing edge slope. Extracted from Zavorotny <i>et al.</i> 2014 [Zav14].	40
1.19	Example of path separation estimation strategies. Extracted from Nogués i Cervelló <i>et al.</i> 2021 [Nog21].	41
1.20	Residual phase difference between the direct and the reflected path. Extracted from Roesler <i>et al.</i> 2020 [Roe20].	41
2.1	Urban scenario considered in Chapter 2.	47
2.2	MPEE for (a) GPS L1 C/A and (b) GALILEO E1B signals.	52
2.3	Scenario (a): Estimation of the delay (left) and the Doppler frequency (right) for $\Delta\tau = 2$ L1 C/A chips with CRE. (top) is for a GPS L1 C/A signal, (bottom) is for an LFM signal.	58
2.4	Scenario (b): Estimation of the delay (left) and the Doppler frequency (right) for $\Delta\tau = 1/4$ L1 C/A chips with CRE. (top) is for a GPS L1 C/A signal, (bottom) is for an LFM signal.	59
2.5	Scenario (c1): Estimation of the delay (left) and the Doppler frequency (right) for $\Delta\tau = 1/8$ L1 C/A chips with CRE. (top) is for a GPS L1 C/A signal, (bottom) is for an LFM signal.	60
2.6	Scenario (c2): Estimation of the delay (left) and the Doppler frequency (right) for $\Delta\tau = 1/8$ L1 C/A chips with 2S-MLE. (top) is for a GPS L1 C/A signal, (bottom) is for an LFM signal.	61
2.7	Estimation of the LOS time delay τ_0 with respect to the path separation for (a) GPS L1 C/A at SNR = 31 dB and (b) GALILEO E1B at SNR = 34 dB.	62
2.8	Estimation of the LOS time delay τ_0 with respect to the path separation for (a) GPS L1 C/A and (b) GALILEO E1B, at path separation set to 150m.	63
2.9	Averaged (a) $CCBR_\tau$ and (b) $CCBR_b$ for the GPS L1 C/A signal with $B_R = 1, 2, 4, 8$ MHz, and ϕ_Γ uniformly distributed in $(0, \pi)$	69

2.10	CCBR _{τ} envelope (left) and CCB _{b} envelope (right) for GPS L1 C/A (top) and GALILEO E1B (bottom) signal with $B_R = 24$ MHz.	70
2.11	CCBR _{τ} envelope for (a) GPS L5-I with $B_R = 24$ MHz and (b) GALILEO E5 with $B_R = 60$ MHz.	71
2.12	Averaged CRB _{$\tau_0 \epsilon$} in presence of a single multipath as an application of the averaged CCB _{τ} on GPS L1 C/A (continuous lines) and GALILEO E1B (dashed lines) signals, sampled at $B_R = 24$ MHz for three different representative SNR.	72
2.13	(a) Averaged CRB _{$\tau_0 \epsilon$} in presence of a single multipath as an application of the averaged CCB _{τ} on GPS L1 C/A (continuous lines) and GALILEO E1B (dashed lines) signals, sampled at $B_R = 24$ MHz for three different representative SNR. (b) Corresponding MPEE when applying the MEDLL on the GPS (blue) and the GALILEO (green) signals.	73
2.14	Estimation of the delay (a), the Doppler frequency (b), the amplitude (c) and the phase (d) of the GPS L1 C/A LOS signal in presence of a single multipath using a MMLE and comparison of the RMSE with the corresponding MCRB, CRB and bias.	80
2.15	Estimation of the delay (a), the Doppler frequency (b), the amplitude (c) and the phase (d) of the GALILEO E1B LOS signal in presence of a single multipath using a MMLE and comparison of the RMSE with the corresponding MCRB, CRB and bias.	81
3.1	Typical GNSS-R geometry with the local elevation angle e and receiver height h	85
3.2	Geometrical direct to reflected signal path separation $c\Delta\tau$ for different receiver height h and satellite elevation e . (b) is a zoom-in for small values of h	86
3.3	Location of the Ayrolle Pond in France (a) and relatively to Toulouse (b) (credit: www.vidiani.com and www.google.com/maps).	89
3.4	Site location at the Ayrolle Pond (credit: www.geoportail.gouv.fr).	89
3.5	Satellite view of the experiment site with the associated mask (credit: www.geoportail.gouv.fr).	90
3.6	Picture (a) and Sketch (b) of the experiment site and relation between r_{\min} and e_{\max}	90
3.7	Examples of two tools to predict GNSS satellites positions: (a) GNSSView and (b) GNSS Planning Online.	91
3.8	Example of a skyplot computed using the GNSS simulator based on the SGP4 propagator.	92
3.9	Predicted visibility of GPS satellites (block IIF and III only) from the Gruissan experiment site. Color means visible, thick red means out of the mask.	93
3.10	Predicted visibility of GALILEO satellites from the Gruissan experiment site. Color means visible, thick red means out of the mask.	93
3.11	Mast with antenna near the Ayrolle Pond.	94
3.12	CNES dual polarization antenna (credit: CNES).	94
3.13	Buoy on the Ayrolle Pond.	95
3.14	(a) Experiment set-up with the buoy on the bottom right corner and the mast on the cliff on the top left corner and (b) around the mast (credit: CNES).	96
3.15	Experiment set-up of the control table.	97
3.16	Gruissan experiment schematic.	98

3.17 Skyplots for (a) GPS and (b) GALILEO satellites during rec. #3.	99
3.18 Skyplots for (a) GPS and (b) GALILEO satellites during rec. #6.	99
3.19 Estimated height using RTK technique for (a) the mast antenna and (b) the buoy antenna.	100
3.20 Estimated SNR for GPS satellite 27 during recording #6 on channel ch0 (L1, RHCP).	101
3.21 RMSE for the estimation of the main signal delay τ with 1S-MLE in the presence of a secondary signal with relative amplitudes $ \Gamma = 0.01, 0.1, 0.3, 0.5$ and different $\Delta\tau$ and F_s , for both GPS L1 C/A and L5I signals.	107
3.22 RMSE for the estimation of the reflected signal delay τ with the CRE (a–e) and 2S-MLE (d,f) in the presence of a secondary signal with relative amplitudes $ \Gamma = 0.01, 0.1, 0.3, 0.5$ and different excess delay $\Delta\tau$, for both GPS L1 C/A and L5I signals.	109
3.23 RMSE for the delay τ estimation considering a GPS L1 C/A signal at $F_s = 8$ MHz in blue and at $F_s = 20$ MHz in black (a) and a GPS L5I signal at $F_s = 20$ MHz (b) . The case study with a misspecified number of sources: one source is present, but a dual source CRE is used.	109
3.24 Non-coherent scenarios illustration each block is either white where the phase of the reflected path is equal to the phase of the coherent LOS signal, or colored where the phase is random.	110
3.25 RMSE results for the reflected signal delay estimation considering two GPS L1 C/A signals at $F_s = 8$ MHz, $\Delta\tau = 1/4$, $ \Gamma = 0.5$. (a) presents the VE performance and (b) presents the NC-CRE performance.	111
3.26 Path separation evolution with regard to the local elevation e of the transmitting satellite for a receiver height $h = 25$ m.	113
3.27 Illustration of the likelihood criterion Taylor approximations at different orders and relative delay $\Delta\tau$	117
3.28 Exact (plain lines) and 4 th order Taylor approximation (dashed lines) auto-correlation function for different sampling frequencies $F_s \in \{4, 8, 24\}$ MHz.	119
3.29 Relation between the path separation $\Delta\tau$, the sampling frequency F_s (expressed in number of $F_0 = 1.023$ MHz) and the relative error between the exact auto-correlation function and its 4 th Taylor approximation.	119
3.30 RMSE for the estimation of the path separation $c\Delta\tau$. (a) is with $\Delta\phi = \pi/3$ and (b) is with $\Delta\phi = 2\pi/3$. $\Delta\tau = 0.09$ C/A chips and relative amplitude is 0.5. 121	
3.31 RMSE for the estimation of the main signal time delay $c\tau_0$ with AMLE, 2S-MLE and 1S-MLE. (a) is with $\Delta\phi = \pi/3$ and (b) is with $\Delta\phi = 2\pi/3$	122
3.32 GPS PRN 27 elevation evolution during recording #6 of Gruissan data set.	123
3.33 MPEE of a 1S-MLE (a) and a CRE (b) in presence of crosstalk for GPS L5Q signal sampled at $F_s = 20$ MHz.	123
3.34 Estimated SNR at the output of the single matched filter processed with a 1S-MLE for channel ch2 (RHCP) and ch3 (LHCP) of recording #6.	124
3.35 Estimated path separation (a) and correspond height (b) between the reflected channel ch3 (LHCP) and the direct channel ch2 (RHCP) using a 1S-MLE.	125
3.36 Estimated SNR of the dual source matched filter using a dual source CRE on the RHCP ch2 channel (a) and the LHCP ch3 channel (b) . Results with the 1S-MLE approach are also displayed for comparison.	126

3.37	Estimated height between the reflected channel ch3 (LHCP) and the direct channel ch2 (RHCP) using a CRE.	127
3.38	Overview of a subsection of recording #6. (Left) is the estimated SNR on ch2, (Middle) the estimated SNR on ch3 and (Right) the estimated height using a CRE.	127
4.1	Derivation of the Rayleigh criterion. (a) for low elevation angle and (b) for large elevation angle.	133
4.2	Sunset Reflection over the sea surface (credit: Xavier Lubeigt).	134
4.3	Definition of the scattering vector \mathbf{q} along with the scattering angle β	134
4.4	Site location at the Puig Major on Mallorca Island, Spain (credit: www.stepmap.de).	136
4.5	Example of Mallorca experiment processed data. (Left) are the direct paths, (Right) are the reflected paths, (Top) are the L1 channels and (Bottom) are the L5 channels. Horizontal axis is in samples and vertical axis is in seconds (credit: IEEC).	138
4.6	Example of GPS L5 (a) and GALILEO E5A (b) reflected path carrier phase time series from complex waveforms averaged over 10 seconds.	139
4.7	ROC curves for the simple difference coherence test.	141
4.8	Histograms based on 3000 samples in the coherent regime (a) at minute 1, (b) at minute 3 and in the non-coherent regime (c) at minute 6 and (d) at minute 9.	142
4.9	Example of a comparison between empirical and theoretical CDF.	143
4.10	Example of GPS L5 (a) and GALILEO E5A (b) reflected path carrier phase time series from complex waveforms averaged over 10 seconds.	144
4.11	Mallorca experiment centered on the specular point with iso- β_0 and iso-delay lines.	146
4.12	Illustration of the diffuse reflection.	147
4.13	Equivalent block diagram of the reflecting surface.	147
4.14	Evolution of the constrained CRB obtained after reparameterization of the general dual source CRB for $F_s = \{2, 4, 8\}$ MHz as a function of the path separation $\Delta\tau$ expressed in GPS L1 C/A chips. The three points are the evaluation of the CRB derived in this contribution. This figure was obtained for a GPS L1 C/A signal with a noise level $\text{SNR}_{\text{out}}=33\text{dB}$, amplitudes $\boldsymbol{\rho}^T = (1, 0.5)$ and phases $\boldsymbol{\phi}^T = (0, 0)$. The vertical axis is multiplied by the speed of light to be converted to meters.	151
4.15	Amplitude-delay-profiles of the scenarios considered. It consists of (a) a set of four consecutive echoes with $\boldsymbol{\rho}_1^T = (1, 3/4, 1/2, 1/3)$ for scenario (a) and (b) $\boldsymbol{\rho}_2^T = (1, 0, 1/2, 1/3)$ for scenario (b). For these scenarios, the sampling frequency is set to $F_s = 4$ MHz.	153
4.16	Scenario (a): RMSE for the estimation of the parameters with IR-MLE($4, T_s$).	155
4.17	Scenario (b): RMSE for the estimation of the parameters with IR-MLE($4, T_s$).	156
4.18	Output of the misspecified IR-MLE(M, T_s) ($M = 6$): (a) Scenario (a) and (b) Scenario (b), $K = 4$	160
G.1	Projection of \mathbf{s}_{P+1} on the space spanned by the columns of \mathbf{A}_P , $P = 2$, $F_s = 8F_0$	204

List of Tables

1.1	List of GPS signals and their characteristics. From [TM17] and Navipedia [Eur].	22
1.2	List of GALILEO signals and their characteristics. From [TM17] and Navipedia [Eur].	24
2.1	Simulations scenarios for the CRB validation: (a) two signals totally parted ($\Delta\tau = 2$ chips), (b) a secondary path very close to the main signal ($\Delta\tau = 1/4$ chip), and (c) considered to showcase the difference between the 2S-MLE and CRE ($\Delta\tau = 1/8$ chip).	57
2.2	MCRB simulation settings for GPS L1 C/A signal.	79
2.3	MCRB simulation settings for GALILEO E1B signal.	79
3.1	Summary of the Guissan experiment recordings with corresponding configurations.	99
3.2	Overview of a subsection of recording #6.	128
G.1	Exemples of k_σ for GPS L1 C/A with $P = 2$	205

Table of Abbreviations and Acronyms

ACF	Auto-Correlation Function
AIC	Akaike Information Criterion
ALL	Amplitude Lock Loop
AltBOC	Alternative Binary Offset Carrier
AMLE	Approximate Maximum Likelihood Estimator
APE	Alternative Projecting Estimator
BOC	Binary Offset Carrier
bps	bits per second
BPSK	Binary Phase Shift Keying
CADLL	Coupled Amplitude Delay Lock Loop
CBOC	Composite Binary Offset Carrier
CCBR	Clean-to-Composite Bound Ratio
CCF	Cross-Correlation Function
CDF	Cumulative Density Function
cGNSS-R	Conventional Global Navigation Satellite System Reflectometry
CNES	Centre National d'Études Spatiales
CRB	Cramér-Rao Bound
CRE	CLEAN-RELAX Estimator
CSM	Condition Signal Model
CYGNSS	Cyclone Global Navigation Satellite System
DDM	Delay Doppler Map
DLL	Delay Lock Loop
DPE	Direct Positioning Estimation
DSSS	Direct Sequence Spread Spectrum
eCADLL	enhanced Coupled Amplitude Delay Lock Loop
ESA	European Space Agency
E-L	Early minus Late
FIM	Fisher Information Matrix
FIMLA	Fast Iterative Maximum Likelihood Algorithm
GLONASS	Global Navigation Satellite System
GLRT	Generalized Likelihood Ratio Test
GNSS	Global Navigation Satellite Systems

GNSS-IR	Global Navigation Satellite Systems Interferometric Reflectometry
GNSS-R	Global Navigation Satellite Systems Reflectometry
GPS	Global Positioning System
HRC	High Resolution Correlator
ICD	Interface Control Document
IEEC	Institut d'Estudis Espacials de Catalunya
IF	Intermediate Frequency
iGNSS-R	Interferometric Global Navigation Satellite System Reflectometry
IPT	Interference Pattern Technique
I/Q	In-phase/Quadrature
IR-MLE	Impulse Response Maximum Likelihood Estimator
KLD	Kullback-Leibler Divergence
LEO	Low Earth Orbit
LFM	Linear Frequency Modulation
LHCP	Left-Hand Circular Polarization
LIMS	Least-squares-based Iterative Multipath Super-resolution
LNA	Low Noise Amplifier
LOS	Line-of-Sight
LR	Likelihood Ratio
MCRB	Misspecified Cramér-Rao Bound
MDL	Minimum Descriptive Length
MDR	Multipath-to-Direct amplitude Ratio
MEDLL	Multipath Estimating Delay Lock Loop
MEO	Medium Earth Orbit
MLE	Maximum Likelihood Estimator
MMLE	Misspecified Maximum Likelihood Estimator
MMSE	Minimum Mean Squared Error
MMT	Multipath Mitigation Technique
MPEE	Multipath Error Envelope
MSE	Mean Squared Error
Msps	Megasamples per second
MUSIC	Multiple Signal Classification
NASA	National Aeronautics and Space Agency
NavIC	Navigation with Indian Constellation
NAVSTAR	Navigation System with Timing and Ranging
NC	Narrow Correlator
NC-CRE	Non-Coherent CLEAN-RELAX Estimator

NLOS	Non-Line-of-Sight
NORAD	North American Aerospace Defense Command
OS	Open Service
PAC	Pulse Aperture Correlator
PARIS	Passive Reflectometry and Interferometry System
PD	Probability of Detection
PDF	Probability Density Function
PDP	Power Delay Profile
PFA	Probability of False Alarm
PLL	Phase Lock Loop
PRN	Pseudo-Random Noise
PSD	Power Spectral Density
PVT	Position-Velocity-Time
QZSS	Quasi-Zenith Satellite System
RF	Radio Frequency
RHCP	Right-Hand Circular Polarization
RMSE	Root Mean Squared Error
ROC	Receiver Operator Characteristic
RTK	Real-Time Kinematic
SAGE	Space-Alternating Generalized Expectation-maximization
SGP	Simplified General Perturbations
SNR	Signal-to-Noise Ratio
SPIR	Software PARIS Interferometric Receiver
SV	Space Vehicle
TDS-1	Technology Demonstration Satellite-1
TLE	Two-Line Element
TMBOC	Time-Multiplexed Binary Offset Carrier
UAV	Unmanned Aerial Vehicle
UK	United Kingdom
US	United States
USM	Unconditional Signal Model
UTC	Universal Time Coordinated
VC	Vision Correlator
VE	Variance Estimator
1S-MLE	Single Source Maximum Likelihood Estimator
2S-MLE	Dual Source Maximum Likelihood Estimator

Introduction

Context

Global Navigation Satellite Systems (GNSS) have been used for decades as a way to obtain position, velocity and timing anywhere on Earth. GNSS receivers are now integrated into many different devices, ranging from smartphones to Low Earth Orbit (LEO) satellites. It is fascinating how such a system was revisited even before the first GPS constellation was fully operational. In 1993, researchers from the European Space Agency (ESA) published a first study on how to exploit GNSS signals as signals of opportunity [Mar93]. The idea was to collect signals reflected from the Earth's surface to extract information on the the reflecting surface geophysical properties, a concept called GNSS reflectometry (GNSS-R). Since then, GNSS-R has been applied to different GNSS constellations (e.g., GPS, GALILEO, BeiDou), and from different platforms: from ground-based stations to aircraft or satellites. With the recent commissioning of GPS Block III in 2019, that broadcast wideband signals over the L5 band, and the coming commissioning of the last GALILEO satellites in 2024, that transmit wideband AltBOC signals over the E5 band, GNSS, and therefore GNSS-R, face new challenges in terms of achievable performance and robustness.

For GNSS applications, these wideband signals were designed to be more robust to multipath, that is, to the reception of multiple reflections from the environment such as buildings, and to provide a better ranging accuracy. As a matter of fact, in ground-based GNSS-R, the challenges are the same: the presence of a strong reflection affects the use of standard GNSS-R techniques. Consequently, recent GNSS signals are promising for both navigation purposes and ground-based reflectometry.

On the other hand, in 2021 ESA gave its go-ahead for the satellite mission HydroGNSS (to be launched end of 2024) [Unw21], that consists of a pair of LEO satellites that will provide GNSS-R products to study permafrost, biomass, soil moisture and wetlands. This proves a clear interest for GNSS-R and its potential applications for climate observation.

Thesis Objectives

In this context, it is of great interest to understand how these recent signals improve existing techniques performance, and what can be expected from coming experiments. The main goal of this thesis is to provide comprehensive tools to assess the performance of GNSS-R techniques in different configurations.

A natural opening is to first focus on the GNSS multipath problem, which has been well studied ever since the first GNSS were operational. In Chapter 2, multipath, modeled as a dual source signal, is studied. A set of multipath mitigation strategies are compared using

the standard multipath metric: the multipath error envelope (MPEE). This first order metric is completed with a second order one, that comes from estimation theory: the Cramér-Rao bound (CRB). The derivation of the CRB in the dual source context paves the way to a better understanding of the effect of multipath on the ranging performance, and allows to build helpful metrics for future GNSS signal design. This bound is however not achievable for many low-cost receivers when exposed to multipath. An insight at the exact impact of multipath on such receivers is also proposed, under the scope of misspecified estimation.

In Chapter 3, the multipath is not seen as a nuisance anymore but a source of information. The signal model being the same, the goal is now to adapt the results from the previous chapter to ground-based GNSS-R. Multipath is now referred to as crosstalk and, using the CRB, standard GNSS-R techniques are compared to proposed algorithms. Two main approaches are investigated: i) when processing legacy narrowband signals for which standard GNSS-R techniques do not perform well, and ii) when processing more recent wideband signals that allow a user to get rid of the crosstalk effect. This work is supported by experimental data collected during this Ph.D. in collaboration with the *Centre National d'Études Spatiales* (CNES).

Finally, in Chapter 4, a geometry at a higher altitude is considered, and the dual source signal model is left behind, since the effect of the reflecting surface distorts the reflected signal. This is the case for airborne and spaceborne scenarios. In such scenarios, the signal is less coherent and tracking the carrier phase is not possible anymore. Tools to characterize the nature of the reflection are then needed if one wants to perform carrier phase-based GNSS-R, as in the future HydroGNSS mission for grazing elevation angles. Coherence indicators are then studied and applied to a data set provided by the *Institut d'Estudis Espacials de Catalunya* (IEEC). The reflected signal model, distorted by the reflecting surface, can be modeled as the convolution between the transmitted signal and the reflecting surface impulse response, that can be large in the case of a diffuse reflection. The CRB and estimators adapted to this model are then derived and validated. A final discussion on the determination of the size of the impulse response is drawn, with proposed hypothesis-based tests to tackle this detection problem.

In short, this thesis covers three distinct topics: i) GNSS multipath in harsh environments, ii) ground-based GNSS-R with an application to still water reflections, and iii) non-coherent reflections and diffuse scattering with an application to sea water reflection. These three topics and the general outline of this document are graphically displayed in Figure 1.

Chapters just mentioned are referring to tools and concepts from estimation theory, GNSS principles, multipath particularities and GNSS-R signal processing techniques. These notions are introduced in Chapter 1, which should be seen as a reference chapter.

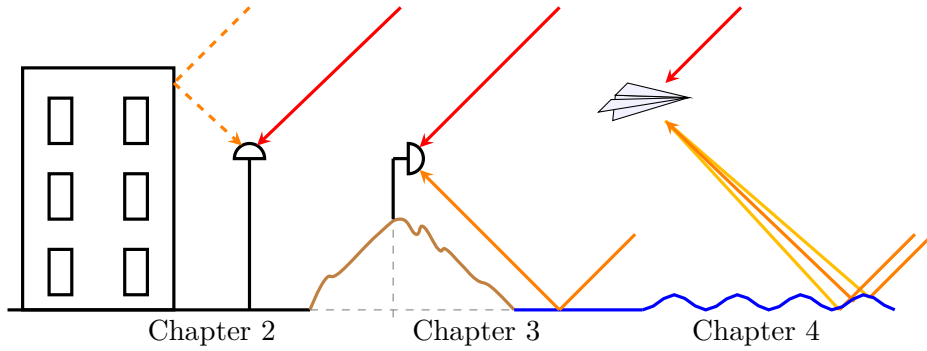


Figure 1: Graphical summary of the thesis.

Contributions

This thesis led to the following contributions:

- | | | |
|-----------|---|---|
| Chapter 2 | } | <p>GNSS Harsh Environment Performance</p> <ul style="list-style-type: none"> → Derivation of the MSE lower bound (CRB) and implementation of the corresponding MLE for the dual source conditional signal model. → Overview of existing multipath mitigation techniques using both existing tools (MPEE) and new ones (CRB). → Proposition of a new metric based on a ratio between the dual source and the single source signal model, named CCB_R, for future signal design. → Derivation and validation of the MCRB for multipath and interference scenarios, to account for the impact of a mismatched signal model. |
| Chapter 3 | } | <p>Ground-based GNSS-R Signal Processing</p> <ul style="list-style-type: none"> → Characterization of the crosstalk effect in close-to-ground GNSS-R scenarios. → Derivation and implementation of the AMLE, an algorithm adapted to (very) close in time sources based on a 3rd Taylor expansion. → Theoretical and experimental demonstration of the performance improvement using dual source estimators on wideband GNSS signals. |

Chapter 4	}	Non-Coherent Reflections and Diffuse Scattering
		→ Implementation of coherence detection procedure based on hypotheses tests, applied to real data sets.
		→ Derivation of the MSE lower bound (CRB), and implementation of the corresponding MLE, for the reflected signal modeled as the convolution with the reflecting surface impulse response.
		→ Proposition of different source detection procedures adapted to the impulse response signal model.

Collaboration

During this thesis, a four-month visit at the IEEC in Barcelona was done to collaborate on the coherence detection problem exposed in Chapter 4. This stay was the opportunity for two approaches to finally meet: the theoretical approach from Toulouse and the more practical approach from Barcelona. Results from this stay: i) a few results on coherence detection that may help future research, and ii) the conviction that theory and practice are just two sides of the same coin, and then it is worth working with both.

Publications

The following publications resulted from this thesis:

International Journal Articles

Published

- ❖ Corentin Lubeigt et al. “Joint Delay-Doppler Estimation Performance in a Dual Source Context.” In: *Remote Sensing* 12.23 (2020), p. 3894.
- ❖ Corentin Lubeigt et al. “On the Impact and Mitigation of Signal Crosstalk in Ground-Based and Low Altitude Airborne GNSS-R.” in: *Remote Sensing* 13.6 (2021), p. 1085.
- ❖ Corentin Lubeigt et al. “Clean-to-Composite Bound Ratio: A Multipath Criterion for GNSS Signal Design and Analysis.” In: *IEEE Transactions on Aerospace and Electronic Systems* 58.6 (2022), pp. 5412–5424.
- ❖ Corentin Lubeigt et al. “Untangling First and Second Order Statistics Contributions in Multipath Scenarios.” In: *Signal Processing* 205 (2023), p. 108868.

Submitted

- ✧ Lorenzo Ortega et al. “On the GNSS Synchronization Performance Degradation under Interference Scenarios: Bias and Misspecified CRB” submitted to *Navigation*.
- ✧ Corentin Lubeigt et al. “Band-Limited Impulse Response Estimation Performance” submitted after major revision to *Signal Processing*.
- ✧ Corentin Lubeigt et al. “Approximate Maximum Likelihood Time-Delay Estimation for Two Closely Spaced Sources” submitted after major revision to *Signal Processing*.

International Conference Papers

Published

- ✧ Corentin Lubeigt et al. “Multipath Estimating Techniques Performance Analysis.” In: *IEEE Aerospace Conference (AERO)*. 2022, pp. 1–6.
- ✧ Corentin Lubeigt et al. “Close-to-Ground Single Antenna GNSS-R.” in: *ESA Workshop on Satellite Navigation Technologies and European Workshop on GNSS Signals and Signal Processing (NAVITEC)*. 2022.

Accepted

- ✧ Lorenzo Ortega et al. “GNSS L5/E5 Maximum Likelihood Synchronization Performance Degradation Under DME Interferences.” In: *IEEE/ION Position, Location and Navigation Symposium*. 2023.

National Conference Papers

Published

- ✧ Corentin Lubeigt et al. “Les Signaux à Bande Large au Service de la Réflectométrie par GNSS à Site Bas.” In: *Groupe de Recherche et d’Etudes de Traitement du Signal et des Images (GRETSI)*. 2022.

Technical Notes

- ✧ Corentin Lubeigt et al. “Developments for MCRB Computation in Multipath Scenarios.” 2022.
- ✧ Corentin Lubeigt et al. “Details on Impulse Response Estimation and Size Determination.” 2022.

Concepts and Tools: From Estimation Theory to GNSS-R

Contents

1.1	Introduction	8
1.2	Background on Deterministic Estimation Theory	9
1.2.1	Conditional Signal Model	10
1.2.2	Misspecified Estimation	16
1.2.3	The Detection Problem	17
1.2.4	Wrap-Up on Estimation Theory	17
1.3	Global Navigation Satellite Systems	17
1.3.1	Principle	18
1.3.2	Constellations and Signals	18
1.3.3	GNSS Signal Processing	23
1.3.4	Wrap-Up on GNSS	27
1.4	The Multipath Problem	28
1.4.1	Multipath Models	28
1.4.2	Multipath Effect and Mitigation Solutions	30
1.4.3	Multipath Effect Metrics	33
1.4.4	Wrap-Up on Multipath	35
1.5	GNSS Reflectometry	35
1.5.1	GNSS-R Geometry	35
1.5.2	GNSS-R Processing Techniques	37
1.5.3	GNSS-R Observables	39
1.5.4	Performance Analysis	42
1.5.5	Wrap-Up on GNSS-R	42
1.6	Conclusion	42

Résumé

Ce premier chapitre a pour objectif de présenter les outils et concepts de la littérature sur lesquels s'appuient les chapitres suivants. En effet, le problème de réflectométrie par signaux de navigation ne peut être abordé que par la bonne compréhension des systèmes de navigation par satellites, GNSS, ainsi que de leurs limitations telles que les multitrajets. Ces systèmes qui permettent de se positionner sur Terre cachent donc un problème d'estimation qui s'appuie à son tour sur tout une théorie qu'il est bon d'introduire. Tout problème d'estimation repose sur des hypothèses (par exemple, sur la densité de probabilité du signal, sur les paramètres à estimer) qui permettent d'établir des bornes théoriques sur la précision de l'estimation. C'est donc bien en partant des concepts de base de la théorie de l'estimation qu'il faut aborder le domaine de la réflectométrie par signaux de navigation.

Le chapitre commence donc avec la Section 1.2 par un premier volet sur la théorie de l'estimation : de la définition d'un problème d'estimation jusqu'à la caractérisation d'un estimateur et de son lien avec la borne de Cramér-Rao. S'ensuit, dans la Section 1.3, une présentation générale des systèmes de navigation par satellite avec une attention particulière sur les systèmes américain (GPS) et européen (GALILEO). Ces systèmes de positionnement s'accompagnent de leurs challenges, notamment en zones urbaines dans lesquelles un récepteur GNSS reçoit également des signaux réfléchis sur les éléments urbains. Ces réflexions, connues sous le nom de multitrajets, viennent détériorer les performances sur le positionnement final du récepteur. La Section 1.4 développe la problématique du multitrajet et les moyens existants pour les mesurer et les contrer. Il n'y plus qu'un pas à faire pour voir les multitrajets non pas comme une interférence mais comme une source d'information. L'étude des signaux GNSS réfléchis sur la surface de la Terre est connue sous le nom de réflectométrie par GNSS, ou GNSS-R. Le GNSS-R exploite donc les signaux de navigation comme signaux d'opportunité ce qui ouvre la porte à de nombreuses applications de télédétection. Ces différentes techniques, applications et les challenges associés sont présentés dans la Section 1.5.

1.1 Introduction

This chapter proposes a general approach to the main concepts handled in this thesis. Global Navigation Satellite Systems (GNSS) Reflectometry (GNSS-R) has been a research topic for the last thirty years. GNSS-R exploits the reflection of GNSS signals on the Earth's surface, then using GNSS signals that were originally meant for navigation and timing applications as signals of opportunity. GNSS reflected signals have not always been of such interest. Indeed, in the early days of GNSS, and in most of today's high precision navigation applications, reflected signals, also referred to as multipath, are seen as a nuisance or interference that one wants to avoid. For this reason, the understanding of GNSS-R concepts and existing techniques requires the understanding of GNSS itself, along with its challenges such as the multipath problem. A GNSS consists of a constellation of satellites broadcasting known synchronized signals towards the Earth's surface. A receiver able to collect these signals is allegedly able to compute its position, velocity and timing on Earth. There are many different

GNSS, like the Global Positioning System (GPS) or GALILEO, and all of them have their own characteristics. In particular, they use ranging signals to allow the receiver to determine its distance to the transmitting satellite. This range determination is an estimation problem whose performance is limited by the design of the transmitted signal and the resources at hand. Having a clear idea of estimation theory main results would then help to understand how good a ranging system is, and what precision can be expected in a given scenario.

In short, this first chapter first aims at providing the very basic tools to approach GNSS-R. A first Section 1.2 is dedicated to estimation theory applied to signal processing, where the concept of the estimator and how to characterize it is addressed. Then a general presentation of GNSS, which hides an estimation problem, is proposed in Section 1.3, in which two main constellations, GPS and GALILEO, are considered. Section 1.4 reviews the GNSS multipath problem and its existing metrics and mitigation strategies. Finally, a last Section 1.5 is dedicated to the GNSS-R field of study with its current techniques and applications.

1.2 Background on Deterministic Estimation Theory

In many signal processing applications, users aim at extracting relevant information from a signal collected by a sensor. For instance, a radar system evaluates the distance and velocity of a target, and a communication system estimates bit values in order to demodulate a transmitted message. In all these examples, the received signal has a number of properties:

- it is a random process, either due to the environment noise (e.g., thermal noise) or the nature of the signal itself (e.g., speech, images),
- it depends on a vector of unknown parameters $\boldsymbol{\theta}$ which contains the information to be extracted,
- it can be sampled, so that a signal can always be represented as a vector of numbers.

An estimation problem can generally be expressed as follows: a vector of observations $\mathbf{x} = [x(1), \dots, x(N)]^T$ whose Probability Density Function (PDF), written as $p(\mathbf{x}; \boldsymbol{\theta})$, is parameterized by a vector of unknown parameters $\boldsymbol{\theta} = [\theta_1, \dots, \theta_L]^T$ that one wants estimate. To do this, one looks for an estimator $\hat{\boldsymbol{\theta}}$ that is a function of the observed data $\hat{\boldsymbol{\theta}} = \mathbf{g}(\mathbf{x})$.

Depending on the nature of the unknown vector of parameters $\boldsymbol{\theta}$, whether it is deterministic or not, and depending on whether the observed data PDF is known or not, the estimation problem at hand lies on a branch or another of estimation theory. In this thesis, the following assumption are made:

- the vector of unknown parameters is deterministic, that is, its components are assumed deterministic (no known prior),

- unless said otherwise, the observed data true PDF will always be known. In particular, as it will be mentioned repeatedly in the rest of this thesis, the assumed PDF will systematically be a multivariate complex Gaussian.

Under these assumptions, all the signal models seen in this thesis can be described as Conditional Signal Models (CSMs). The next section describes this signal model, along with a series of properties and tools that will be of use for the work presented in the rest of this document.

1.2.1 Conditional Signal Model

A CSM refers to a model for which the signal of interest is assumed non-random. The vector of unknown parameters $\boldsymbol{\theta}$ is deterministic. On the contrary, Unconditional Signal Model, or USM describe a model for which the signal of interest is assumed random: $\boldsymbol{\theta}$ has a prior distribution that needs to be taken into account. The link between these two models has been studied for decades and a number of results can be found in [SN90].

Let one consider the following CSM:

$$\mathbf{x} = \mathbf{A}(\boldsymbol{\theta})\boldsymbol{\alpha} + \mathbf{n} \quad (1.1)$$

where $\mathbf{A}(\boldsymbol{\theta}) = [\mathbf{a}(\theta_1), \dots, \mathbf{a}(\theta_L)]$ is the matrix of the measured signals \mathbf{a} that depends on the components of the unknown parameters $\boldsymbol{\theta}$, $\boldsymbol{\alpha}^T = (\alpha_1, \dots, \alpha_L)$ is the vector of real or complex amplitudes of the observed signals. Finally, \mathbf{n} is the noise vector. It is often assumed to be an additive complex circular white Gaussian noise vector with unknown variance σ_n^2 so that $\mathbf{n} \sim \mathcal{CN}(\mathbf{0}, \sigma_n^2 \mathbf{I}_N)$. Consequently the observed data PDF is also Gaussian with $\mathbf{x} \sim \mathcal{CN}(\mathbf{A}(\boldsymbol{\theta})\boldsymbol{\alpha}, \sigma_n^2 \mathbf{I}_N)$ and

$$p(\mathbf{x}; \boldsymbol{\theta}) = \frac{1}{(\pi\sigma_n^2)^N} e^{-\frac{1}{\sigma_n^2} \|\mathbf{x} - \mathbf{A}(\boldsymbol{\theta})\boldsymbol{\alpha}\|^2} \quad (1.2)$$

The CSM described in (1.1) fits a large number of applications such as radar and sonar [Van01b; Men11], spectral analysis [SM05], direction of arrival estimation [VBC13; VBC14; ZW88] and navigation [Das19]. It is adapted to multiple sensors systems such as antenna arrays [Van04] and to multiple sources scenarios as for an extended target [ZH16; Gar22].

1.2.1.1 Estimator Quality

Considering the CSM defined in (1.1) along with its PDF (1.2), the vector that contains all the unknown parameters can be defined as $\boldsymbol{\epsilon}^T = (\sigma_n^2, \boldsymbol{\theta}^T, \boldsymbol{\alpha}^T)$. Let $\hat{\boldsymbol{\epsilon}}$ be an estimator of this vector. In order to characterize this estimator and to compare it with other candidate estimators, a number of notions are needed:

- an estimator is a **random variable**. It is a function of the data and is consequently a

function of random variables with its own properties,

- by evaluating the distance between the expectation of the estimator and the true value of the vector of parameters to be estimated, one gets the **bias** of the estimator:

$$\mathbf{b}(\hat{\boldsymbol{\epsilon}}) \triangleq E\{\hat{\boldsymbol{\epsilon}}\} - \boldsymbol{\epsilon}, \quad (1.3)$$

where $E\{\cdot\}$ is the expectation operator.

A biased estimator is an estimator with $\mathbf{b}(\hat{\boldsymbol{\epsilon}}) \neq 0$, which implies a systematic error in the estimation. Naturally, one would rather work on unbiased estimators.

- The dispersion around the mean value of an estimator is characterized by its **variance** defined for a scalar estimator as:

$$\text{var}(\hat{\epsilon}) \triangleq E\left\{(\hat{\epsilon} - E\{\hat{\epsilon}\})^2\right\}. \quad (1.4)$$

For vectors, one refers to the **covariance matrix**:

$$\mathbf{C}_{\hat{\boldsymbol{\epsilon}}} \triangleq E\left\{(\hat{\boldsymbol{\epsilon}} - E\{\hat{\boldsymbol{\epsilon}}\})(\hat{\boldsymbol{\epsilon}} - E\{\hat{\boldsymbol{\epsilon}}\})^T\right\}. \quad (1.5)$$

The smaller this variance or covariance matrix is, the better the estimation is in terms of precision.

- Another metric that includes both bias and variance is the **Mean Squared Error** (MSE) defined as:

$$\text{MSE}(\epsilon_i) \triangleq E\left\{(\hat{\epsilon}_i - \epsilon_i)^2\right\} = \text{b}(\hat{\epsilon}_i)^2 + \text{var}(\hat{\epsilon}_i), \text{ for } i \in [1, L]. \quad (1.6)$$

For unbiased estimators, variance and MSE are the same.

Now let $\hat{\boldsymbol{\epsilon}}_N$ be an estimator of $\boldsymbol{\epsilon}$ based on N signal samples. $\hat{\boldsymbol{\epsilon}}_N$ is a **wide sense consistent** estimator if it converges in probability:

$$\lim_{N \rightarrow +\infty} P[\|\hat{\boldsymbol{\epsilon}}_N - \boldsymbol{\epsilon}\| < \delta] = 1, \quad \forall \delta > 0, \forall \boldsymbol{\epsilon} \quad (1.7)$$

where $P[\text{event}]$ denotes the probability of *event*. Similarly, $\hat{\boldsymbol{\epsilon}}_N$ is **consistent in mean square** if:

$$\lim_{N \rightarrow +\infty} E\left\{(\hat{\boldsymbol{\epsilon}}_N - \boldsymbol{\epsilon})(\hat{\boldsymbol{\epsilon}}_N - \boldsymbol{\epsilon})^T\right\} = 0, \quad \forall \boldsymbol{\epsilon} \quad (1.8)$$

and if an estimator is consistent in mean square, it is wide sense consistent as well.

Usually, users are more interested in consistency in mean square because it is more tractable for proofs and it implies the wide sense consistency (Markov-Bienaymé-Chebyshe inequality) means that the larger the number of samples N , the more the estimator is concentrated around the true value. The remaining question is then the convergence speed which may vary from an estimator to another. An optimal estimator would be a consistent estimator with a fast convergence, that is a minimum variance.

A tool that provides a lower bound to the variance of any locally unbiased estimator is the Cramér-Rao bound (CRB). Such lower bound is a key tool to compare different estimators and to evaluate how much an estimator can be improved. An unbiased estimator with its variance equal to the corresponding CRB is called an **efficient estimator**.

The CRB is defined for cases where the PDF $p(\mathbf{x}; \boldsymbol{\epsilon})$ fits the following regularity condition

$$E \left\{ \frac{\partial \ln p(\mathbf{x}; \boldsymbol{\epsilon})}{\partial \boldsymbol{\epsilon}} \right\} = \mathbf{0}, \quad \forall \boldsymbol{\epsilon}. \quad (1.9)$$

Then, for any unbiased estimator $\hat{\boldsymbol{\epsilon}}$, its covariance matrix $\mathbf{C}_{\hat{\boldsymbol{\epsilon}}}$ satisfies

$$\mathbf{C}_{\hat{\boldsymbol{\epsilon}}} - \mathbf{F}_{\boldsymbol{\epsilon}|\boldsymbol{\epsilon}}^{-1}(\boldsymbol{\epsilon}) \geq \mathbf{0}, \quad (1.10)$$

where $\mathbf{F}_{\boldsymbol{\epsilon}|\boldsymbol{\epsilon}}(\boldsymbol{\epsilon})$ is the Fisher Information Matrix (FIM) defined as

$$\mathbf{F}_{\boldsymbol{\epsilon}|\boldsymbol{\epsilon}}(\boldsymbol{\epsilon}) = -E \left\{ \frac{\partial^2 \ln p(\mathbf{x}; \boldsymbol{\epsilon})}{\partial \boldsymbol{\epsilon} \partial \boldsymbol{\epsilon}^T} \right\}, \quad (1.11)$$

and the second derivative is expressed at the true value of $\boldsymbol{\epsilon}$.

As a reminder, let \mathbf{M} be an hermitian matrix so that $\mathbf{M}^H = \mathbf{M}$. \mathbf{M} is positive semi-definite (also noted $\mathbf{M} \geq 0$) if and only if $\forall \mathbf{y}, \mathbf{y}^H \mathbf{M} \mathbf{y} \geq 0$.

As mentioned before, in a lot of applications, the signal model has a complex circular Gaussian distribution: $\mathbf{x} \sim \mathcal{CN}(\boldsymbol{\mu}(\boldsymbol{\epsilon}), \mathbf{C}(\boldsymbol{\epsilon}))$ where $\boldsymbol{\mu}(\boldsymbol{\epsilon})$ is the mean vector and $\mathbf{C}(\boldsymbol{\epsilon})$ is the covariance matrix. The Slepian-Bangs formulas [YB92; Kay93] give a simple expression of each component of the FIM:

$$\left[\mathbf{F}_{\boldsymbol{\epsilon}|\boldsymbol{\epsilon}}(\boldsymbol{\epsilon}) \right]_{k,l} = 2\text{Re} \left\{ \frac{\partial \boldsymbol{\mu}^H(\boldsymbol{\epsilon})}{\partial \epsilon_k} \mathbf{C}(\boldsymbol{\epsilon})^{-1} \frac{\partial \boldsymbol{\mu}(\boldsymbol{\epsilon})}{\partial \epsilon_l} \right\} + \text{Tr} \left\{ \mathbf{C}(\boldsymbol{\epsilon})^{-1} \frac{\partial \mathbf{C}(\boldsymbol{\epsilon})}{\partial \epsilon_k} \mathbf{C}(\boldsymbol{\epsilon})^{-1} \frac{\partial \mathbf{C}(\boldsymbol{\epsilon})}{\partial \epsilon_l} \right\}, \quad (1.12)$$

where $\text{Tr}\{\cdot\}$ denotes the trace operator.

Knowing the standard tools to characterize an estimator, the goal now is to build one as good as possible, ideally an efficient estimator. This is not always possible and the next section aims at defining a family of estimators based on the maximum likelihood principle.

1.2.1.2 Maximum Likelihood-based Estimators

It is not always possible to find an efficient estimator for a given problem. In signal processing [Ott93], a common alternative is to resort to the Maximum Likelihood Estimator (MLE) which has a number of asymptotic properties that makes it a relevant choice.

The MLE principle is simply to find the parameter $\boldsymbol{\epsilon}$ that maximizes the likelihood function

$p(\mathbf{x}; \boldsymbol{\epsilon})$, which is the PDF when \mathbf{x} is fixed and equal to the observed data,

$$\widehat{\boldsymbol{\epsilon}} = \arg \max_{\boldsymbol{\epsilon}} p(\mathbf{x}; \boldsymbol{\epsilon}) \quad (1.13)$$

In other words the MLE looks for the $\boldsymbol{\epsilon}$ that makes the observed data the most likely.

The MLE has a key particularity that makes it worth studying: it is asymptotically efficient, i.e., when the number of observation gets large [Van01a; SN90] or when the signal-to-noise ratio (as it will be defined later) gets large [Ren06], the MLE turns unbiased and its variance is equal to the CRB.

Jumping back to the general CSM (1.1) and its PDF (1.2), the MLE is looking for the vector $\boldsymbol{\epsilon}$ that maximizes the likelihood. One is often tempted to look at the log-likelihood to get rid of the exponential term

$$\widehat{\boldsymbol{\epsilon}} = \arg \max_{\boldsymbol{\epsilon}} \{\ln p(\mathbf{x}; \boldsymbol{\epsilon})\} = \arg \max_{\boldsymbol{\epsilon}} \left\{ -N \ln(\pi) - N \ln(\sigma_n^2) - \frac{1}{\sigma_n^2} \|\mathbf{x} - \mathbf{A}(\boldsymbol{\theta})\boldsymbol{\alpha}\|^2 \right\}. \quad (1.14)$$

For the estimation of the variance term, σ_n^2 , one can find the σ_n^2 that cancels the first derivative of the log-likelihood,

$$\frac{\partial \ln p(\mathbf{x}; \boldsymbol{\theta})}{\partial \sigma_n^2} = -\frac{N}{\sigma_n^2} + \frac{1}{\sigma_n^4} \|\mathbf{x} - \mathbf{A}(\boldsymbol{\theta})\boldsymbol{\alpha}\|^2, \quad (1.15)$$

so that that maximum likelihood estimate of the noise variance is simply:

$$\widehat{\sigma}_n^2 = \frac{1}{N} \|\mathbf{x} - \mathbf{A}(\boldsymbol{\theta})\boldsymbol{\alpha}\|^2. \quad (1.16)$$

By replacing this estimate in the log-likelihood (1.14) and omitting the constant terms, the MLE problem becomes

$$(\widehat{\boldsymbol{\theta}}, \widehat{\boldsymbol{\alpha}}) = \arg \max_{\boldsymbol{\theta}, \boldsymbol{\alpha}} \left\{ -\ln(\|\mathbf{x} - \mathbf{A}(\boldsymbol{\theta})\boldsymbol{\alpha}\|^2) \right\} = \arg \min_{\boldsymbol{\theta}} \left\{ \|\mathbf{x} - \mathbf{A}(\boldsymbol{\theta})\boldsymbol{\alpha}\|^2 \right\}. \quad (1.17)$$

Let $\mathbf{P}_{\mathbf{A}} = \mathbf{A}(\boldsymbol{\theta}) \left(\mathbf{A}(\boldsymbol{\theta})^H \mathbf{A}(\boldsymbol{\theta}) \right)^{-1} \mathbf{A}(\boldsymbol{\theta})^H$ be the orthogonal projector on the vector space defined by the column of $\mathbf{A}(\boldsymbol{\theta})$, also referred as the data vector space. Then $\mathbf{P}_{\mathbf{A}}^\perp = \mathbf{I} - \mathbf{P}_{\mathbf{A}}$ is the orthogonal projector on the noise space, and one can decompose the norm to be minimized as follows:

$$\|\mathbf{x} - \mathbf{A}(\boldsymbol{\theta})\boldsymbol{\alpha}\|^2 = \left\| \left(\mathbf{P}_{\mathbf{A}} + \mathbf{P}_{\mathbf{A}}^\perp \right) (\mathbf{x} - \mathbf{A}(\boldsymbol{\theta})\boldsymbol{\alpha}) \right\|^2 = \left\| \mathbf{P}_{\mathbf{A}} (\mathbf{x} - \mathbf{A}(\boldsymbol{\theta})\boldsymbol{\alpha}) \right\|^2 + \left\| \mathbf{P}_{\mathbf{A}}^\perp (\mathbf{x} - \mathbf{A}(\boldsymbol{\theta})\boldsymbol{\alpha}) \right\|^2, \quad (1.18)$$

and resorting to the definition of the projectors, one gets

$$\|\mathbf{x} - \mathbf{A}(\boldsymbol{\theta})\boldsymbol{\alpha}\|^2 = \left\| \mathbf{A} \left(\left(\mathbf{A}(\boldsymbol{\theta})^H \mathbf{A}(\boldsymbol{\theta}) \right)^{-1} \mathbf{A}(\boldsymbol{\theta})^H - \boldsymbol{\alpha} \right) \right\|^2 + \left\| \mathbf{P}_{\mathbf{A}}^\perp \mathbf{x} \right\|^2. \quad (1.19)$$

Remembering (1.17), the goal is to minimize both terms of (1.19). The first term minimization

yields a closed-form for the estimation of the complex amplitude:

$$\hat{\alpha} = \left(\mathbf{A}(\boldsymbol{\theta})^H \mathbf{A}(\boldsymbol{\theta}) \right)^{-1} \mathbf{A}(\boldsymbol{\theta})^H \mathbf{x}, \quad (1.20)$$

and the minimization problem reduces to

$$\hat{\boldsymbol{\theta}} = \arg \min_{\boldsymbol{\theta}} \left\{ \left\| \mathbf{P}_{\mathbf{A}}^{\perp} \mathbf{x} \right\|^2 \right\} = \arg \max_{\boldsymbol{\theta}} \left\{ \left\| \mathbf{P}_{\mathbf{A}} \mathbf{x} \right\|^2 \right\}. \quad (1.21)$$

Three interpretations can be proposed for this reduced MLE:

- $\mathbf{P}_{\mathbf{A}(\hat{\boldsymbol{\theta}})} \mathbf{x}$ maximizes the projection of the noisy data \mathbf{x} on the data vector space defined by \mathbf{A} ,
- $\mathbf{P}_{\mathbf{A}(\hat{\boldsymbol{\theta}})} \mathbf{x}$ can be seen as a correlation coefficient between the received signal \mathbf{x} and the signal model $\mathbf{A}(\boldsymbol{\theta})$,
- the operation $\mathbf{P}_{\mathbf{A}} \mathbf{x}$ can be seen as matched filtering as detailed in Section 1.3.3.

The MLE is then a powerful estimator thanks to its asymptotic properties, but depending on the signal model and the number of parameters to estimate, it may turn to be a multi-dimensional, highly non-linear optimization problem, which can make it intractable because of the computational cost. For this reason, a lot of alternative algorithms that aim at simplify the MLE were derived in the literature. In particular, for the multiple sources problem, the joint M sources MLE can be quite long to solve and users apply a sub-optimal processing by dividing this M -dimensional search into M 1-dimensional search, for instance. Here are two examples that operate this dimensional reduction:

- the CLEAN-RELAX estimator (CRE) [LS96] which is an extension of the CLEAN algorithm used in astrophysics. The idea is to iteratively minimize the likelihood term with regard to a single source: in practice, in order to update the estimation of the k -th signal, the algorithm subtracts the $M - 1$ other signals and applies a single source processing on the remaining data. In a dual source context, the CRE simply estimates a source with a single source MLE processing and then removes this estimate from the received signal, in order to estimate the other source in the residue. Then, it subtracts the secondary source from the received signal and updates the estimate of the first one. This goes on until the total likelihood value does not change much from an iteration to the next. Figure 1.1 shows the first and last steps of the CRE in a dual source context. The displayed curves are the output of each single source processing for the first (blue) and the secondary (orange) sources. The problem here is a problem of two signals with an unknown delay.
- the Alternating Projection estimator (APE) introduced in [ZW88] aims at minimizing the likelihood term iteratively with regard to a single source but considering the amplitudes of all the sources: in short, it iteratively minimizes the likelihood criterion by changing only the parameters of the considered source and keeping fixed the estimates

of the other sources. In a dual source context, if each source has only one parameter to be estimated, $\boldsymbol{\theta}^T = (\theta_1, \theta_2)$, this minimization can be graphically seen as a stair-shape optimization process, as shown in Figure 1.2.

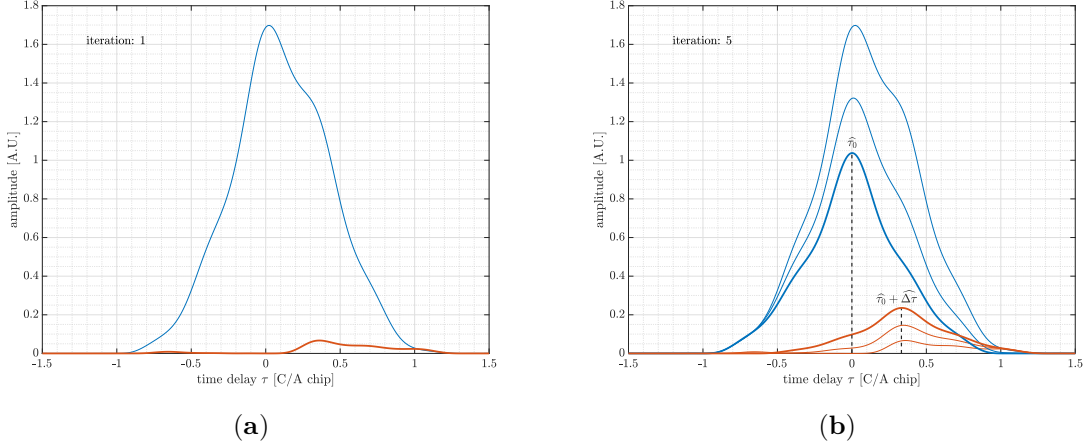


Figure 1.1: Example of the CRE algorithm for the estimation of the time-delay of two sources. (a) is the single source likelihood term of the first iteration (the expected shapes should be symmetric). (b) is the three consecutive steps where the blue curves are associated to one source and the orange curves are associated to the other. The final curves, marked with the vertical black lines, are symmetric as expected.

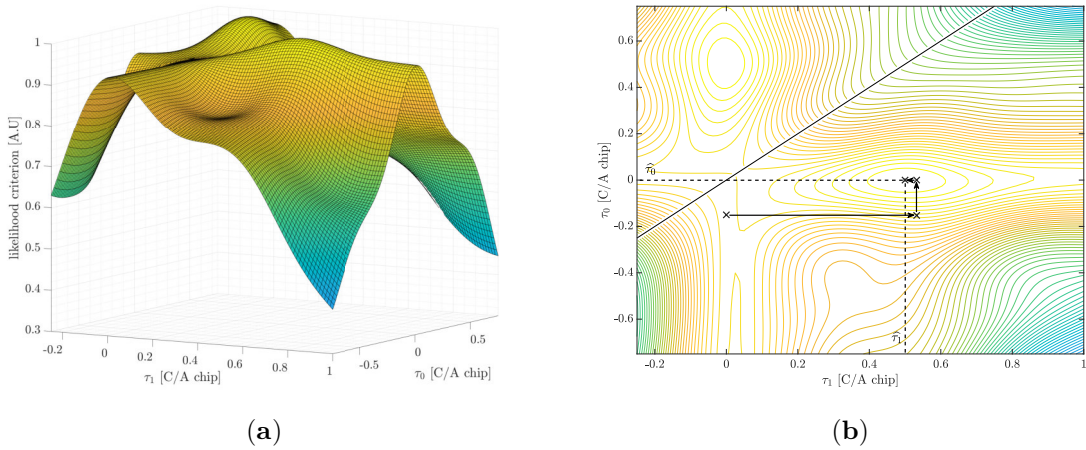


Figure 1.2: Example of the APE algorithm for the estimation of the time-delay of two sources. (a) is the dual source likelihood function to be maximized and (b) is a contour plot of the same function with the stair-shaped trajectory of the APE algorithm iterative steps.

Other approaches exist to tackle the problem of the MLE complexity. In some cases, assumptions on the signal model can lead to simplifications as in [VBC14] with the Approximate Maximum Likelihood Estimator (AMLE). In different configurations, as in an array of sensors, powerful algorithms have been studied for decades and are still used as a reference, like the Multiple Signal Classification (MUSIC) [Sch86] or even the Capon algorithm [Cap69].

1.2.2 Misspecified Estimation

So far, the estimation problem was assuming a good knowledge of the signal model under study. With this knowledge, the data PDF can be written, the corresponding CRB evaluated and the MLE or at least sup-optimal versions of it can be implemented. However, the signal model is not always well known, or alternatively, the true model leads to too complex estimators and a way to tackle this issue is to assume a simplified signal model. When the assumed model differs from true data model, it is said to be misspecified. Such a misspecification may affect the overall estimation performance in terms of bias and variance. This problem has been studied for a long time [Hub67; Aka74; Whi82].

Let $p(\mathbf{x})$ be the PDF of the true data signal model and $f(\mathbf{x}; \boldsymbol{\theta})$ be the PDF of the assumed data signal model. If one applies the misspecified MLE (MMLE), that is, the MLE that corresponds to the assumed signal model, to the observed data \mathbf{x} , in the limit of large sample support or at high SNR for the CSM, the estimated $\hat{\boldsymbol{\theta}}$ would be the one that minimizes the Kullback-Leibler Divergence (KLD) between the PDF of the true and the assumed signal model:

$$\hat{\boldsymbol{\theta}} = \arg \max_{\boldsymbol{\theta}} \{f(\mathbf{x}; \boldsymbol{\theta})\} = \arg \min_{\boldsymbol{\theta}} \{D(p_{\mathbf{x}}||f_{\mathbf{x}})\} = \arg \min_{\boldsymbol{\theta}} \{E_p \{\ln p(\mathbf{x}) - \ln f(\mathbf{x}; \boldsymbol{\theta})\}\} \quad (1.22)$$

Such estimate may vary significantly from the expected value depending on the degree of misspecification of the considered scenario.

An important result, recalled in [For17], regarding the MMLE is that, asymptotically:

- it converges in probability to a fixed value called pseudo-true parameter, noted $\boldsymbol{\theta}_{pt}$,
- it is consistent and the corresponding variance is equal to a lower bound provided by the so-called Misspecified CRB (MCRB).

In short the MMLE is an efficient estimator of this pseudo-true parameter.

The MCRB is a generalization of the CRB introduced in Section 1.2.1.1, its expression is:

$$\mathbf{MCRB}(\boldsymbol{\theta}_{pt}) = \mathbf{A}(\boldsymbol{\theta}_{pt})^{-1} \mathbf{B}(\boldsymbol{\theta}_{pt}) \mathbf{A}(\boldsymbol{\theta}_{pt})^{-1}, \quad (1.23)$$

where,

$$[\mathbf{A}(\boldsymbol{\theta}_{pt})]_{k,l} = E_p \left\{ \left. \frac{\partial^2 \ln f(\mathbf{x}; \boldsymbol{\theta})}{\partial \theta_k \partial \theta_l} \right|_{\boldsymbol{\theta}=\boldsymbol{\theta}_{pt}} \right\}, \quad (1.24)$$

$$[\mathbf{B}(\boldsymbol{\theta}_{pt})]_{k,l} = E_p \left\{ \left. \frac{\partial \ln f(\mathbf{x}; \boldsymbol{\theta})}{\partial \theta_k} \right|_{\boldsymbol{\theta}=\boldsymbol{\theta}_{pt}} \cdot \left. \frac{\partial \ln f(\mathbf{x}; \boldsymbol{\theta})}{\partial \theta_l} \right|_{\boldsymbol{\theta}=\boldsymbol{\theta}_{pt}} \right\}. \quad (1.25)$$

These expressions highly depend on the model misspecification. Depending on the scenario, they can be further developed to obtain nicer forms.

With this section, one is now able to characterize misspecified estimators when the data model is unknown and a misspecification cannot be avoided. Another way to go around the problem is naturally to try and change the assumed signal model in order to find a better specification. For instance, when the number of sources is unknown, it might be worth trying to add a source in the signal model rather than getting biased estimates. The next section presents different approaches to determine the number of sources.

1.2.3 The Detection Problem

The detection problem refers to the problem of determining the number of sources that are contained in the received signal. It applies to radar, sonar [BSK85], navigation [Kap] and many other applications where the user wants to know if there is a source and how many there are.

In the literature, many ways were developed to tackle this signal detection problem. In high resolution arrays, the number of sources is estimated based on the study of the eigenstructure of the observations covariance matrix with information-theoretic criterion to minimize [WK85], such as the Akaike Information Criterion (AIC) [Aka74] or the Minimum Descriptive Length (MDL) [WZ89; Ris78]. These criteria may be simplified considering the relevancy of the parameters to estimate [Won90]. It can also be done by performing series of hypothesis tests with bootstrapping [BZP02] or resorting to the Benjamini-Hochberg procedure [Chu07; BH95]. Other studies propose a solution based on random matrix theory [KN09] or subspace considerations [Gar19; WA21].

1.2.4 Wrap-Up on Estimation Theory

In this section the main tools of deterministic estimation (and detection) theory were introduced in a rather general case. A focus was however done on the Gaussian CSM that fits a large number of applications. In the following, one of these applications, namely satellite-based navigation, will be further detailed.

1.3 Global Navigation Satellite Systems

Navigation refers to the science of monitoring and controlling the movement of an object from a point to another. It can be a person hiking in the mountain and using a paper map, a compass and landmarks to find its way to the peak. It can also be any vehicle, on Earth, sailing or flying, that needs to know its position, its velocity and possibly its orientation. It is clear that depending on the aids used, there are many ways to navigate. The category of navigation solutions that exploit RF signals is called radionavigation.

In the late 1970's the United States (US) launched their very first Navigation System

with Timing and Ranging (NAVSTAR) satellite. This was the first satellite of the Global Positioning System (GPS) whose initial application was to obtain an estimate of the position, velocity and attitude of an object anywhere in the world. Since then, other countries developed their own navigation satellite system: among them the main ones are the Russian Federation Global Navigation Satellite System (GLONASS), the Chinese BeiDou system, the European GALILEO system, India's Navigation with Indian Constellation (NavIC), and Japan's Quasi-Zenith Satellite System (QZSS). The collection of all these systems and their augmentations is known as GNSS.

1.3.1 Principle

GNSS generally consists of a constellation of Medium Earth Orbit (MEO) satellites, or Space Vehicles (SV) that are dispatched on three or six orbital planes. The constellation features are such that from anywhere on the Earth surface a user can see four to eight satellites at any time.

Each satellite of the constellation is continuously transmitting towards the Earth's surface a known ranging signal. A GNSS receiver is then able to collect this signal and to identify the SV that sent it. It will also be able to estimate the time τ between the transmission and the reception of the signal. The time traveled in vacuum, τ , multiplied by the speed of light c is a measure of the radio-electric distance between the SV and the receiver. By doing this range estimation with three satellites and provided the fact that the receiver knows the position of all the SVs, it is possible to compute the position of the receiver by trilateration. This is the basic principle of GNSS as depicted in Figure 1.3.

To the three measurements, one has to add a fourth one to estimate the receiver clock uncertainty. Receiver clocks are usually standard quality oscillators that need to be continuously estimated, while SV have highly stable and precise atomic clocks. Solving the trilateration problem to get an estimate of the receiver position along with its velocity, using the Doppler effect, and the time, is also referred to as obtaining a Position-Velocity-Time (PVT) solution.

1.3.2 Constellations and Signals

1.3.2.1 General GNSS Signal Structure

The challenge in GNSS signal design is to build a family of signals that allows the receiver not only to detect them, but also to identify them to their corresponding transmitting SV. Besides, the chosen signal should guarantee a high ranging precision in order to solve accurately the PVT solution. For these reasons, a spreading technique, namely the Direct Sequence Spread Spectrum (DSSS) is applied on GNSS signals. This spreading technique consists of multiplying a low data rate data signal with a high data rate Pseudo-Random Noise (PRN) sequence. Once the signal is received, the spreading can be removed by cross-correlating the received signal with the correct PRN sequence. The choice of the PRN sequence must respect a number of

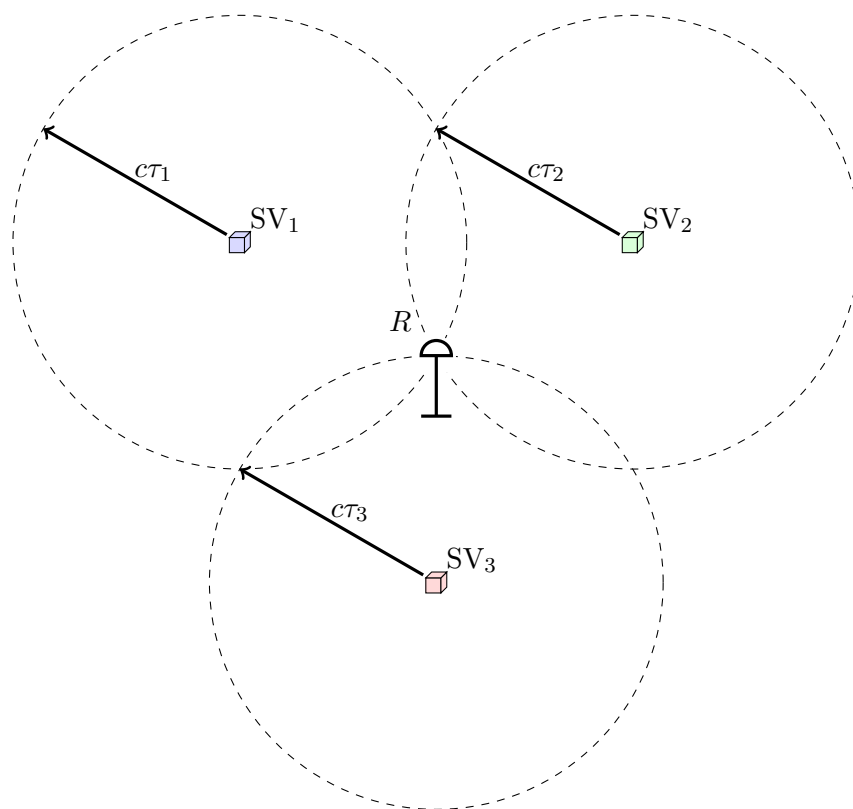


Figure 1.3: General Principle of GNSS.

properties: i) the auto-correlation function (ACF) of a given sequence should present a main peak significantly higher than the others, ideally this peak should be as sharp as possible to obtain a good estimation performance, and ii) the cross-correlation function (CCF) between two different sequences, corresponding to two different SVs of the same constellation, should have very low values. These properties ensure quasi-orthogonality between PRN codes. As an example, Figure 1.4 presents the ACF of GPS L1 C/A PRN 1 and the CCF between this sequence and the PRN 2. As it will be seen in the next two sections, depending on the constellation, various signals exist that present different signal waveforms, sequence length, etc. All the GNSS signals considered here can be described with three main elements:

- carrier frequency f_c which describes the center frequency of the transmitted signal,
- ranging code or PRN sequence $c(t)$, a family of codes that should be quasi-orthogonal. Each ranging code is a set of N_c discrete values of duration T_c called chips. The ranging code are often sent at a high rate, e.g., $F_0 = 1023000$ Hz or multiple of F_0 ,
- navigation message $d(t)$ that contains all the data necessary, for instance, to compute the position of the transmitting satellite, which is in turn needed to get a PVT solution. This coded message is sent on the GNSS data channels at a slow rate (for GPS L1 C/A, it is sent at 50 Hz). For modernized signals, only the data channel has a navigation message.

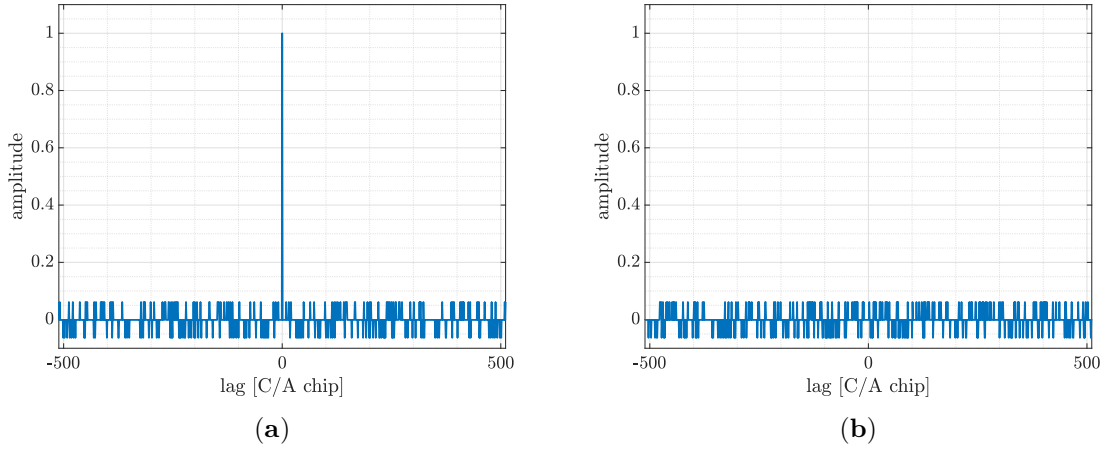


Figure 1.4: Quasi-orthogonality property of a PRN sequence. (a) is the ACF of GPS PRN 1 and (b) is the CCF of the same PRN with GPS PRN 2.

Note that for signals of the BOC family, an extra feature, the sub-carrier $sc(t)$ is also part of the signal definition. This sub-carrier allows to tune the spectral occupancy and the signal ranging performance.

The transmitted signal is then a product of all these components, modulated at frequency f_c ,

$$s_{Tx}(t) = d(t)c(t) \cos(2\pi f_c t) \quad (1.26)$$

This can also be seen as a layered structured signal, as graphically pictured in Figure 1.5 for a GPS L1 C/A signal, for which there is not sub-carrier signal $sc(t)$ and both the ranging code and navigation message have a rectangular pulse shape.

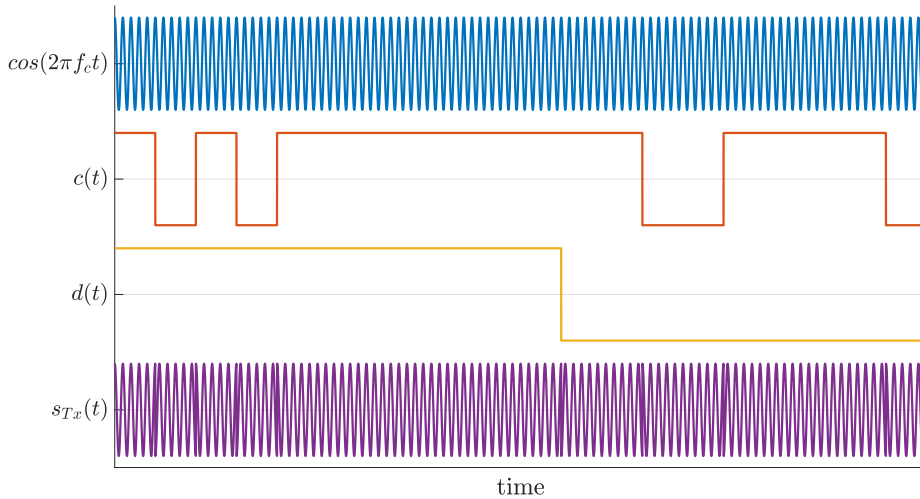


Figure 1.5: Layered structure of a GNSS signal.

1.3.2.2 GPS

The NAVSTAR GPS space segment consists of 24 or more satellites placed and equally spaced on 6 quasi-circular orbital planes with an inclination of 55° . With this layout, four or more satellites are always in view from any point on Earth, which allows a user's receiver to be able to get a PVT solution anywhere. The average altitude of the satellites is 20200 km and they have a revolution period of half a sidereal day. Consequently, taking into account the rotation of the Earth, the satellite ground tracks are revisited every sidereal day.

There are several GPS signals broadcast by all or part of the satellites on three bands: L1 with carrier frequency $f_{L1} = 1575.42$ MHz, L2 with $f_{L2} = 1227.60$ MHz and L5 with $f_{L5} = 1176.45$ MHz. Historically, the first signals sent over L1 were modulated by the Coarse Acquisition (C/A) code and the Precise (Encrypted) (P(Y)) code. The former being for civil open-access use, it is by far the most used. It is fully specified in the interface control document (ICD) [U.S22a]. It consists of a low rate navigation message (50 bits per second, or bps) spread with a PRN code from the Gold family [Gol67] of length $N_c = 1023$. The PRN code is modulated using a rectangular chip pulse shaping known as Binary Phase Shift Keying (BPSK) modulation at a clock rate of 1.023 MHz, also referred to as BPSK(1), where the number in parentheses is a multiple of the frequency $f_0 = 1.023$ MHz. Consequently, the code duration is of 1 ms and the main lobe of its Power Spectral Density (PSD) is 2.046 MHz wide.

Since the first generation of satellites, the GPS system has been modernized several times and now includes blocks IIR(M), IIF and more recently blocks III satellites that transmit military M code, L1C, L2C and L5 codes which have their own time and spectral properties. For instance the latter, L5 signal, fully described in its corresponding ICD [U.S22b] has the particularity to be separated into two orthogonal channels: i) the in-phase channel which has a BPSK(10) modulation and also carries the navigation message (data channel), and ii) the quadrature channel that also has a BPSK(10) modulation but no navigation message on top of it (pilot channel). Pilot channels are meant for long integration processing.

All the signals transmitted by the GPS satellites are summarized in Table 1.1 and their spectrum occupancy is depicted in Figure 1.6.

1.3.2.3 GALILEO

The GALILEO program is a European project to design and operate its own GNSS. The GALILEO space segment consists of 30 MEO satellites evenly dispatched on three quasi-circular orbital planes with a 56° inclination and at an average altitude of 23222 km. It takes 14 hours for a satellite to orbit the Earth. This yields a satellite ground track revisiting time of 7 sidereal days.

GALILEO signals are broadcast over three bands: E1 with carrier frequency $f_{E1} = f_{L1}$, E5 with carrier frequency $f_{E5} = 1191.795$ MHz and E6 with carrier frequency $f_{E6} = 1278.75$

Table 1.1: List of GPS signals and their characteristics. From [TM17] and Navipedia [Eur].

Band	Signal	Modulation	Chip Rate [Mbps]	Signal Bandwidth [MHz]	Codes Length [chip]	Data Rate [bps]
L1	C/A	BPSK(1)	1.023	2.046	1023	50
	P(Y)	BPSK(10)	10.23	20.46	-	50
	L1C	TMBOC(6,1)	1.023	14.322	10230	100
	M	BOCsin(10,5)	5.115	30.69	-	-
L2	P(Y)	BPSK(10)	10.23	20.46	-	-
	M	BOCsin(10,5)	5.115	30.69	-	-
	L2C (CM)	BPSK(1)	0.5115	2.046	10230	50
	L2C (CL)		0.5115	2.046	767250	-
L5	L5I	BPSK(10)	10.23	20.46	10230/10	100
	L5Q	BPSK(10)	10.23	20.46	10230/20	-

MHz. Moreover the E5 band can be seen as two side-by-side bands: E5A with carrier frequency $f_{E5A} = f_{L5}$ and E5B with carrier frequency $f_{E5B} = 1207.14$ MHz. One can then notice that E1 and E5A bands have the same carrier frequency as GPS L1 and L5 bands. This ensures interoperability between both constellations: a GPS receiver would only need an update on the processing stage but not on the RF front-end to become a GALILEO receiver. For GALILEO E1 Open Service (OS) signals, which are the most common signals, two channels, i) the data stream E1B and ii) the pilot stream E1C are sent simultaneously. Both components have a spreading code with 4092 chips during 4 ms and modulated by a Composite Binary Offset Carrier CBOC(6,1) modulation. A CBOC is defined as a combination of two Binary Offset Carrier BOC modulations [Bet01; HBS04], a BOC(1,1) and a BOC(6,1). BOC(m,n) is just an alternative to the BPSK pulse shaping. It is described by a sub-carrier $f_s = m \cdot f_0$ and a code chipping rate $f_c = n \cdot f_0$ and consists of the product of a rectangular pulse of frequency f_c and a sine or a cosine square wave sub-carrier of frequency f_s [TM17]. Depending on n , m and the choice between cosine and sine, the resulting modulation has different temporal and spectral properties.

The E5 band has a peculiar structure. As mentioned before, it can be seen as two side-by-side band that are constructed in a similar way: on both E5A and E5B bands, the transmitted signals are BPSK(10) modulations with an in-phase data channel and a quadrature pilot channels. If taken together, the resulting signals transmitted over the entire E5 band is then a complex signal called Alternative BOC or AltBOC [LAI08] that has a very wide band and allow potential high accuracy measurements.

All the OS GALILEO signals are fully described in the ICD [Eur21]. The different PRN, signal waveforms and spectral particulars can be found there in order to implement a GALILEO receiver. Besides, all the signals transmitted by the GALILEO satellites are summarized in Table 1.2 and their spectrum occupancy is displayed in Figure 1.7.

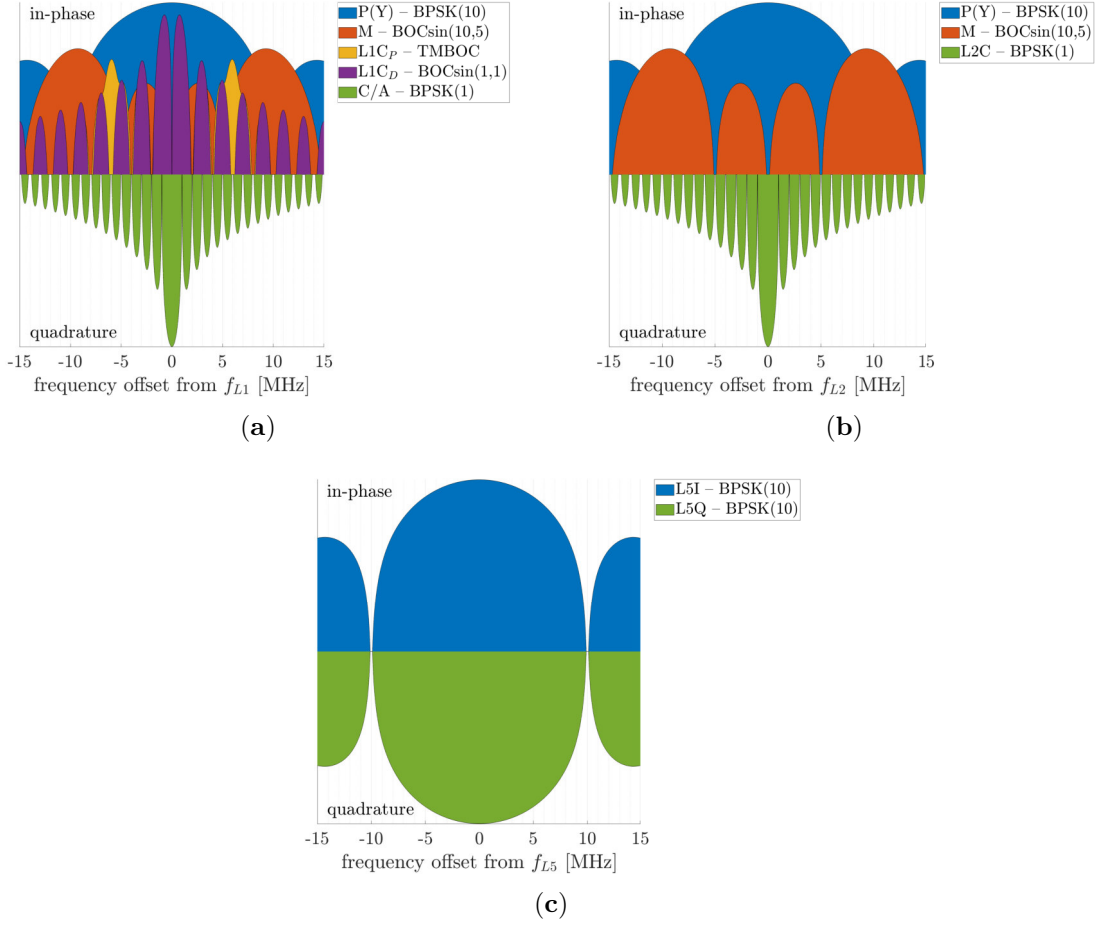


Figure 1.6: GPS signals power spectral density for all three bands: (a) is L1 band, (b) is L2 and (c) is L5.

1.3.3 GNSS Signal Processing

Now that an overview of the main GNSS signals has been done, the question of how these signals are processed to obtain a final position must be addressed. In particular, in this section, the focus is done on the two very first steps of a standard GNSS signal processing, namely, the acquisition and the tracking stages whose outputs are the pseudo-ranges between the receiver and each satellites in view.

Considering the reception of four different satellite signals of the same constellation and assuming an ideal model (all clocks synchronized, no group delay at transmitters and receiver level, no group delay from ionosphere and troposphere, no relativistic effect), the baseband signal, that is, after filtering, down-conversion and sampling, can be written as:

$$\mathbf{x} = \sum_{i=1}^4 \alpha_i \mathbf{s}_i(\tau_i, F_{d,i}) + \mathbf{w} \quad (1.27)$$

Table 1.2: List of GALILEO signals and their characteristics. From [TM17] and Navipedia [Eur].

Band	Signal	Modulation	Chip Rate [Mbps]	Signal Bandwidth [MHz]	Codes Length [chip]	Data Rate [sps]
E1	PRS	BOCcos(15,2.5)	2.5575	35.8	-	-
	E1B OS	CBOC(6,1)	1.023	14.322	4092	250
	E1C OS	CBOC(6,1)	1.023	14.322	4092/25	-
E5	E5AI	BPSK(10)	10.23	20.46	10230/20	50
	E5AQ	BPSK(10)	10.23	20.46	10230/100	-
	E5BI	BPSK(10)	10.23	20.46	10230/4	250
	E5BQ	BPSK(10)	10.23	20.46	10230/100	-
	E5	AltBOC(15,10)	10.23	51.15	10230	-
E6	PRS	BOCcos(10,5)	5.115	30.69	-	-
	E6B CS	BPSK(5)	5.115	10.23	5115	1000
	E6C CS	BPSK(5)	5.115	10.23	5115/100	-

where, \mathbf{w} is a complex additive white Gaussian noise so that $\mathbf{w} \sim \mathcal{CN}(\mathbf{0}, \sigma_n^2 \mathbf{I}_N)$ and for $n \in [1, N]$ the sample index,

$$\mathbf{x}^T = (\dots, x(nT_s), \dots), \quad (1.28)$$

$$\mathbf{s}_i(\tau_i, F_{d,i})^T = (\dots, s(nT_s - \tau_i) e^{-j2\pi F_{d,i}(nT_s - \tau_i)}, \dots), \quad (1.29)$$

$$\mathbf{w}^T = (\dots, w(nT_s), \dots), \quad (1.30)$$

T_s the sampling period, for $i \in [1, 4]$, α_i is the complex amplitude of the i -th signal, τ_i is the time-delay and $F_{d,i}$ is the Doppler frequency. This model or its continuous-time version are typical models that are used in most of the GNSS literature [Kap; TM17; Mor21].

For the considered CSM (1.27), the acquisition step aims to provide an estimate of $(\tau_i, F_{d,i})$ for each satellite in view. The classical approach is to compute the cross-correlation between the received signal and each satellite PRN code, and take the set (τ, F_d) that maximizes this function. This is somehow equivalent to a single source maximum likelihood estimator or 1S-MLE, as predicted in the interpretation of the MLE in Section 1.2.1.2. This CCF, also known as ambiguity function, can be defined as

$$R_{\mathbf{x}, \mathbf{s}_i}(\tau, F_d) = T_s \mathbf{s}_i(\tau, F_d)^H \mathbf{x} \quad (1.31)$$

Thanks to the quasi-orthogonality of the PRN sequences, if the signal of the i -th SV is in the received signal, the CCF will present a single peak that is located around the true values of $(\tau_i, F_{d,i})$. Otherwise, the CCF will present only small values that correspond to the noise floor. As an example, Figure 1.8 present the ambiguity function between a noisy received signal \mathbf{x} containing a single PRN with a given delay and Doppler frequency, say GPS L1 C/A PRN 1, and two clean replicas to test the presence of PRN 1 and PRN 2.

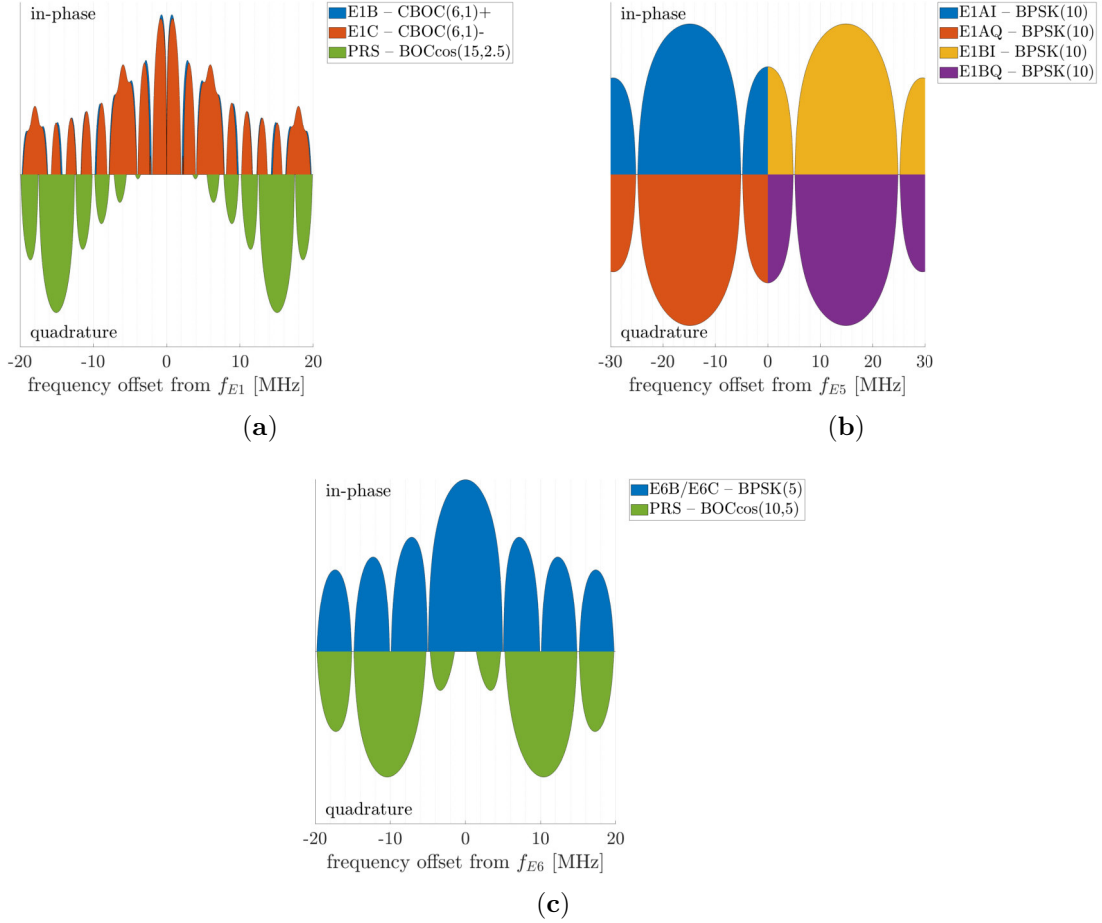


Figure 1.7: GALILEO signals power spectral density for all three bands: (a) is E1 band, (b) is E5 and (c) is E6.

Once a first rough estimation of $(\tau_i, F_{d,i})$ is obtained, they initialize the loops used for tracking the signal. To get an estimation of the position for a long time, this tracking step is necessary because both the receiver and the transmitting satellite are constantly moving, the geometry is varying through time. A standard tracking architecture called Early-minus-Late (E-L) uses a bank of three correlators called early ($E = R_{\mathbf{x},s_i}(\tau_{i,E}, F_{d,i})$), prompt ($P = R_{\mathbf{x},s_i}(\tau_{i,P}, F_{d,i})$) and late ($L = R_{\mathbf{x},s_i}(\tau_{i,L}, F_{d,i})$). The prompt correlator is centered between the early and the late correlators: $\tau_{i,L} - \tau_{i,P} = \tau_{i,P} - \tau_{i,E} = d/2$, where d is called the correlator spacing. Knowing that the CCF should be symmetric, by comparing the early and the late correlators should inform where the peak is relatively to the prompt correlator. As an illustration, in Figure 1.9, two scenarios are displayed, in Figure 1.9a the prompt correlator is on the left-hand side of the correlation triangle, it is too early. Equivalently, the early correlator amplitude is smaller than the late correlator: $E - L < 0$, in that case the next iteration should increase the estimated delay and this way shift all three correlators to the right-hand side. Figure 1.9b is the opposite scenario, the prompt is too late and the difference $E - L > 0$, the next iteration will aim at shifting all three correlators towards the left-hand

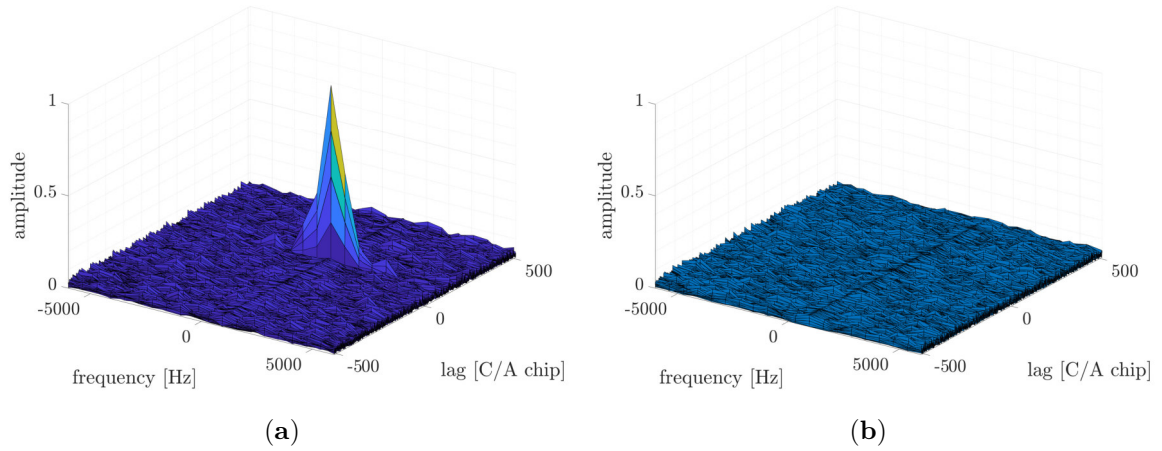


Figure 1.8: Example of ambiguity function in two cases, **(a)** the PRN tested is present in the received signal and **(b)** the PRN tested is not present in the received signal.

side. In short, the sign of the difference $E - L$ provides the direction in which the correlators should be shifted to place the prompt close to the peak. This is part of the Delay-Locked Loop

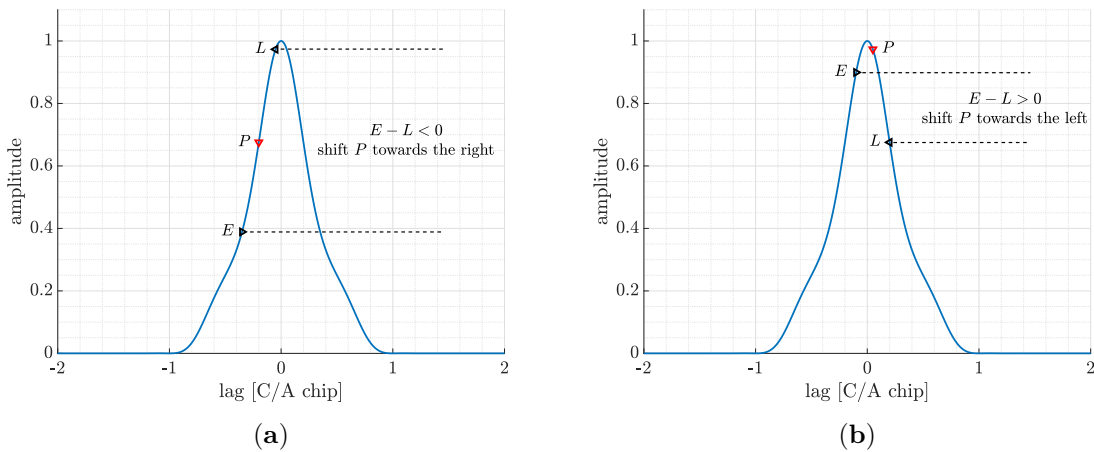


Figure 1.9: Example of the Early-minus-Late tracking architecture. **(a)** presents a scenario where the prompt is too early, and **(b)** presents the opposite scenario where it is too late.

(DLL), equivalently, a Phase-Locked Loop (PLL) is also implemented in order to track the variation of the phase. From the phase tracking, the Doppler frequency can also be computed. A standard implementation can be found in GNSS books such as [Kap; TM17] and will not be further discussed in this thesis.

So far the notion of noise was merely mentioned. In GNSS, as in any estimation problem, the noise is a fundamental parameter that determines if the estimation is possible or not, and with what performance. For the sake of clarity, in the following the Doppler frequency will be assumed compensated and will not appear anymore. Considering the reception of a signal s with an additive white Gaussian noise, the signal-to-noise ratio (SNR) can be defined at

the output of the matched filter as follows:

$$\text{SNR} \triangleq \frac{\|\alpha\|^2 \mathbf{s}^H \mathbf{s}}{\sigma_n^2} = (C/N_0) T_I \quad (1.32)$$

where σ_n^2 is the variance of the additive white Gaussian noise. C/N_0 is the carrier-to-noise density ratio and T_I is the integration time (proportional to the length of the considered signal).

With this SNR definition, if one generates 50 times the same 1 ms long signal with independent noise realizations at SNR= 15 dB, that is, $C/N_0 = 45$ dB.Hz, which is a realistic value, and then process this signal to estimate the time-delay (i.e., as in the acquisition processing), one would get Figure 1.10. The dispersion, or variance, observed in Figure 1.10b

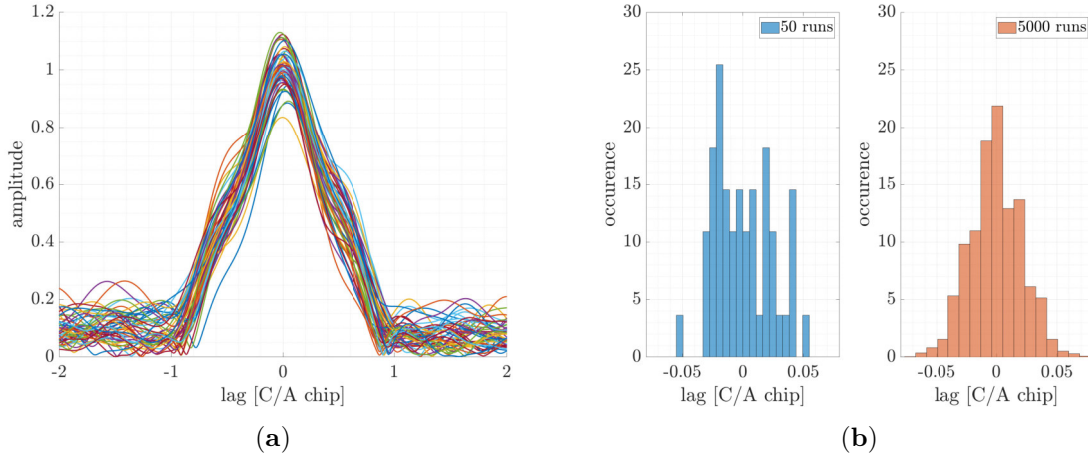


Figure 1.10: 50 realizations of a noisy signal in presence of noise. **(a)** presents the corresponding cross-correlation functions and **(b)** presents the histogram of the estimated time-delays for the 50 realizations and for 5000 realizations.

is induced by the presence of noise. As a matter of fact, this is an illustration of the behavior of the MLE. In the asymptotic regime, that is for large enough SNR, this variance should be equal to the CRB. In [Med20; Das20a], closed-form CRB for the navigation problem were derived and validated with the asymptotic properties of the MLE. Other signal models considering for instance the acceleration were also studied in [McP21].

1.3.4 Wrap-Up on GNSS

This section covered the main features of a branch of navigation: GNSS, which is based on constellations of satellites transmitting ranging codes along with navigation data. GNSS first processing steps are joint time-delay and Doppler frequency estimation problems, which can be fully characterized by the estimation theory tools introduced in Section 1.2. So far, GNSS was presented in an ideal way, but in practice, the received signal is not only polluted by additive noise but also by interfering signals such as multipath. This last concept is

introduced in the next section.

1.4 The Multipath Problem

In harsh environments such as urban canyons, a GNSS receiver may receive not only the LOS signal but also several replicas due to reflection and diffraction of the LOS signal upon reflecting objects, such as buildings, ponds, cars, etc. These allegedly undesired NLOS tend to degrade the performance of the GNSS receiver. This phenomenon, called multipath for a short version of *multiple paths*, is considered a self interference [Dov15] and remains an open issue in urban navigation, mainly because of its strong impact and its randomness. Being a great challenge for accurate positioning in urban environments, the multipath problem has dedicated chapters through several GNSS books as in [Kap, Ch. 9.5], [TM17, Ch. 15] or [Mor21, Ch. 22]. The following sections aim to summarize the main models used to characterize multipath, different mitigation strategies that can be found in the literature and metrics to assess the actual impact of multipath for GNSS signal or receiver architecture design.

1.4.1 Multipath Models

1.4.1.1 Dual Source Model

A simple way to apprehend the multipath problem is to consider a receiver that would collect the LOS signal along with a single specular reflection, which may occur on reflecting objects that span a significant fraction of a cross-section of the first Fresnel zone [BS87]. The first Fresnel zone is an ellipsoid about the LOS path between a transmitting antenna and a receiving antenna consisting of all points each with a combined path length to the receiving and transmitting antennas that is one-half wavelength longer than the LOS distance [TM17]. Under this hypothesis, if thermal noise is ignored and if the Doppler frequency is assumed perfectly compensated, the LOS signal (indexed 0) corrupted by a single multipath (indexed 1), at the output of the Hilbert's filter, can be written as:

$$x(t) = \rho_0 e^{j\phi_0} s(t - \tau_0) + \rho_1 e^{j\phi_1} s(t - \tau_1) \quad (1.33)$$

where for $i \in \{0, 1\}$, τ_i is the time-delay, ρ_i is the positive real amplitude and ϕ_i is the phase. For such a model, one can define several parameters that fully characterize the multipath scenario:

- the excess time-delay or path separation: $\Delta\tau = \tau_1 - \tau_0$, which is always positive since a NLOS path is always longer than the LOS,
- the multipath-to-direct amplitude ratio or MDR: $\text{MDR} = \rho_1/\rho_0$, which is generally smaller than 1 since reflection is attenuating the reflected signal,

- the phase difference $\Delta\phi = \phi_1 - \phi_0$.

Interestingly, for reflection-induced multipaths, it is possible to predict both the path separation and the phase difference thanks to geometry considerations. The reflection obeys the Snell-Descartes law, and the transmitting satellite is so far compared to the distance between the receiver and the reflecting point, that the two rays can be considered parallel. These assumptions naturally lead to the multipath scenario depicted in Figure 1.11. Consequently,

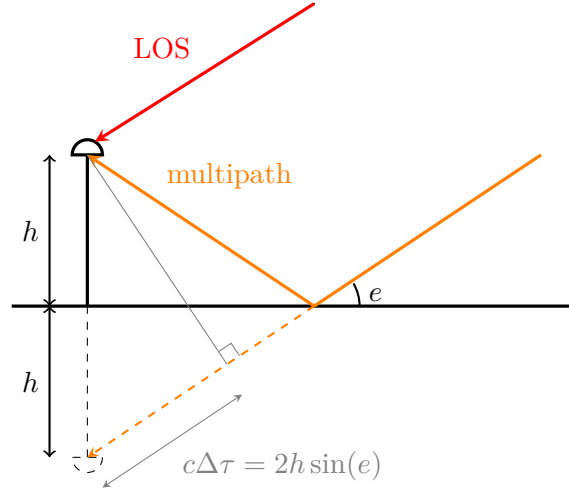


Figure 1.11: Ground multipath scenario and path separation prediction thanks to geometry consideration.

with the knowledge of the satellite elevation angle e and the height between the receiver and the ground h , one can deduce the path separation between direct and reflected paths.

1.4.1.2 Towards Realistic Models

The two-ray model is useful for multipath impact analysis, as it will be seen further, but it is very simplistic and other models, more representative, were developed in order to better understand the multipath effect.

A first and natural extension to the two-ray model is a N -ray model such as in [Kap]:

$$x(t) = \rho_0 e^{j\phi_0} \left(s(t - \tau_0) + \sum_{n=1}^{N-1} \frac{\rho_n}{\rho_0} e^{j\Delta\phi_n} s(t - \tau_0 - \Delta\tau_n) \right) \quad (1.34)$$

where, for the multipath indexed n , $\Delta\tau_n$ is its excess time-delay, ρ_n/ρ_0 its MDR and $\Delta\phi_n$ its phase difference. The expression (1.34) can also be displayed under a Power Delay Profile (PDP) as in Figure 1.12. This model, usually assumed time-invariant compared to the coherent integration time for the correlation, does fit multipaths on aircraft where reflections are often due to the airplane structure, but is less representative of terrestrial application where the propagation channel properties can vary significantly. This last example can correspond

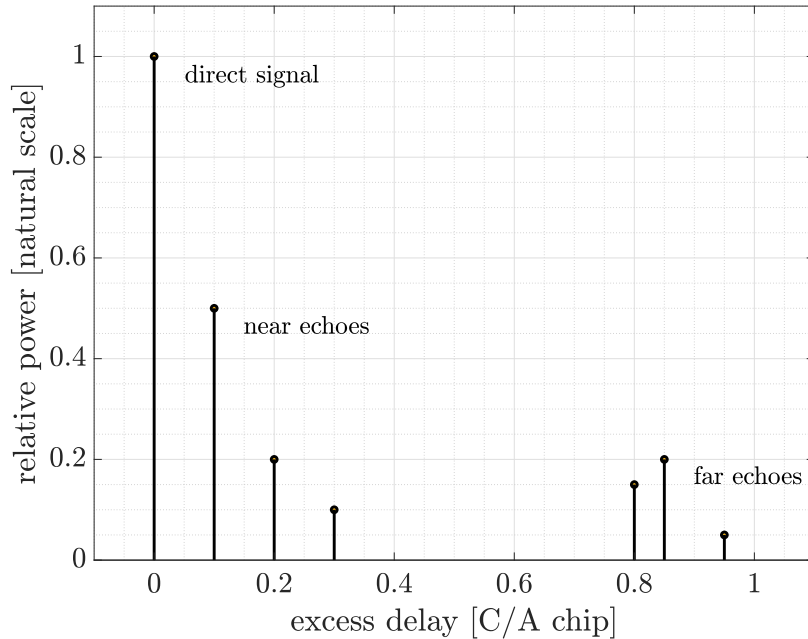


Figure 1.12: Example of PDP with the direct signal, near echoes and far echoes.

to a car driving in a city center for instance. In these cases multipath can be modeled by a large number of scatterers [BRS98] or by multipath fading channels as in [PS07, Ch. 13.1].

In [JBH96], a statistical model of the propagation channel was proposed, modeling the shadowing of the direct signal amplitude with a Rice distribution when there is LOS and Rayleigh when the direct signal is masked by an object. Besides, the number of near and far echoes are Poisson distributed, and their amplitudes are exponential distributed for the near echoes and Rayleigh distributed for the far echoes. Such a model allows enough flexibility to properly cover different environments.

1.4.2 Multipath Effect and Mitigation Solutions

As previously mentioned, multipath is a self-interference that pollutes the LOS signal and degrades the overall performance of the receiver. An illustration of this effect can be observed in Figure 1.13, where the cross-correlation of a received signal is displayed for different phase differences, a GPS L1 C/A signal with the RF front-end bandwidth set to 4 MHz, the excess time delay set to 0.25 L1 C/A chips and the MDR set to 0.5. From these figures, it is clear that multipath has a varying effect depending on the relative phase. The reflection can be constructive or destructive, which would affect the overall SNR and distort the triangular shape so that if an algorithm is tracking the maximum of this shape, it will necessarily be biased.

The next two sections list a number of existing strategies to mitigate this multipath

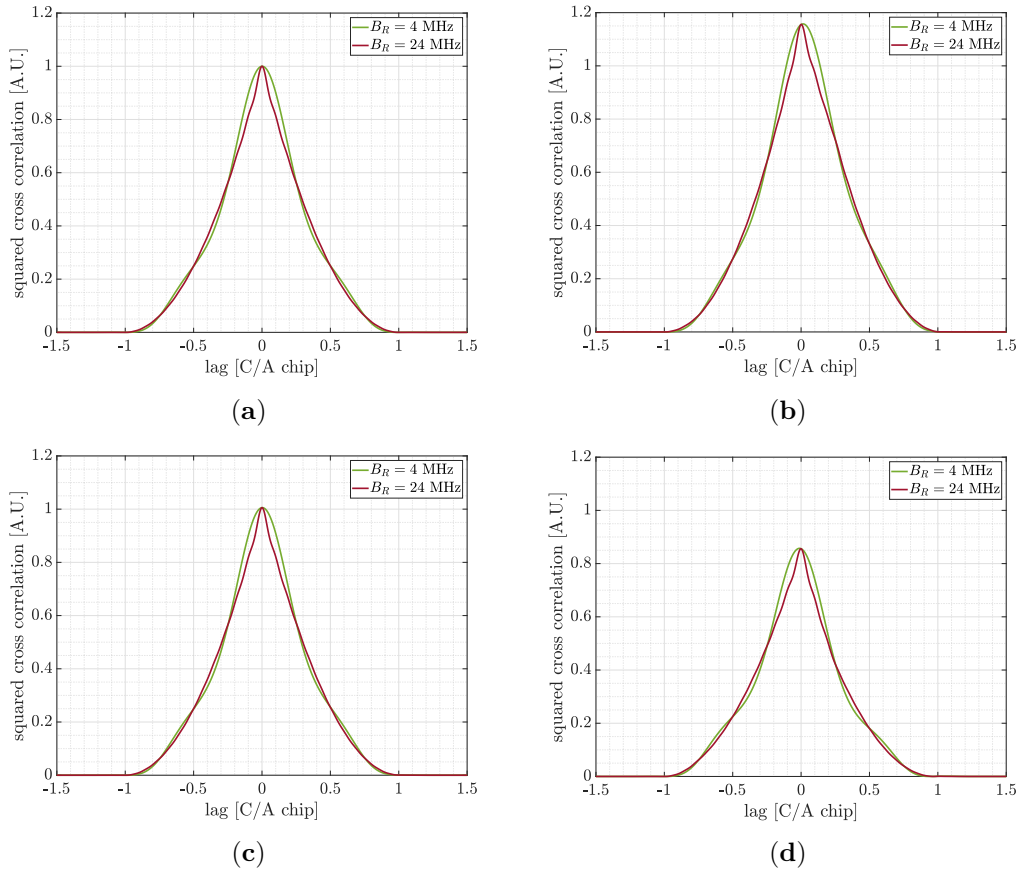


Figure 1.13: Multipath effect on the cross-correlation function between the single-multipath-corrupted signal and a clean replica of a GPS L1 C/A signal. (a) shows the auto-correlation function (without multipath), (b) shows the cross-correlation when the single multipath is in-phase with the LOS ($\Delta\phi = 0$), (c) is when the single multipath is in quadrature ($\Delta\phi = \pi/2$) and (d) is when it is out-of-phase ($\Delta\phi = \pi$). RF front-end bandwidth is equal to 4 MHz in green and 24 MHz in red, excess delay is equal to 0.25 L1 C/A chips and MDR equal to 0.1.

distortion effect. They are of two sorts:

- Non-estimating techniques: the algorithms of this category are trying to limit the effect of the multipath on the CCF but they are not trying to estimate the parameters of the multipath itself.
- Estimating techniques: the multipath is seen as an additional source with deterministic parameters and the algorithms of this section try to estimate them.

1.4.2.1 Non-Estimating Solutions

A first family of multipath mitigation strategy consists of modifying the bank of correlators in the receiver, in order to implement an algorithm that is more robust than the simple E-L

discriminator. A simple and very intuitive solution is the Narrow Correlator (NC) [VFF92] in which the spacing is reduced to a very small fraction of the width of the correlation triangle. Another common-sense approach is to add a couple of correlators (very early and very late) to evaluate the slope on each side of the correlation triangle, as it is done with the Early-Late Slope [TF94], the High Resolution Correlator (HRC) [MB99] or the Pulse Aperture Correlator (PAC) [JFS04]. A last group of estimators is directly working on the transmitted signal: it is either gated [MB99], that is, rearranged in time chunks in order to modify the CCF so that it is narrower, or averaged to try and reconstruct the transition chip as in [FJ05] with the Vision Correlator (VC).

1.4.2.2 Estimating Solutions

A second family of multipath mitigation strategy gathers algorithms which see the additional multipath as a deterministic signal with its own parameters (time-delay, amplitude, phase). There are many existing tools, but most of them are variants of the dual source MLE. A pioneer algorithm in multipath mitigation technology is the Multipath Estimating Delay Lock Loop (MEDLL) introduced by Van Nee in [Van92] and later in [Tow95]. This algorithm can be seen as a hardware implementation of the CRE seen in Section 1.2.1.2: it assumes a bank of several correlators which allow to estimate each multipath component using a maximum likelihood criteria. These estimated multipath signals are then subtracted from the measured signal. The cleansed signal can then be tracked with a standard E-L DLL. This approach has later been improved using a Newton method for the time-delay estimation with the Fast Iterative Maximum Likelihood Algorithm (FIMLA), presented in [SA08], or by coupling the DLL with an Amplitude Lock Loop (ALL) as in the Coupled Amplitude Delay Lock Loop (CADLL) introduced in [CDP10], further improved and tested in [CD11] and [Che13]. Other search dimension reduction were proposed for multi-source estimation, as in [Fle99], where a Space-Alternating Generalized Expectation-maximization (SAGE) was proposed for the general multipath problem. The SAGE can be related to the existing approach APE presented in Section 1.2.1.2. Similarly to the MEDLL, the maximization of a criterion of size P is alternately reduced to P maximization of a criterion of size one.

Naturally, the direct resolution of the multi-source likelihood has also been investigated. In [Wei02] Weill proposed a simple implementation of the 2S-MLE based on simplifications on the estimation of the complex amplitudes. This was named the Multipath Mitigation Technique (MMT). In the same paper, the author compared the MMT performance with the MMSE estimator [Wei95] that was seen at the moment as the best estimator for multipath, regardless the computational cost, and was used as a reference in terms of MSE substituting the CRB. Other contributions [NK13] based on least-squares approaches were also proposed, such as the Least-squares-based Iterative Multipath Super-resolution technique (LIMS).

As a conclusive remark the estimation of the multipath parameters is a challenging problem because of the increasing complexity. Starting from the MLE, and similarly to other fields like in radar, researchers tried to tackle the high dimensional maximization problem by dividing it into smaller and simpler problems. This is usually done under certain assumptions

which rarely hold when the relative path separation between consecutive multipath decreases.

1.4.3 Multipath Effect Metrics

As it has been seen so far, multipath is an additional interference term that is strongly correlated to the LOS signal. This tends to distort it, which inevitably leads to a performance degradation. The way to characterize this performance degradation is by looking at the error induced on the estimation of the LOS time-delay. Based on the multipath model used, different approaches to assess the multipath impact were proposed [HTB04]. These approaches differ in the multipath model considered and the assumptions on the multipath channel features and thermal noise level. The next sections present different metrics for multipath effect analysis: the first is a widely used tool and the others are variations of it.

1.4.3.1 Multipath Error Envelope

The Multipath Error Envelope (MPEE) aims at providing a rough rather than realistic idea of how much a signal is affected by a single multipath. Considering the simple two-ray model presented in Section 1.4.1.1 in a noise-free environment, one can build a first metric that captures all the possible errors on the LOS signal time-delay estimates in presence of a single multipath. This error depends on several parameters: the path separation between the LOS and the NLOS, the relative amplitude, or MDR and the relative phase $\Delta\phi$. By fixing the MDR, one can actually plot the error envelope of this induced error. This envelope is the MPEE and can be defined as follows [Kap, (9.65)]:

$$\text{MPEE} \triangleq (\max_{\Delta\phi} \{e(\text{MDR}, \Delta\tau, \Delta\phi)\}, \min_{\Delta\phi} \{e(\text{MDR}, \Delta\tau, \Delta\phi)\}) \quad (1.35)$$

where $e(\cdot)$ is the induced bias on the estimation of the LOS delay. For most of the receiver architectures, the min and max of the MPEE definition (1.35) are obtained when LOS and NLOS signals are in-phase (relative phase $\Delta\phi = 0$) and out-of-phase ($\Delta\phi = \pi$).

To compute the MPEE, one can simply apply a receiver architecture to a signal composed with a direct path and a multipath with an excess delay ranging from 0 to whatever. A well-known method to compute it is to use the estimated PSD of the modulation considered, and to exploit the Wiener-Lee relation to link the PSD with the ACF. The problem of this method is that it does not take into account the PRN code which slightly differentiate each signal. It also supposes a perfect knowledge of the entire PSD (at any frequency) which has no sense in a time limited world. The result cannot be something else than an estimation of the PSD convolved with a sine cardinal function because the signal is multiplied by a temporal gate. In this work, the MPEE are computed numerically by applying the algorithm under study on simulated signals. The effect of the RF front-end bandwidth along with the PRN code can then be observed directly. Figure 1.14 shows the MPEE for a GPS L1 C/A signal and a GALILEO E1B signal using a simple E-L architecture with two different spacing: one is a typical spacing of 1 C/A chip and the other is 0.1 C/A chip that corresponds to a NC. From

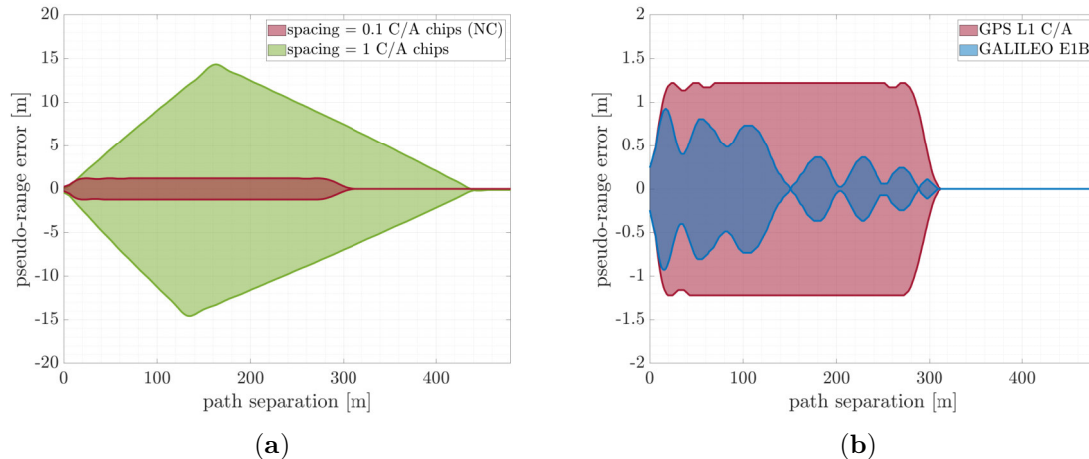


Figure 1.14: MPEE applied to a E-L architecture (a) with different spacing for a GPS L1 C/A signal and (b) with a fixed spacing for different signals: GPS L1 C/A and GALILEO E1B. Front-end filter bandwidth set to 24 MHz, MDR = 0.1 and integration time $T_I = 4$ ms.

these figures, it is possible to either compare the performance of two different architecture as in Figure 1.14a where the E-L spacing is changed, or to compare the performance of two different signals as in Figure 1.14b. It is clear that the MPEE is very informative and quickly provides an idea of the sensitivity of a given signal and a given receiver architecture to multipath, even though such a model is not realistic. This is the reason why the MPEE is so widely used for multipath impact analysis [TM17; Mor21; Jov10].

As a last remark, from a statistical point of view, since the study is done in a noise-free environment, the MPEE can be seen as the bias envelope of the misspecified estimator considered: for instance, without multipath the NC architecture is perfectly estimating the LOS time-delay, it is an unbiased estimator when the assumed signal model fits the true signal model, but when the true signal model includes a single multipath the NC assumed signal model is not correct anymore and a bias appears. These considerations can be related to model misspecifications introduced in Section 1.2.2.

1.4.3.2 More Realistic Approaches

MPEE is a very simple metric that can easily be tuned to be more informative. In [IAH05], the author lists different variants of MPEE with various complexity to take into account different features. As a first example, one can look at the area enclosed by the MPEE. The smaller this area is, the better the considered algorithm/signal performance is. Alternatively, the MPEE and its area can be averaged with or without weights to assess the performance for specific conditions. Another alternative to the MPEE can be obtained considering thermal noise and setting a fixed SNR. Then the idea is to evaluate the RMSE of the estimated time-delay of a considered estimator, as it is used in [BN12]. The multipath impact with a random relative phase uniformly distributed in $(0, 2\pi)$ is also studied in [Wei02], where the result is

linked to the MMSE estimator asymptotic performance. Finally, it is possible to evaluate a mean multipath error based on statistical channel models, as introduced in Section 1.4.1.2. These models can be more or less sophisticated depending on the scenario considered. Due to the complexity to obtain mean values because of the large number of random parameters, this study is however a little tedious compared to the simple and graphical MPEE.

1.4.4 Wrap-Up on Multipath

Multipath is a challenging problem in GNSS applications because of its randomness and its large impact in the overall estimation performance. For these reasons, it is often seen as a nuisance to be avoided or compensated, but reflected GNSS signals also carry their own information which could be of use in alternative applications. The next section proposes to dig into one of these alternative applications offered by reflected GNSS signals.

1.5 GNSS Reflectometry

The concept of GNSS reflectometry, or GNSS-R, is roughly 30 years old [Mar93]. Instead of considering reflected GNSS signals, such as multipath, as a nuisance or interference that the receiver must mitigate to obtain the best positioning solution, reflected signals are used as an additional source of information (i.e. signals of opportunity) for a different purpose.

GNSS-R can be seen as a bistatic radar [Sko08]: while most radar systems have the transmitter and the receiver at the same location (monostatic radar), bistatic systems use transmitters and receivers separated by a considerable distance. Such systems have been used for studying certain atmospheric phenomena and for military applications. This bistatic radar concept can naturally be extended to satellite signals. Since signals transmitted by a satellite get scattered off the Earth's surface, detecting these reflections by a separated passive receiver could provide some information about such surface. While, in principle, any satellite signal could be used, GNSS signals turn out to be particularly useful. In GNSS-R a single receiver picks up direct and reflected signals coming from multiple GNSS satellites to retrieve geo-physical parameters of the scattering surface (multistatic configuration). With the increasing number of GNSS satellites, a single receiver could potentially get signals from more than 20 emitters at the same time, thus obtaining a high number of independent observations of the same scene, which could either be used to increase the instrument's swath, or to reduce the noise in the estimation of geo-physical parameters.

1.5.1 GNSS-R Geometry

Depending on the nature of the platform that carries the receiver, the GNSS-R geometry varies significantly. For ground-based receivers [Rod10], reflected signals come from near the receiver: path separation is very small and the reflecting surface can be assumed flat. It is a

scenario very close to GNSS multipath. In such configuration, the reflection is often assumed coherent and specular, that is, since the reflected energy comes from part of the intersection between the Earth’s surface and the first Fresnel zone around the reflected path [Cam20], the surface that reflects most of the energy is very small and reduces to a point called the specular point.

For airborne receivers (e.g., Unmanned Aerial Vehicle (UAV) or aircraft) [Fab19], the Earth’s curvature must be taken into account. Depending on the surface roughness and the satellite elevation angle, the reflected signal may come from a small surface defined by the first Fresnel zone around the reflected path or from a larger surface called glistening zone [ZV00]. It consists now of a mix of coherent and non-coherent components. Finally, for spaceborne receivers such as United Kingdom (UK) TechDemoSat-1 (TDS-1) launched in 2013, or National Aeronautics and Space Agency (NASA) Cyclone GNSS (CYGNSS) launched in 2016, the altitude of the Low Earth Orbit (LEO) satellite is so large that, in the case of non-coherent reflections, that is when the reflecting surface is rough, this surface can spread over tens of kilometers and the reflected signal can be significantly distorted. Coherent reflections may occur over very smooth reflecting surfaces such as inland water bodies or ice. Figure 1.15 presents an example of this spaceborne case geometry with a sketch of the reflecting surface whose size varies depending on its characteristics (e.g., roughness, moisture level).

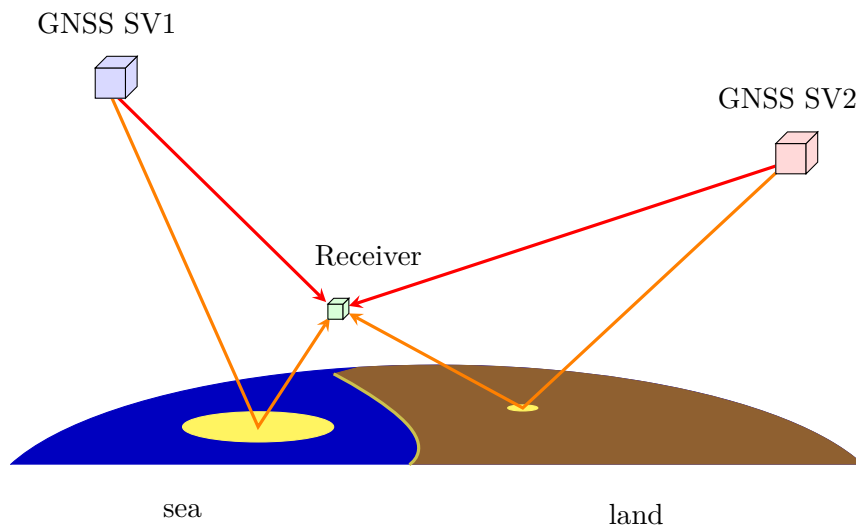


Figure 1.15: Typical spaceborne GNSS-R geometry.

For ground-based scenarios, the reflection is usually assumed mirror-like and the reflected signal is modeled as a simple attenuated and delayed replica of the direct signal. In the airborne and spaceborne scenarios the reflecting surface distorts the signal and the mirror-like model becomes too simplistic. In [ZV00], a fundamental signal model was proposed that starts from the bistatic radar equation.

1.5.2 GNSS-R Processing Techniques

In order to perform GNSS-R for all the geometry presented, one can distinguish three main approaches: i) the GNSS Interferometric Reflectometry (GNSS-IR) [And00] and in particular the single antenna interference pattern technique (IPT), where the antenna points towards the horizon and collects the combined direct and reflected signals [Mun20; Rou15], ii) dual antenna conventional GNSS-R (cGNSS-R), where the reflected signal is correlated with a clean replica of the direct signal [KG96; Les16] (as done in conventional GNSS to recover the signal delay and Doppler), and iii) dual antenna interferometric GNSS-R (iGNSS-R), where the direct and reflected signals are cross-correlated [Mar93].

1.5.2.1 GNSS-IR Processing

This first technique exploits the strong interference between direct and reflected paths when the receiver is close to the ground, or when the satellite elevation angle is small. In these cases, the path separation between both signals is so small that they coherently interfere at the RF front-end level. This results in oscillations of the overall SNR as the signals add up when they are in-phase, and subtract when they are out-of-phase. A formal analysis of this technique and the corresponding performance bounds were proposed in [Rib14].

1.5.2.2 Standard GNSS-R Processing

GNSS-R geometry and physics suggest to work with two antennas to collect both signals: an uplooking antenna, with a Right-Hand Circular Polarization (RHCP) that collects the direct signal and a downlooking antenna, with either a RHCP or a Left-Hand Circular Polarization (LHCP) that collects the reflected one. The choice of the polarization depends on the geometry: for very low elevation angles, below the Brewster angle, the reflected signal has the same polarization as the transmitted signal but for larger elevation angles, the polarization is inverted and most of the reflected energy has a LHCP. The processing of these signals may then vary:

- **Conventional GNSS-R** or cGNSS-R, relies on the standard GNSS single source processing as sketched in Section 1.3.3. The idea is to estimate the parameters of the direct signal and to generate a clean replica to process the reflected signal. In this case the user has a full control of the signal processing technique applied to both direct and reflected signal channels, but the exact knowledge of the received signal is required in order to generate the replica. This excludes using military codes.
- **Interferometric GNSS-R** or iGNSS-R, samples the direct signal and uses it directly to correlate the reflected signal with it. This way, the resulting correlation may be twice as noisier but it captures all the received signals, whether they are from an open service or from a restricted service. The challenge is then to identify each peak of the cross-correlation to each satellites depending on the excess delay and the CCF shape.

1.5.2.3 Coherent and Non-coherent Processing

Due to the presence of both coherent and non-coherent components in the reflected signal [Cam16], it is common practice in GNSS-R to perform the non-coherent integration of shorter coherent correlation outputs up to some tens of seconds [Mar14a; Gle05] as Figure 1.16 illustrates. Indeed, the non-coherent approach is useful to deal with long integration times and

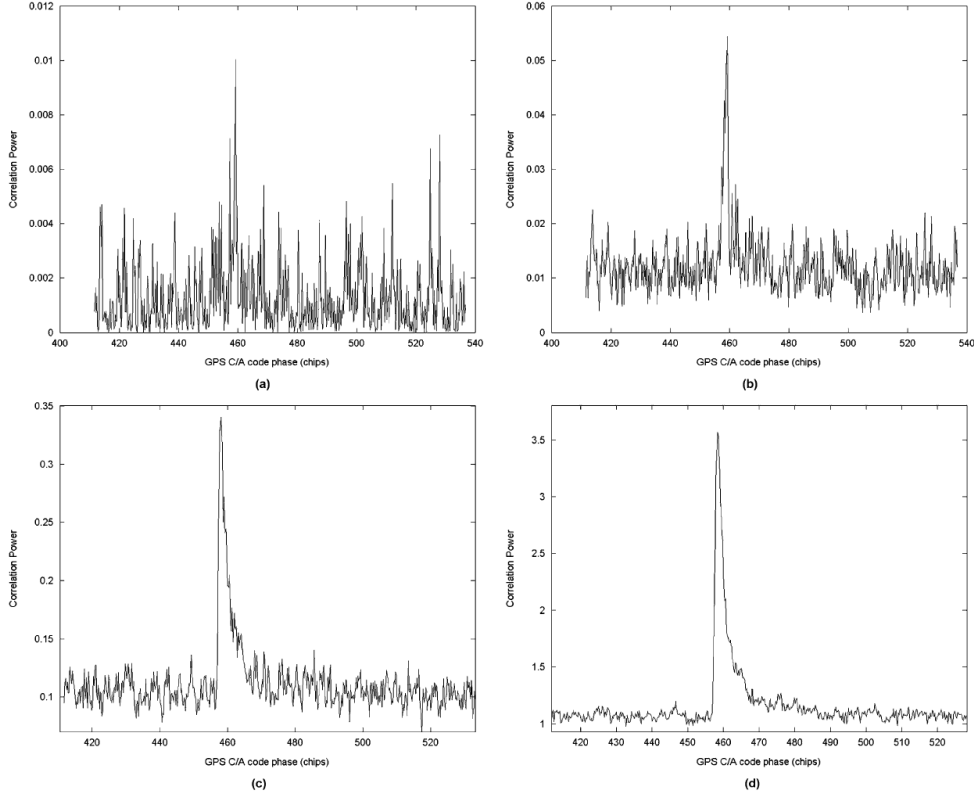


Figure 1.16: Example of non-coherent integration effect with integration time set to (a) 1 ms, (b) 10 ms, (c) 100 ms and (d) 1 s. Extracted from Gleason *et al.* 2005 [Gle05].

when the signal itself is non-coherent, which is typically the case when dealing with complex reflecting surfaces. Considering a total signal duration $T = N_{NC}T_I$ with T_I the individual standard processing coherent observation time, one can express coherent, noted $(\cdot)^C$, and non-coherent, noted $(\cdot)^{NC}$ estimators as follows. First, let y_k be $y_k(\boldsymbol{\eta}_i) = \frac{\mathbf{a}_i^H(\boldsymbol{\eta}_i)\mathbf{x}_k}{\mathbf{a}_i^H(\boldsymbol{\eta}_i)\mathbf{a}_i(\boldsymbol{\eta}_i)}$, the output of the coherent matched filter, or equivalently of a 1S-MLE as mentioned in Section 1.2.1.2, at the k^{th} time slot for a coherent observation time T_I , then:

$$\hat{\boldsymbol{\eta}}_i^C = \arg \max_{\boldsymbol{\eta}_i} \left\{ \left| \sum_{k=1}^{N_{NC}} y_k(\boldsymbol{\eta}_i) \right|^2 \right\}; \quad \hat{\boldsymbol{\eta}}_i^{NC} = \arg \max_{\boldsymbol{\eta}_i} \left\{ \sum_{k=1}^{N_{NC}} |y_k(\boldsymbol{\eta}_i)|^2 \right\}. \quad (1.36)$$

These definitions apply to any kind of estimator (e.g., single source, dual source). In [Mar14b], an estimator adapted to non-coherent reflections was proposed based on these coherent and

non-coherent processing strategies. In particular, the non-coherent Variance Estimator (VE) is formulated as:

$$\hat{\boldsymbol{\eta}}_i^{\text{VE}} = \arg \max_{\boldsymbol{\eta}_i} \left\{ \sum_{k=1}^{N_{NC}} |y_k(\boldsymbol{\eta}_i)|^2 - \left| \sum_{k=1}^{N_{NC}} y_k(\boldsymbol{\eta}_i) \right|^2 \right\}, \quad (1.37)$$

where the coherent part of the signal is subtracted from the non-coherently averaged one.

1.5.3 GNSS-R Observables

1.5.3.1 Delay Doppler Maps

Since the first satellite GNSS-R missions with TDS-1, one of the most common product of reflectometry is the so-called Delay Doppler Map (DDM) [ZV00; Mar09]. This object can be seen as an image of the scattering coefficient in the delay-Doppler domain. It is usually associated to a map of the reflecting surface cut into cells following iso-delay and iso-Doppler lines, as presented in [Mar93]. The link between the reflecting surface and the DDM is illustrated in Figure 1.17. This figure is the output of a simulated geometry assuming

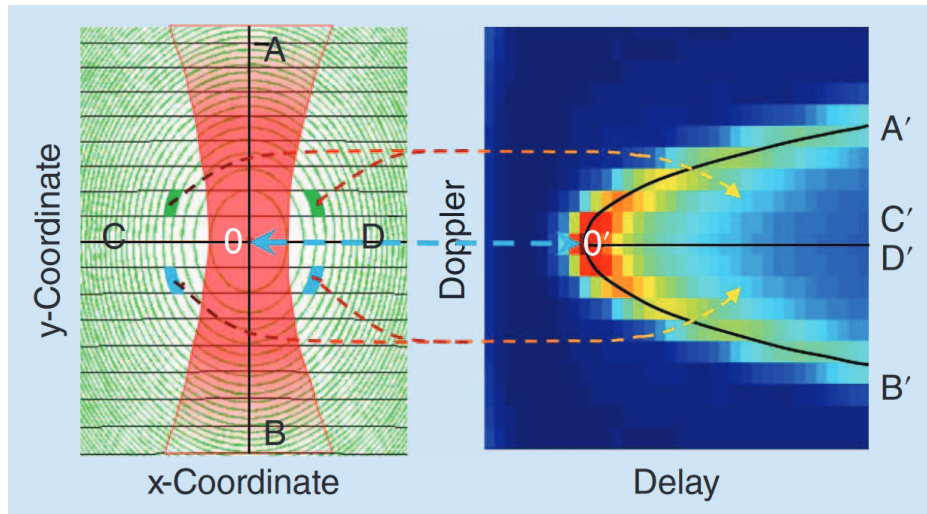


Figure 1.17: Example of delay-Doppler mapping. On the left, horizontal black lines are iso-Doppler lines and green ellipses are iso-delay lines. Each cell can be associated to a cell of the DDM. Extracted from Zavorotny *et al.* 2014 [Zav14].

the receiver embedded on a LEO satellites. For a spaceborne receiver, and for sea surface reflections, the relative velocities, the Earth curvature and the sea state are such that the DDM is often distorted with this horseshoe shape. For other reflecting surface like ice sheet or a receiver at lower altitude, the DDM may reduce to a single point, which simply corresponds to the ambiguity function as described in Section 1.3.3.

1.5.3.2 Complex Waveforms

Another widely-used product of GNSS-R receivers is the complex waveform, which consists of a cut of the DDM at the center Doppler frequency. These waveforms adopt various shapes depending on the geometry and the nature of the reflecting surface. For instance, it is possible to link the waveform trailing edge to the sea surface roughness and to surface wind speed, as it is suggested in [ZV00; Elf97] and done with the CYGNSS mission. An illustration of the impact of surface windspeed on the waveform can be found in Figure 1.18.

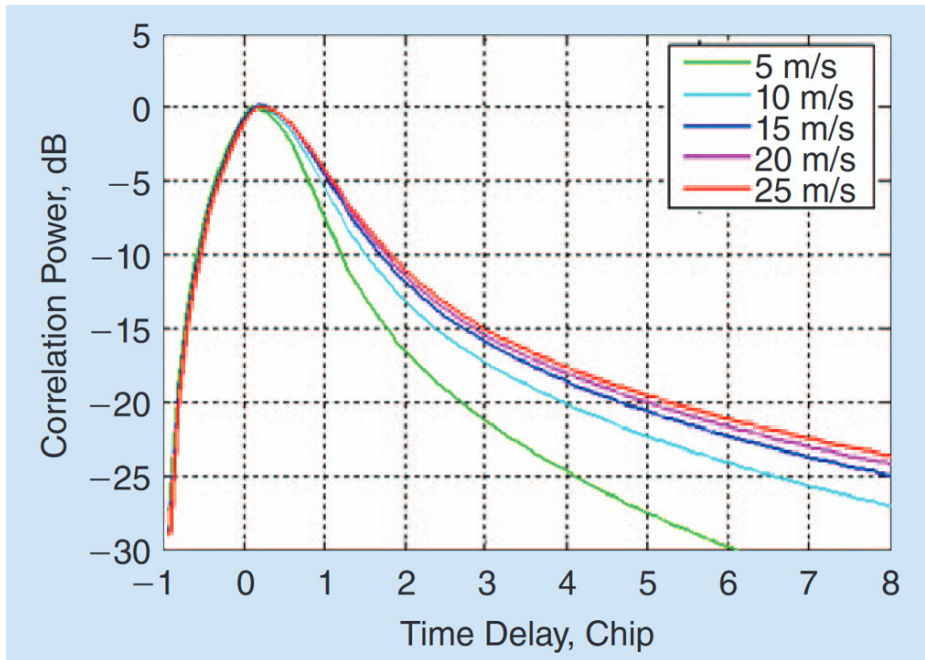


Figure 1.18: Example of complex waveform and the effect of surface wind speed on the trailing edge slope. Extracted from Zavorotny *et al.* 2014 [Zav14].

Another feature to be extracted from complex waveforms is the specular point time-delay, which is necessary to obtain an altimetric product. Depending on how distorted the waveform is, it is not straightforward to determine where this time-delay is: it can be at the peak of the waveform or where the second derivative is maximum [Nog21], as illustrated in Figure 1.19.

Finally, the complex amplitude of the waveform is also of particular interest because it informs on the Fresnel reflection coefficient. Estimating this parameter is useful for soil moisture and biomass studies [Egi12]. Besides, the tracking of the phase of this amplitude also gives an insight of the coherence of the reflection. Indeed, it was shown that the coherence of a reflected signal can be observed through the time series of the residual phase difference [Liu17; Roe21], as illustrated in Figure 1.20. By knowing the statistical distribution of this observed phase [CGH07] a number of coherence detection test or coherence indicators can be thought of. Other coherence tests were also proposed based on entropy concepts, as in [Rus21]. These tests would be crucial for the future European Space Agency (ESA) HydroGNSS mission

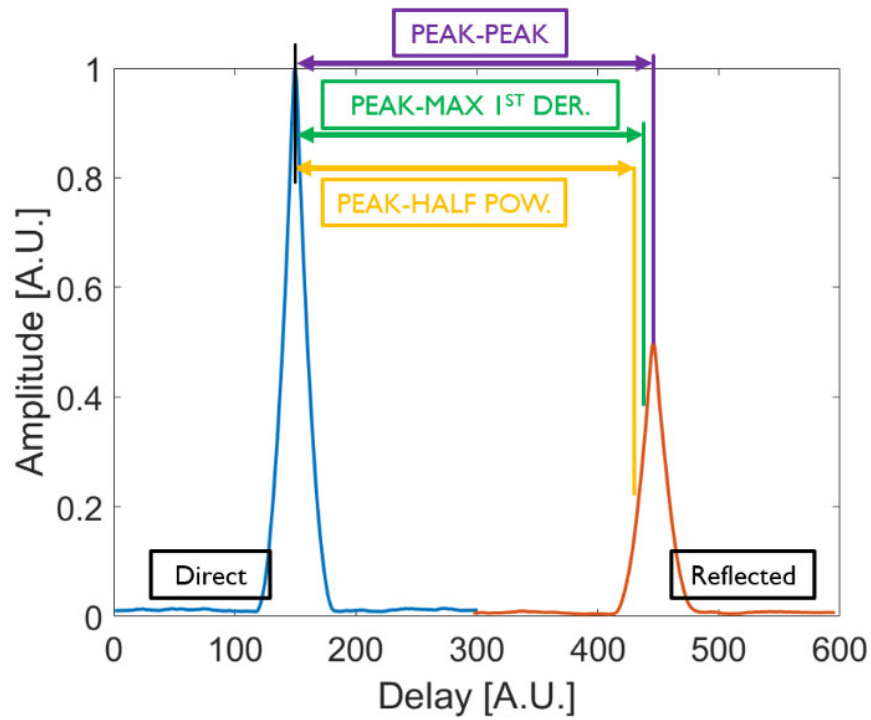


Figure 1.19: Example of path separation estimation strategies. Extracted from Nogués i Cervelló *et al.* 2021 [Nog21].

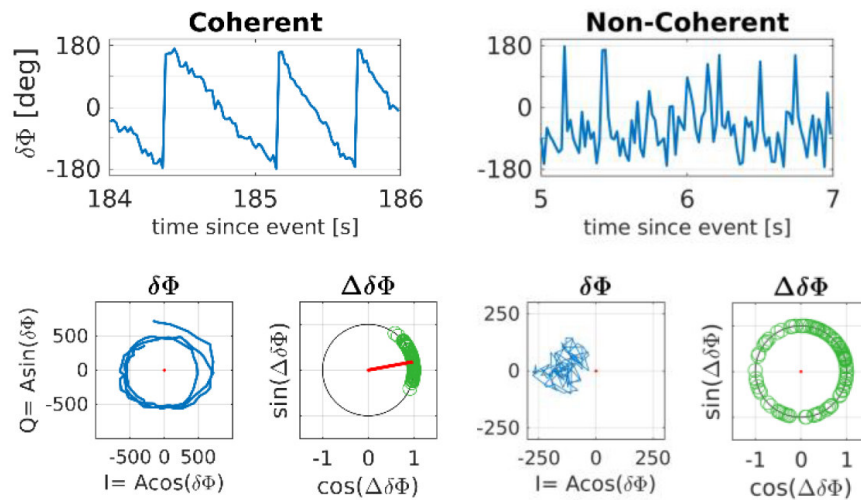


Figure 1.20: Residual phase difference between the direct and the reflected path. Extracted from Roesler *et al.* 2020 [Roe20].

[Unw21] in order to do high precision altimetry measurements based on the carrier phase observation.

1.5.4 Performance Analysis

The precision one can obtain with GNSS-R has been studied for more than 20 years now. Precision was soon used to justify the GNSS-R approach as in [Tre01; Low02; ZZ01], but the first reference to the best achievable performance such as the CRB introduced in Section 1.2.1.1 appeared in [GR06]. Then different expressions were proposed depending on the geometry: [Rib14] for GNSS-IR, [Pas14] for cGNSS-R, [RBF16] for ground-based cGNSS-R and other approaches for more complex reflected signal models [Cam14; Li18]. More recently, results on the impact of coherent versus non-coherent processing were also published [OVC22].

1.5.5 Wrap-Up on GNSS-R

GNSS-R is a technique that exploits GNSS signals that reflect from the Earth's surface. The reflected signals carry information on the position and the nature of the reflecting surface. GNSS-R is then a field of study with many remote sensing applications, and with different challenges depending on the considered geometry. It goes from local sensing, such as field soil moisture or snow depth and nature, with ground-based receivers, up to airborne and spaceborne receivers, with a global coverage and the study of mesoscale events such as hurricanes. It is still a very active field of research as suggested by the coming space mission HydroGNSS, whose launch is expected in 2024 and is soliciting most of the community members.

1.6 Conclusion

In this chapter, an overview of the tools and concepts on which lie the coming chapters was proposed. For this reason it touches a large number of topics to help the reader better understand the rest of this document.

It had to start with the fundamentals of the estimation theory: what is an estimation problem? what is an estimator? how good is an estimator? These questions were covered with a focus on the notion of the CSM, and in particular for the case of additive complex circular white Gaussian noise.

One of the numerous applications in which the Gaussian CSM appears is the first stages of a GNSS receiver. These systems, such as GPS or GALILEO, allow a receiver to determine its position on Earth thanks to ranging signals broadcasted by a constellation of satellites. GNSS systems were then properly introduced along with the underlying joint delay-Doppler estimation problem.

Then, the main challenge of GNSS, namely multipath or the fact of receiving reflections of the signal of interest along with the LOS signal, was presented with its metrics and mitigation strategies.

Finally, seeing this multipath as a source of information rather than an interference,

opened the door to an unsuspected remote sensing application: GNSS-R, which is the study of reflected GNSS signals, taken as signals of opportunity. In fact, these signals carry information on the position and nature of the reflecting surface, and it can be performed from ground-based stations for local remote sensing (e.g., soil moisture, snow depth) but it can also be performed from a spacecraft, as in successful past satellite missions TDS-1 or CYGNSS, but also in the coming HydroGNSS.

Multipath Effect and Its Impact on Positioning Performance

Contents

2.1	Introduction	46
2.1.1	Chapter Organization	48
2.1.2	Signal Models	48
2.2	MPEE for Different Multipath Mitigation Techniques	51
2.2.1	Estimators and Signals Considered	51
2.2.2	Link with the Signal Model	51
2.2.3	MPEE for Different Multipath Mitigation Techniques	52
2.2.4	Wrap-up on the MPEE Metric	52
2.3	Joint Delay-Doppler Estimation Performance in a Dual Source Context	53
2.3.1	Cramér-Rao Bound for the Joint Delay-Doppler Estimation	53
2.3.2	Validation Using the Dual Source Maximum Likelihood Estimator	55
2.3.3	RMSE for Different Multipath Mitigation Techniques	60
2.3.4	Wrap-up on MSE vs CRB Considerations	64
2.4	A Metric for Multipath-Robust Signal Design and Analysis	64
2.4.1	Insights and Extension of the Dual Source CRB	64
2.4.2	A Criterion Based on Cramér-Rao Bounds: Clean-to-Composite Bound Ratio	66
2.4.3	Numerical Results	68
2.4.4	Wrap-up on the CCBR Metric	72
2.5	Misspecified Cramér-Rao Bounds in Multipath Scenarios	73
2.5.1	Note on the Signal Models	74
2.5.2	Misspecified Maximum Likelihood Estimator	74
2.5.3	Closed-Form MCRBs for Delay/Doppler Estimation under Multipath	76
2.5.4	Validation Using the Misspecified Maximum Likelihood Estimator	78
2.5.5	Wrap-up on the MCRB	81
2.6	Conclusion	82

Résumé

Ce chapitre suppose un récepteur GNSS au sol, dans un milieu urbain. Ce type de milieu est propice aux multitrajets, c'est à dire à la réception de plusieurs répliques due à la réflexion du signal d'intérêt sur les éléments urbains. L'impact du multitrajet a été abondamment étudié dans la littérature en supposant un modèle très simple dans lequel un seul multitrajet est reçu en plus du signal en ligne de vue. Cependant, ces études se limitent à des analyses à l'aide d'outils graphiques qui ne s'intéressent qu'au biais induit sur la mesure du retard ou de la phase du signal d'intérêt. La limite de cette approche est qu'il devient alors difficile de comparer des architectures de récepteurs pour lesquelles un multitrajet n'entraînent pas de biais comme c'est le cas pour les récepteurs qui estiment à la fois les paramètres du signal d'intérêt et ceux du multitrajet. Il est alors intéressant de regarder comment la présence d'un multitrajet peut affecter l'erreur quadratique moyenne de ces récepteurs sans biais. La borne de Cramér-Rao est alors l'outil indiqué pour donner une limite théorique à l'erreur quadratique moyenne. Cette borne inférieure est un résultat très général qui peut s'étendre sous la forme d'une métrique utile à la conception de futurs signaux de navigation. Bien entendu, il n'est pas toujours possible d'implémenter un algorithme sans biais et la plupart des récepteurs bon marché ne s'adaptent pas à la présence de multitrajets. Pour ces récepteurs, que l'on dit mal spécifiés, il est tout de même possible de fournir une information sur l'erreur quadratique moyenne minimum atteignable à l'aide d'une généralisation des bornes de Cramér-Rao pour le cas mal spécifié.

Ainsi, à travers ce chapitre, la question de l'effet du multitrajet sur la performance de différents algorithmes qui tiennent compte ou non de la présence du multitrajet, est traitée sous plusieurs aspects. Partant d'un outil existant, la *Multipath Error Envelope* (MPEE), qui informe sur le biais induit par le multitrajet, le besoin d'un outil informant sur l'erreur quadratique moyenne est mis en avant dans la Section 2.2. Dans la Section 2.3, la borne de Cramér-Rao pour le cas à deux sources est alors calculée et validée par simulations. S'ensuit, dans la Section 2.4, une proposition de métrique pour la conception de futurs signaux de navigation qui s'appuie sur le calcul de la borne de Cramér-Rao. Enfin, dans la Section 2.5, l'étude des performances limites d'un estimateur mal spécifié à l'aide des borne de Cramér-Rao pour le cas mal spécifié clôt cette étude de l'impact du multitrajet.

2.1 Introduction

This chapter assumes a GNSS ground-based receiver in a urban environment, as it is illustrated in Figure 2.1.

In many GNSS applications in harsh propagation conditions, such as urban environments, multipath is one of the main challenges impairing navigation capabilities. As simply defined in [Kap], "*multipath is the reception of multiple reflected or diffracted replicas of the desired signal, along with the direct path signal.*" Receiving several replicas when only one is expected inevitably leads to a performance degradation. As presented in Section 1.4, there are

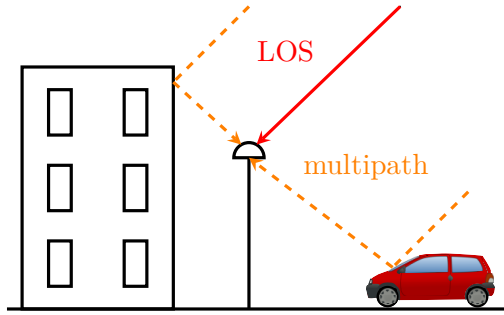


Figure 2.1: Urban scenario considered in Chapter 2.

many ways to tackle the multipath problem, either by hardware implementations (choke ring, beamforming) or by software implementations with multipath non-estimating techniques (see Section 1.4.2.1) or estimating techniques (see Section 1.4.2.2). Another path is to think of new GNSS signals that would be less sensitive to multipath (with larger bandwidth signals, for instance).

In any case, whatever the architecture or the signal considered, to assess the impact of possible multipath conditions into the final system performance, accurate metrics are required. From the literature, it is clear that the de facto metric used to characterize the multipath effect is the so-called MPEE, which displays for a given receiver architecture and a given signal, the range of possible multipath-induced errors considering a simple dual source model without noise. This tool is simple to handle but it becomes less informative when it is a flat zero-valued line, that is, when the estimator under consideration is unbiased. Based on the MPEE it becomes hard to compare two unbiased estimators, their performance can no longer be characterized through such a simple metric. In that case the estimator performance is only given by its variance, which in turn can only be evaluated in a noisy environment.

A way to characterize a given receiver architecture - provided the fact that it is unbiased - is to evaluate its MSE in the presence of noise for a set of SNR or path separation values, and determine the threshold region where the MSE converges, or not, to the CRB that corresponds to the scenario under study. A reference estimator that is usually compared to the CRB, due to its asymptotic properties, is the MLE. The CRB provides the best achievable performance of a locally unbiased estimator in terms of MSE. Then, it is meaningful to compare different architecture solutions according to their MSE when their corresponding MPEE is a flat zero, that is, when the estimator is unbiased. The CRB and the MPEE are complementary approaches.

The generality of the CRB suggests a fundamentally different and, therefore, very general approach to multipath error characterization. A metric to evaluate the robustness to multipath of any band-limited signal candidate can be derived by resorting to the CRB. Such a tool would turn out to be very useful for future GNSS signal design.

However, having an unbiased estimator implemented in a receiver is not always possible. For low-cost receiver architectures, multipath directly leads to a ranging/positioning estima-

tion performance degradation, induced by an estimation bias that the receiver does not take into account. Indeed, from a system model perspective, ignoring the possible presence of multipath implies to consider a LOS single source model instead of the true multi source signal. Such assumption is known as model misspecification, of interest in several disciplines.

The performance of misspecified estimators was discussed in Section 1.2.2. In particular, it was shown that the MMLE converges to a fix value that minimizes the KLD between the true data model and the misspecified PDFs. Moreover, when the number of data points or the SNR are large enough, its MSE converges to the so-called MCRB. Such lower bound allows to properly characterize the performance of standard receivers not accounting for the multipath effect, which was not possible with the results available in the literature.

2.1.1 Chapter Organization

In this chapter, the multipath problem is deeply studied under various angles. Based on the literature, a first approach in Section 2.2 is to apply the widely used MPEE on different receiver architectures and signals to better understand its nature and its limits. This first study will highlight the need of a second order statistics tool to complete the information provided by the MPEE. This is possible by deriving the CRB for the dual source signal model considered. This derivation along with a validation procedure and the comparison with the MSE of the receiver architecture is done in Section 2.3. In Section 2.4, a tool, the clean-to-composite bound ratio (CCBR), based on the derived CRB, is built and further studied for different signals. Finally, the question of low-cost receiver performance in presence of multipath is dealt with through the notion of misspecified estimation and the corresponding MCRB that is derived, validated and discussed in Section 2.5.

These different sections all gravitate around specific signal models which must be first detailed. This is the aim the of the next section where the single source and the dual source signals that will be used for the rest of the chapter are presented.

2.1.2 Signal Models

Let a transmitter T and a receiver R have uniform linear motions such that the positions can be described as $\mathbf{p}_T(t) = \mathbf{p}_T + \mathbf{v}_T t$ and $\mathbf{p}_R(t) = \mathbf{p}_R + \mathbf{v}_R t$, where \mathbf{p} and \mathbf{v} are the position and velocity vectors, respectively. Under such conditions, the distance between T and R at instant t can be approximated by a first order distance-velocity model:

$$\begin{aligned} \|\mathbf{p}_{TR}(t)\| &\triangleq \|\mathbf{p}_R(t) - \mathbf{p}_T(t - \tilde{\tau}(t))\| = c\tilde{\tau}(t) \approx d + vt, \\ \tilde{\tau}(t) &\approx \tau + bt, \quad \tau = \frac{d}{c}, \quad b = \frac{v}{c}, \end{aligned} \quad (2.1)$$

where d is the T-to-R absolute distance when $t = 0$, v is the T-to-R radial velocity, τ is the time-delay due to the propagation path, $(1 - b)$ is the dilatation induced by the Doppler effect, and c is the speed of light in a vacuum.

2.1.2.1 Single Source Signal Model

First a nominal transmission is considered, the receiver collects only the LOS signal. Using (2.1), the single source complex analytic signal at the output of the receiver's antenna is:

$$x_R(t) = d_R(t; \boldsymbol{\eta}, \rho, \phi_R) + w_R(t), \quad (2.2)$$

$$d_R(t; \boldsymbol{\eta}, \rho, \phi_R) = \rho e^{j\phi_R} s((1-b)(t-\tau)) e^{j\omega_c(1-b)t} e^{-j\omega_c\tau}, \quad (2.3)$$

where $w_R(t)$ is a zero-mean white complex circular Gaussian noise, $\omega_c = 2\pi f_c$, $\boldsymbol{\eta}^T = (\tau, b)$, ρ strictly positive. ρ and ϕ_R are the amplitude and phase of the complex coefficients induced by the propagation characteristics, polarization mismatches, antenna gains. Under the narrowband signal hypothesis [Ric03], i.e., the time-frequency product $B \cdot T_I$ (with T_I the coherent integration time) is smaller than the inverse Doppler term c/v , the Doppler effect on the band-limited baseband signal $s(t)$ is usually neglected, $s((1-b)(t-\tau)) \approx s(t-\tau)$. Therefore, the baseband output of the receiver's Hilbert filter containing a direct signal and a single specular reflection can be approximated by

$$x(t) \triangleq x_R(t) e^{-j\omega_c t} = d(t; \boldsymbol{\theta}) + w(t), \quad (2.4)$$

$$d(t; \boldsymbol{\theta}) \triangleq \rho e^{j\phi} s(t-\tau) e^{-j\omega_c b(t-\tau)}, \quad (2.5)$$

where $\boldsymbol{\theta}^T = (\boldsymbol{\eta}^T, \rho, \phi)$, $\phi = \phi_R - \omega_c(1+b)\tau$. Now considering the acquisition of $N = N_2 - N_1 + 1$ samples at a sampling frequency $F_s = 1/T_s$, set equal to the front-end bandwidth of the receiver B_R , the discrete signal model yields to the following single source CSM,

$$\mathbf{x} = \mathbf{a}(\boldsymbol{\eta}) \rho e^{j\phi} + \mathbf{w}, \quad \mathbf{w} \sim \mathcal{CN}(0, \sigma_n^2 \mathbf{I}_N), \quad (2.6)$$

with, for $n \in [N_1, N_2]$,

$$\mathbf{a}^T(\boldsymbol{\eta}) = (\dots, s(nT_s - \tau) e^{-j\omega_c b(nT_s - \tau)}, \dots), \quad (2.7)$$

$$\mathbf{x}^T = (\dots, x(nT_s), \dots), \quad (2.8)$$

$$\mathbf{w}^T = (\dots, w(nT_s), \dots). \quad (2.9)$$

2.1.2.2 Dual Source Signal Model

Similarly, the dual source complex analytic signal at the output of the receiver's antenna is

$$x_R(t) = d_R(t; \boldsymbol{\eta}_0, \rho_0, \phi_{R,0}) + d_R(t; \boldsymbol{\eta}_1, \rho_1, \phi_{R,1}) + w_R(t),$$

$$d_R(t; \boldsymbol{\eta}_i, \rho_i, \phi_{R,i}) = \rho_i e^{j\phi_{R,i}} s((1-b_i)(t-\tau_i)) e^{j\omega_c(1-b_i)t} e^{-j\omega_c\tau_i},$$

where $w_R(t)$ is a zero-mean white complex circular Gaussian noise, $\omega_c = 2\pi f_c$, and for $i \in \{0, 1\}$, $\boldsymbol{\eta}_i^T = (\tau_i, b_i)$, ρ_i and $\phi_{R,i}$ the amplitude (strictly positive) and phase of the complex coefficients induced by the propagation characteristics (fading, reflection, *etc.*), the polarization mismatches and the antenna gains.

Similarly to the single source model, under the narrowband signal hypothesis, $s((1-b)(t-\tau)) \approx s(t-\tau)$. Therefore, the baseband output of the receiver's Hilbert filter containing a direct signal and a single multipath can be approximated by

$$x(t) \triangleq x_R(t)e^{-j\omega_c t} = d(t; \boldsymbol{\theta}_0) + d(t; \boldsymbol{\theta}_1) + w(t) , \quad (2.10)$$

$$d(t; \boldsymbol{\theta}_i) \triangleq \rho_i e^{j\phi_i} s(t - \tau_i) e^{-j\omega_c b_i (t - \tau_i)} , \quad (2.11)$$

where for $i \in \{0, 1\}$, $\boldsymbol{\theta}_i^T = (\boldsymbol{\eta}_i^T, \rho_i, \phi_i)$, $\phi_i = \phi_{R,i} - \omega_c(1 + b_i)\tau_i$. Now if one considers the acquisition of $N = N_2 - N_1 + 1$ samples at a sampling frequency $F_s = 1/T_s$, set equal to the front-end bandwidth of the receiver B_R , the discrete signal model yields to the following dual source CSM,

$$\mathbf{x} = \mathbf{A}(\boldsymbol{\eta}_0, \boldsymbol{\eta}_1)\boldsymbol{\alpha} + \mathbf{w}, \quad \mathbf{w} \sim \mathcal{CN}(0, \sigma_n^2 \mathbf{I}_N) , \quad (2.12)$$

with, for $n \in [N_1, N_2]$,

$$\mathbf{x}^T = (\dots, x(nT_s), \dots) , \quad (2.13)$$

$$\mathbf{A}(\boldsymbol{\eta}_0, \boldsymbol{\eta}_1) = [\mathbf{a}_0, \mathbf{a}_1] , \quad (2.14)$$

$$\mathbf{a}_i^T = (\dots, s(nT_s - \tau_i) e^{-j\omega_c b_i (nT_s - \tau_i)}, \dots) , \quad (2.15)$$

$$\boldsymbol{\alpha}^T = (\rho_0 e^{j\phi_0}, \rho_1 e^{j\phi_1}) , \quad (2.16)$$

$$\mathbf{w}^T = (\dots, w(nT_s), \dots) . \quad (2.17)$$

2.1.2.3 Signal-to-Noise Ratio

Most of the results will be presented with regard to the noise level, represented by the SNR. Indeed, when it comes to validate the CRB or the MCRB, the way to proceed is to exploit the asymptotic behavior of the MLE or the MMLE. In the following, asymptotic will mean when the SNR gets large. For this reason, the SNR needs to be properly defined once and for all. For the rest of the chapter, SNR, or SNR_{out} will always refer to the SNR of the LOS at the output of the matched filter such that

$$\text{SNR} \triangleq \frac{\left| \int_{\mathbb{R}} s(t - \tau_0)^* \rho_0 e^{j\phi_0} s(t - \tau_0) dt \right|^2}{E \left\{ \left| \int_{\mathbb{R}} s(t - \tau_0)^* w(t) dt \right|^2 \right\}} = \frac{\rho_0^2 \mathbf{s}^H \mathbf{s}}{\sigma_n^2} = (C/N_0) T_I \quad (2.18)$$

where \mathbf{s} is the vector of the baseband samples also defined in (C.29), σ_n^2 , the variance of the additive white Gaussian noise. C/N_0 is the carrier-to-noise density ratio. Details to obtain this compact expression can be found as a particular case of the development of (C.20).

2.2 MPEE for Different Multipath Mitigation Techniques

2.2.1 Estimators and Signals Considered

In order to better understand the multipath problem, it is worth trying to apply it to different multipath mitigation solutions to have a reference for further studies. This is done in this first section where the MPEE is applied to both non-estimating (Section 1.4.2.1) and estimating (Section 1.4.2.2) techniques. In particular, the following existing techniques are considered:

- PAC, which is a non-estimating technique that uses four correlators (very early, early, late and very late) to estimate the slope at each side of the correlation function peak, and if there is any asymmetry, the algorithm compensates for it by assuming that a single multipath is causing this asymmetry. In this implementation, the correlator spacing was set to 1/12 of L1 C/A chips (Section 1.4.2.2).
- MEDLL, which is a multipath estimating technique and is seen here as a relaxed version of a dual source CLEAN algorithm, namely the CRE (Section 1.2.1.2).
- MMT, which is also a multipath estimating technique that is an implementation of the 2S-MLE (Section 1.2.1.2).

Along with these existing techniques, another from the array processing community is also considered:

- APE, which is an estimating technique that alternately maximizes the likelihood criterion with regard to a subset of parameters (Section 1.2.1.2).

These estimators are then applied to two GNSS signals: GPS L1 C/A and GALILEO E1B, which are fully described in Section 1.3.2. For the numerical simulations presented in Section 2.2.3 and Section 2.3.3, the following parameters were fixed:

- the RF front-end bandwidth $B = F_s$ is equal to 12 Mhz,
- the MDR is set to 0.5,
- the coherent integration time of the GPS L1 C/A signal T_I^{GPS} is set to 1 ms and the one of the GALILEO E1B signal T_I^{GAL} to 4 ms,
- for the RMSE estimation, 1000 Monte Carlo runs were performed and the relative phase $\Delta\phi$ was set to 0.

2.2.2 Link with the Signal Model

In this first approach, the dual source signal model considered in this chapter (2.12) is simplified to fit the simple multipath model as described in Section 1.4.1.1. Here, to evaluate the

MPEE, a noise-free scenario is considered and the Doppler effect is assumed fully compensated.

2.2.3 MPEE for Different Multipath Mitigation Techniques

Evaluating the MPEE can be done numerically by looking at the output of the considered estimator, in the presence of a single multipath and without noise, for different path separations and relative phases. Figure 2.2 shows the resulting MPEE for the considered estimators. A first result that can be drawn from these figures is that the PAC MPEE (in magenta), however small, never reduces to zero. Consequently, it can be said of this architecture that the presence of a multipath will irremediably affect the precision of the LOS time delay estimation. On the other hand, MEDLL (in blue) and APE (in orange) MPEEs both present interesting behaviors: there is a path separation threshold above which these algorithms estimate the LOS time delay with no bias. Note that for GPS L1 C/A (Figure 2.2a), the MEDLL and APE MPEEs thresholds are around 140m and 40m, respectively. For GALILEO E1B (Figure 2.2b), both algorithms present a similar threshold at 40m. As expected, the MMT does not present any bias as this method correctly estimates the two sources in a noiseless environment.

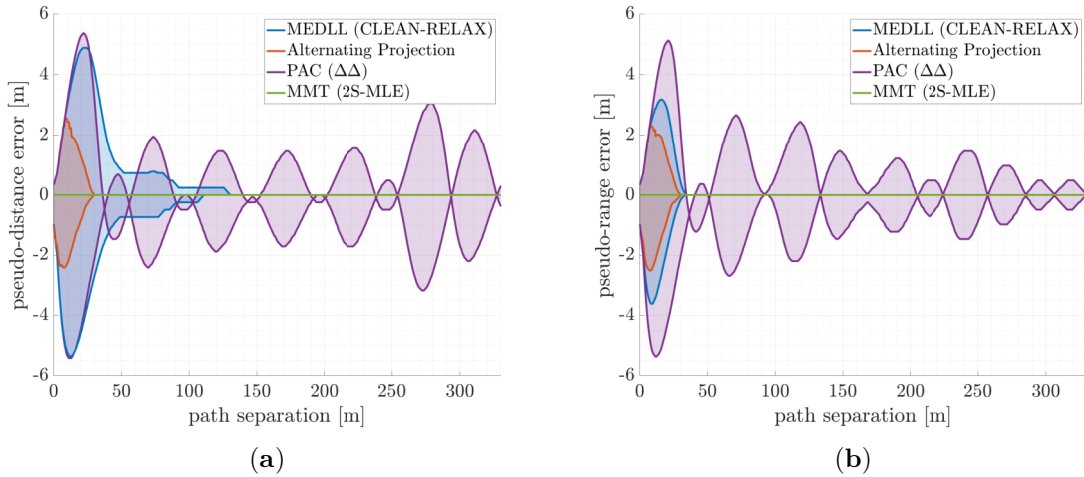


Figure 2.2: MPEE for (a) GPS L1 C/A and (b) GALILEO E1B signals.

2.2.4 Wrap-up on the MPEE Metric

By looking at the MPEE for different algorithms one may be frustrated by the impossibility to further compare unbiased estimators: in the region where the MEDLL, the APE and the MMT estimate the LOS time delay with no bias, one cannot tell if there is a solution better than the others. To allow the user to further compare these algorithms a solution is to look at what happens in presence of an additive white Gaussian noise. In this case for a given

noise level, the MSE of each solution can be compared to a lower bound, namely the CRB.

2.3 Joint Delay-Doppler Estimation Performance in a Dual Source Context

An expression of the CRB is then required to compare the MSE of different solutions. This section provides details on the derivation of a compact analytic expression of the delay-Doppler CRB for the dual source model in (2.12) and the estimation of the vector of unknown parameters:

$$\boldsymbol{\epsilon}^T = (\sigma_n^2, \boldsymbol{\eta}_0^T, \rho_0, \phi_0, \boldsymbol{\eta}_1^T, \rho_1, \phi_1) \quad (2.19)$$

2.3.1 Cramér-Rao Bound for the Joint Delay-Doppler Estimation

From (2.12), one can write $\mathbf{x} \sim \mathcal{CN}(\mathbf{A}(\boldsymbol{\eta}_0, \boldsymbol{\eta}_1)\boldsymbol{\alpha}, \sigma_n^2 \mathbf{I}_N)$ and express the PDF as,

$$p(\mathbf{x}, \boldsymbol{\epsilon}) = \frac{1}{(\pi\sigma_n^2)^N} e^{-\frac{1}{\sigma_n^2} \|\mathbf{x} - \mathbf{A}(\boldsymbol{\eta}_0, \boldsymbol{\eta}_1)\boldsymbol{\alpha}\|^2}. \quad (2.20)$$

The corresponding CRB for the estimation of $\boldsymbol{\epsilon}$ is defined as the inverse of the FIM [Van01a],

$$\mathbf{CRB}_{\boldsymbol{\epsilon}|\boldsymbol{\epsilon}} = \mathbf{F}_{\boldsymbol{\epsilon}|\boldsymbol{\epsilon}}^{-1}(\boldsymbol{\epsilon}), \quad \mathbf{F}_{\boldsymbol{\epsilon}|\boldsymbol{\epsilon}}(\boldsymbol{\epsilon}) = -E \left[\frac{\partial^2 \ln p(\mathbf{x}, \boldsymbol{\epsilon})}{\partial \boldsymbol{\epsilon} \partial \boldsymbol{\epsilon}^T} \right]. \quad (2.21)$$

Note that for the Gaussian CSM of interest the Slepian-Bangs formulas recalled in section 1.12 provides the direct evaluation of the FIM terms,

$$\left[\mathbf{F}_{\boldsymbol{\epsilon}|\boldsymbol{\epsilon}}(\boldsymbol{\epsilon}) \right]_{k,l} \triangleq F_{\epsilon_k, \epsilon_l|\boldsymbol{\epsilon}}(\boldsymbol{\epsilon}) = \frac{2}{\sigma_n^2} \text{Re} \left\{ \left(\frac{\partial \mathbf{A} \boldsymbol{\alpha}}{\partial \epsilon_k} \right)^H \left(\frac{\partial \mathbf{A} \boldsymbol{\alpha}}{\partial \epsilon_l} \right) \right\} + \frac{N}{\sigma_n^4} \frac{\partial \sigma_n^2}{\partial \epsilon_k} \frac{\partial \sigma_n^2}{\partial \epsilon_l}, \quad (2.22)$$

where the noise power appears to be independent from the other parameters, and the FIM reduces to

$$\mathbf{F}_{\boldsymbol{\epsilon}|\boldsymbol{\epsilon}}(\boldsymbol{\epsilon}) = \begin{bmatrix} F_{\sigma_n^2|\boldsymbol{\epsilon}}(\boldsymbol{\epsilon}) & \mathbf{0} & \mathbf{0} \\ \mathbf{0} & \mathbf{F}_{\boldsymbol{\theta}_0|\boldsymbol{\epsilon}}(\boldsymbol{\epsilon}) & \mathbf{F}_{\boldsymbol{\theta}_0, \boldsymbol{\theta}_1|\boldsymbol{\epsilon}}(\boldsymbol{\epsilon}) \\ \mathbf{0} & \mathbf{F}_{\boldsymbol{\theta}_1, \boldsymbol{\theta}_0|\boldsymbol{\epsilon}}(\boldsymbol{\epsilon}) & \mathbf{F}_{\boldsymbol{\theta}_1|\boldsymbol{\epsilon}}(\boldsymbol{\epsilon}) \end{bmatrix}, \quad (2.23)$$

where

- $F_{\sigma_n^2|\boldsymbol{\epsilon}}(\boldsymbol{\epsilon}) = N/\sigma_n^4$.
- $\mathbf{F}_{\boldsymbol{\theta}_0|\boldsymbol{\epsilon}}(\boldsymbol{\epsilon})$ and $\mathbf{F}_{\boldsymbol{\theta}_1|\boldsymbol{\epsilon}}(\boldsymbol{\epsilon})$ correspond to the FIMs of the signals when they are totally decoupled. These matrices have been derived and studied in [Das19] without the Doppler frequency estimation, and in [Med20] and [Das20a] for the general Gaussian CSM. The main results of these last references, concerning the single source CSM FIM terms are summarized in section 2.3.1.1.

- $\mathbf{F}_{\theta_0, \theta_1 | \epsilon}(\epsilon) = \mathbf{F}_{\theta_1, \theta_0 | \epsilon}(\epsilon)^T$ characterizes the interference between both signals. The derivation of such FIM terms is given in section 2.3.1.2.

2.3.1.1 Decoupled Fisher Information Matrix Terms

The two last diagonal blocks of the FIM (2.23) were derived for the single source CSM case in [Med20] and [Das20a]. The main results are recalled in the sequel:

$$\mathbf{F}_{\theta_i | \epsilon}(\epsilon) = \frac{2F_s}{\sigma_n^2} \text{Re} \left\{ \mathbf{Q}_i \mathbf{W} \mathbf{Q}_i^H \right\}, \quad (2.24)$$

where \mathbf{Q}_i , $i \in \{1, 2\}$ is defined in (C.2) and \mathbf{W} is defined as:

$$\mathbf{W} = \begin{bmatrix} w_1 & w_2^* & w_3^* \\ w_2 & W_{2,2} & w_4^* \\ w_3 & w_4 & W_{3,3} \end{bmatrix}, \quad (2.25)$$

with the easy-to-use formulation with regard to the baseband signal samples:

$$\begin{aligned} w_1 &= \frac{1}{F_s} \mathbf{s}^H \mathbf{s}, \quad w_2 = \frac{1}{F_s^2} \mathbf{s}^H \mathbf{D} \mathbf{s}, \quad w_3 = \mathbf{s}^H \mathbf{V}^{\Delta,1}(0) \mathbf{s}, \quad w_4 = \frac{1}{F_s} \mathbf{s}^H \mathbf{D} \mathbf{V}^{\Delta,1}(0) \mathbf{s}, \\ W_{2,2} &= \frac{1}{F_s^3} \mathbf{s}^H \mathbf{D}^2 \mathbf{s}, \quad W_{3,3} = F_s \mathbf{s}^H \mathbf{V}^{\Delta,2}(0) \mathbf{s}, \end{aligned} \quad (2.26)$$

where \mathbf{s} , the baseband sample vector, is defined in (C.29), \mathbf{D} in (C.32), $\mathbf{V}^{\Delta,1}(\cdot)$ in (C.35) and $\mathbf{V}^{\Delta,2}(\cdot)$ in (C.37). The inversion of (2.24) proposed in [Med20] and [Das20a] leads to a closed-form CRB expression for the delay, Doppler, phase and amplitude estimation, where a noteworthy feature is that the CRBs are expressed with regard to the baseband signal samples. Such CRBs were studied for different GNSS signals in [Das20b] and [Ort20].

2.3.1.2 Interference Fisher Information Matrix Terms

From the Slepian-Bangs formula the non-diagonal blocks of the FIM, referred to as interference FIMs, are expressed as follows:

$$\mathbf{F}_{\theta_1, \theta_0 | \epsilon}(\epsilon) = \frac{2F_s}{\sigma_n^2} \text{Re} \left\{ \mathbf{Q}_1 \mathbf{W}^{\Delta} \mathbf{Q}_0^H \right\}, \quad (2.27)$$

where \mathbf{Q}_0 , \mathbf{Q}_1 are defined in (C.2) and \mathbf{W}^{Δ} is defined as

$$\mathbf{W}^{\Delta} = \begin{bmatrix} W_{1,1}^{\Delta} & W_{1,2}^{\Delta} & W_{1,3}^{\Delta} \\ W_{2,1}^{\Delta} & W_{2,2}^{\Delta} & W_{2,3}^{\Delta} \\ W_{3,1}^{\Delta} & W_{3,2}^{\Delta} & W_{3,3}^{\Delta} \end{bmatrix} e^{j\Delta\psi} e^{-j\omega_c \Delta b \tau_0}, \quad (2.28)$$

where Δb and $\Delta\psi$ are defined in (C.8) and with the different components of the matrix \mathbf{W}^Δ expressed w.r.t the baseband signal samples given by

$$W_{1,1}^\Delta = \frac{1}{F_s} \mathbf{s}^H \mathbf{U} \left(\frac{f_c \Delta b}{F_s} \right) \mathbf{V}^{\Delta,0} \left(\frac{\Delta\tau}{T_s} \right) \mathbf{s}, \quad (2.29)$$

$$W_{1,2}^\Delta = \frac{1}{F_s^2} \mathbf{s}^H \mathbf{D} \mathbf{U} \left(\frac{f_c \Delta b}{F_s} \right) \mathbf{V}^{\Delta,0} \left(\frac{\Delta\tau}{T_s} \right) \mathbf{s}, \quad (2.30)$$

$$W_{1,3}^\Delta = -\mathbf{s}^H \mathbf{U} \left(\frac{f_c \Delta b}{F_s} \right) \mathbf{V}^{\Delta,1} \left(\frac{\Delta\tau}{T_s} \right) \mathbf{s} + \frac{j\omega_c \Delta b}{F_s} \mathbf{s}^H \mathbf{U} \left(\frac{f_c \Delta b}{F_s} \right) \mathbf{V}^{\Delta,0} \mathbf{s}, \quad (2.31)$$

$$W_{2,1}^\Delta = \frac{1}{F_s^2} \mathbf{s}^H \mathbf{U} \left(\frac{f_c \Delta b}{F_s} \right) \mathbf{V}^{\Delta,0} \left(\frac{\Delta\tau}{T_s} \right) \mathbf{D} \mathbf{s}, \quad (2.32)$$

$$W_{2,2}^\Delta = \frac{1}{F_s^3} \mathbf{s}^H \mathbf{D} \mathbf{U} \left(\frac{f_c \Delta b}{F_s} \right) \mathbf{V}^{\Delta,0} \left(\frac{\Delta\tau}{T_s} \right) \mathbf{D} \mathbf{s}, \quad (2.33)$$

$$W_{2,3}^\Delta = -\frac{1}{F_s} \mathbf{s}^H \mathbf{U} \left(\frac{f_c \Delta b}{F_s} \right) \mathbf{V}^{\Delta,1} \left(\frac{\Delta\tau}{T_s} \right) \mathbf{D} \mathbf{s} + \frac{j\omega_c \Delta b}{F_s^2} \mathbf{s}^H \mathbf{U} \left(\frac{f_c \Delta b}{F_s} \right) \mathbf{V}^{\Delta,0} \left(\frac{\Delta\tau}{T_s} \right) \mathbf{D} \mathbf{s}, \quad (2.34)$$

$$W_{3,1}^\Delta = \mathbf{s}^H \mathbf{U} \left(\frac{f_c \Delta b}{F_s} \right) \mathbf{V}^{\Delta,1} \left(\frac{\Delta\tau}{T_s} \right) \mathbf{s}, \quad (2.35)$$

$$W_{3,2}^\Delta = \frac{1}{F_s} \mathbf{s}^H \mathbf{D} \mathbf{U} \left(\frac{f_c \Delta b}{F_s} \right) \mathbf{V}^{\Delta,1} \left(\frac{\Delta\tau}{T_s} \right) \mathbf{s}, \quad (2.36)$$

$$W_{3,3}^\Delta = F_s \mathbf{s}^H \mathbf{U} \left(\frac{f_c \Delta b}{F_s} \right) \mathbf{V}^{\Delta,2} \left(\frac{\Delta\tau}{T_s} \right) \mathbf{s} + j\omega_c \Delta b \mathbf{s}^H \mathbf{U} \left(\frac{f_c \Delta b}{F_s} \right) \mathbf{V}^{\Delta,1} \left(\frac{\Delta\tau}{T_s} \right) \mathbf{s}, \quad (2.37)$$

where \mathbf{s} , the baseband sample vector, is defined in (C.29), \mathbf{D} in (C.32), $\mathbf{U}(\cdot)$ in (C.31), $\mathbf{V}^{\Delta,0}(\cdot)$ in (C.33), $\mathbf{V}^{\Delta,1}(\cdot)$ in (C.35) and $\mathbf{V}^{\Delta,2}(\cdot)$ in (C.37).

Proof. refer to Appendix C. □

An interesting and reassuring fact is that when the difference between LOS and NLOS signals (i.e., signal 0 and signal 1) is set to zero: $\Delta\tau = \tau_1 - \tau_0 = 0$, $\Delta b = b_1 - b_0 = 0$, $\Delta\phi = \phi_1 - \phi_0 = 0$, $\rho_1 = \rho_0$, then, $\mathbf{Q}_0 = \mathbf{Q}_1$ and $\mathbf{W}^\Delta = \mathbf{W}$. This result could be expected but the FIM terms equations obtained confirm it. Indeed, if both signals are indistinguishable, they must have the same FIM and their interference FIM must coincide (total interference between both signals).

2.3.2 Validation Using the Dual Source Maximum Likelihood Estimator

To validate the CRBs derived in Section 2.3.1, the asymptotic properties of the MLE are exploited: for a high SNR regime, the MLE behaves as an efficient estimator, that is, all the estimates are asymptotically unbiased and their MSE is equal to the CRB. This paves the way to a validation procedure: the CRBs are compared to the MSE of the MLE estimates, if they coincide, it will validate all the expressions derived.

2.3.2.1 Estimators Considered

From the dual source CSM (2.12) and its PDF (2.20), the estimator $\hat{\mathbf{e}}$ that maximizes the likelihood is such that $(\hat{\boldsymbol{\eta}}_0, \hat{\boldsymbol{\eta}}_1)$ maximizes the projection of the received signal onto the subspace defined by the mixing matrix \mathbf{A} [Ott93]. Its expression is presented in Section 1.2.1.2 and reminded hereafter.

$$(\hat{\boldsymbol{\eta}}_0, \hat{\boldsymbol{\eta}}_1) = \arg \max_{\boldsymbol{\eta}_0, \boldsymbol{\eta}_1} \|\mathbf{P}_{\mathbf{A}} \mathbf{x}\|^2 \quad (2.38)$$

$$\hat{\rho}_i = \left| \left[\left(\hat{\mathbf{A}}^H \hat{\mathbf{A}} \right)^{-1} \hat{\mathbf{A}}^H \mathbf{x} \right]_i \right| \quad (2.39)$$

$$\hat{\phi}_i = \arg \left\{ \left[\left(\hat{\mathbf{A}}^H \hat{\mathbf{A}} \right)^{-1} \hat{\mathbf{A}}^H \mathbf{x} \right]_i \right\} \quad (2.40)$$

$$\hat{\sigma}_n^2 = \frac{1}{N} \|\mathbf{P}_{\hat{\mathbf{A}}}^\perp \mathbf{x}\|^2 \quad (2.41)$$

where the projectors are defined as $\mathbf{P}_{\mathbf{A}} = \mathbf{A} \left(\mathbf{A}^H \mathbf{A} \right)^{-1} \mathbf{A}^H$, $\mathbf{P}_{\hat{\mathbf{A}}}^\perp = \mathbf{I} - \mathbf{P}_{\hat{\mathbf{A}}}$ and $\hat{\mathbf{A}} \triangleq \mathbf{A} (\hat{\boldsymbol{\eta}}_0, \hat{\boldsymbol{\eta}}_1)$.

In order to deal with the 2S-MLE heavy computational load, alternative estimators can be used. In this section, the CRE, also introduced in Section 1.2.1.2 is implemented. The CRE can be seen as a sub-optimal estimator because it works only under certain assumptions: the sources must not be too close in time or in frequency. Consequently the CRE is not expected to perform well when the two signals are very close in time. On the other hand, when the signals are separable, it asymptotically behaves as the 2S-MLE.

2.3.2.2 Signals Considered

Two representative signals are considered: i) a GPS L1 C/A signal as described in Section 1.3.2, and ii) a LFM chirp signal classically defined as follows:

$$s(t) = e^{j\phi(t)}, \quad \phi(t) = \pi B T \left(\frac{t}{T} - \frac{1}{2} \right)^2, \quad T = N T_s, \quad (2.42)$$

with B the chirp bandwidth and N the number of samples. The received signal is built with two delayed and attenuated replicas with arbitrary values of Doppler frequencies.

2.3.2.3 Scenarios Considered

Three scenarios are considered: scenario (a) presents the simple case where signals are clearly parted. Scenarios (b) and (c) present the case where the secondary signal is within 1 C/A chip, in this case, there is a strong interference between both signals. The parameters for the three scenarios considered are given in Table 2.1. Notice that the L1 C/A chips unit is 1/1023 ms. In this table ρ_1/ρ_0 is the ratio between the NLOS signal amplitude and the LOS signal one (also referred to as MDR) and $F_{di} = b_i f_c$ refers to the Doppler frequency in Hertz

corresponding to the Doppler stretch b_i , f_c is the carrier frequency.

Table 2.1: Simulations scenarios for the CRB validation: (a) two signals totally parted ($\Delta\tau = 2$ chips), (b) a secondary path very close to the main signal ($\Delta\tau = 1/4$ chip), and (c) considered to showcase the difference between the 2S-MLE and CRE ($\Delta\tau = 1/8$ chip).

	Estimator	$\Delta\tau$ (L1 C/A Chips and m)	Fd_0/Fd_1 (Hz)	ρ_1/ρ_0	$\Delta\phi$ ($^\circ$)
(a)	CRE	2 (600)	20/50	0.5	15
(b)	CRE	1/4 (75)	20/50	0.5	15
(c1)	CRE	1/8 (37.5)	20/50	0.5	15
(c2)	CMLE	1/8 (37.5)	20/50	0.5	15

As discussed in Section 2.3.2.1, depending on the time-delay difference between the two replicas $\Delta\tau$, one can apply a sub-optimal estimator such as the CRE, which may behave like a 2S-MLE in the asymptotic region (high SNR). In this case it is possible to see the estimator threshold region in a reasonable computation time. However, when it comes to very small values of $\Delta\tau$, meaning less than $1/F_s$ chip delay, a sub-optimal algorithm is in general not able to converge to the CRB. Consequently, during the simulations, when the product $\Delta\tau F_s$ is smaller than or equal to 1, the CRE is no longer efficient. In such limit cases, a direct implementation of the 2S-MLE is preferred. Computational cost soars but at very high SNR it is possible to limit the search area at 3σ , where σ is the expected variance of the estimated values, directly provided by the derived CRBs. Therefore the 2S-MLE simulation is valid only at very high SNR where the estimates are actually concentrated in the considered search area.

2.3.2.4 Numerical Results

For this section results, the baseband signal is sampled at a sampling frequency set equal to the front-end RF bandwidth $F_s = B = 8$ MHz. The RMSE values presented in the figures were estimated through 1000 runs of Monte Carlo simulation.

Scenario (a) In this scenario, a relative delay of two L1 C/A chips is considered, this corresponds to a path difference of around 600 m. In this case, the two signals are clearly parted and the estimation of the main signal could almost be decoupled from the estimation of the secondary signal. Figure 2.3 (left hand side plots) shows the RMSE for the time-delay estimation. One can see the threshold for the LFM signal at SNR = 20 dB and for the GPS L1 C/A signal at SNR = 21 dB. For a SNR larger than this threshold the estimator reaches the CRB: i) this validates the CRB expression, and ii) provides the receiver conditions to be in a correct operation region. It is worth pointing out the impact that having two sources have on the time-delay estimation with regard to the single source case, where the threshold region for a GPS signal is usually at SNR = 15 dB (refer to [Das20a]). Figure 2.3 (right hand side plots) show the RMSE for the Doppler frequency estimation. In this case, the performance for both LOS and NLOS signals is on the CRB in the range of SNR values considered. Again,

this result validates again the CRB expressions derived in Section 2.3.1.

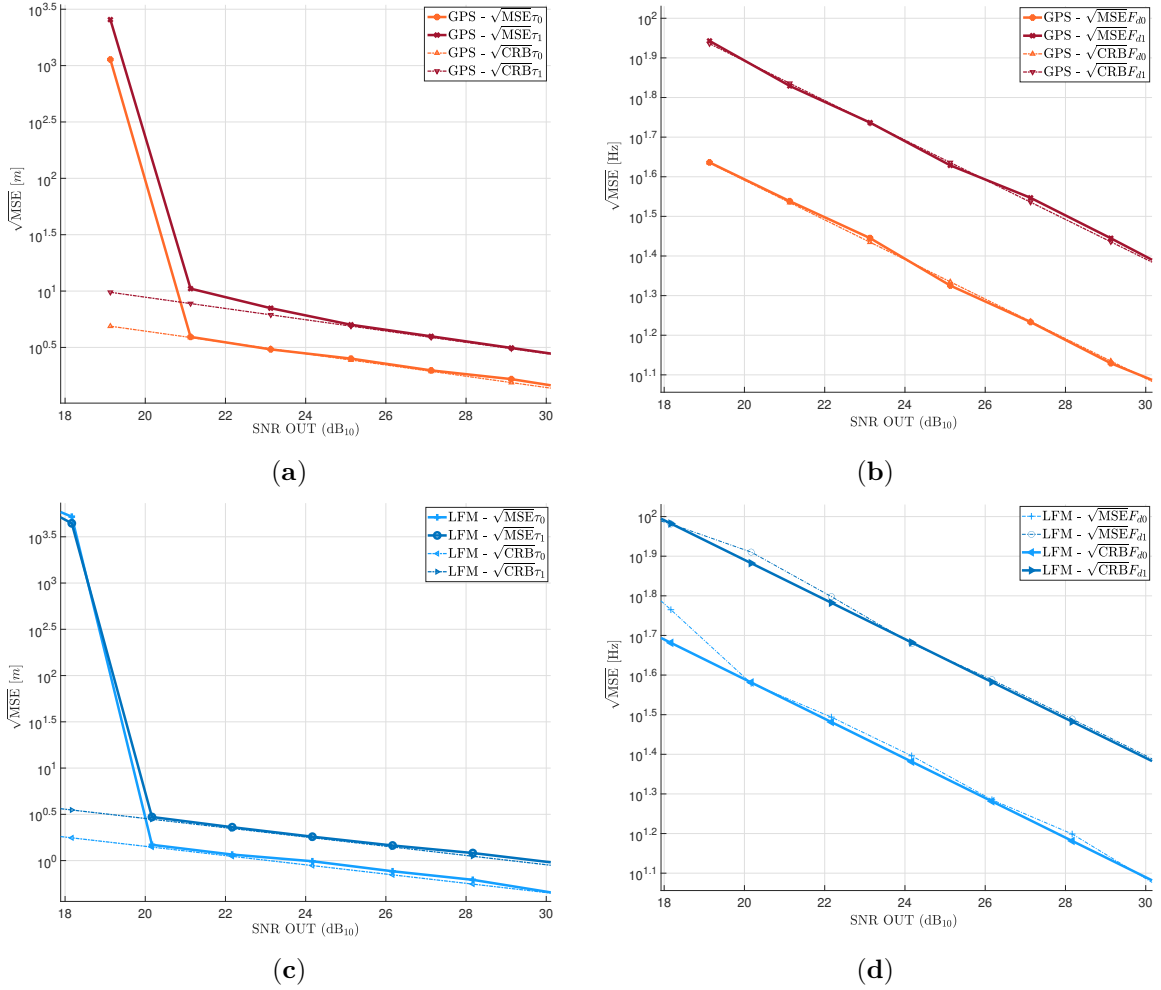


Figure 2.3: Scenario (a): Estimation of the delay (**left**) and the Doppler frequency (**right**) for $\Delta\tau = 2$ L1 C/A chips with CRE. (**top**) is for a GPS L1 C/A signal, (**bottom**) is for an LFM signal.

Scenario (b) In this scenario, a relative delay of a quarter of a chip is considered, this corresponds to about 75 m of path difference. In this case, there is a strong interference between the two signals. The results are shown in Figure 2.4. One can observe that even with such a strong interference, the time-delay estimation with the CRE is possible. However, having a close secondary signal has an impact on the estimation threshold, which is now $\text{SNR} = 22$ dB for the LFM signal, and $\text{SNR} = 27$ dB for the GPS signal. Besides, the proximity of the sources also rises the time-delay CRB as expected since they are harder to separate.

Scenario (c) In this scenario, a relative delay of an eighth of a L1 C/A chip, which accounts for a path delay of about 37.5m is considered. In this case, there is such a strong interference

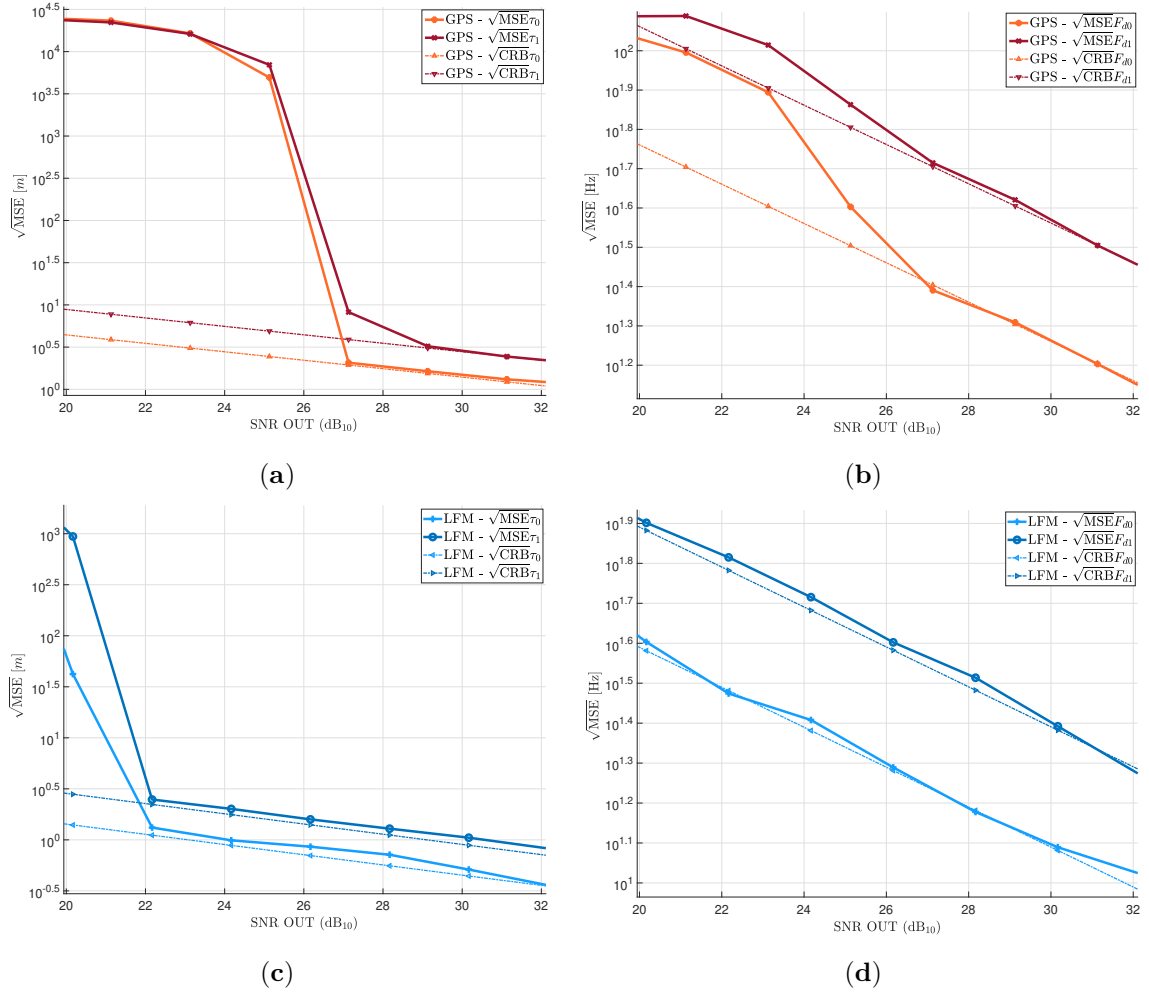


Figure 2.4: Scenario (b): Estimation of the delay (**left**) and the Doppler frequency (**right**) for $\Delta\tau = 1/4$ L1 C/A chips with CRE. (**top**) is for a GPS L1 C/A signal, (**bottom**) is for an LFM signal.

between both signals that the CRE cannot be efficient anymore. This limit is clearly shown in Figure 2.5. For both signals, the time-delay estimation never reaches the optimal performances set by the CRB. Interestingly, the LFM signal seems to be more robust for the Doppler estimation, reaching the CRB for the LOS signal but not for the NLOS one.

Figure 2.6 shows the results for the 2S-MLE. One can observe a good fit between the RMSE and the root CRB. This result supports the fact that the CRE limitations can be overcome by the 2S-MLE, and also validates again the CRB expressions for the dual source estimation problem derived in Section 2.3.1.

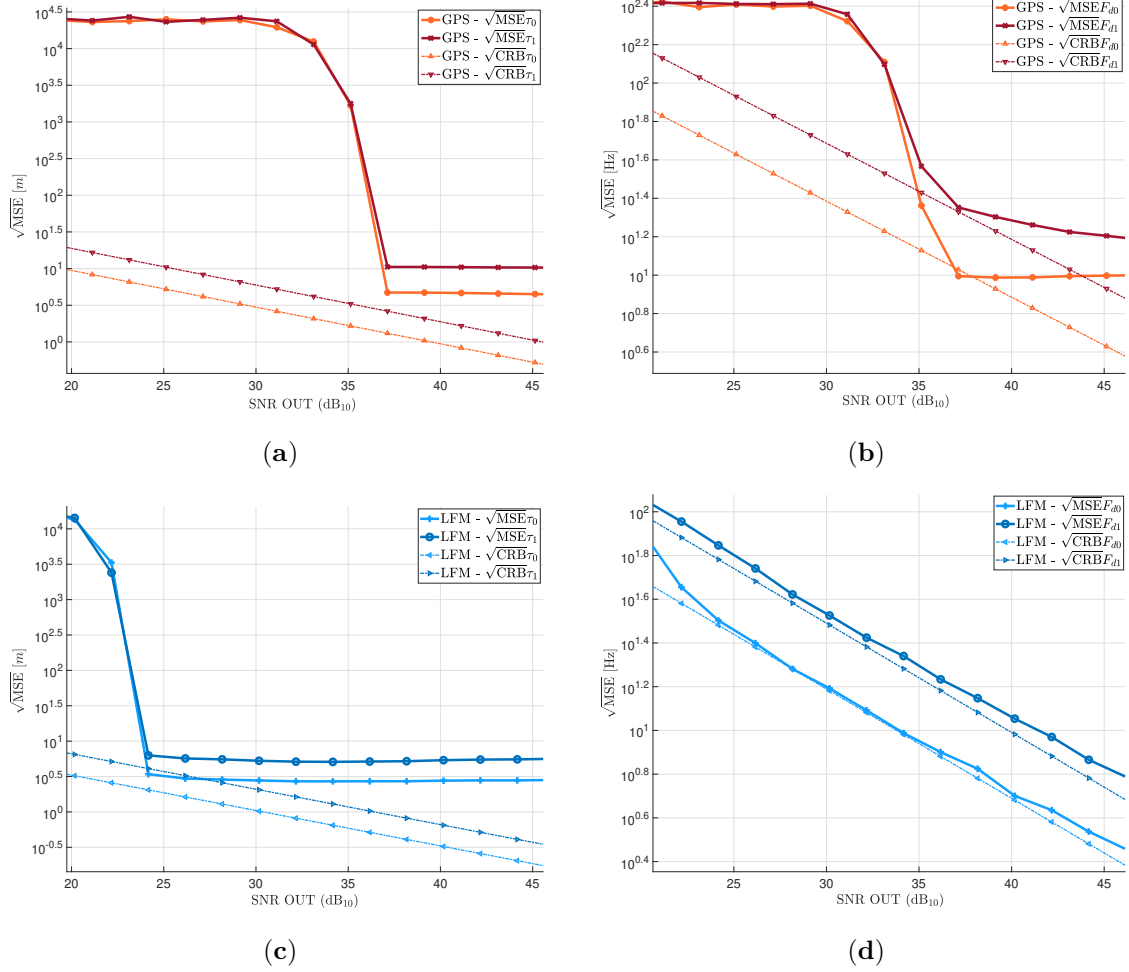


Figure 2.5: Scenario (c1): Estimation of the delay (**left**) and the Doppler frequency (**right**) for $\Delta\tau = 1/8$ L1 C/A chips with CRE. (**top**) is for a GPS L1 C/A signal, (**bottom**) is for an LFM signal.

2.3.3 RMSE for Different Multipath Mitigation Techniques

Armed with easy-to-use CRB expressions, it is now possible to compare the RMSE of the estimators considered in Section 2.2.1 in presence of an additive white Gaussian noise. Similarly to the MPEE approach, the RMSE can be displayed as a function of the path separation, but it is worth looking at it as a function of the SNR since it provides information on the threshold region, that is, the minimum SNR required above which a given algorithm is efficient. Section 2.3.3.2 and Section 2.3.3.3 propose the study of the considered estimators RMSE depending of i) the path separation and ii) the SNR. But first a note on CRB reparameterization should be added to link the very general CRB expressions derived in Section 2.3.1 to the simple multipath model.

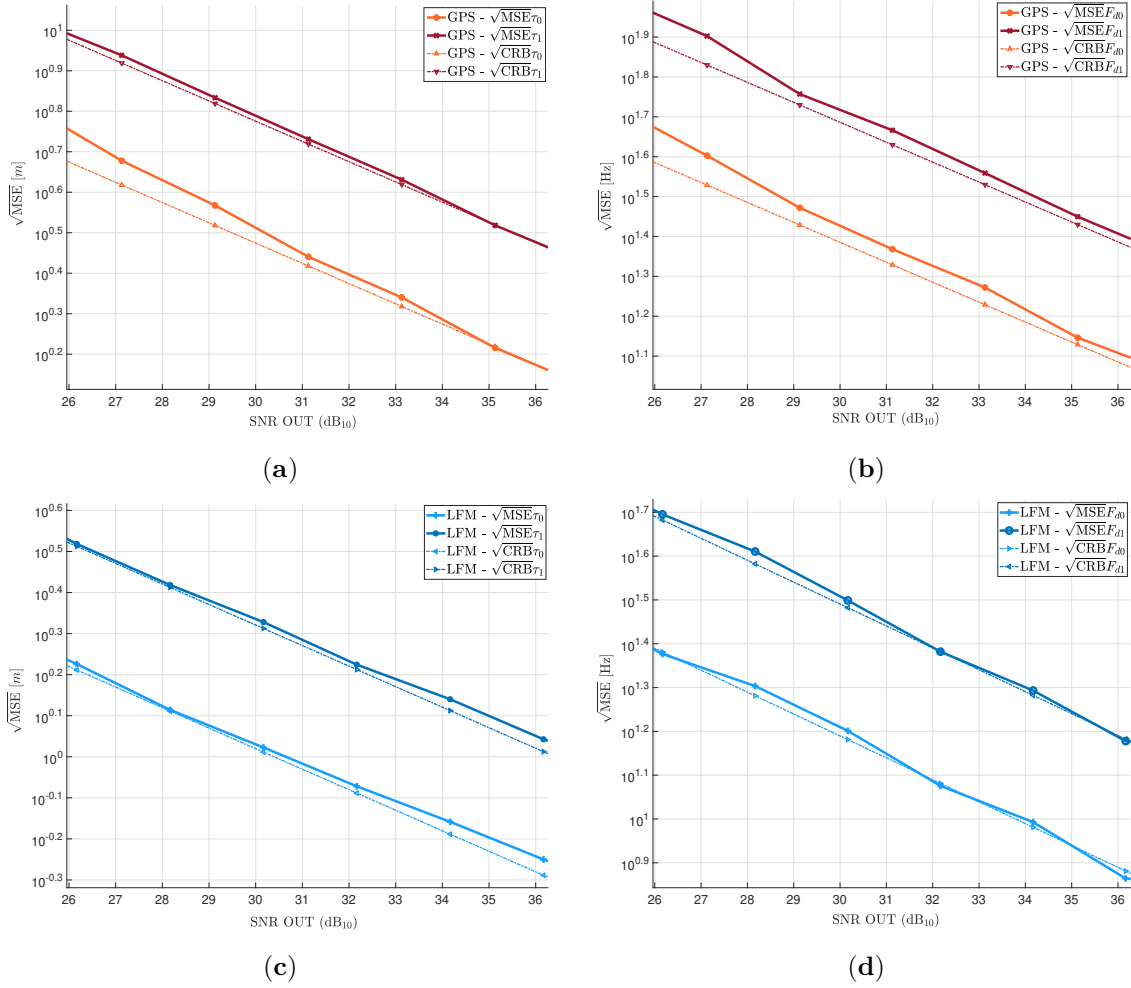


Figure 2.6: Scenario (c2): Estimation of the delay (**left**) and the Doppler frequency (**right**) for $\Delta\tau = 1/8$ L1 C/A chips with 2S-MLE. (**top**) is for a GPS L1 C/A signal, (**bottom**) is for an LFM signal.

2.3.3.1 Reparameterization of the Fisher Information Matrix

It is possible to express the vector of unknown parameters of the simple multipath model $\xi^T = (\tau_0, \rho_0, \phi_0, \tau_1, \rho_1, \phi_1)$, that assumes the Doppler known and compensated, as a function of the general vector of unknown parameters ϵ considered to derive the CRB:

$$\xi = \xi(\epsilon) = \begin{bmatrix} \tau_0 \\ \rho_0 \\ \phi_0 \\ \tau_1 \\ \rho_1 \\ \phi_1 \end{bmatrix} = \begin{bmatrix} 1 & 0 & 0 & 0 & 0 & 0 & 0 & 0 \\ 0 & 0 & 1 & 0 & 0 & 0 & 0 & 0 \\ 0 & 0 & 0 & 1 & 0 & 0 & 0 & 0 \\ 0 & 0 & 0 & 0 & 1 & 0 & 0 & 0 \\ 0 & 0 & 0 & 0 & 0 & 0 & 1 & 0 \\ 0 & 0 & 0 & 0 & 0 & 0 & 0 & 1 \end{bmatrix} \epsilon = \frac{\partial \xi(\epsilon)}{\partial \epsilon^T} \epsilon. \quad (2.43)$$

Based on this, the FIM of the vector $\boldsymbol{\xi}$ can be obtain using the reparameterization equation:

$$\mathbf{F}_{\boldsymbol{\epsilon}|\boldsymbol{\epsilon}}^r(\boldsymbol{\epsilon}) = \left(\frac{\partial \boldsymbol{\xi}(\boldsymbol{\epsilon})}{\partial \boldsymbol{\epsilon}^T} \right)^T \mathbf{F}_{\boldsymbol{\xi}|\boldsymbol{\xi}}(\boldsymbol{\xi}) \frac{\partial \boldsymbol{\xi}(\boldsymbol{\epsilon})}{\partial \boldsymbol{\epsilon}^T} \quad (2.44)$$

where $\mathbf{F}_{\boldsymbol{\epsilon}|\boldsymbol{\epsilon}}^r(\boldsymbol{\epsilon})$ is the reparameterized FIM from the CRB expression derived in Section 2.3.1 and relation (2.43).

2.3.3.2 RMSE with Regard to the Path Separation

Figure 2.7 illustrates the RMSE of the LOS signal time delay estimate as a function of the path separation. Moreover, the CRB (black solid line) is also illustrated. When the path separation is close to zero, the CRB for the estimation of the LOS time delay naturally soars to infinity since it becomes impossible to identify the LOS signal from the multipath signal. In this region all the estimators behaves better than the CRB because only one source is perceived.

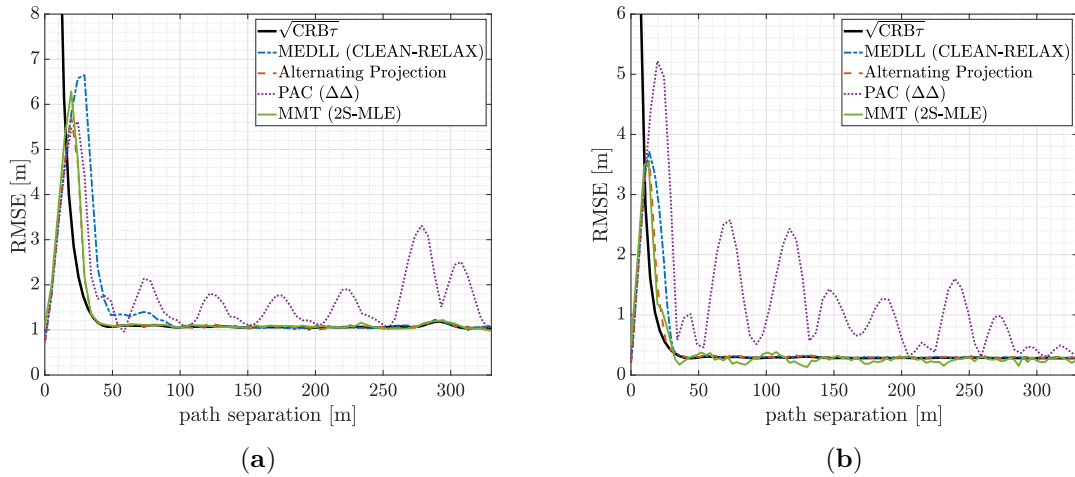


Figure 2.7: Estimation of the LOS time delay τ_0 with respect to the path separation for (a) GPS L1 C/A at SNR = 31 dB and (b) GALILEO E1B at SNR = 34 dB.

Except for the PAC RMSE, which is altered by a non-zero bias, it can be observed that the other three algorithms satisfyingly reach the root CRB at a given path separation. For GPS L1 C/A, when the MEDLL is used, the RMSE reaches the root CRB at about 100m of path separation, which is a little before becoming fully unbiased according to its MPEE. It is noteworthy to remark that in Figure 2.2a, between 100m and 140m the upper bound of the MPEE, which corresponds to the in-phase case, is at about 0.2m and in Figure 2.7a the resulting RMSE around this area is at about 1m. This involves that the bias observed from the MPEE is masked by a larger value of RMSE. The APE RMSE coherently reaches the root CRB at about 40m as hinted by its MPEE.

Finally, the MMT estimator was supposed to stick to the CRB at any path separation.

However, it does not behave so in the range between 0 to 40m due to the small value of SNR or the practical implementation, i.e., the search area for τ_0 and τ_1 was limited for computational load reasons and it did not allow large output values. In short, in this range of path separation, the estimation of the time delays may have been helped by the limited search area. Similar comments apply for Figure 2.7b.

2.3.3.3 RMSE with Regard to the SNR

For low SNR, an algorithm might not be able to detect a signal over the thermal noise. Then, there is a strong interest to understand how the considered algorithms behave when the SNR varies. The main feature that one might look for is, for a given path separation, the SNR threshold, i.e., the minimum SNR level necessary to estimate the signal in an efficient way.

Figure 2.8 illustrates the RMSE for each algorithm and for both GNSS signals with respect to the SNR. Both figures can be divided into three areas: in the left-hand side the SNR is so small that any estimator is outputting meaningless random estimates; then when the SNR rises, there is a transition area in which the RMSE is not yet reaching the CRB but is not out of range. Finally, in the right-hand side, there is a particular operation point where the SNR is large enough for the estimators to behave efficiently. It is exactly that transition point that is referred to as the SNR threshold.

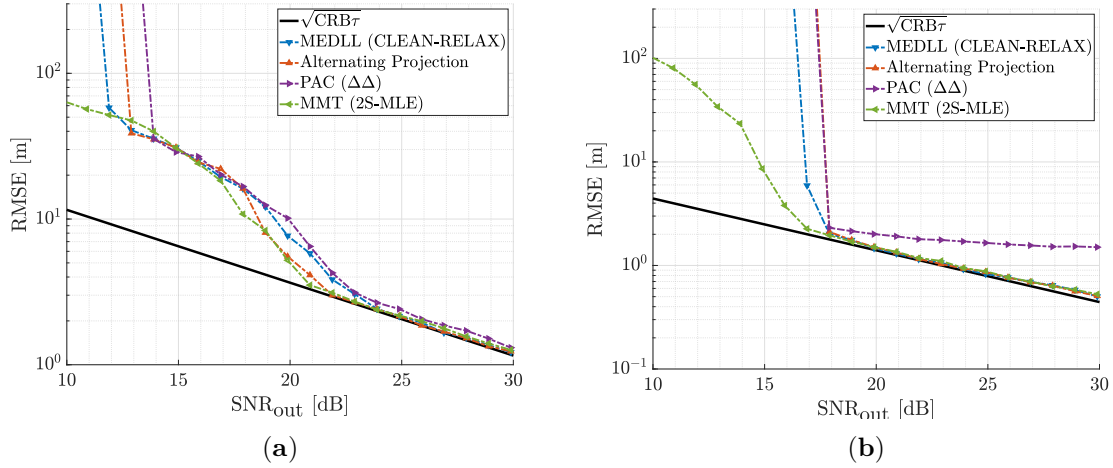


Figure 2.8: Estimation of the LOS time delay τ_0 with respect to the path separation for (a) GPS L1 C/A and (b) GALILEO E1B, at path separation set to 150m.

From Figure 2.8a, the considered estimators can be compared according to their behavior: the threshold is slightly better for the MMT algorithm (SNR = 21 dB), followed by the APE (SNR = 22 dB) and the MEDLL (SNR = 24 dB). The RMSE of the PAC algorithm (in magenta) does not seem to reach the CRB. Note that this is due to the fact that a biased estimator does not necessarily have a RMSE lower bounded by the computed CRB. This is particularly visible in the case of the GALILEO signal, in Figure 2.8b, where the PAC RMSE

converges to a constant value of about 1.5m, which is exactly the value of the PAC upper bound MPEE for this specific path separation of 150m (refer to Figure 2.2b).

2.3.4 Wrap-up on MSE vs CRB Considerations

By considering the signal polluted by a single multipath in the presence of an additive white Gaussian noise and by looking at the MSE of the algorithms under study it is now possible to compare them with one another and with an absolute lower bound. In short, the second order statistic provided by the MSE, along with the corresponding CRB naturally completes the information brought by the MPEE which is a first order metric. However, the estimation of the MSE is a tedious work because of the multiplicity of the parameters. Unfortunately, for receiver architecture design, there is no way to avoid the computation of the MSE, at least to compare it to the CRB. On the other hand, since the CRB does not depend on the receiver architecture, it could be used to build a very general and helpful metric for future signal design. The next section aims at building such a metric.

2.4 A Metric for Multipath-Robust Signal Design and Analysis

In order to build a relevant metric based on the CRB, one should consider the rearranged vector of unknown parameters ϵ :

$$\epsilon^T = (\sigma_n^2, \underbrace{\boldsymbol{\eta}_0^T, \boldsymbol{\eta}_1^T}_{\bar{\boldsymbol{\eta}}_2^T}, \rho_0, \phi_0, \rho_1, \phi_1) \quad (2.45)$$

where the parameters of interest $\boldsymbol{\eta}_0$ and $\boldsymbol{\eta}_1$, gathered in the concatenated vector $\bar{\boldsymbol{\eta}}_2$, have been put at the beginning of the vector. This formulation will simplify the operations on the FIM in the next few sections.

2.4.1 Insights and Extension of the Dual Source CRB

From [Ott93, (4.68)], the expression of the CRB for the estimation of the parameters of interest gathered in the concatenated vector $\bar{\boldsymbol{\eta}}_2$ based on a single observation of the signal is:

$$\mathbf{CRB}_{\bar{\boldsymbol{\eta}}_2|\epsilon}^{-1}(\epsilon) = \frac{2}{\sigma_n^2} \text{Re} \left\{ \boldsymbol{\Phi}(\bar{\boldsymbol{\eta}}_2) \odot \left(\mathbf{R}_{\boldsymbol{\alpha}}^T \otimes \begin{bmatrix} 1 & 1 \\ 1 & 1 \end{bmatrix} \right) \right\}, \quad (2.46)$$

$$\mathbf{R}_{\boldsymbol{\alpha}} = \boldsymbol{\alpha}\boldsymbol{\alpha}^H = \begin{bmatrix} \rho_0^2 & \rho_0\rho_1 e^{-j(\phi_1-\phi_0)} \\ \rho_0\rho_1 e^{j(\phi_1-\phi_0)} & \rho_1^2 \end{bmatrix}, \quad (2.47)$$

$$\Phi(\bar{\eta}_2) = \begin{bmatrix} \frac{\partial \mathbf{a}^H(\eta_0)}{\partial \eta_0} \\ \frac{\partial \mathbf{a}^H(\eta_1)}{\partial \eta_1} \end{bmatrix} \mathbf{P}_{\mathbf{A}}^\perp \begin{bmatrix} \frac{\partial \mathbf{a}^H(\eta_0)}{\partial \eta_0} \\ \frac{\partial \mathbf{a}^H(\eta_1)}{\partial \eta_1} \end{bmatrix}^H, \quad (2.48)$$

where, again, $\mathbf{P}_{\mathbf{A}} = \mathbf{I} - \mathbf{P}_{\mathbf{A}}^\perp = \mathbf{A} (\mathbf{A}^H \mathbf{A})^{-1} \mathbf{A}^H$ is the orthogonal projector onto the subspace defined by the set of the column vectors of matrix \mathbf{A} , \odot denotes the Hadamard product and \otimes denotes the Kronecker product.

Now, if one notes $\Gamma = |\Gamma|e^{j\phi_\Gamma}$ such that $\rho_1 e^{j\phi_1} = \Gamma \rho_0 e^{j\phi_0}$, the CRB defined in (2.46) can be further developed and written as:

$$\mathbf{CRB}_{\bar{\eta}_2|\epsilon}^{-1}(\epsilon) = \frac{2\rho_0^2}{\sigma_n^2} \text{Re} \left\{ \begin{bmatrix} \Phi_{1,1} & \Gamma^* \Phi_{2,1}^H \\ \Gamma \Phi_{2,1} & |\Gamma|^2 \Phi_{2,2} \end{bmatrix} \right\}. \quad (2.49)$$

Proof. see Appendix C.2 for details on the derivation of submatrices $\Phi_{i,j}$, $i, j = \{1, 2\}$. \square

Then, using the block matrix inversion lemma (B.2) on (2.49), the inverse of $\mathbf{CRB}_{\eta_0|\epsilon}$ can be expressed as

$$\mathbf{CRB}_{\eta_0|\epsilon}^{-1}(\epsilon) = \frac{2\rho_0^2}{\sigma_n^2} (\mathbf{A}_\Phi - \mathbf{B}_\Phi - \cos(2\phi_\Gamma) \mathbf{C}_\Phi + \sin(2\phi_\Gamma) \mathbf{D}_\Phi), \quad (2.50)$$

where, with superscript R and I standing for real and imaginary parts, respectively,

$$\mathbf{A}_\Phi = \Phi_{1,1}^R, \quad (2.51)$$

$$\mathbf{B}_\Phi = \frac{1}{2} \left(\Phi_{2,1}^R (\Phi_{2,2}^R)^{-1} \Phi_{2,1}^R + \Phi_{2,1}^I (\Phi_{2,2}^R)^{-1} \Phi_{2,1}^I \right), \quad (2.52)$$

$$\mathbf{C}_\Phi = \frac{1}{2} \left(\Phi_{2,1}^R (\Phi_{2,2}^R)^{-1} \Phi_{2,1}^R - \Phi_{2,1}^I (\Phi_{2,2}^R)^{-1} \Phi_{2,1}^I \right), \quad (2.53)$$

$$\mathbf{D}_\Phi = \frac{1}{2} \left(\Phi_{2,1}^R (\Phi_{2,2}^R)^{-1} \Phi_{2,1}^I + \Phi_{2,1}^I (\Phi_{2,2}^R)^{-1} \Phi_{2,1}^R \right). \quad (2.54)$$

Proof. In (2.49), the real part of the diagonal elements are directly the real part of the Φ matrix, denoted $\Phi_{1,1}^R$ and $\Phi_{2,2}^R$. On the other hand, the real part of the non-diagonal elements are affected by the complex number Γ :

$$\begin{aligned} \text{Re} \{ \Gamma \Phi_{2,1} \} &= \text{Re} \{ \Gamma^* \Phi_{2,1}^H \} \\ &= |\Gamma| \left(\cos(\phi_\Gamma) \Phi_{2,1}^R - \sin(\phi_\Gamma) \Phi_{2,1}^I \right). \end{aligned}$$

where $\Phi_{2,1}^R$ and $\Phi_{2,1}^I$ are the real and imaginary parts of $\Phi_{2,1}$, respectively. Then, in order to

obtain a closed-form of $\mathbf{CRB}_{\eta_0|\epsilon}(\epsilon)$, the block matrix inversion lemma is used (B.2),

$$\begin{aligned}\mathbf{CRB}_{\eta_0|\epsilon}^{-1}(\epsilon) &= \frac{2\rho_0^2}{\sigma_n^2} \left(\mathbf{\Phi}_{1,1}^R - |\Gamma| \left(\cos(\phi_\Gamma) \mathbf{\Phi}_{2,1}^R - \sin(\phi_\Gamma) \mathbf{\Phi}_{2,1}^I \right) \right) \\ &\quad \times \frac{1}{|\Gamma|^2} \left(\mathbf{\Phi}_{2,2}^R \right)^{-1} |\Gamma| \left(\cos(\phi_\Gamma) \mathbf{\Phi}_{2,1}^R - \sin(\phi_\Gamma) \mathbf{\Phi}_{2,1}^I \right) \\ &= \frac{2\rho_0^2}{\sigma_n^2} \left(\mathbf{\Phi}_{1,1}^R - \left(\cos(\phi_\Gamma) \mathbf{\Phi}_{2,1}^R - \sin(\phi_\Gamma) \mathbf{\Phi}_{2,1}^I \right) \right) \\ &\quad \times \left(\mathbf{\Phi}_{2,2}^R \right)^{-1} \left(\cos(\phi_\Gamma) \mathbf{\Phi}_{2,1}^R - \sin(\phi_\Gamma) \mathbf{\Phi}_{2,1}^I \right).\end{aligned}$$

Then, simply developing the expression and rearranging the matrices in terms of $\cos(2\phi_\Gamma)$ and $\sin(2\phi_\Gamma)$, the wanted expression (2.50) is obtained. \square

Note that in (2.50), the CRB does not depend on $|\Gamma|$. This means that in the asymptotic region of operation of the 2S-MLE, the estimation of both the time delay and the Doppler frequency of the LOS signal is not affected by the relative amplitude of the NLOS but only by its relative delay, Doppler and phase.

Equation (2.50) being a two-by-two matrix, it is easy to evaluate its inverse and then extract a closed-form of $\mathbf{CRB}_{\tau_0|\epsilon}$:

$$\mathbf{CRB}_{\tau_0|\epsilon}(\epsilon) = \frac{\sigma_n^2}{2\rho_0^2} \frac{[\mathbf{A}_\Phi - \mathbf{B}_\Phi - \cos(2\phi_\Gamma)\mathbf{C}_\Phi + \sin(2\phi_\Gamma)\mathbf{D}_\Phi]_{2,2}}{\det(\mathbf{A}_\Phi - \mathbf{B}_\Phi - \cos(2\phi_\Gamma)\mathbf{C}_\Phi + \sin(2\phi_\Gamma)\mathbf{D}_\Phi)} \quad (2.55)$$

where $\det(\cdot)$ is the determinant of the matrix in argument.

Similarly, a closed-form expression of the CRB for the estimation of the LOS Doppler parameter b_0 can be easily obtained by taking the other diagonal term of the inverse matrix:

$$\mathbf{CRB}_{b_0|\epsilon}(\epsilon) = \frac{\sigma_n^2}{2\rho_0^2} \frac{[\mathbf{A}_\Phi - \mathbf{B}_\Phi - \cos(2\phi_\Gamma)\mathbf{C}_\Phi + \sin(2\phi_\Gamma)\mathbf{D}_\Phi]_{1,1}}{\det(\mathbf{A}_\Phi - \mathbf{B}_\Phi - \cos(2\phi_\Gamma)\mathbf{C}_\Phi + \sin(2\phi_\Gamma)\mathbf{D}_\Phi)} \quad (2.56)$$

As a side note, the derived CRB presented in (2.55) and (2.56) are just alternative formulations of the CRB that were already derived in Section 2.3.1.

2.4.2 A Criterion Based on Cramér-Rao Bounds: Clean-to-Composite Bound Ratio

2.4.2.1 Definition for the time-delay

The case without signal reflection is equivalent to a known standard single source scenario. The corresponding closed-form CRB was derived in [Med20]. The resulting CRB is recalled

here:

$$\text{CRB}_{\tau_0|\theta_0,\sigma_n^2} = \frac{\sigma_n^2}{2\rho_0^2} \left[\mathbf{A}_{\Phi|\eta_1=\mathbf{0}}^{-1} \right]_{1,1}. \quad (2.57)$$

where $\mathbf{A}_{\Phi|\eta_1=\mathbf{0}}$ is the matrix \mathbf{A}_{Φ} defined in (2.51) where all the NLOS components are set to zero: $\boldsymbol{\eta}_1 = \mathbf{0}$. This way the interference terms are eliminated and the result is exactly the closed-form bound from [Med20, (17a)].

Then, by simply dividing the CRB in a single source context (2.57) by the corresponding CRB in a dual source source context (2.55), a generalized closed-form formulation of a CCBR for the time-delay estimation is obtained, which is expressed with the baseband signal samples (i.e., valid for any band-limited signal):

$$\begin{aligned} \text{CCBR}_{\tau}(\Delta\tau, b_0, b_1, \phi_{\Gamma}) &\triangleq \frac{\text{CRB}_{\tau_0|\theta_0,\sigma_n^2}}{\text{CRB}_{\tau_0|\epsilon}} \\ &= \frac{\left[\mathbf{A}_{\Phi}^{-1} \right]_{1,1} \det(\mathbf{A}_{\Phi} - \mathbf{B}_{\Phi} - \cos(2\phi_{\Gamma})\mathbf{C}_{\Phi} + \sin(2\phi_{\Gamma})\mathbf{D}_{\Phi})}{\left[\mathbf{A}_{\Phi} - \mathbf{B}_{\Phi} - \cos(2\phi_{\Gamma})\mathbf{C}_{\Phi} + \sin(2\phi_{\Gamma})\mathbf{D}_{\Phi} \right]_{2,2}} \end{aligned} \quad (2.58)$$

where the dependency on $\Delta\tau = \tau_1 - \tau_0$ was shown in Section 2.3.1.

First, notice that the CCBR_{τ} does not depend on the SNR of the LOS and the NLOS. Besides, as previously noticed, this ratio does not depend on the relative amplitude of the reflected signal either but it depends on the relative phase between the LOS and the NLOS signals. Actually, the CCBR_{τ} is π -periodic w.r.t. ϕ_{Γ} which reduces its study to the interval $(0, \pi)$ as shown in the next section.

2.4.2.2 Statistics of the Clean-to-Composite Bound Ratio

The π -periodicity of the CCBR can be used to easily obtain the maximum and minimum values for each scenario defined by the set of parameters of interest $(\Delta\tau, b_0, b_1)$. Indeed, by implementing the different matrices required to compute this ratio, it is quite direct to obtain these values. If one sets a PDF to the relative phase ϕ_{Γ} , it is then also possible to obtain an average value of the CCBR. For instance, one can assume the relative phase to be a random variable uniformly distributed over $(0, \pi)$, then the average can be numerically obtained as:

$$E_{\phi_{\Gamma}} \{ \text{CCBR}_{\tau} \} (\Delta\tau, b_0, b_1) = \frac{1}{\pi} \int_0^{\pi} \text{CCBR}_{\tau}(\Delta\tau, b_0, b_1, \phi) d\phi, \quad (2.59)$$

and, similarly for the Doppler CCBR:

$$E_{\phi_{\Gamma}} \{ \text{CCBR}_b \} (\Delta\tau, b_0, b_1) = \frac{1}{\pi} \int_0^{\pi} \text{CCBR}_b(\Delta\tau, b_0, b_1, \phi) d\phi. \quad (2.60)$$

2.4.2.3 Definition for the Doppler frequency

Similarly, it is possible to construct a CCBR_b that can be defined as the ratio between the CRB for the estimation of the LOS Doppler parameter b_0 in a single source context,

$$\text{CRB}_{b_0|\theta_0,\sigma_n^2} = \frac{\sigma_n^2}{2\rho_0^2} \left[\mathbf{A}_{\Phi|\eta_1=\mathbf{0}}^{-1} \right]_{2,2}, \quad (2.61)$$

and the corresponding CRB in a dual source context (2.56):

$$\begin{aligned} \text{CCBR}_b(\Delta\tau, b_0, b_1, \phi_\Gamma) &\triangleq \frac{\text{CRB}_{b_0|\theta_0,\sigma_n^2}}{\text{CRB}_{b_0|\epsilon}} \\ &= \frac{\left[\mathbf{A}_{\Phi}^{-1} \right]_{2,2} \det(\mathbf{A}_{\Phi} - \mathbf{B}_{\Phi} - \cos(2\phi_\Gamma)\mathbf{C}_{\Phi} + \sin(2\phi_\Gamma)\mathbf{D}_{\Phi})}{\left[\mathbf{A}_{\Phi} - \mathbf{B}_{\Phi} - \cos(2\phi_\Gamma)\mathbf{C}_{\Phi} + \sin(2\phi_\Gamma)\mathbf{D}_{\Phi} \right]_{1,1}} \end{aligned} \quad (2.62)$$

Again, this CCBR_b does not depend on the SNR nor the relative amplitude. It is also π -periodic with regard to ϕ_Γ .

2.4.3 Numerical Results

2.4.3.1 Averaged CCBR

The resulting CCBR (either for the delay or for the Doppler) with respect to the path separation starts from 0 when the LOS and NLOS signals are perfectly superimposed, in this case both sources are extremely hard to separate and estimating them both properly would imply a very large variance. Then the CCBR tends towards unity when the path separation gets large, and it may present local minima in its transition region. Considering a GPS L1 C/A signal, averaged CCBR results are presented in Figure 2.9 for different receivers' RF front-ends. For these figures and consistently with the assumptions taken so far, the sampling frequency is assumed equal to the front-end bandwidth: $B_R = 1$ MHz denotes then a low cost receiver and $B_R = 8$ MHz corresponds to higher quality one. In these figures, the relative phase is assumed uniformly distributed in $(0, \pi)$ and, the Doppler frequencies of both signals are arbitrarily set to 0 Hz, the average expression are taken based on (2.59) and (2.60). For the delay and Figure 2.9a, one can see the effect of the RF front-end bandwidth B_R : when it gets larger, the main signal is less affected by the multipath. It is interesting to see how the averaged CCBR_τ oscillates when the path separation is below 300 meters (i.e., 1 L1 C/A chip), especially for $B_R = 8$ MHz, where a peak at about 300 meters suggests a strong sensitivity to multipath of the C/A code for this specific path separation. In other words, for BPSK(1) modulations, the LOS signal time-delay estimation is particularly affected when the reflected signal appears at around 1 L1 C/A chip. Regarding the Doppler frequency and Figure 2.9b, one can remark that when B_R increases, the averaged CCBR_b tends to reach 1 for smaller path separations but oscillations appear for $B_R = 4$ MHz and $B_R = 8$ MHz that lead to make smaller B_R more robust to multipath than larger B_R . As a concrete example,

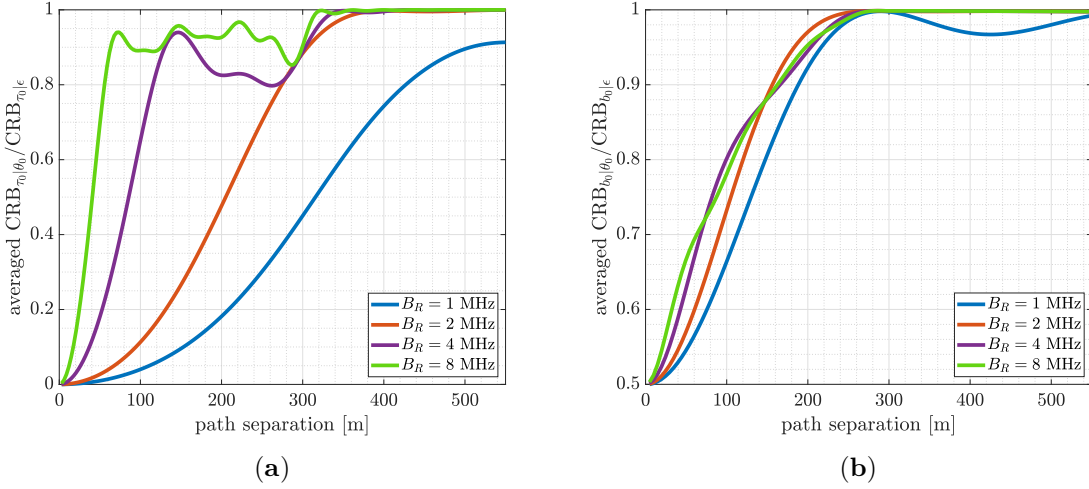


Figure 2.9: Averaged (a) CCBR_τ and (b) CCBR_b for the GPS L1 C/A signal with $B_R = 1, 2, 4, 8$ MHz, and ϕ_Γ uniformly distributed in $(0, \pi)$.

for path separation between 140m and 250m, signals filtered at 2 MHz are less affected by the presence of a multipath for the estimation of the Doppler frequency.

2.4.3.2 Min-Max Analysis: CCBREnvelope

In Figure 2.10, the GPS L1 C/A signal is compared to a GALILEO E1B signal at $B_R = 24$ MHz. In these figures, the envelopes between the minimum and maximum values of the CCBR_τ and CCBR_b are displayed. These values can easily be obtained numerically by evaluating the ratio for each value of relative phase. For the delay and the left-hand figures, a first interesting remark concerning these displays is that the min and max curves occasionally meet at specific path separations, for which the CCBR_τ does not depend on the relative phase. In Figure 2.10c, one can see that for the GALILEO signal, the CCBR_τ might oscillate more within the 300 meters but it remains above 0.9, while for the GPS signal, Figure 2.10a presents a depression at around 300m which goes down to 0.75. As of the Doppler frequency CCBR_b , it is worth pointing out that there is a relative phase for which the presence of a multipath does not affect the estimation performance of the LOS Doppler frequency. This corresponds to the flat upper bound of the envelopes. Then, considering GPS signal and Figure 2.10b, the lower bound CCBR_b is smooth and slowly increases up to 1 when the path separation reaches about 300m (or 1 C/A chip). For GALILEO signal and Figure 2.10d, the upper bound CCBR_b slope is steeper but oscillates before finally reaching 1 at about 250m of path separation. These observations support the fact that when the path separation is large enough the LOS Doppler frequency estimation is not affected anymore by the multipath.

Figure 2.11 presents two other examples of CCBR_τ envelopes for GPS L5-I and GALILEO E5 signals (defined in Section 1.3.2) when their entire bandwidth is sampled. These figures focus on the first 50 meters of path separation since the corresponding CCBR_τ are close to 1

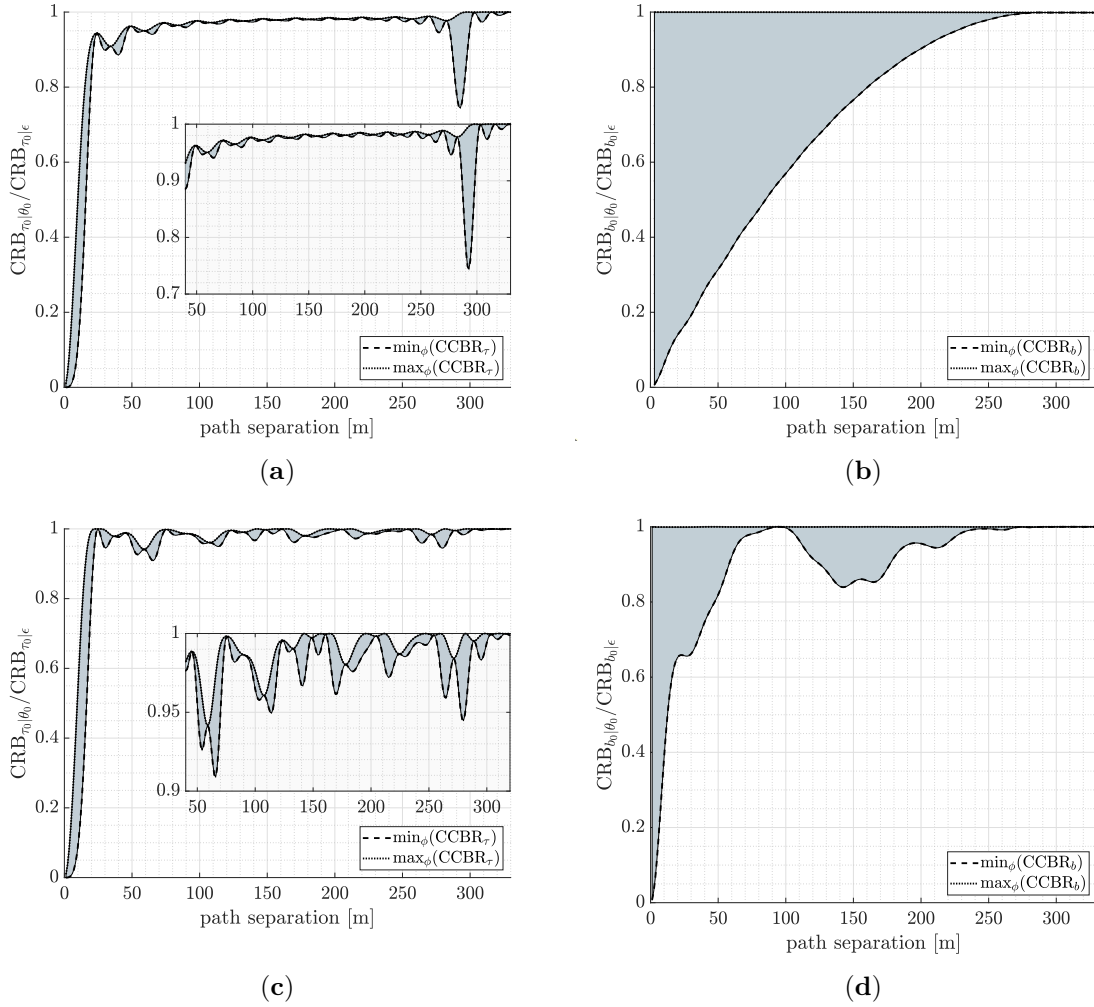


Figure 2.10: CCBR_{τ} envelope (**left**) and CCBR_b envelope (**right**) for GPS L1 C/A (**top**) and GALILEO E1B (**bottom**) signal with $B_R = 24$ MHz.

for larger path separation. In Figure 2.11a, the CCBR_{τ} can vary a lot in the range of path separation between 10 and 20 meters (CCBR_{τ} is in a 0.4 wide range), then for path separation larger than 30 meters, the multipath does not affect the estimation of the LOS time delay anymore (CCBR_{τ} larger than 0.9). For the E5 signal, Figure 2.11b, the shape of the envelope is less smooth, but overall thinner. For a path separation of 10 meters, it presents a large range of possible CCBR_{τ} values (between 0.6 and 1) but then the CCBR_{τ} goes above 0.9 at around 20 meters and flattens out. As a conclusive remark for these two figures, the E5 signal is slightly more resilient than the L5 signal when path separation increases since it is almost not affected anymore above 20 meters.

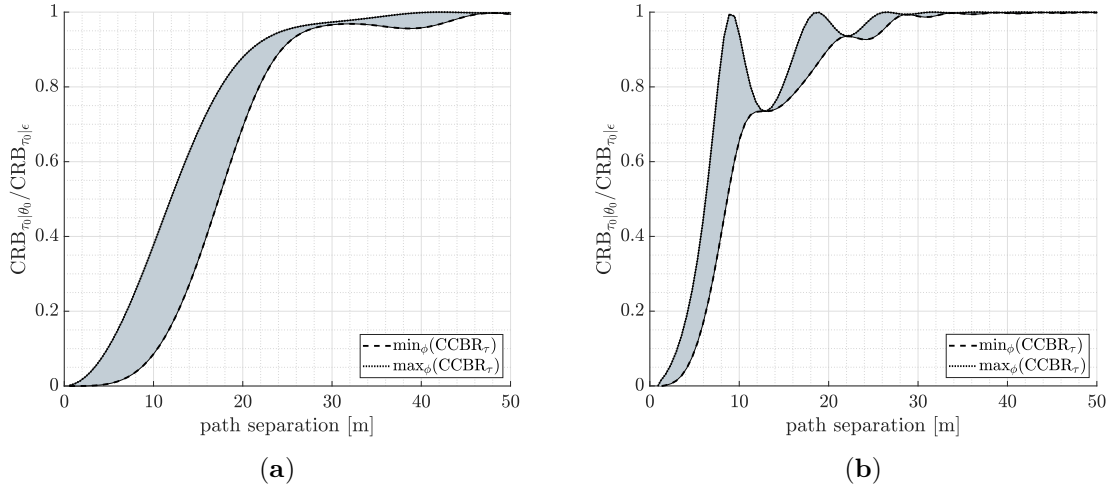


Figure 2.11: CCBR_τ envelope for (a) GPS L5-I with $B_R = 24$ MHz and (b) GALILEO E5 with $B_R = 60$ MHz.

2.4.3.3 Performance Considerations

From the results presented in Figures 2.10a and 2.10c, it is then possible to obtain the average RMSE of a given scenario, assuming a uniformly distributed relative phase ϕ_Γ over $(0, \pi)$. The single source CRB in [Med20], recalled in (2.57), is typically shown as a function of the output SNR, defined in (2.18). Then, for a specific SNR (i.e., a given receiver operation point), it is simple to use the CCBR_τ to obtain an evaluation of the best achievable accuracy for the time-delay estimation in presence of a single multipath using (2.59), this is not a bound anymore but it can provide an order of magnitude of the averaged bound:

$$E_{\phi_\Gamma} \left\{ \text{CRB}_{\tau_0|\epsilon} \right\} = \frac{\text{CRB}_{\tau_0|\theta_0, \sigma_n^2}}{E_{\phi_\Gamma} \{ \text{CCBR}_\tau \}} \quad (2.63)$$

Note that the result will consequently be averaged over the possible phase differences. Figure 2.12 coherently completes the example proposed in [Wei02, Fig. 5], in which the bounds are replaced by a ML-based estimator, and the results are obtained taking the RMSE of several Monte Carlo simulations with random secondary path relative phase. Three representative values of SNR are considered: 15, 25, and 33 dB. Notice that the first value, 15 dB, corresponds to a nominal $C/N_0 = 45$ dB-Hz and $T_I = 1$ ms, the minimum integration time for a GPS L1 C/A signal. The second one, 25 dB, under the same nominal conditions, corresponds to a standard integration time $T_I = 10$ ms, and the last one, 33 dB, is obtained for instance using an extended integration around 64ms. Equivalently, as done in high-sensitivity receivers, these values may correspond to larger non-coherent integration times for lower C/N_0 values.

It is worth pointing out that the results in Figure 2.12 differ from the work presented in [Wei02] when the path separation gets very small (less than 5 meters): where the averaged $\text{CRB}_{\tau_0|\epsilon}$ tends to infinity here, it goes down to a smaller value in [Wei02, Fig. 5]. This is due to the assumptions on the estimator. In [Wei02], the author presents the results of an

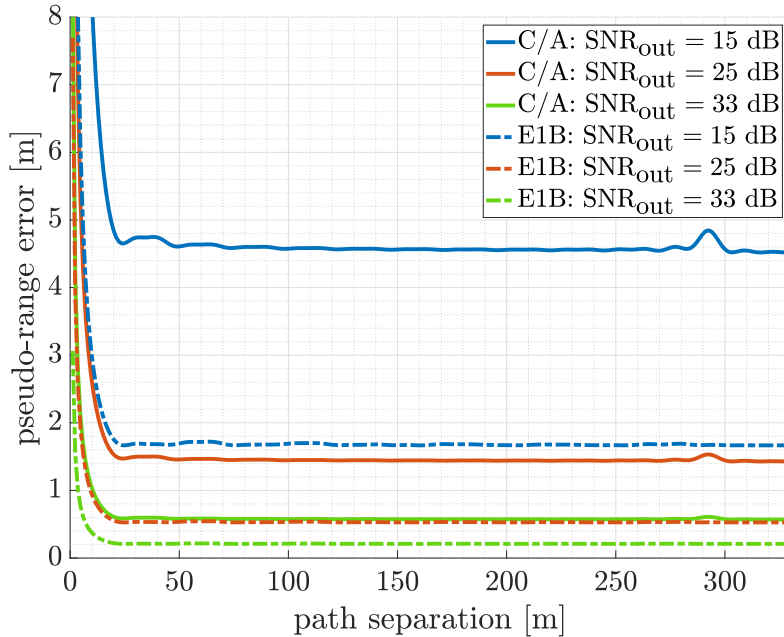


Figure 2.12: Averaged $\text{CRB}_{\tau_0|\epsilon}$ in presence of a single multipath as an application of the averaged CCBR_{τ} on GPS L1 C/A (continuous lines) and GALILEO E1B (dashed lines) signals, sampled at $B_R = 24$ MHz for three different representative SNR.

MMSE estimator considering amplitude of the LOS larger than the NLOS and the LOS signal arriving prior to the NLOS. This estimator appears to be biased and the CRB is a lower bound for any unbiased estimator. If one considers the estimation of two signals very close in time, the CCBR_{τ} tells that the variance of an unbiased dual source estimator will tend to infinity. This was also pointed out by the same author in [Wei95, Sec. IV], or more recently in [SA08, Sec. VI].

Finally, it is interesting to see how the peak at 300 meter observed in Figure 2.10a is reflected: at $\text{SNR} = 15$ dB, a multipath with a path separation around 300m would then induce an additional 20 cm error compared to a slightly different path separation. Such a behavior could be observed in Figure 2.7a. As expected, the GALILEO E1B signal performance is less affected than the GPS C/A signal one, given that the BOC modulation has a narrower correlation function.

2.4.4 Wrap-up on the CCBR Metric

Using an easy-to-use expression of the CRB it has then been possible to build a metric, the CCBR that is between 0 and 1 and that does not depend on the noise level nor the relative amplitude of the multipath signal. As a conclusive illustration, Figure 2.13 shows the averaged $\text{CRB}_{\tau_0|\epsilon}$ resulting from the CCBR_{τ} compared with the information provided by the MPEE in the case of two signals (GPS L1 C/A and GALILEO E1B) when the MEDLL is applied. From

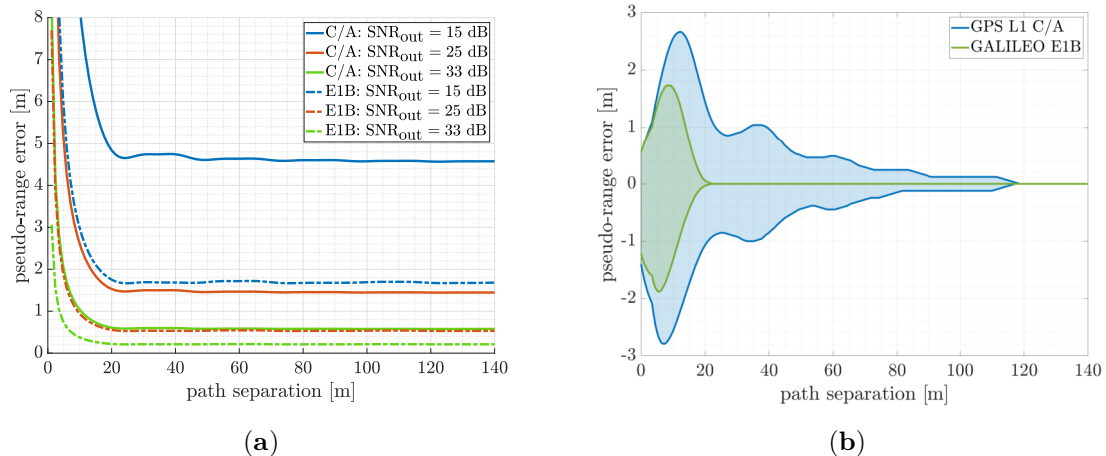


Figure 2.13: (a) Averaged $\text{CRB}_{\tau_0|\epsilon}$ in presence of a single multipath as an application of the averaged CCBR_{τ} on GPS L1 C/A (continuous lines) and GALILEO E1B (dashed lines) signals, sampled at $B_R = 24$ MHz for three different representative SNR. (b) Corresponding MPEE when applying the MEDLL on the GPS (blue) and the GALILEO (green) signals.

these figures, it is possible to see that, due to thermal noise, the best achievable performance of an unbiased estimator may be larger than the actual error predicted by the MPEE. Such a set of figure gives an insight of the contributions of both the error induced by the multipath thanks to the MPEE and the error induced by thermal noise thanks to the CCBR approach. For low SNR it is clear that the latter is more significant than the former.

The CCBR is then a helpful tool for signal design, but it is relevant if it is possible to implement unbiased dual source estimators, which can result difficult because of high computational complexity. Low cost receiver architectures are usually simple in order to comply with real-time constraints. In general, these implementations are not able to detect the presence of a multipath and keep on working based on a single source signal model. Using a single source signal model when there are two is known as a misspecified signal model. This misspecification can be taken into account to derive the misspecified CRB, which would provide information on the best achievable performance a misspecified estimator can reach. The next and final section of this chapter aims at deriving this MCRB.

2.5 Misspecified Cramér-Rao Bounds in Multipath Scenarios

The notion of misspecified signal model appears when one applies an algorithm that assumes the wrong signal model. In case of multipath, it is naturally the fact of applying an algorithm that ignore the presence of a multipath. As it has been well developed in Section 2.2, the consequence of such ignorance is a varying bias that can be captured by the MPEE. Interestingly, ignoring the presence of a multipath can also affect the resulting MSE. This effect is described by the so-called MCRB which will be studied in this section.

2.5.1 Note on the Signal Models

In this section, the different signal models and definitions are reminded to clarify both the notation and the wording.

2.5.1.1 True Signal Model

In presence of a single multipath signal, the true signal model is the dual source signal model defined in Section 2.1.2.1. As a reminder, at the output of the Hilbert filter, it can be written as:

$$\mathbf{x} = \alpha_0 \mathbf{a}_0 + \alpha_1 \mathbf{a}_1 + \mathbf{w}, \quad \mathbf{w} \sim \mathcal{CN}(0, \sigma_n^2 \mathbf{I}_N). \quad (2.64)$$

Consequently, the true data model PDF, noted $p_{\mathbf{x}}(\mathbf{x}; \boldsymbol{\theta}_0, \boldsymbol{\theta}_1)$, is written as,

$$p_{\mathbf{x}}(\mathbf{x}; \boldsymbol{\theta}_0, \boldsymbol{\theta}_1) = \mathcal{CN}(\alpha_0 \mathbf{a}_0 + \alpha_1 \mathbf{a}_1, \sigma_n^2 \mathbf{I}_N). \quad (2.65)$$

2.5.1.2 Misspecified Signal Model

As previously stated, standard receiver architectures do not account for the presence of possible multipath conditions, which reduces to consider a single source signal model. The misspecified signal model is then the one defined in Section 2.1.2.1, which is reminded hereafter:

$$\mathbf{x} = \rho_{pt} e^{j\phi_{pt}} \mathbf{a}_{pt} + \mathbf{w}, \quad \mathbf{w} \sim \mathcal{CN}(0, \sigma_n^2 \mathbf{I}_N), \quad (2.66)$$

with, $\alpha_{pt} = \rho_{pt} e^{j\phi_{pt}}$ and, for $n \in [N_1, N_2]$, $\mathbf{a}_{pt}^T = (\dots, s(nT_s - \tau_{pt}) e^{-j\omega_c b_{pt}(nT_s - \tau_{pt})}, \dots)$ and where the subscript pt refers to *pseudo-true*, which will necessarily depend on the true values $\boldsymbol{\theta}_0$ and $\boldsymbol{\theta}_1$, as discussed in the next section. Then, the misspecified data model PDF, noted $f_{\mathbf{x}}(\mathbf{x}|\boldsymbol{\theta}_{pt})$ is written as,

$$f_{\mathbf{x}}(\mathbf{x}; \boldsymbol{\theta}_{pt}) = \mathcal{CN}(\alpha_{pt} \mathbf{a}_{pt}, \sigma_n^2 \mathbf{I}_N), \quad (2.67)$$

where $\boldsymbol{\theta}_{pt}^T = (\boldsymbol{\eta}_{pt}^T, \rho_{pt}, \phi_{pt})$ is the vector of pseudo-true parameters. This vector of pseudo-true parameters is the one that minimizes the KLD between the true (2.65) and the misspecified (2.67).

2.5.2 Misspecified Maximum Likelihood Estimator

2.5.2.1 Definition of the MMLE

Given the misspecified model (2.67), the MMLE is simply a single source MLE that aims at estimating the vector of pseudo-true parameters $\boldsymbol{\theta}_{pt}$ by maximizing the likelihood given the

set of data \mathbf{x} . This maximization problem can be written as follows [Ott93]:

$$\hat{\boldsymbol{\eta}}_{pt} = \arg \max_{\boldsymbol{\eta}} |R_{\mathbf{x},\mathbf{a}}(\boldsymbol{\eta})|^2, \quad (2.68)$$

$$\hat{\rho}_{pt} = |R_{\mathbf{x},\mathbf{a}}(\hat{\boldsymbol{\eta}}_{pt})|, \quad (2.69)$$

$$\hat{\phi}_{pt} = \arg \left(R_{\mathbf{x},\mathbf{a}}(\hat{\boldsymbol{\eta}}_{pt}) \right), \quad (2.70)$$

$$R_{\mathbf{x},\mathbf{a}}(\boldsymbol{\eta}) = \frac{\mathbf{a}^H(\boldsymbol{\eta})\mathbf{x}}{\|\mathbf{a}(\boldsymbol{\eta})\|}, \quad (2.71)$$

with $R_{\mathbf{x},\mathbf{a}}(\boldsymbol{\eta})$ the normalized complex cross ambiguity function between the received signal \mathbf{x} and a clean replica \mathbf{a} .

2.5.2.2 Properties and Applications

In the case of a misspecified configuration, that is, in presence of a multipath, the estimator's outputs can be biased as it is illustrated by the MPEE when the multipath excess delay with regard to the LOS signal delay ($\tau_0 - \tau_1$) is small. In this case, the interference between both signals distorts the ambiguity function to be maximized, which in turn results in a biased LOS time-delay estimate. Similarly, if the difference between LOS and multipath Doppler frequencies is small, it can also lead to a bias on the estimated frequency.

Even if the MMLE appears to be biased with respect to the true LOS signal parameters, it has the property to be a misspecified-unbiased estimator of the pseudo-true parameters vector $\boldsymbol{\theta}_{pt}$ [For17]. Moreover, its MSE asymptotically tends to the MCRB, which makes it an asymptotically efficient estimator of the pseudo-true parameters.

Indeed, in [Hub67] and [Whi82], it was shown that the MMLE converges almost surely to the vector of pseudo-true parameters $\boldsymbol{\theta}_{pt}$, that is, for the considered observation models (2.65) and (2.67):

$$\boldsymbol{\theta}_{pt} = \arg \min_{\boldsymbol{\theta}} \{D(p_{\mathbf{x}}\|f_{\mathbf{x}})\} \Leftrightarrow \begin{cases} \boldsymbol{\eta}_{pt} = \arg \max_{\boldsymbol{\eta}} \{|R_{\alpha_0\mathbf{a}_0+\alpha_1\mathbf{a}_1,\mathbf{a}}(\boldsymbol{\eta})|^2\} \\ \alpha_{pt} = R_{\alpha_0\mathbf{a}_0+\alpha_1\mathbf{a}_1,\mathbf{a}}(\boldsymbol{\eta}) \end{cases} \quad (2.72)$$

Proof.

$$D(p_{\mathbf{x}}\|f_{\mathbf{x}}) = E_p \{ \ln(p_{\epsilon}(\mathbf{x}; \boldsymbol{\theta}_0, \boldsymbol{\theta}_1)) - \ln(f_{\mathbf{x}}(\mathbf{x}; \boldsymbol{\theta})) \} \quad (2.73)$$

$$\boldsymbol{\theta}_{pt} = \arg \min_{\boldsymbol{\theta}} \{D(p_{\mathbf{x}}\|f_{\mathbf{x}})\} = \arg \min_{\boldsymbol{\theta}} \{E_p \{-\ln(f_{\mathbf{x}}(\mathbf{x}; \boldsymbol{\theta}))\}\}, \quad (2.74)$$

where $E_p\{\cdot\}$ is the expectation with respect to the true model's PDF, and

$$-\ln(f_{\mathbf{x}}(\mathbf{x}; \boldsymbol{\theta})) = -N \ln(\pi) - 2N \ln(\sigma_n) + \frac{1}{\sigma_n^2} \|\mathbf{x} - \alpha\mathbf{a}(\boldsymbol{\eta})\|^2. \quad (2.75)$$

The last term of (2.75) can be expanded as follows:

$$\|\mathbf{x} - \alpha \mathbf{a}(\boldsymbol{\eta})\|^2 = \|\mathbf{x} - (\alpha_0 \mathbf{a}_0 + \alpha_1 \mathbf{a}_1) + (\alpha_0 \mathbf{a}_0 + \alpha_1 \mathbf{a}_1) - \alpha \mathbf{a}(\boldsymbol{\eta})\|^2 \quad (2.76)$$

$$\begin{aligned} &= \|\mathbf{x} - (\alpha_0 \mathbf{a}_0 + \alpha_1 \mathbf{a}_1)\|^2 + \|\alpha_0 \mathbf{a}_0 + \alpha_1 \mathbf{a}_1 - \alpha \mathbf{a}(\boldsymbol{\eta})\|^2 \\ &\quad + (\mathbf{x} - (\alpha_0 \mathbf{a}_0 + \alpha_1 \mathbf{a}_1))^H (\alpha_0 \mathbf{a}_0 + \alpha_1 \mathbf{a}_1 - \alpha \mathbf{a}(\boldsymbol{\eta})) \\ &\quad + (\alpha_0 \mathbf{a}_0 + \alpha_1 \mathbf{a}_1 - \alpha \mathbf{a}(\boldsymbol{\eta}))^H (\mathbf{x} - (\alpha_0 \mathbf{a}_0 + \alpha_1 \mathbf{a}_1)) \end{aligned} \quad (2.77)$$

The expectation of the first term of (2.77) is the noise covariance, which cannot be minimized and the expectations of the last two terms of (2.77) are null. Consequently, to minimize the expectation of (2.75) with regard to the argument $\boldsymbol{\theta}$, the equation can be simplified as,

$$\arg \min_{\boldsymbol{\theta}} \{E_p \{-\ln(f_{\mathbf{x}}(\mathbf{x}; \boldsymbol{\theta}))\}\} = \arg \min_{\boldsymbol{\theta}} \left\{ \|\alpha_0 \mathbf{a}_0 + \alpha_1 \mathbf{a}_1 - \alpha \mathbf{a}(\boldsymbol{\eta})\|^2 \right\}. \quad (2.78)$$

Let $\mathbf{P}_{\mathbf{a}}$ be the orthogonal projector and $\mathbf{P}_{\mathbf{a}}^{\perp} = \mathbf{I}_N - \mathbf{P}_{\mathbf{a}}$ with $\mathbf{P}_{\mathbf{a}} = \frac{\mathbf{a}(\boldsymbol{\eta})\mathbf{a}(\boldsymbol{\eta})^H}{\|\mathbf{a}(\boldsymbol{\eta})\|^2}$, which leads to

$$\|\alpha_0 \mathbf{a}_0 + \alpha_1 \mathbf{a}_1 - \alpha \mathbf{a}(\boldsymbol{\eta})\|^2 = \left\| (\mathbf{P}_{\mathbf{a}} + \mathbf{P}_{\mathbf{a}}^{\perp}) (\alpha_0 \mathbf{a}_0 + \alpha_1 \mathbf{a}_1 - \alpha \mathbf{a}(\boldsymbol{\eta})) \right\|^2 \quad (2.79)$$

$$= \left\| \mathbf{P}_{\mathbf{a}} (\alpha_0 \mathbf{a}_0 + \alpha_1 \mathbf{a}_1 - \alpha \mathbf{a}(\boldsymbol{\eta})) \right\|^2 + \left\| \mathbf{P}_{\mathbf{a}}^{\perp} (\alpha_0 \mathbf{a}_0 + \alpha_1 \mathbf{a}_1 - \alpha \mathbf{a}(\boldsymbol{\eta})) \right\|^2 \quad (2.80)$$

$$= \left\| \mathbf{a}(\boldsymbol{\eta}) \left(\frac{\mathbf{a}(\boldsymbol{\eta})^H}{\|\mathbf{a}(\boldsymbol{\eta})\|^2} (\alpha_0 \mathbf{a}_0 + \alpha_1 \mathbf{a}_1) - \alpha \right) \right\|^2 + \left\| \mathbf{P}_{\mathbf{a}}^{\perp} (\alpha_0 \mathbf{a}_0 + \alpha_1 \mathbf{a}_1) \right\|^2, \quad (2.81)$$

then the parameters that minimize the KLD are,

$$\boldsymbol{\theta}_{pt} = \arg \min_{\boldsymbol{\theta}} \left\{ \|\alpha_0 \mathbf{a}_0 + \alpha_1 \mathbf{a}_1 - \alpha \mathbf{a}(\boldsymbol{\eta})\|^2 \right\} \Leftrightarrow \begin{cases} \boldsymbol{\eta}_{pt} = \arg \max_{\boldsymbol{\eta}} \left\{ \left\| \mathbf{P}_{\mathbf{a}}^{\perp} (\alpha_0 \mathbf{a}_0 + \alpha_1 \mathbf{a}_1) \right\|^2 \right\} \\ \alpha_{pt} = \frac{\mathbf{a}(\boldsymbol{\eta}_{pt})^H}{\|\mathbf{a}(\boldsymbol{\eta}_{pt})\|^2} (\alpha_0 \mathbf{a}_0 + \alpha_1 \mathbf{a}_1) \end{cases} \quad (2.82)$$

with $\alpha_{pt} = \rho_{pt} e^{j\Phi_{pt}}$. This result shows that minimizing the KLD between the true and the misspecified distribution is equivalent to performing misspecified maximum likelihood estimation. \square

Even if there is no closed-form for (2.72), it can be easily evaluated numerically. Then, once the MCRB expression is obtained, a way to check its exactness is to run Monte Carlo simulations in order to compute the MSE of the MMLE, and compare it to the MCRB.

2.5.3 Closed-Form MCRBs for Delay/Doppler Estimation under Multipath

In [RH15], the MCRB have been described as an extension of the Slepian-Bangs formulas, which were then expressed as a combination of two information matrices in [For17]: $\mathbf{A}(\boldsymbol{\theta}_{pt})$ and $\mathbf{B}(\boldsymbol{\theta}_{pt})$,

$$\text{MCRB}(\boldsymbol{\theta}_{pt}) = \mathbf{A}(\boldsymbol{\theta}_{pt})^{-1} \mathbf{B}(\boldsymbol{\theta}_{pt}) \mathbf{A}(\boldsymbol{\theta}_{pt})^{-1}, \quad (2.83)$$

where,

$$[\mathbf{A}(\boldsymbol{\theta}_{pt})]_{p,q} = \frac{2}{\sigma_n^2} \text{Re} \left\{ (\delta \mathbf{a})^H \left(\frac{\partial^2 \alpha_{pt} \mathbf{a}_{pt}}{\partial \theta_p \partial \theta_q} \right) \right\} \Big|_{\boldsymbol{\theta}=\boldsymbol{\theta}_{pt}} - [\mathbf{B}(\boldsymbol{\theta}_{pt})]_{p,q}, \quad (2.84)$$

$$[\mathbf{B}(\boldsymbol{\theta}_{pt})]_{p,q} = \frac{2}{\sigma_n^2} \text{Re} \left\{ \left(\frac{\partial \alpha_{pt} \mathbf{a}_{pt}}{\partial \theta_p} \right)^H \left(\frac{\partial \alpha_{pt} \mathbf{a}_{pt}}{\partial \theta_q} \right) \right\} \Big|_{\boldsymbol{\theta}=\boldsymbol{\theta}_{pt}}, \quad (2.85)$$

and $\delta \mathbf{a} \triangleq \alpha_0 \mathbf{a}_0 + \alpha_1 \mathbf{a}_1 - \alpha_{pt} \mathbf{a}_{pt}$ is the difference of the means between the true and the misspecified data models. The covariance matrices between both models are assumed to be equal.

2.5.3.1 Single Source Fisher Information Matrix

In the matrix $\mathbf{B}(\boldsymbol{\theta}_{pt})$, one can recognize the FIM of a single source CSM. A compact expression of this matrix, that depends only on the baseband signal samples, was derived in [Med20] and recalled in (2.24),

$$\mathbf{B}(\boldsymbol{\theta}_{pt}) = \frac{2F_s}{\sigma_n^2} \text{Re} \{ \mathbf{Q} \mathbf{W} \mathbf{Q}^H \}, \quad \mathbf{W} = \begin{bmatrix} w_1 & w_2^* & w_3^* \\ w_2 & W_{2,2} & w_4^* \\ w_3 & w_4 & W_{3,3} \end{bmatrix}, \quad (2.86)$$

with \mathbf{Q} defined in (D.6) and the elements in \mathbf{W} are expressed with regard to the baseband signal samples as recorded in (2.26).

2.5.3.2 Model Mismatch Information Matrix

The matrix $\mathbf{A}(\boldsymbol{\theta}_{pt})$ accounts for the model misspecification. Its elements can also be expressed in a compact form as a function of the baseband samples as,

$$[\mathbf{A}(\boldsymbol{\theta}_{pt})]_{p,q} = \frac{2F_s}{\sigma_n^2} \text{Re} \{ [\mathbf{Q}_q]_{p,\cdot} \mathbf{W}^{\mathbf{A}} \} - [\mathbf{B}(\boldsymbol{\theta}_{pt})]_{p,q}, \quad (2.87)$$

where $[\mathbf{Q}_q]_{p,\cdot}$ is the p -th row of the matrix \mathbf{Q}_q , $\mathbf{W}^{\mathbf{A}}$ is defined as $\mathbf{W}^{\mathbf{A}} = \alpha_0 \mathbf{w}^{\mathbf{A}}(\boldsymbol{\eta}_0) + \alpha_1 \mathbf{w}^{\mathbf{A}}(\boldsymbol{\eta}_1) - \alpha_{pt} \mathbf{w}^{\mathbf{A}}(\boldsymbol{\eta}_{pt})$ and, for $k \in \{0, 1, pt\}$, $\Delta \tau_k = \tau_k - \tau_{pt}$, $\Delta b_k = b_k - b_{pt}$, $\mathbf{w}^{\mathbf{A}}(\boldsymbol{\eta}_k)$

is a six-element column vector whose components are

$$\mathbf{w}_1^{\mathbf{A}}(\boldsymbol{\eta}_k)^* = \frac{1}{F_s} \mathbf{s}^H \mathbf{U} \left(\frac{f_c \Delta b_k}{F_s} \right) \mathbf{V}^{\Delta,0} \left(\frac{\Delta \tau_k}{T_s} \right) \mathbf{s} e^{j\omega_c b_k \Delta \tau_k}, \quad (2.88)$$

$$\mathbf{w}_2^{\mathbf{A}}(\boldsymbol{\eta}_k)^* = \frac{1}{F_s^2} \mathbf{s}^H \mathbf{D} \mathbf{U} \left(\frac{f_c \Delta b_k}{F_s} \right) \mathbf{V}^{\Delta,0} \left(\frac{\Delta \tau_k}{T_s} \right) \mathbf{s} e^{j\omega_c b_k \Delta \tau_k}, \quad (2.89)$$

$$\mathbf{w}_3^{\mathbf{A}}(\boldsymbol{\eta}_k)^* = \frac{1}{F_s^3} \mathbf{s}^H \mathbf{D}^2 \mathbf{U} \left(\frac{f_c \Delta b_k}{F_s} \right) \mathbf{V}^{\Delta,0} \left(\frac{\Delta \tau_k}{T_s} \right) \mathbf{s} e^{j\omega_c b_k \Delta \tau_k}, \quad (2.90)$$

$$\mathbf{w}_4^{\mathbf{A}}(\boldsymbol{\eta}_k)^* = \left(-\mathbf{s}^H \mathbf{U} \left(\frac{f_c \Delta b_k}{F_s} \right) \mathbf{V}^{\Delta,1} \left(\frac{\Delta \tau_k}{T_s} \right) \mathbf{s} + \frac{j\omega_c \Delta b_k}{F_s} \mathbf{s}^H \mathbf{U} \left(\frac{f_c \Delta b_k}{F_s} \right) \mathbf{V}^{\Delta,0} \left(\frac{\Delta \tau_k}{T_s} \right) \mathbf{s} \right) e^{j\omega_c b_k \Delta \tau_k}, \quad (2.91)$$

$$\begin{aligned} \mathbf{w}_5^{\mathbf{A}}(\boldsymbol{\eta}_k)^* &= \left(-\frac{1}{F_s} \mathbf{s}^H \mathbf{U} \left(\frac{f_c \Delta b_k}{F_s} \right) \mathbf{V}^{\Delta,0} \left(\frac{\Delta \tau_k}{T_s} \right) \mathbf{s} - \frac{1}{F_s} \mathbf{s}^H \mathbf{D} \mathbf{U} \left(\frac{f_c \Delta b_k}{F_s} \right) \mathbf{V}^{\Delta,1} \left(\frac{\Delta \tau_k}{T_s} \right) \mathbf{s} \right. \\ &\quad \left. + j \frac{\omega_c \Delta b_k}{F_s^2} \mathbf{s}^H \mathbf{D} \mathbf{U} \left(\frac{f_c \Delta b_k}{F_s} \right) \mathbf{V}^{\Delta,0} \left(\frac{\Delta \tau_k}{T_s} \right) \mathbf{s} \right) e^{j\omega_c b_k \Delta \tau_k}, \end{aligned} \quad (2.92)$$

$$\begin{aligned} \mathbf{w}_6^{\mathbf{A}}(\boldsymbol{\eta}_k)^* &= \left(-F_s \mathbf{s}^H \mathbf{U} \left(\frac{f_c \Delta b_k}{F_s} \right) \mathbf{V}^{\Delta,2} \left(\frac{\Delta \tau_k}{T_s} \right) \mathbf{s} - j 2\omega_c \Delta b_k \mathbf{s}^H \mathbf{U} \left(\frac{f_c \Delta b_k}{F_s} \right) \mathbf{V}^{\Delta,1} \left(\frac{\Delta \tau_k}{T_s} \right) \mathbf{s} \right. \\ &\quad \left. - \frac{(\omega_c \Delta b_k)^2}{F_s} \mathbf{s}^H \mathbf{U} \left(\frac{f_c \Delta b_k}{F_s} \right) \mathbf{V}^{\Delta,0} \left(\frac{\Delta \tau_k}{T_s} \right) \mathbf{s} \right) e^{j\omega_c b_k \Delta \tau_k}, \end{aligned} \quad (2.93)$$

where \mathbf{s} , the baseband sample vector, is defined in (C.29), \mathbf{D} in (C.32), \mathbf{U} in (C.31), $\mathbf{V}^{\Delta,0}$ in (C.33), $\mathbf{V}^{\Delta,1}$ in (C.35) and $\mathbf{V}^{\Delta,2}$ in (C.37).

Proof. refer to Appendix D. □

2.5.4 Validation Using the Misspecified Maximum Likelihood Estimator

2.5.4.1 Methodology and Simulation Set-Up

In order to validate the MCRB expressions, the properties of the MMLE (see Section 2.5.2.2) are exploited. Indeed, the MMLE being an asymptotically efficient misspecified-unbiased estimator of $\boldsymbol{\theta}_{pt}$, its MSE evaluated with regard to the pseudo-true parameters is expected to asymptotically converge to the corresponding MCRB. Classically two representative GNSS signals, GPS L1 C/A and GALILEO E1B, are considered, for both signals, the sampling frequency is set at $F_s = 8$ MHz, the coherent integration time at $T_I = 4$ ms and a single multipath is added. The MMLE MSE is obtained from 2000 Monte Carlo runs, for different SNR values. The SNR is still defined at the output of the matched filter with regard to the LOS source as in (2.18). The true parameters values are gathered in Table 2.2 and Table 2.3, where the last column was obtained by running a noiseless simulation, since it has been shown that the MMLE is known to be misspecified-unbiased and converges to the vector of pseudo-true parameters. Two RMSEs are then computed, one with regard to the true parameters and the other one with regard to the pseudo-true parameters, which are defined

Table 2.2: MCRB simulation settings for GPS L1 C/A signal.

	θ_0	θ_1	θ_{pt}
τ [C/A chip]	0	0.25	0.0238
F_d [Hz]	0	100	24
ρ [-]	1	0.5	1.2342
ϕ [rad]	0	0.2618	0.0351

Table 2.3: MCRB simulation settings for GALILEO E1B signal.

	θ_0	θ_1	θ_{pt}
τ [C/A chip]	0	0.125	0.0138
F_d [Hz]	0	100	6
ρ [-]	1	0.5	1.0973
ϕ [rad]	0	0.2618	-0.041666

for the i -th element of the vector of parameters θ as follows,

$$\text{RMSE}([\theta_0]_i) \triangleq E \left\{ \left([\hat{\theta}]_i - [\theta_0]_i \right)^2 \right\}, \quad \text{RMSE}([\theta_{pt}]_i) \triangleq E \left\{ \left([\hat{\theta}]_i - [\theta_{pt}]_i \right)^2 \right\}, \quad (2.94)$$

In addition, the bias induced by the model mismatch is also displayed in the results, which is defined for any element i of the vector of parameters θ as

$$\text{bias}([\theta]_i) = [\theta_{pt}]_i - [\theta_0]_i. \quad (2.95)$$

Finally, the MCRBs are compared to the dual source CRBs corresponding to the true signal model (2.65), which were derived in section 2.3.1.

2.5.4.2 Numerical Results

Figure 2.14 and Figure 2.15 show, for both the GPS and the GALILEO signals, the RMSEs (2.94) for each of the MMLE estimates: τ , $F_d = bF_c$, ρ and ϕ , with regard to the true and pseudo-true parameters, which are displayed along with i) their corresponding square-root MCRBs (2.83), ii) the bias induced by the multipath (2.95), and iii) the dual source CRB ($2S\sqrt{\text{CRB}}$) for the corresponding LOS parameter estimation.

First, notice that in all the figures, the MMLE estimators' RMSE with regard to the pseudo-true parameters converges to the proposed MCRBs when the SNR gets large enough, which is in accordance with the theory [DK11]. This proves the validity and exactness of the compact MCRB expressions derived in this section 2.5.3, and the asymptotic efficiency of the MMLE estimator with regard to the pseudo-true parameters. Second, the MMLE estimators' RMSE with regard to the true parameters converges to the corresponding $\sqrt{\text{bias}^2 + \text{MCRB}}$, that is, there is a clear performance degradation induced by the bias term, which for large

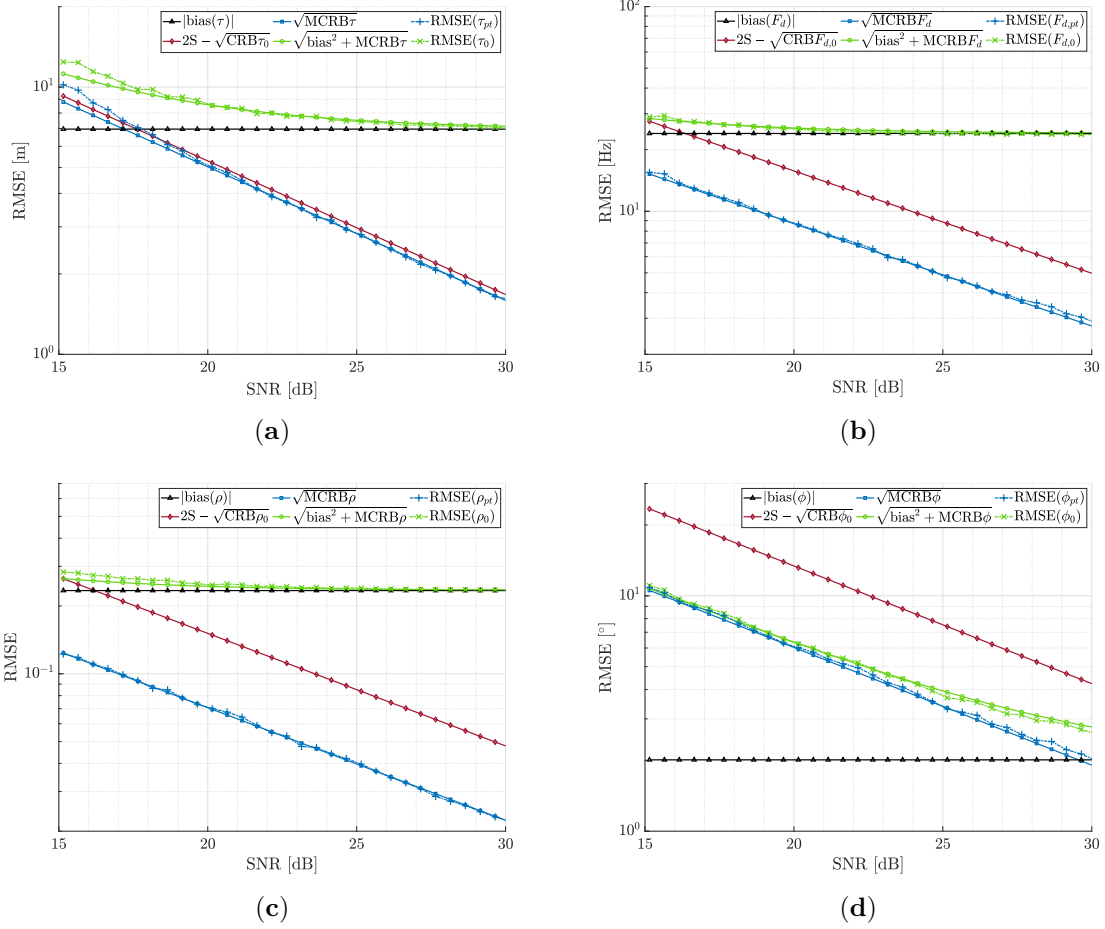


Figure 2.14: Estimation of the delay (a), the Doppler frequency (b), the amplitude (c) and the phase (d) of the GPS L1 C/A LOS signal in presence of a single multipath using a MMLE and comparison of the RMSE with the corresponding MCRB, CRB and bias.

SNR values dominates in front of the MCRB ($\sqrt{\text{bias}^2 + \text{MCRB}} \rightarrow \text{bias}$). A typical GNSS receiver operation point is around $\text{SNR} = 25$ dB at the output of the matched filter. At this noise level, in the case of the time-delay estimation, that is the main parameter of interest to solve the positioning problem, the performance degradation induced by the multipath is around 4.5m (from 3m to 7.5m) for GPS L1 C/A as in Figure 2.14a and around 2.75m (from 1.25m to 4m) for GALILEO E1B as in Figure 2.15a. Also, it is interesting to see that, except for the time-delay estimation of the GALILEO signal (Figure 2.15a) the 2S-CRB is above the MCRB for all the estimated parameters: using the MMLE would then allow the user to get a biased estimate but with a smaller variance. Last point is that for the considered scenarios, the phase estimate is much less impacted by the multipath.

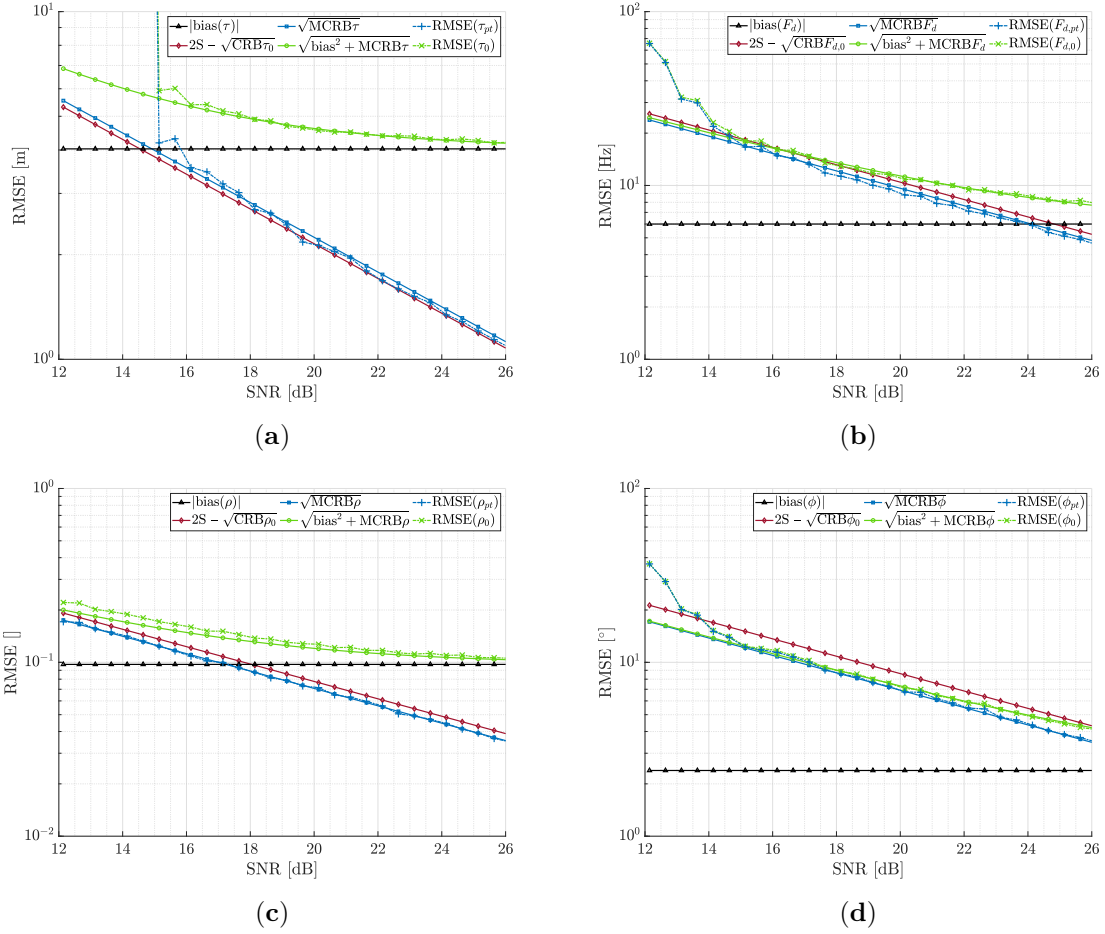


Figure 2.15: Estimation of the delay (a), the Doppler frequency (b), the amplitude (c) and the phase (d) of the GALILEO E1B LOS signal in presence of a single multipath using a MMLE and comparison of the RMSE with the corresponding MCRB, CRB and bias.

2.5.5 Wrap-up on the MCRB

In this last section, the same operations used for the CRB led to the derivation of a closed-form expression of the MCRB for the study of the impact of a single multipath. These expressions depend on the signal baseband samples and are easy to implement and to use. The properties of the so-called MMLE as a misspecified-unbiased estimator as presented in [For17] were used to validate the MCRB expressions based on the asymptotic behavior of the estimator. The results show good fitting between theory and simulation.

The study of the MCRB allows the user to better understand the roles of both the bias and the variance when using a misspecified estimator. This is useful for low-cost receivers, to assess the sensitivity to a single multipath, and may lead to future metrics as it has been done for the CCBR in Section 2.4.

2.6 Conclusion

In this chapter, the reception of a GNSS signal in a harsh environment such as urban canyons was considered. In such an environment, a receiver collects not only the signal of interest but also multiple reflections of it from the surrounding buildings, this phenomenon is called multipath.

Starting from a very simple dual source model and using a graphical tool called MPEE that provides information on the bias induced by the multipath in a noise-free environment, the study of the impact of a single multipath was done for several estimators. It was shown that for the category of estimators that estimate the multipath parameters along with the LOS ones, the bias induced may reduce to zero, which makes the MPEE a non-informative tool to compare these estimators with one another.

A way to cope with this lack of information is to look at what happens on the MSE when there is an additive white Gaussian noise. This way, the first order statistic provided by the MPEE can be completed by a second order statistic. Since the idea is to compare the MSE of unbiased estimators, the CRB comes in naturally. A closed-form expression of this bound for the dual source signal model was then derived which depends on the signal baseband samples. A validation procedure, based on the properties of the MLE was done to ensure the validity of the derived expressions through simulations. With the corresponding CRB, it has been possible to compare unbiased estimators with one another and with the bounds itself.

The great generality of the CRB suggested to use it to build a meaningful metric that could be useful for future navigation signal design. This metric, called CCB_R, is a ratio between the single source CRB and the dual source CRB. It is contained between 0 and 1 and does not depend on the SNR nor on the ratio of the amplitudes. It comes as a complementary tool to the MPEE for signal design.

Finally, for the numerous low-cost estimators that cannot account for the presence of multipath, a closed-form MCRB adapted to the misspecification of the estimator with regard to the presence of multipath has also been derived, and validated thanks to the properties of the MMLE. This misspecified bound comes as an extension of the single source CRB and provides information on both the bias and the variance change due to the presence of multipath. In short, they allow a good understanding of the impact of the multipath.

Ground-Based GNSS-R

Contents

3.1	Introduction	84
3.1.1	Chapter Organization	86
3.1.2	Signal Model	87
3.2	Gruissan Data Campaign	88
3.2.1	Purpose	88
3.2.2	Campaign Preparation	88
3.2.3	Data Collection	93
3.2.4	Data Set Description	96
3.2.5	Example of Processed Data	100
3.2.6	Wrap-up on Data Collection	102
3.3	Crosstalk Characterization	103
3.3.1	Coherent Estimation	103
3.3.2	Non-Coherent Estimation	108
3.3.3	Wrap-Up on Crosstalk Characterization	112
3.4	Approximate Maximum Likelihood for Narrowband GNSS Signals	112
3.4.1	Close-to-Ground Assumptions	113
3.4.2	Approximation of the Maximum Likelihood Criterion	114
3.4.3	Description of the Algorithm	116
3.4.4	Discussion on the Approximation Validity	118
3.5	Performance on Simulated Data	120
3.5.1	Simulation Set-Up	120
3.5.2	Cramér-Rao Bounds	120
3.5.3	Numerical Results	121
3.5.4	Wrap-Up on the AMLE	121
3.6	Altimetry Using Wideband GNSS Signals	122
3.6.1	Crosstalk and Multipath	122
3.6.2	Single Source Processing	124
3.6.3	Dual Source Processing	125
3.6.4	Wrap-Up on Wideband Signals Processing	128
3.7	Conclusion	128

Résumé

Ce chapitre suppose à nouveau un récepteur GNSS proche du sol. Cependant, le multitrajet n'est plus perçu comme une nuisance mais comme une source d'information. En effet, l'étude de la réflexion des signaux GNSS, connue sous le nom de GNSS-R, permet d'obtenir des informations sur la hauteur entre le récepteur et la surface de réflexion par exemple. Le GNSS-R se fait en général au moyen de deux antennes, l'une pointant vers le haut pour recevoir le trajet direct et l'autre pointant vers le bas pour recevoir le trajet réfléchi. Idéalement, chaque antenne ne reçoit que le signal qui l'intéresse mais lorsque le récepteur est proche du sol ou que l'élévation du satellite est faible, la différence de chemin entre le trajet direct et le trajet réfléchi est relativement également faible, ce qui conduit à des interférences au sein des antennes très similaires à un multitrajet simple. Dans le cas du GNSS-R, ce parasitage entre les antennes affecte les performances pour l'estimation de la hauteur par exemple. Il est donc capital de bien comprendre dans quelle mesure ce parasitage pose problème en fonction du traitement choisi et du signal GNSS considéré. Fort de cette compréhension, deux cas apparaissent : un premier cas pour lequel la différence de chemin est si faible que le parasitage ne peut être évité. Dans de telles conditions où des traitements à deux sources sont soit impossibles, soit très coûteux, il est alors possible d'approximer le critère du maximum de vraisemblance par une série de Taylor tronquée. Cette approximation réduit la dimension du critère à maximiser et rend possible le GNSS-R pour des cas extrêmes. Le deuxième cas issu de l'étude de l'effet du parasitage est lorsque celui-ci n'est pas trop important. Alors la mise en place d'un traitement à deux sources sur chacune des voies du récepteur permet de réduire voire d'annuler complètement l'effet du parasitage.

Pour bien comprendre la problématique du parasitage entre les antennes pour le GNSS-R proche du sol en vue de lui trouver une solution, une première partie de ce chapitre, Section 3.2, s'intéresse à la campagne de mesure effectuée par le CNES près de Gruissan qui fournit pour le reste du chapitre un jeu de données à traiter ainsi que des ordres de grandeur réalistes pour les différentes analyses. S'ensuit dans la Section 3.3 une étude approfondie de l'effet du parasitage basée sur son effet sur l'erreur quadratique moyenne de différents algorithmes, comparée à la borne de Cramér-Rao correspondante. De cette étude, deux cas peuvent être distingués : un premier cas, étudié dans la Section 3.4, où la différence de chemin est si faible que le parasitage ne peut être évité. Dans ce cas, une approximation de Taylor permet de réduire la dimension du problème. Dans le second cas, étudié dans la Section 3.6, l'effet du parasitage est plus faible et un traitement à deux sources sur chaque antenne est envisageable pour le réduire voire l'annuler.

3.1 Introduction

As seen in Chapter 2, GNSS signals are known to be reflected from various surfaces. The reception of the direct signal along with these reflections is called multipath, and these reflections are often seen as a nuisance to be avoided because they tend to degrade the positioning performance. However, by giving a closer look at the reflected paths, one may realize that

they carry information, such as the reflecting surface location relative to the receiver. The study of the reflected GNSS signal upon the Earth’s surface is called GNSS Reflectometry or GNSS-R. As presented in Section 1.5, altimetry is not the only GNSS-R application, and depending on the nature of the platform on which the receiver is located (static station, airplane, spacecraft), the application may vary. Hereafter, as an extension of the previous chapter, a static ground-based receiver is considered as it is illustrated in Figure 3.1.

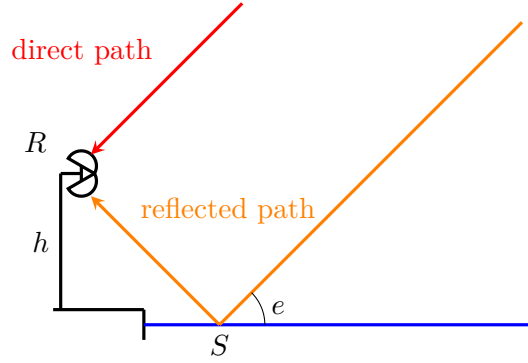


Figure 3.1: Typical GNSS-R geometry with the local elevation angle e and receiver height h .

The particular case of ground-based GNSS-R exposes the receiver to collect two signals, the direct and the reflected, with a very small path separation. Similarly to multipath, when the path separation is very small, there is a strong interference between both signals and standard GNSS-R processing may not perform very well. In fact, in a standard configuration, the receiver has two antennas, one uplooking, dedicated to the direct signal and the other, downlooking and dedicated to the reflected signal. Ideally, each antenna should collect only the signal for which it is dedicated.

In order to better understand the challenges of ground-based GNSS-R, a geometrical analysis of the realistic time difference between reflected and direct paths: $\Delta\tau = \tau_1 - \tau_0$ is provided here. This path separation, converted in meters is obtained using the classic geometric relation (3.1).

$$c\Delta\tau = 2h \sin(e) \quad (3.1)$$

Figure 3.2 presents the path separation for different receiver heights h and satellite local elevations e . In Figure 3.2 the values equivalent to $\Delta\tau = 1, 1/2, 1/4, 1/8, 1/10$ and $1/20$ L1 C/A chips are also depicted. Remember that $1/10$ L1 C/A chips is equal to 1 L5 chip which is the same chip length for the GALILEO E5A or E5B. This quick geometry study suggests that for small receiver height or for low satellite elevation the expected path separation is of the order or smaller than the considered GNSS signals chip. This means that depending on the scenario, if an antenna collects both signals, say the downlooking antenna receives part of the direct signal, a strong interference is to be expected between both signals. Such an interference is known as signal crosstalk and can be seen as a single multipath.

Knowing this, evaluating the impact of crosstalk on the estimation of each channel signal time-delay, which is the parameter needed to obtain an estimation of the height h , is of

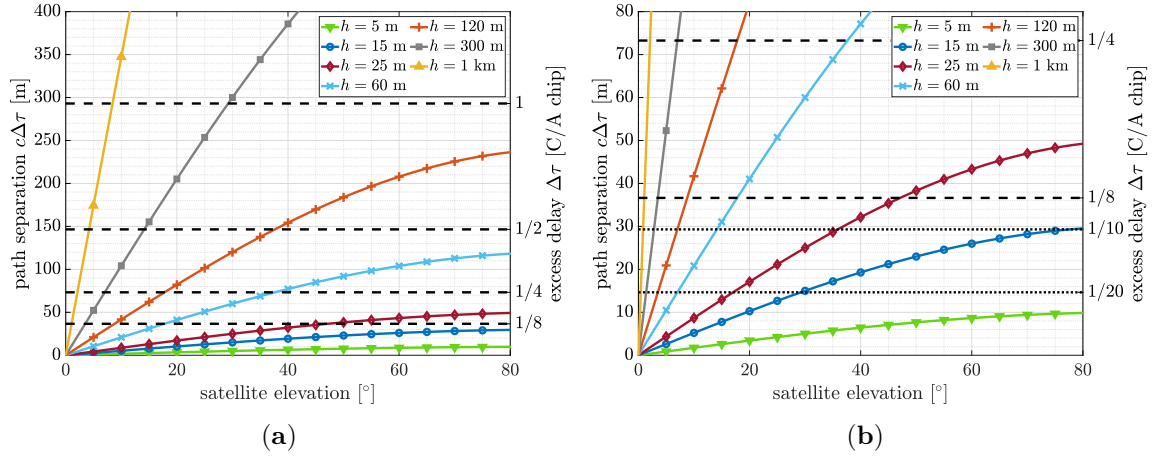


Figure 3.2: Geometrical direct to reflected signal path separation $c\Delta\tau$ for different receiver height h and satellite elevation e . (b) is a zoom-in for small values of h .

great interest. A way to assess this impact is to study the accuracy performance of different algorithms for different crosstalk scenarios, that is, study the algorithms MSE and compare it to the CRB that corresponds to the signal model. Fortunately, this signal model is similar to the multipath two-ray signal model developed in the previous chapter.

Once the crosstalk effect is better understood, one can identify two configurations:

- A first case is when the crosstalk effect is important as in the very short path separation case. For such scenarios, classic solutions are either non-tractable or computationally costly. However it is possible to get around this high resolution problem by formulating an assumption on the path separation shortness. In fact, the path separation is so small that one can accurately approximate the dual source likelihood criterion to maximize with truncated Taylor series. By doing so, the criterion is simplified and the maximum search becomes affordable.
- A second case is when the crosstalk effect is small because the path separation is of the order of the considered signal chip rate. In ground-based configuration, this is something that may happen with wideband GNSS signals for which the chip rate is small enough (about 30 meters for GPS L5). Then a well chosen dual source algorithm is able to decouple the signal of interest from the interfering signal and then reduce or even cancel the crosstalk effect.

3.1.1 Chapter Organization

In this chapter the question of ground-based GNSS-R is explored. In order to set a clear framework, a first Section 3.2 is dedicated to a data collection campaign done by CNES near Gruissan in the south of France. This section presents all the parameters and constraints to take into account for ground-based GNSS-R and will provide not only real data that will

support the discussion but also relevant orders of magnitude for the rest of this chapter. In Section 3.3, a thorough study of the impact of crosstalk is done based on algorithms MSE with regard to their corresponding CRB, and with different GNSS signals. Finally, this crosstalk study paves the way to two distinct approaches: Section 3.4 tackles the issue when the crosstalk effect is important, and cannot be avoided, by introducing an algorithm based on a Taylor approximation of the dual source likelihood criterion; and Section 3.6 presents a simple dual source processing in the case the crosstalk effect is less important. This last processing is done on the Gruissan data set.

The entire chapter is based on a signal model which is equivalent to the multipath two-ray model from Chapter 2. It is quickly reminded in the next section.

3.1.2 Signal Model

If one looks at Figure 3.1, the signal model received by each antenna would ideally be a single source signal model such as defined in Section 2.1.2.1. However, as mentioned before, since the receiver is very close to the ground, both antennas collect both signals. For this reason the only signal model considered in this chapter is the general dual source CSM as defined in Section 2.1.2.2, and recalled here in its discrete expression,

$$\mathbf{x} = \mathbf{A}(\boldsymbol{\eta}_0, \boldsymbol{\eta}_1)\boldsymbol{\alpha} + \mathbf{w}, \quad \mathbf{w} \sim \mathcal{CN}(0, \sigma_n^2 \mathbf{I}_N), \quad (3.2)$$

with, for $n \in [N_1, N_2]$,

$$\boldsymbol{\eta}_i^T = (\tau_i, b_i), \quad (3.3)$$

$$\mathbf{x}^T = (\dots, x(nT_s), \dots), \quad (3.4)$$

$$\mathbf{A}(\boldsymbol{\eta}_0, \boldsymbol{\eta}_1) = [\mathbf{a}_0, \mathbf{a}_1], \quad (3.5)$$

$$\mathbf{a}_i^T = (\dots, s(nT_s - \tau_i)e^{-j\omega_c b_i(nT_s - \tau_i)}, \dots), \quad (3.6)$$

$$\boldsymbol{\alpha}^T = (\rho_0 e^{j\phi_0}, \rho_1 e^{j\phi_1}), \quad (3.7)$$

$$\mathbf{w}^T = (\dots, w(nT_s), \dots), \quad (3.8)$$

and where for $i \in \{0, 1\}$, τ_i is the time-delay, $(1 - b_i)$ is the dilatation induced by the Doppler effect, ρ_i and ϕ_i are the amplitude and phase of the complex coefficient of signal i . T_s is the sampling period, $F_s = 1/T_s$ the sampling frequency and $\omega_c = 2\pi f_c$, f_c is the signal carrier frequency.

3.1.2.1 Signal-to-Noise Ratio

As in the previous chapter, some results will be presented with regard to the noise level, represented by the SNR. For the rest of the chapter, SNR, or SNR_{out} will always refer to the SNR of the strongest signal at the output of the matched filter. In a two antenna scenario, the strongest signal is the direct signal in the uplooking antenna and the reflected signal in

the downlooking one. This can be written as follows,

$$\text{SNR} \triangleq \frac{\left| \int_{\mathbb{R}} s(t - \tau_i)^* \rho_i e^{j\phi_i} s(t - \tau_i) dt \right|^2}{E \left\{ \left| \int_{\mathbb{R}} s(t - \tau_i)^* w(t) dt \right|^2 \right\}} = \frac{\rho_i^2 \mathbf{s}^H \mathbf{s}}{\sigma_n^2} = (C/N_0) T_I \quad (3.9)$$

with $i = \{0, 1\}$ depending on the antenna considered, \mathbf{s} is the vector of the baseband samples also defined in (C.29), σ_n^2 , the variance of the additive white Gaussian noise and C/N_0 is the carrier-to-noise density ratio.

3.2 Gruissan Data Campaign

In order to illustrate the work presented in the rest of this chapter, a data collection campaign is first presented. This campaign, organized by CNES, took place on July 27, 2021 at the Ayrolle Pond, near Gruissan, France.

3.2.1 Purpose

For this thesis work, the aim of this campaign was to obtain a large and rich data set of GNSS signals in a close-to-ground configuration where strong interferences would exist between the direct and the reflected signals. The reflection needed to be close-to-specular so that the simple two-ray signal model would correctly describe the received signal.

3.2.2 Campaign Preparation

Prior to the campaign day, an important preparatory work had to be done. This involved the site and day selection to optimize the number of satellites in view during a given time window.

3.2.2.1 Site Location and Particulars

The site had to verify a number of constraints:

- it should be close to a large and smooth reflecting surface, like a lake, or calm sea water,
- it should be at a relatively small height of the reflecting surface but not too low to avoid intractable scenarios,
- it should be oriented as southward as possible to maximize the number of satellites in view,
- it should be located not too far from Toulouse to allow a short mission length.

Regarding these many constraints, the elected site was the Ayrolle Pond, a pond located in the south of France near Gruissan as it can be seen in Figure 3.3. Around the pond, a series

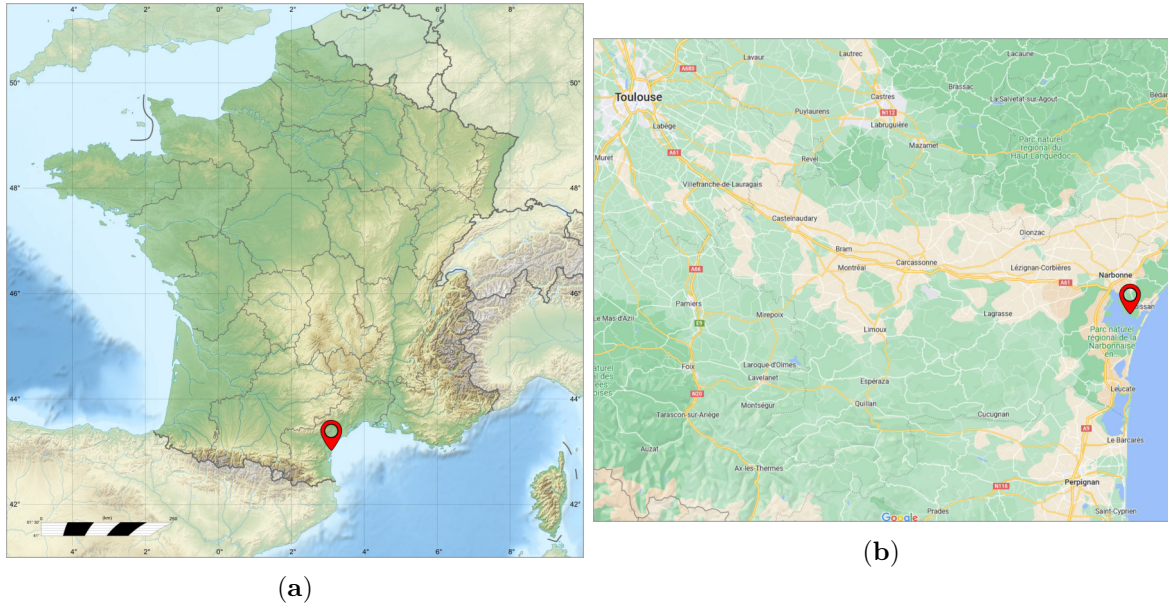


Figure 3.3: Location of the Ayrolle Pond in France (a) and relatively to Toulouse (b) (credit: www.vidiani.com and www.google.com/maps).

of small cliffs can be found that overhang the water. The height of these cliffs can go up to 30 meters. A particular site in the northern part of the pond was selected where a flat enough platform at 25 meters above the water allowed to install the experiment equipment. Figure 3.4 presents the exact site location. As one can notice in this figure, the receiver will have to look westward to capture the reflected GNSS signals.



Figure 3.4: Site location at the Ayrolle Pond (credit: www.geoportail.gouv.fr).

Now, looking closer at the site, if the receiver is placed at the marked point in Figure 3.5, there is a large area from which no reflected signals will be received. In particular the area between the receiver and the pond water will not reflect properly the signals. For this reason, a mask adapted to the site features needs to be build for the rest of the campaign

preparation. This mask will allow to automatically discard all the reflections that may come from the area defined by it when it will come to the satellite-in-view prediction step in Section 3.2.2.2. In Figure 3.5, the corresponding mask has been added in red. This mask can be fully

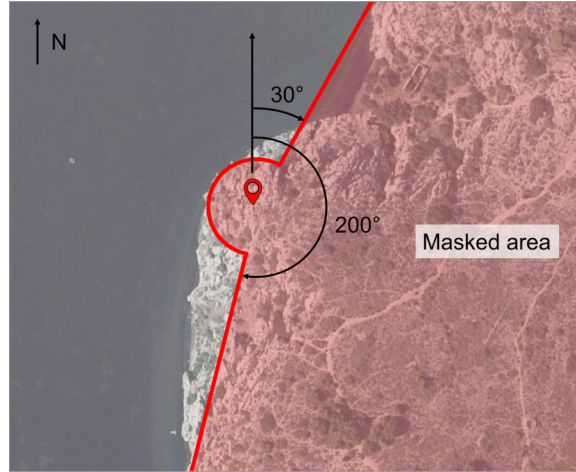


Figure 3.5: Satellite view of the experiment site with the associated mask (credit: www.geoportail.gouv.fr).

defined by two azimuth angles and a maximum radius. The minimum radius, noted r_{\min} , is the minimum horizontal distance between the receiver and the pond water. Thanks to simple geometry considerations sketched in Figure 3.6, this minimum radius can be converted into a maximum elevation angle e_{\max} using the receiver height h : For the selected scenario, $h \approx 25$

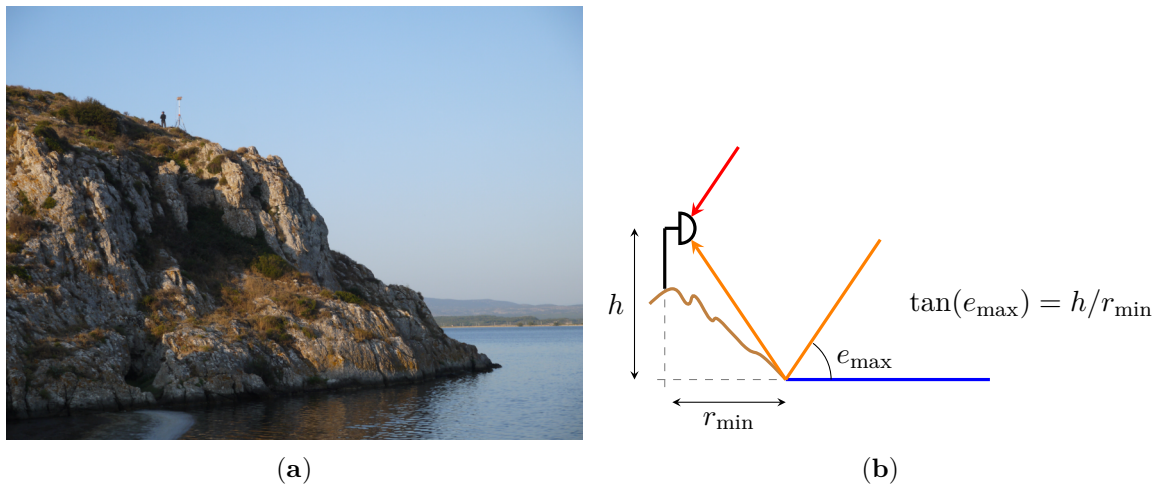


Figure 3.6: Picture (a) and Sketch (b) of the experiment site and relation between r_{\min} and e_{\max} .

m, $r_{\min} \approx 30$ m and the maximum elevation e_{\max} is equal to about 50.2° . The mask spans between the azimuth angles 30° and 200° .

Once the site location is fixed, and a first analysis allowed to build a mask meant to discard any satellite candidate whose elevation angle and azimuth do not fit this constraint,

the next step is to identify a time window during which a large number of satellites is passing out of this mask.

3.2.2.2 Satellite-in-View Prediction

Online Prediction Tool In order to predict the position of the satellites for the experiment, a number of open access tools are available online. For illustration, one can use the Japanese GNSSView [QSS] or the GNSS Planning Online [Tri] tool developed by Trimble. Examples of the skyplot output of these tools can be found in Figure 3.7. A skyplot is a polar plot where a concentric circle corresponds to a given elevation angle and radial axis corresponds to the azimuth angle. Online tools are then very powerful and useful to get a

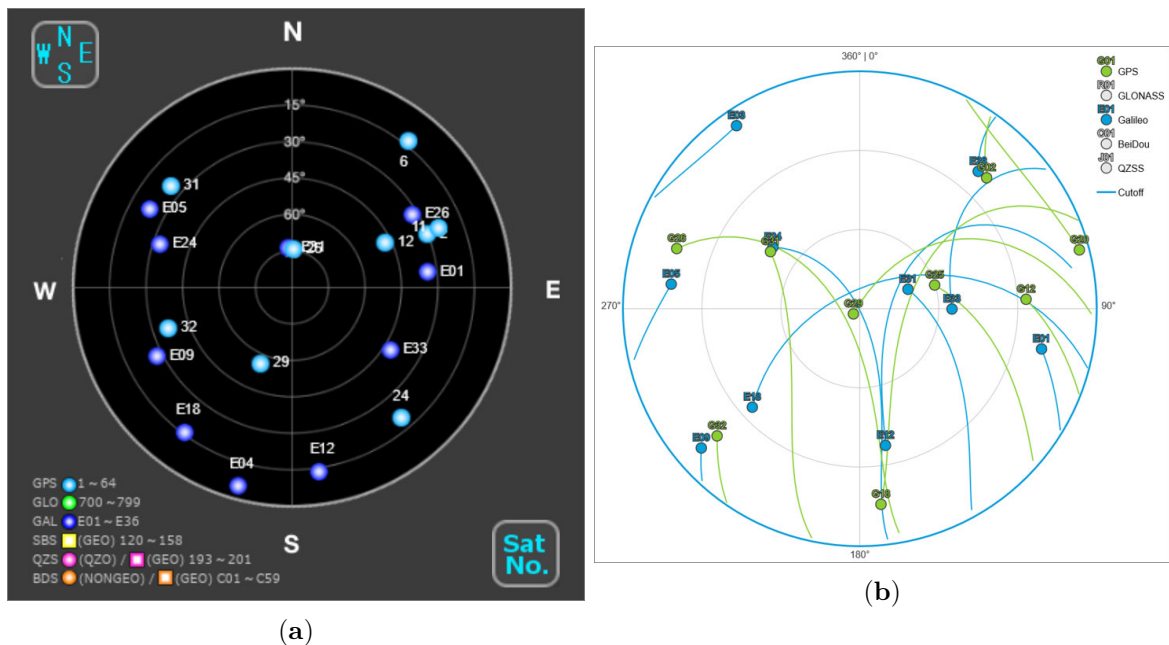


Figure 3.7: Examples of two tools to predict GNSS satellites positions: (a) GNSSView and (b) GNSS Planning Online.

quick idea of how many satellites will be in the sky at a given time. However it is not possible to download the time series that generated the provided charts, and it can result tedious to sort the satellites that are in the masked area defined in the previous section. For this reason it is interesting to develop a tool that will predict the position of the satellites at a given time.

Orbit Propagation Method GNSS satellites are Earth-orbiting objects like other satellites and debris, and their position prediction can be performed using orbit propagation algorithms. In particular, one of the most used algorithms is based on the Simplified General Perturbations (SGP) model [HR80], fed with the Two-Line element (TLE) sets of the considered satellite. TLE is a compact data format that contains all the orbital elements of an Earth-orbiting object. It is generated by observatories for each orbiting object, satellite or

debris, and updated regularly. As presented in Section 1.3.2, the orbital parameters are also part of the navigation message because they allow the user to compute accurately the position of each satellite, which is necessary to obtain a PVT solution. TLE are regularly updated by the North American Aerospace Defense Command (NORAD) and available on websites such as Celestrak¹. The SGP4 orbit propagator [HR80] is an algorithm that takes an object TLE at a given time and, based on Kepler laws and a perturbations model, predicts the position of this object at an other time, past or future. Many libraries have been developed to run SGP4 and in this work, the library [Mah20] was used and adapted to the GNSS application. The developed tool would allow to compute the position of any GNSS satellite during a chosen time frame. In short it provides the same information as the online tools but it allows the user to implement a complex mask in order to select only the satellites of interest. Figure 3.8 is an example of a skyplot for a single GPS satellite during a certain window. The mask designed in the previous section appears clearly. With this tool, it is then possible to compute

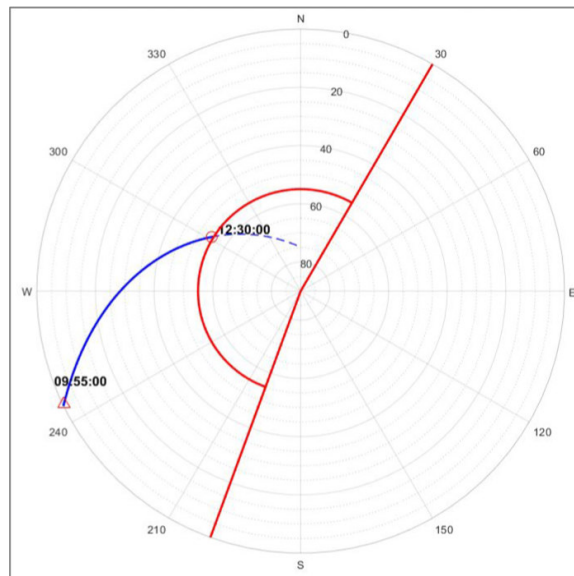


Figure 3.8: Example of a skyplot computed using the GNSS simulator based on the SGP4 propagator.

a constellation visibility with the mask constraint in order to pick an optimal day and optimal time windows during this day to collect as many GNSS signals as possible. Figures 3.9 and 3.10 are typical outputs that present the visibility of an entire constellation during a 6-hour window. If, for a given satellite, that is, for a given row, there is a colored line, it means that the satellite will be visible in the sky, if it is in thick red, it means that it will be out of the mask, this way it is possible to determine when is the best time to turn on and off the recorder. Using these figures and iterating for different days and time-window, the selected day for the experiment was set to July 27, 2021, early in the morning.

¹Celestrak: <https://celestrak.org>.

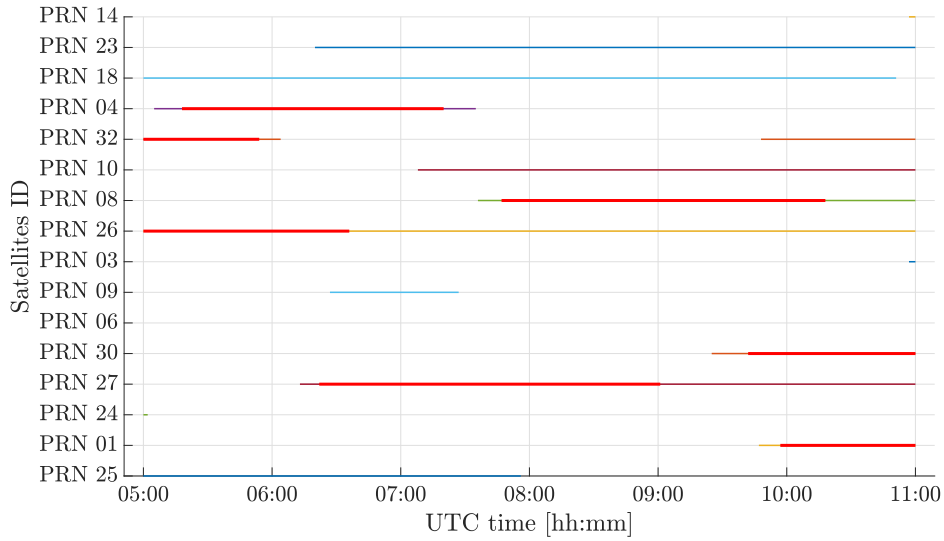


Figure 3.9: Predicted visibility of GPS satellites (block IIF and III only) from the Gruissan experiment site. Color means visible, thick red means out of the mask.

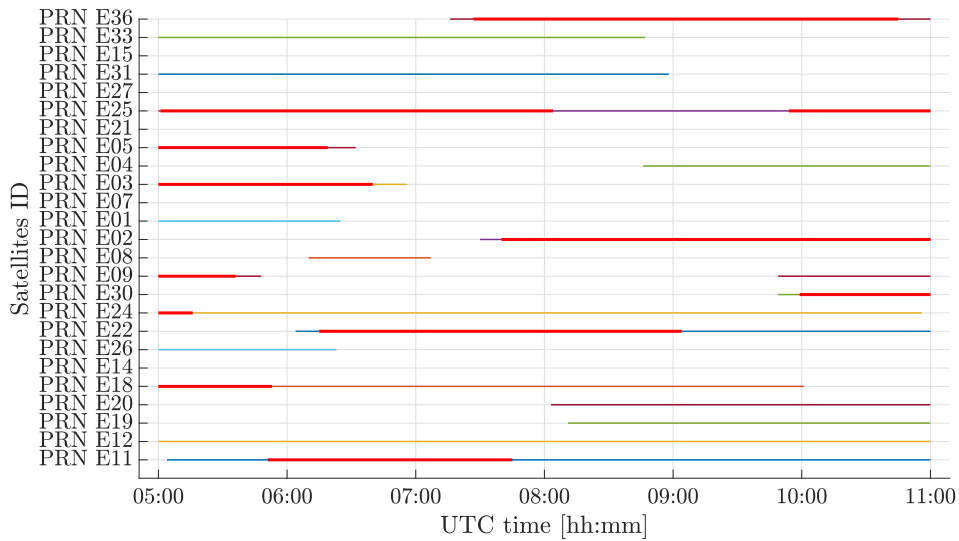


Figure 3.10: Predicted visibility of GALILEO satellites from the Gruissan experiment site. Color means visible, thick red means out of the mask.

3.2.3 Data Collection

3.2.3.1 Equipment for Reflectometry

In order to collect GNSS signals and their reflections, some equipment is required. For the data collection itself, a RF signal recorder connected to an antenna fixed on top of a mast is used. The mast is 3-meter tall and allows to elevate the antenna far from the ground to

avoid very small unwanted multipath. Figure 3.11 present the mast with the antenna on top of it from two points of view to appreciate its size. The antenna used to collect the reflected

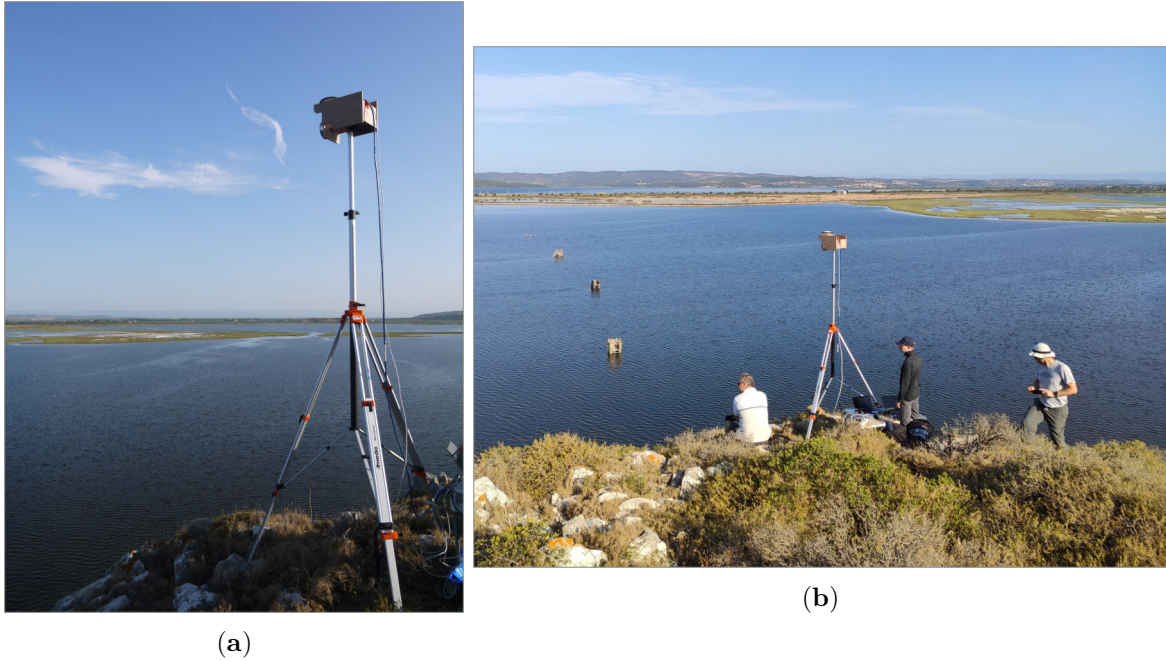


Figure 3.11: Mast with antenna near the Ayrolle Pond.

signal is a dual polarization RHCP/LHCP L1/L5 antenna developed by CNES for GNSS-R purposes. In Figure 3.12, one can see the two output connectors, one for each polarization. This antenna is fixed to a wooden structure that allows the user to orientate it with a chosen



Figure 3.12: CNES dual polarization antenna (credit: CNES).

angle. It can be either downward to capture the LHCP component of the reflected signal or horizontal to try and capture both direct and reflected signals with both polarization.

The receiver is a recorder developed by Ingespace² with the following features:

- 4 synchronized RF channels,

²Ingespace: www.ingespace.com.

- center frequency from 70 MHz to 6000 MHz,
- quantization from 1 to 16 bits I/Q,
- sampling rate from 5 Msps to 205.824 Msps (limited by maximum overall throughput for all RF channels that should not exceed 370 MB/s), Msps: megasamples per second.

These features will allow, for instance, to record both L1 and L5 band signals for both polarizations.

3.2.3.2 Equipment for Ground Truth

The data collected may lead to altimetry products that should be compared to a ground truth. In order to obtain this a set of two additional GNSS receivers is used. A first set is installed along with the GNSS-R recorder. To this purpose a NovAtel VEXXIS GNSS-850 antenna is attached to the mast and connected to a Septentrio PolaRx5 receiver. This receiver will estimate a *true* position for the top of the mast. On the other hand, the pond water level *true* position will be estimated by a receiver attached to a buoy built by CNES that can be found in Figure 3.13. On top of this buoy, a NovAtel VEXXIS GNSS-850 antenna whose center phase is fixed at 791 mm above the water level and inside the buoy, and a Septentrio PolaRx4 is enclosed.



Figure 3.13: Buoy on the Ayrolle Pond.

3.2.3.3 Experimental Set-Up

The full experimental set-up can be seen in Figure 3.14a. Figure 3.14b gives a closer look of the set-up around the mast with one GNSS receiver and one RF signal recorder controlled by two laptops and connected to the antennas fixed on the wooden structure on top of the mast. Finally the receivers and their laptops are organized near the mast as in Figure 3.15

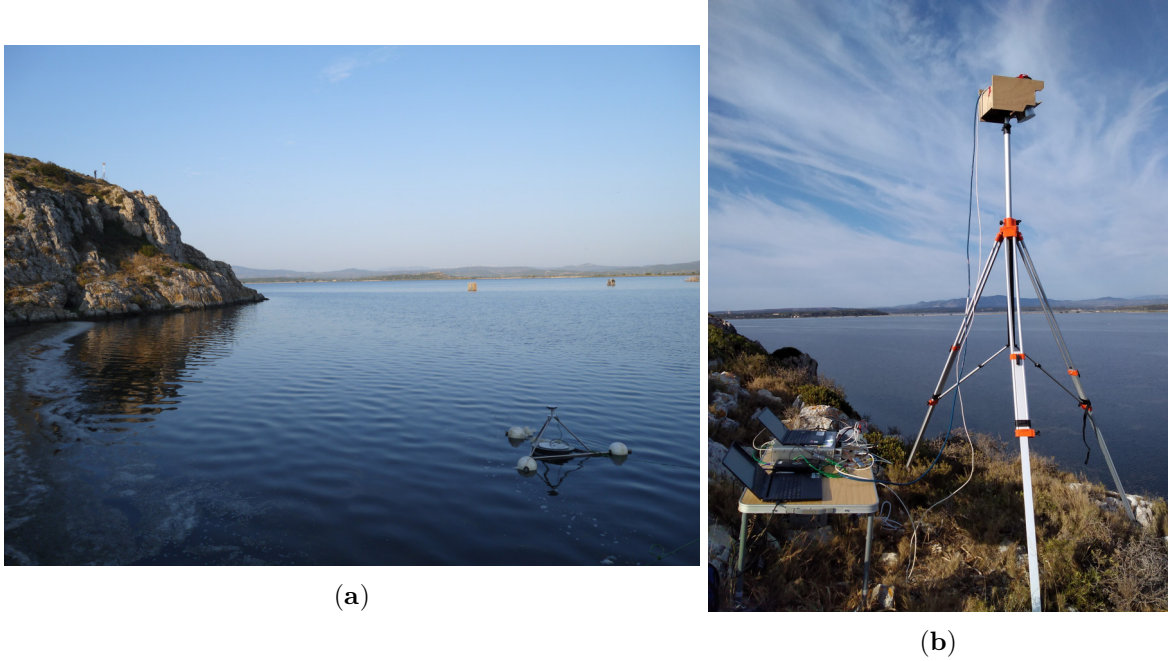


Figure 3.14: (a) Experiment set-up with the buoy on the bottom right corner and the mast on the cliff on the top left corner and (b) around the mast (credit: CNES).

where one can also see additional RF components (low noise amplifiers or LNA, bias tee and filters) needed to have the antennas working properly and get a clean signal.

Figure 3.16 is a schematic of the entire experiment.

3.2.4 Data Set Description

During the experiment, six recordings were collected with different configurations for the receiver and the antenna orientation. For the receiver three settings were used:

- L1: this is the configuration to capture both L1 and E1 signals:
 - center frequency: $F_{L1} = 1575.420$ MHz,
 - sampling frequency: $F_{s,L1} = 6.144$ MHz,
 - quantization: 8 bits I/Q,

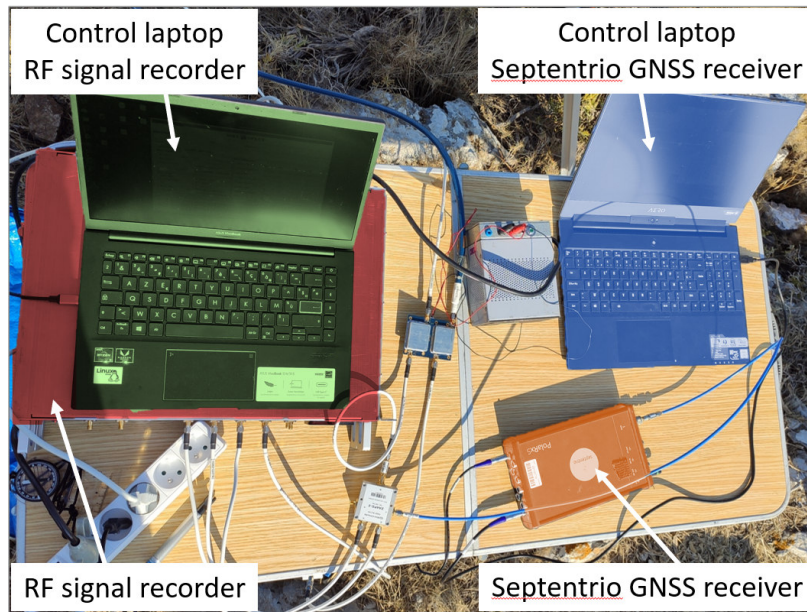


Figure 3.15: Experiment set-up of the control table.

- L5: this is used to record L5 and E5A signals.
 - center frequency: $F_{L5} = 1176.450$ MHz,
 - sampling frequency: $F_{s,L5} = 30.720$ MHz,
 - quantization: 8 bits I/Q,
- E5: this configuration record the entire E5 band (E5A and E5B):
 - center frequency: $F_{E5} = 1191.795$ MHz,
 - sampling frequency: $F_{s,E5} = 61.440$ MHz,
 - quantization: 8 bits I/Q.

Thanks to the four RF channels of the receiver, for each recording, two settings could be used simultaneously. It was always the L1 configuration for channels ch0 and ch1 and either L5 or E5 configuration for channels ch2 and ch3.

As previously mentioned, the dual polarization antenna is fixed on a wooden structure that allows the user to tilt the antenna so that it looks forward or horizontally. Besides, it was possible to change connections to use only the LHCP output of this antenna or both the LHCP and the RHCP outputs. This lead to two antenna configurations that are listed below.

- Nominal: NovAtel RHCP antenna looking upward and CNES LHCP antenna looking downward (tilted of 70° from the horizontal line).
- Reflectometry: CNES RHCP/LHCP antenna looking towards the horizon.

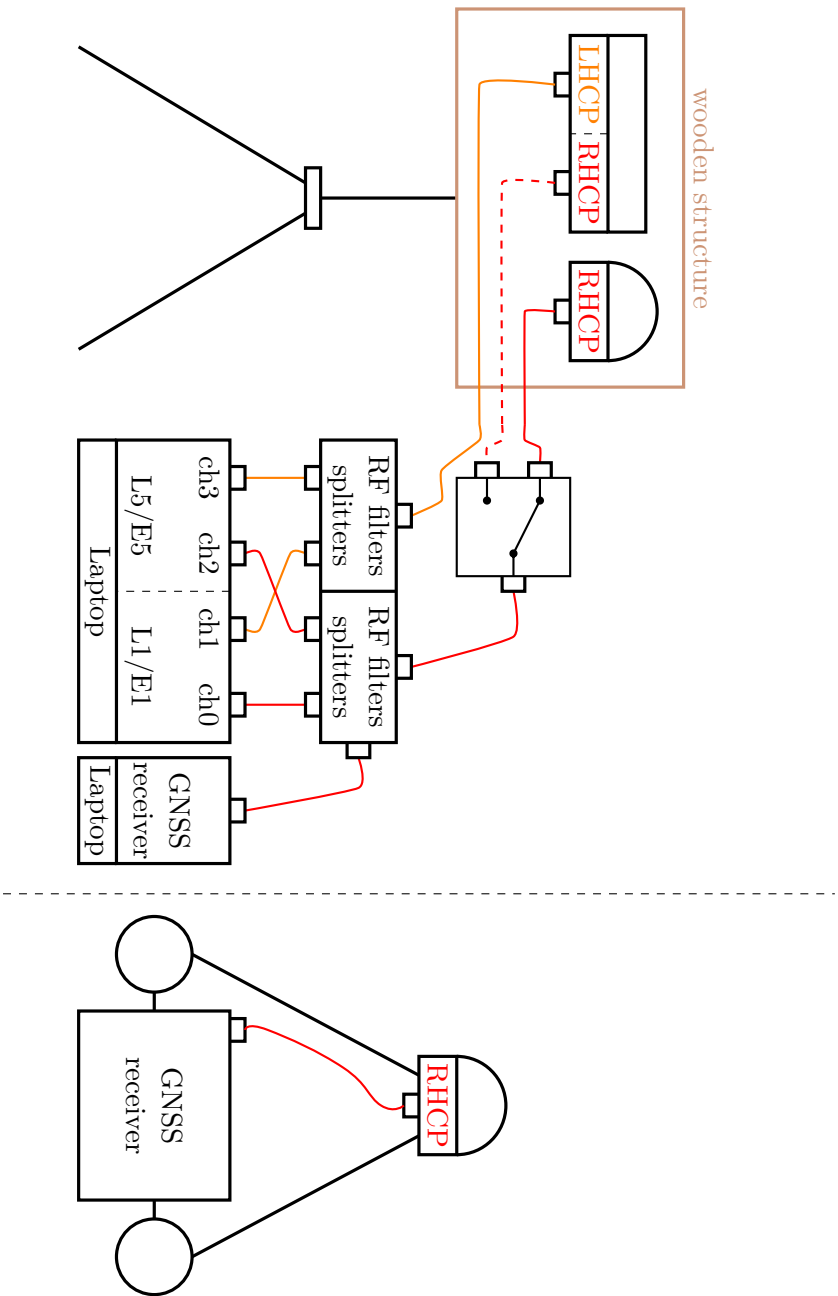


Figure 3.16: Gruissan experiment schematic.

The six recordings are summarized in Table 3.1 along with their duration and receiver/antenna configurations. Among these recordings, a focus is done on the ones using a reflectometry

Table 3.1: Summary of the Gruissan experiment recordings with corresponding configurations.

rec. #	T_0 [UTC]	length [mn]	receiver config.	antenna config.
1	05:00:00	40	L1/E5	nominal
2	05:42:00	26	L1/L5	nominal
3	06:18:00	29	L1/E5	reflectometry
4	07:02:00	6	L1/E5	detection
5	07:16:00	3	L1/E5	detection
6	07:37:00	15	L1/E5	reflectometry

antenna configuration, that is, on recordings #3 and #6. For these specific recordings, the satellite in view out of the masked area are the gathered in Figures 3.17 and 3.18 where the skyplots for GPS and GALILEO satellites are displayed.

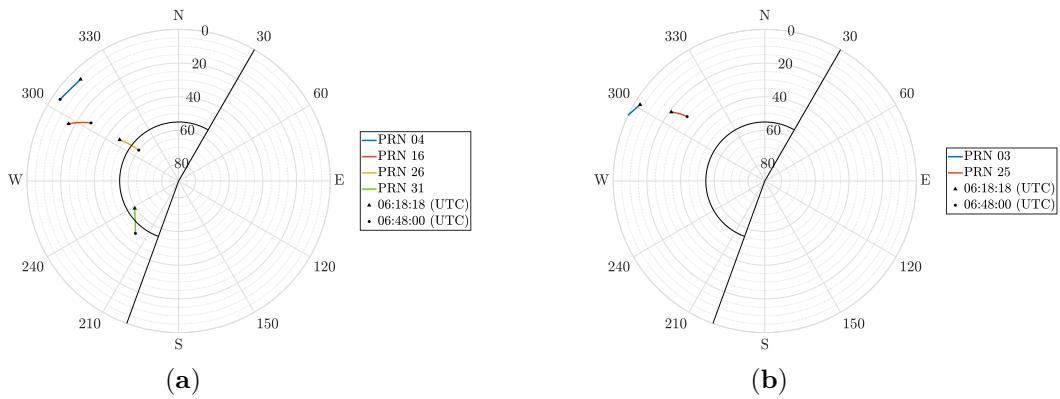


Figure 3.17: Skyplots for (a) GPS and (b) GALILEO satellites during rec. #3.

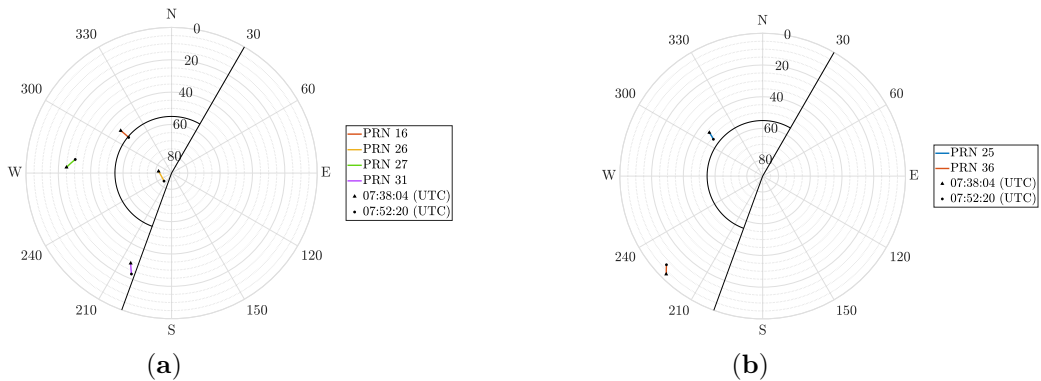


Figure 3.18: Skyplots for (a) GPS and (b) GALILEO satellites during rec. #6.

These figures will support the rest of this chapter for the simulation parameters settings and the data processing steps.

3.2.5 Example of Processed Data

3.2.5.1 Ground Truth Processing

In order to have a reference for future processing, the data collected by the buoy antenna and the zenith RHCP antenna set on the mast were processed using Real-Time Kinematic (RTK) technique, which is a highly accurate carrier phase-based ranging technique. Figure 3.19a and Figure 3.19b show the estimated height of both antennas during the experiment. For the mast antenna, the mean value observed is 73.14 m, this height corresponds to the

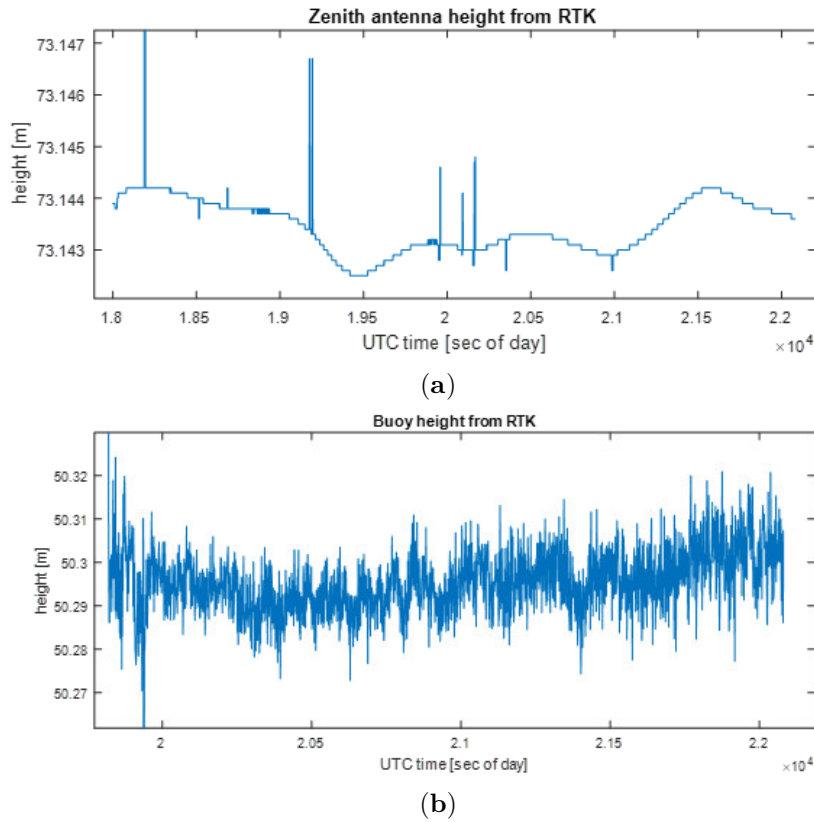


Figure 3.19: Estimated height using RTK technique for (a) the mast antenna and (b) the buoy antenna.

phase center of the Novatel antenna. During the experiment, this phase center was located 23 cm above the phase center of the dual polarization antenna. Consequently the height of the reflectometry antenna was $z_{\text{mast}} = 73.14 - 0.23 = 72.91$ m. For the buoy, the mean value observed is 50.30 m, the antenna was fixed so that its phase center was at 79 cm above the water level, the height of the water level was then $z_{\text{water}} = 50.30 - 0.79 = 49.51$ m. The reference horizontal height between the phase center of the reflectometry antenna and the pond water level was $h_{\text{true}} = z_{\text{mast}} - z_{\text{water}} = 23.40$ m during the experiment.

3.2.5.2 GNSS Interferometric Reflectometry

As an example, if one looks closer at recording #6 in Figure 3.18a, the GPS satellite that transmits PRN 27 has an ideal position in the sky. During the recording, its elevation varies between 25° and 30° , that is, resorting to the geometry equation (3.1), recalled hereafter,

$$c\Delta\tau = 2h \sin(e), \quad (3.10)$$

the expected path separation will vary between 21.1 m and 25 m. For L1 signals this corresponds to a excess delay between 0.072 to 0.085 L1 C/A chips or between 0.72 and 0.85 L5 chips. For the L1 case, it is clear that there will be a strong interference between the direct path and the reflected path in the case where both signals are collected by a single antenna. This is the typical multipath scenario.

If one applies a standard GNSS processing, that is, a 1S-MLE as defined in Section 1.2.1.2, on the L1 RHCP channel to track this GPS satellite, and looks at the estimated SNR during the entire recording, then obtains the Figure 3.20. This figure was obtained with 20 ms of

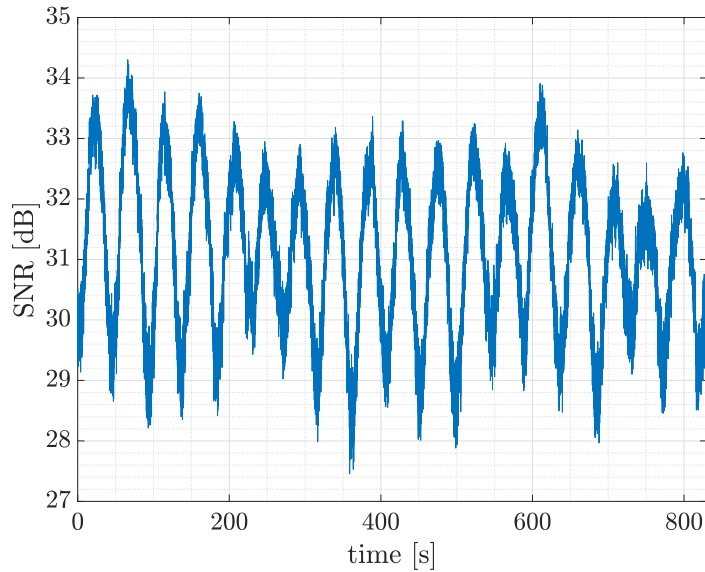


Figure 3.20: Estimated SNR for GPS satellite 27 during recording #6 on channel ch0 (L1, RHCP).

coherent integration and by filtering the sampled signals with a rectangular low-pass filter of bandwidth 4 MHz.

As predicted by the theory recalled in Section 1.5.2.1, the received SNR is oscillating during the recording. This oscillation is due to the slow evolution of the path separation as the satellite elevation evolves. It has been shown in [Rib14, (6)] that the apparent amplitude

of the received composite signal ρ_{comp} , can be modeled as in (3.11).

$$\rho_{\text{comp}}(t) = \sqrt{\rho_0^2 + \rho_1^2 + 2\rho_0\rho_1 \cos(\Delta\phi(t))} \quad (3.11)$$

and, thanks to geometry consideration, the phase difference $\Delta\phi(t)$ is expressed as a function of the elevation $e(t)$ and the height between the receiver and the reflecting surface h :

$$\Delta\phi(t) = \frac{4\pi h}{\lambda_{L1}} \sin(e(t)). \quad (3.12)$$

From (3.12), it is simple to link h to Δe , the satellite elevation variation required to observe one period of ρ_{comp} . or of the resulting SNR:

$$\frac{\lambda_{L1}}{h} = 4 \sin\left(\frac{\Delta e}{2}\right) \cos\left(e(t_0) + \frac{\Delta e}{2}\right) \quad (3.13)$$

During recording #6, the GPS satellite elevation evolution can be modeled as a linear function of time: $e(t) \approx \frac{de}{dt}t + e(0)$ where $\frac{de}{dt}$ is the slope of the time variation of $e(t)$. This way, $\Delta e = \frac{de}{dt}T_{\text{SNR}}$. For recording #6, $e(0) = 24.94^\circ$ and $\frac{de}{dt} = 0.0058^\circ/s$. Besides, a spectral analysis using a Welch's method [Wel67] on Figure 3.20 provides an estimated period $T_{\text{SNR}} \approx 45.60$ s.

Wrapping everything up with equation (3.12) for $t_0 = 400$ s, one can obtain an estimated height of 23.30 meters using the GNSS-IR method. This estimate satisfyingly agrees with the expected value (23.40 m).

3.2.6 Wrap-up on Data Collection

In this section, the Gruissan data collection was presented. This experiment aimed at providing data for ground-based GNSS-R purposes. The data collected consist of several recordings with different antenna and receiver configurations that can be used to perform GNSS-R altimetry with standard techniques, as it was illustrated with the GNSS-IR technique in the previous section, or with other approaches with one or two antennas as it will be shown later in this chapter.

Regarding standard GNSS-R techniques such as cGNSS-R or iGNSS-R where two antennas are required, ground-based scenarios are still challenging due to the strong interference between direct and reflected paths because the RHCP antenna let some LHCP component of the reflected path in, and vice versa. This leakage is also known as signal crosstalk and should be better understood to apply traditional processing techniques.

3.3 Crosstalk Characterization

The main issue that occurs when trying to perform ground-based GNSS-R is the strong interference between the direct and the reflected paths. The GNSS-IR example provided in the previous section proves that sometimes, some reflected signal manage to get in the direct antenna, and vice-versa. This phenomenon, called signal crosstalk may lead to performance degradation if not taken into account. This is very similar to GNSS multipath.

In this section, the focus is made on the downlooking antenna in which part of the direct signal is also collected. Consequently, signal indexed 0 will always refer to the reflected path, which is expected to be stronger, and signal indexed 1 will refer to the interfering direct path that manages to get in the downlooking channel.

In order to better understand the impact of crosstalk for ground-based GNSS-R, a series of simulations will be performed to acknowledge whether or not the crosstalk affect the estimation of the main signal delay (in this case the delay of the reflected path). Similarly to the multipath study, the metric used here will be the MSE of the receiver algorithm compared to the corresponding CRB that was derived in Section 2.3.

The philosophy of this study is to start with a traditional processing technique, here the 1S-MLE, and to check the impact of crosstalk on this specific architecture in terms of MSE when assuming a coherent processing, as defined in Section 1.5.2.3. Then, a dual source approach is proposed and verified using the same procedure. The robustness of this dual source approach is also checked assuming the absence of crosstalk. Finally, a discussion on non-coherent processing is drawn since non-coherent integration is often performed in GNSS-R to obtain targeted SNR levels.

Better understanding crosstalk will allow to identify scenarios in which the crosstalk cannot be avoided and scenarios where the crosstalk is not degrading too much the overall performance.

3.3.1 Coherent Estimation

In this section, the crosstalk impact on coherent estimation is investigated. To do this, a prior study on the 1S-MLE is used to estimate the reflected path time-delay in the presence of crosstalk; this aims at asserting the need for a mitigation technique based on either 2S-MLE or CRE. The performance of these estimators is then presented in a properly specified scenario (presence of crosstalk), and then in a misspecified one (no crosstalk).

3.3.1.1 Parameters of Interest and Simulation Set-Up

Exploiting the single source CRB from [Med20] and its dual source extension derived in Chapter 2, one can properly characterize the impact that the presence of two sources instead

of one (crosstalk) may have on the reflected or direct signal parameter estimation with regard to the single source case.

The two parameters investigated in this study are the excess time delay between the reflected and the direct signal, $\Delta\tau$, and the ratio between signal amplitudes, or MDR, $|\Gamma|$ where Γ is a complex number such that $\Gamma = \rho_1 e^{j\phi_1} / \rho_0 e^{j\phi_0}$. The first parameter, $\Delta\tau$, is determined by the system geometry, that is, the receiver height and the satellite elevation as reminded in Section 3.1. The second parameter, $|\Gamma|$, depends on the antenna radiation pattern, the polarization mismatch between the leaking signal and the antenna, and the incidence angle (again via the system geometry). Given the fact that a two-antenna system is considered, the modulus $|\Gamma|$ is assumed smaller than one, that is, the reflected signal has more energy than the crosstalk signal from the LOS. The other parameters in the signal definition reminded in Section 3.1.2 are set to a fixed value for the rest of this study: the Doppler frequency of the reflected signal $F_{d,0} = f_c \cdot b_0 = 30$ Hz, the Doppler frequency of the LOS signal $F_{d,1} = f_c \cdot b_1 = 50$ Hz, the phase of the reflected complex amplitude $\phi_0 = \pi/3$, and the phase of the LOS complex amplitude $\phi_1 = \pi/4$.

As representative case studies, the following values are considered: $|\Gamma| = \{0.01, 0.1, 0.3, 0.5\}$, $\Delta\tau = \{1/8, 1/4, 1/2, 1\}$ L1 C/A chips for a GPS L1 C/A signal, and $\Delta\tau = \{1/2, 1\}$ L5 chips for a GPS L5I signal. This way a wide range of possible values is covered. For each pair $\{\Delta\tau, |\Gamma|\}$, the time-delay estimation performance in term of RMSE for the GPS L1 C/A signal scenario, as well as for a GPS L5I signal (equivalent to GALILEO E5A or E5B) is obtained. Note that the GPS L1 C/A chip is 10 times larger than the GPS L5I chip because of the difference between the BPSK(1) and BPSK(10) modulations.

As mentioned before, three scenarios are now considered:

- Scenario (a) studies sub-optimal single source estimation where there are two sources, but the corresponding estimator considers only one source.
- Scenario (b) studies optimal dual source estimation where two sources are present and the corresponding estimator is matched to this model.
- Scenario (c) studies misspecified dual source estimation where there is only one source but the estimator looks for two.

Scenario (a) aims at emphasizing the effect of crosstalk for receiver architectures that ignore this phenomenon. Scenario (b) proposes a matched processing, and scenario (c) checks that this matched processing is robust when there is no crosstalk anymore.

In the sequel, for each scenario, the RMSE for the time-delay estimation of the reflected signal, is computed through 1000 Monte Carlo runs with respect to the SNR at the output of the matched filter as defined in (3.9).

3.3.1.2 Numerical Results for Coherent Processing

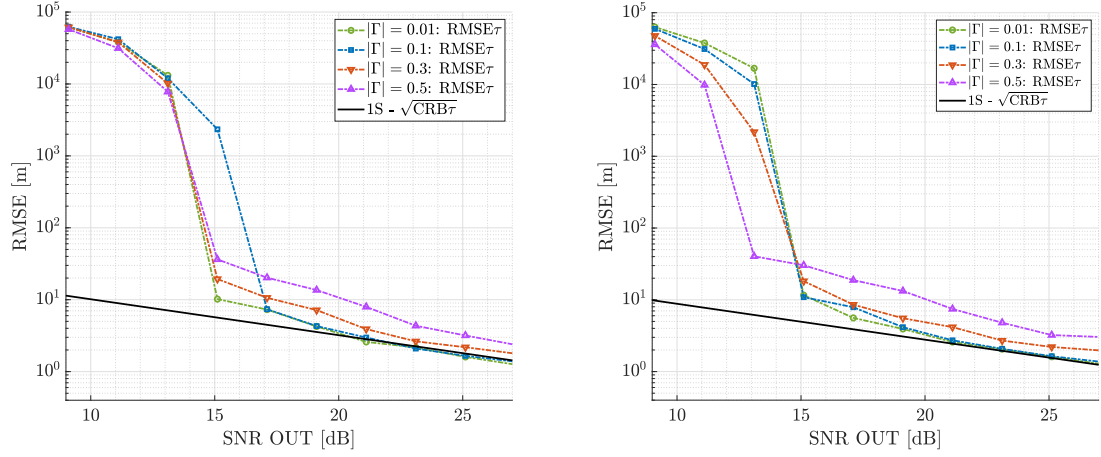
Scenario (a) This analysis provides insights into the performance loss when the possible crosstalk is not taken into account. The 1S-MLE RMSE is compared with the single source CRB. Note that $\Delta\tau = 1/2$ L5I chips = 0.05 L1 C/A chips and $\Delta\tau = 1$ L5I chips = 0.1 L1 C/A chips. The results are shown in Figures 3.21.

In the sequel, in all the figures presented, the MLE/CRE behavior can be divided into three distinct regions: (i) in the a priori region, at a low SNR, the estimate behaves as a random variable uniformly distributed on the search area and leads to a very large RMSE; in this case, the estimate is useless for the user; (ii) the threshold (i.e., where the estimator's RMSE drops significantly) is useful to know the minimum SNR to be in optimal operation conditions; and (iii) the asymptotic region is where the estimator behaves correctly, given that the estimator is asymptotically efficient (i.e., convergence to the CRB).

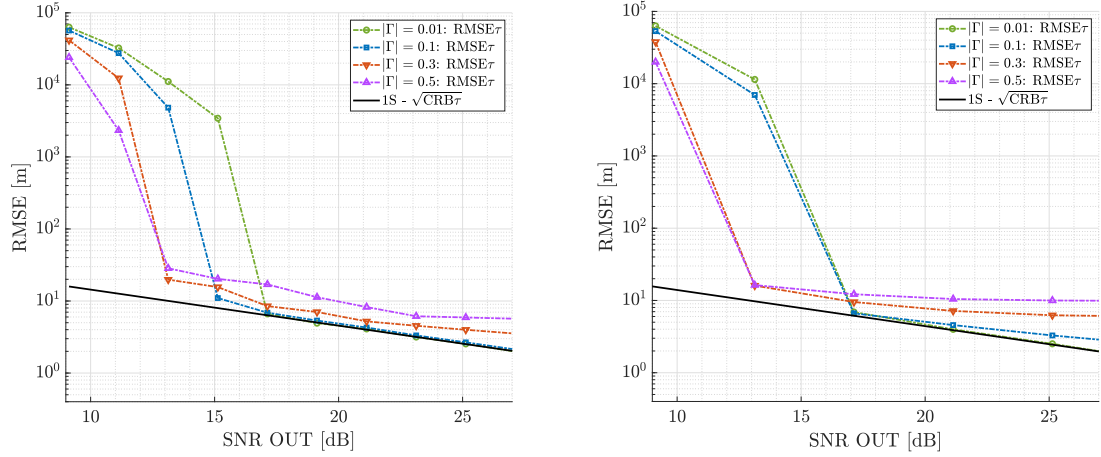
From the GPS L1 C/A results, one can draw three main conclusions: (i) in a dual source context, the single source estimators only converge to the bound for very low values of $|\Gamma|$ (i.e., 0.01 and 0.1 in the $\Delta\tau = 1, 1/2, 1/4$ L1 C/A chips results or only 0.01 in the case of $\Delta\tau = 1/8$ L1 C/A chips). In this case, there is no impact of a possible crosstalk. (ii) For higher values of $|\Gamma|$, the 1S-MLE RMSE never converges to the CRB, and therefore, the crosstalk induces a performance degradation. This significantly impacts the receiver performance for $|\Gamma| = 0.5$ and for $\Delta\tau = 1/8$ L1 C/A chips. It is worth pointing out that in such conditions, the estimator's RMSE reaches a constant floor, which is typical of a biased estimator (easy to spot in Figure 3.21d–f) as seen in Section 2.5 of the previous chapter. This is due to the fact that for a significant value of $|\Gamma|$, the crosstalk distorts the CCF and shifts its maximum, similarly to multipath in a navigation application. Consequently, even if, for larger $|\Gamma|$, the threshold seems to be earlier, the estimated value turns out to be biased. (iii) These results justify the need for dual source estimators or other robust solutions if a possible strong crosstalk is expected. For the GPS L5I case, one can see the same behavior for $\Delta\tau = 1$ L5I chip and a performance saturation for $\Delta\tau = 1/2$ L5I chips (even for $|\Gamma| = 0.1$). This is because the achievable RMSE with an L5I signal is far below the corresponding one with the L1 C/A signal (i.e., the L5I CCF is sharper than the L1 C/A CCF); therefore, small deviations on the CCF have a larger impact on the final performance.

Scenario (b) This analysis provides insights into the optimal achievable performance with respect to the single source case. Recall that with respect to the previous scenario, the presence of two sources is known and the parameters associated with both sources are estimated, either with a CRE or a 2S-MLE when the CRE does not converge because both sources are too close in time. Similarly to the previous scenario, these dual source estimators RMSE for the time-delay estimation of the main signal are compared with the single and dual source CRBs. Results are shown in Figure 3.22.

From the results shown in Figure 3.22, one can draw different conclusions: i) First, at a sufficiently high SNR, the estimators converge to the CRB, irrespective of the values of $\Delta\tau$



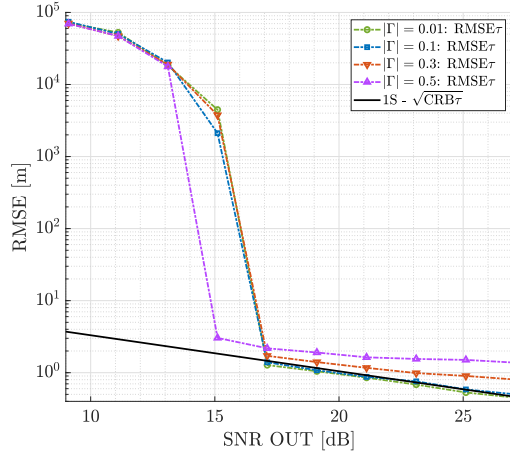
(a) L1 C/A, $F_s = 20$ MHz, $\Delta\tau = 1$ L1 C/A chip (b) L1 C/A, $F_s = 20$ MHz, $\Delta\tau = 1/2$ L1 C/A chips



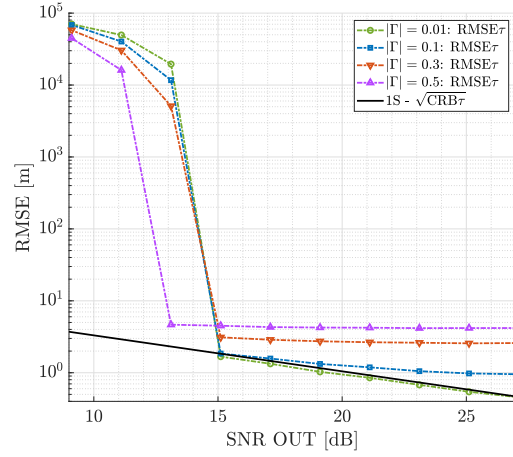
(c) L1 C/A, $F_s = 8$ MHz, $\Delta\tau = 1/4$ L1 C/A chips (d) L1 C/A, $F_s = 8$ MHz, $\Delta\tau = 1/8$ L1 C/A chips

Figure 3.21: *Cont.*

and $|\Gamma|$, which is a known result for MLE [Ren06]. This implies that using a dual source estimator and under certain conditions, it is possible to mitigate the impact of any possible crosstalk. ii) It is also worth pointing out the difference between the single source and the dual source CRB, which is limited for most of the range of $\Delta\tau$ considered in this study. This implies that once the estimator converges to the bound, the crosstalk impact on the estimation performance is limited as well (with respect to the optimal single source case). iii) The third point is the ability of the CRE to converge to the bound for values as low as $\Delta\tau = 1/4$ L1 C/A chips ($F_s = 8$ MHz) for the GPS L1 C/A or 1 L5I chips ($F_s = 20$ MHz) for the GPS L5I. For the GPS L1 C/A case with $\Delta\tau = 1/8$ L1 C/A chips or the GPS L5I case with $\Delta\tau = 0.5$ L5I chips, the CRE did not converge to the CRB because when the path separation is too short, this suboptimal implementation of the MLE is biased, this is the reason why the results were obtained with the 2S-MLE. Note that this CRE limit can be pushed with a better resolution, that is, a higher signal bandwidth. iv) Note also the strong



(e) L5I, $F_s = 20$ MHz, $\Delta\tau = 1$ L5-I chip



(f) L5I, $F_s = 20$ MHz, $\Delta\tau = 1/2$ L5-I chips

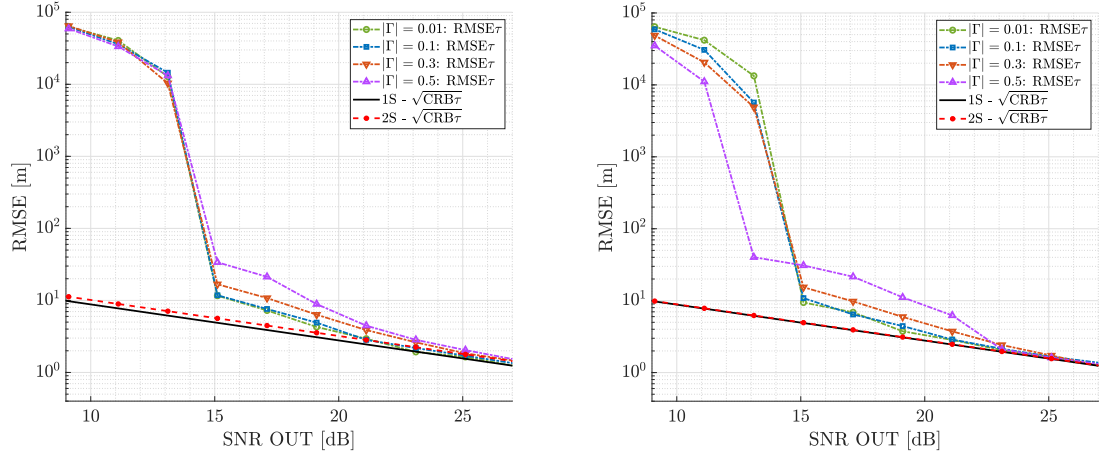
Figure 3.21: RMSE for the estimation of the main signal delay τ with 1S-MLE in the presence of a secondary signal with relative amplitudes $|\Gamma| = 0.01, 0.1, 0.3, 0.5$ and different $\Delta\tau$ and F_s , for both GPS L1 C/A and L5I signals.

impact that $|\Gamma|$ has on the convergence threshold. While for low values such as $|\Gamma| = 0.01$ or 0.1 , the convergence is very fast, for larger values, the convergence is slower and the optimal operation point is reached for larger SNR. v) Lastly, the 2S-MLE performance cannot be below the corresponding CRB, as is the case in the plots. This is because of a reduced parameter space search in the implementation, to avoid a huge computational burden. For the same reason (reduced parameter space search), the threshold could not be observed: the range of possible values did not allow to obtain large RMSE.

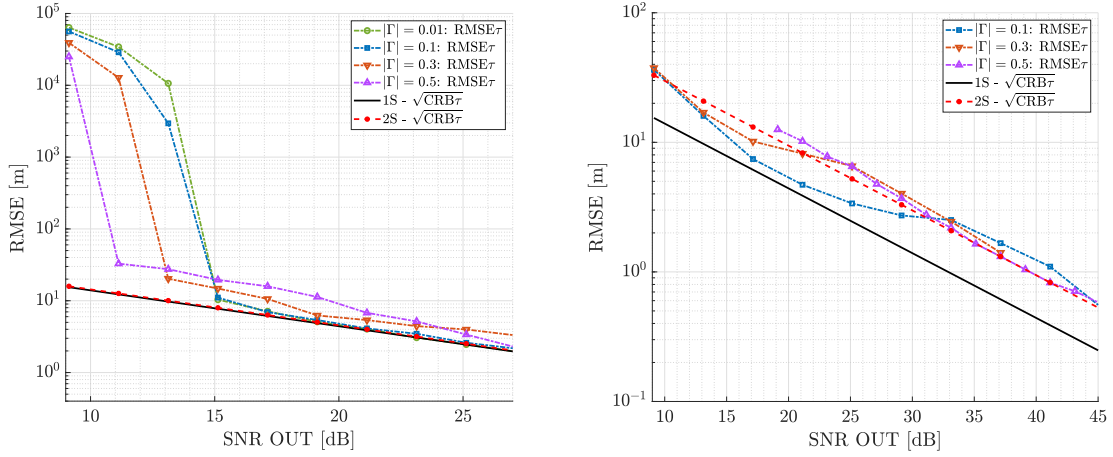
In any case, one can conclude from these figures that (i) for low values of $|\Gamma|$ and using a dual source estimator, crosstalk has almost no impact, and (ii) for large values of $|\Gamma|$, a higher SNR is required in order to mitigate the crosstalk.

Scenario (c) In the previous scenarios, a time-delay estimation performance analysis in a dual source context was investigated. First, considering a single source estimator in order to assess the impact of a possible crosstalk (i.e., not taken into account) with regard to the optimal single source case, and then, considering dual source estimators to assess the impact with regard to the single source case in an optimal set-up. A fundamental question of practical interest remains: what is the performance of dual source estimators when only one source is present? In other words, what is the robustness of dual source estimators when the number of sources is misspecified? In practice, this is the case of interest, because the crosstalk is not always present.

To answer this question let one consider the performance obtained with a CRE looking for two sources, but a single source is present in the signal. For the simulation, the same parameters of Doppler frequency and phase as before are set for the reflected signal, and the



(a) L1 C/A, $F_s = 20$ MHz, $\Delta\tau = 1$ L1 C/A chip. (b) L1 C/A, $F_s = 20$ MHz, $\Delta\tau = 1/2$ L1 C/A chips.



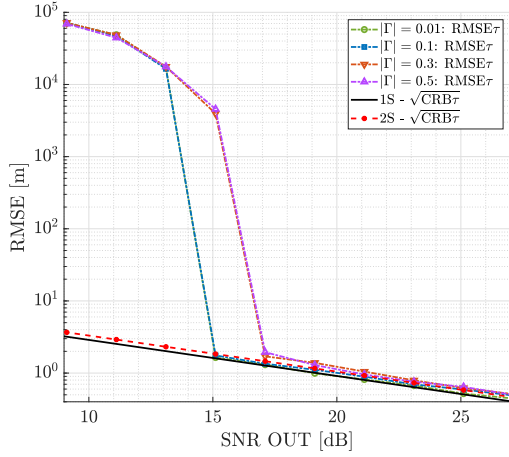
(c) L1 C/A, $F_s = 8$ MHz, $\Delta\tau = 1/4$ L1 C/A chips. (d) L1 C/A, $F_s = 8$ MHz, $\Delta\tau = 1/8$ L1 C/A chips.

Figure 3.22: *Cont.*

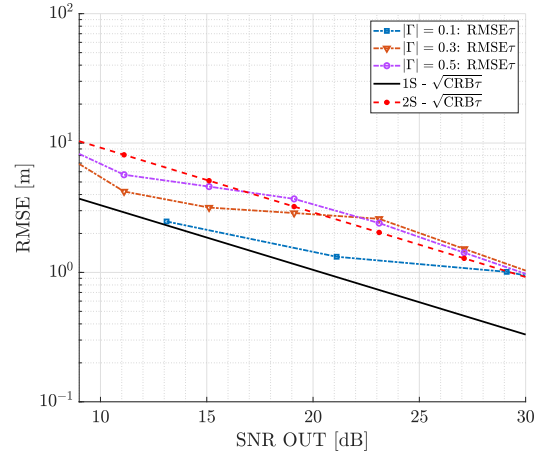
modulus $|\Gamma|$ is set to zero. Results for both GPS L1 C/A and GPS L5I signals are shown in Figure 3.23, where it is clear that the CRE is robust in the case of a misspecified number of sources. Indeed, the CRE properly estimates the reflected signal parameters and sees the rest as noise. This implies that such dual source estimator is a promising option to mitigate possible crosstalk.

3.3.2 Non-Coherent Estimation

Finally, it is interesting to have a look at non-coherent processing techniques since it often happens in GNSS-R because of the low SNR levels [OVC22]. As a case study, a focus is made on the VE estimation performance and how it compares with the CRB and dual source

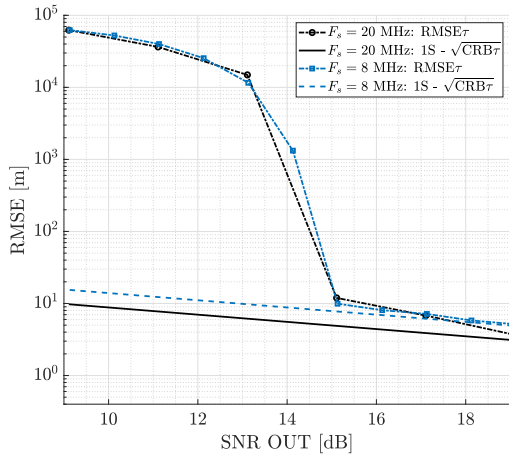


(e) L5I, $F_s = 20$ MHz, $\Delta\tau = 1$ L5I chip.

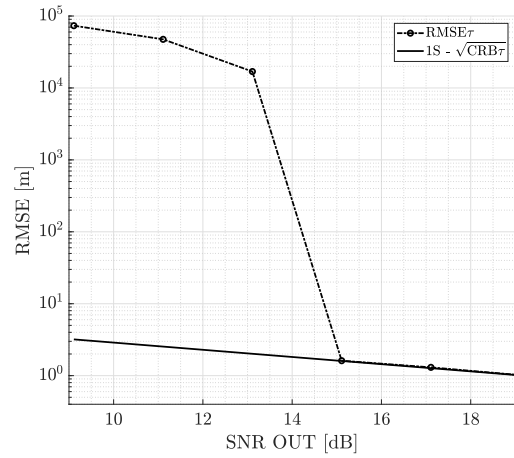


(f) L5I, $F_s = 20$ MHz, $\Delta\tau = 1/2$ L5I chips.

Figure 3.22: RMSE for the estimation of the reflected signal delay τ with the CRE (a–e) and 2S-MLE (d,f) in the presence of a secondary signal with relative amplitudes $|\Gamma| = 0.01, 0.1, 0.3, 0.5$ and different excess delay $\Delta\tau$, for both GPS L1 C/A and L5I signals.



(a) L1 C/A.



(b) L5I.

Figure 3.23: RMSE for the delay τ estimation considering a GPS L1 C/A signal at $F_s = 8$ MHz in blue and at $F_s = 20$ MHz in black (a) and a GPS L5I signal at $F_s = 20$ MHz (b). The case study with a misspecified number of sources: one source is present, but a dual source CRE is used.

estimators such as CRE when implemented for non-coherent integration. For the rest of this section this non-coherent CRE will be referred as NC-CRE.

3.3.2.1 Simulation Set-Up

Recall that the VE given in [Mar14b] and recalled in Section 1.5.2.3 is designed to eliminate the contribution of the coherent part of the signal. Therefore, to cover a set of representative case studies, four different scenarios are considered, where for all of them, there are two superimposed GPS L1 C/A signals with $F_s = 8$ MHz, $\Delta\tau = 1/4$ L1 C/A chips, $|\Gamma| = 0.5$, and a total signal duration of $T = 20$ ms, that is 20 GPS PRN code 1 ms long. The LOS signal is considered to be coherent during the observation time: it has the same phase during T . For the reflected signal whose delay one wants to estimate the following scenarios are considered.

- **Scenario (d1)**: 20 PRNs, each one with a different random phase.
- **Scenario (d2)**: four blocks of 5 PRNs where (i) the first 5 PRNs have the same phase as the LOS signal and (ii) the other three blocks of 5 PRNs have three different random phases.
- **Scenario (d3)**: two blocks of 10 PRNs where (i) the first 10 PRNs have the same phase as the LOS signal and (ii) the other two blocks of 5 PRNs have two different random phases.
- **Scenario (d4)**: four blocks of 5 PRNs where (i) the first 15 PRNs have the same phase as the LOS signal and (ii) the remaining block of 5 PRNs has a random phase.

These scenarios can also be pictures as in Figure 3.24 Note that these four cases cover from

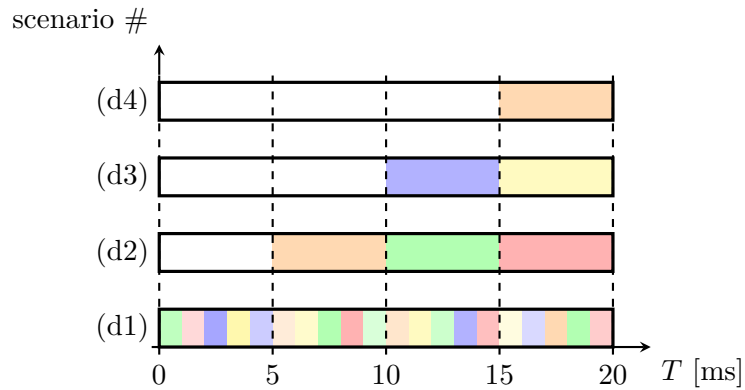


Figure 3.24: Non-coherent scenarios illustration each block is either white where the phase of the reflected path is equal to the phase of the coherent LOS signal, or colored where the phase is random.

the fully non-coherent reflected signal in scenario (d1) to the almost coherent reflected signal in scenario (d4).

3.3.2.2 Numerical Results for Non-Coherent Processing

The RMSE results obtained for the four scenarios with both the VE and NC-CRE are shown in Figure 3.25.

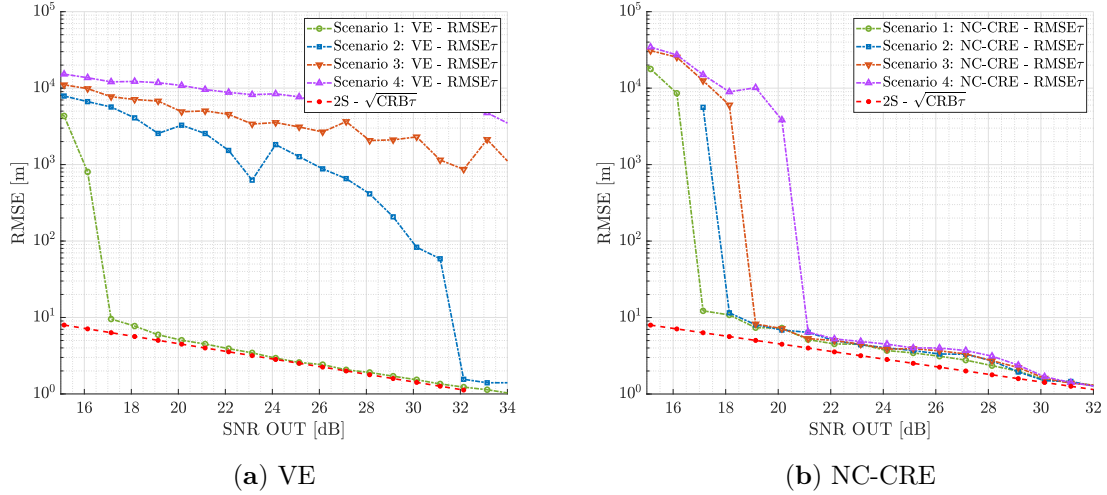


Figure 3.25: RMSE results for the reflected signal delay estimation considering two GPS L1 C/A signals at $F_s = 8$ MHz, $\Delta\tau = 1/4$, $|\Gamma| = 0.5$. (a) presents the VE performance and (b) presents the NC-CRE performance.

First, notice that the VE performance for the fully non-coherent scenario (d1) reaches the corresponding dual source CRB, which is almost equivalent to the single source CRB in these scenarios (refer to Figure 3.22c), at around 17 dB; then, in this case the estimator is asymptotically efficient and behaves similar to the 1S-MLE without crosstalk. In contrast, when the coherent part of the reflected signal increases, as in scenarios (d3) and (d4), its performance drastically degrades, and the VE is not a valid approach anymore, as expected by construction. Therefore, the VE is only useful if considering reflected signals with a dominant non-coherent component such as ocean surfaces, but it is not for specular reflections over ice or for certain land surfaces with a significant coherent signal part. Regarding the NC-CRE, it is asymptotically efficient irrespective of the signal coherence, therefore being a very powerful seamless alternative to the VE. Notice that the NC-CRE for the estimation of the reflected delay does not fully converge to the corresponding dual source CRB until the convergence of the estimation of the secondary delay (in this case, the LOS delay), at 30 dB, but the performance degradation between the first threshold and 30 dB is minor. Then, both methods have their pros and cons, the VE being easier to implement and the NC-CRE being more robust to the type of surface.

3.3.3 Wrap-Up on Crosstalk Characterization

In this section, an analysis, from an estimation point of view, of the possible effect of crosstalk in ground-based and low altitude airborne GNSS-R was proposed. Both the crosstalk impact on standard architectures and possible mitigation strategies were discussed. First, it was found that the 1S-MLE performance is not affected by crosstalk if the reflected-to-direct signal amplitude ratio is low enough; otherwise, there is a performance degradation that must be accounted for. Second, it was shown that both CRE and 2S-MLE are asymptotically optimal irrespective of the amplitude ratio, then being a promising crosstalk mitigation strategy. Note that using the CRE is limited by the time separation between both sources. However, such analysis was performed in a coherent signal context, and in practice, the reflected signal is non-coherently averaged over long integration times. That is the reason why a complementary analysis was provided to assess the performance of a NC-CRE, which was shown to be also asymptotically efficient irrespective of the signal coherence. In contrast, the VE used in the literature was shown to be a valid approach only for non-coherent signals, for which this estimator is asymptotically efficient. Otherwise, for instance in close-to-specular reflections, the VE suffers a significant performance degradation. Then, one can conclude that both the NC-CRE and VE are good ways to mitigate the crosstalk impact, with their pros and cons. Notice that the performance analysis provided here investigated the impact of the LOS signal on the reflected one, but the results are also valid to analyze the impact of the reflected signal on the LOS one. The only difference is that the LOS signal is stronger than the reflected signal, or vice versa. As a side note, the robustness of the CRE for a misspecified number of sources was also discussed.

From this crosstalk impact overview, two approaches may be of interest for ground-based GNSS-R depending on how strong the interference is. In the case of a strong crosstalk impact, that is, for narrowband GNSS signals, the interference is inevitable but so strong that one may estimate both signals (the main one and the interference) from a single channel. This is what is done in GNSS-IR as presented in the example in Section 3.2.5.2 and what is further proposed in Section 3.4. Another approach lays in the case of wideband GNSS signals: as mentioned before, for larger band signals, the crosstalk is less a problem if one applies dual source estimators. This is developed in Section 3.6 where single source and dual source estimators are again compared with one another on the Gruissan data set.

3.4 Approximate Maximum Likelihood for Narrowband GNSS Signals

Thanks to the crosstalk impact analysis done in the previous section it is now possible to identify scenarios in which the crosstalk can or cannot be avoided. This section focuses on scenarios where crosstalk is present. If one refers to the Gruissan experiment presented in Section 3.2, that will be the case for narrowband GNSS signals such as GPS L1 C/A or GALILEO E1 signals for which the width of the auto-correlation function (about 300 meters for GPS L1 C/A) is much larger than the actual path separation (about 40 meters at most).

In such a harsh configuration, applying conventional GNSS-R techniques will only lead to highly biased results which will not be exploitable.

Since both signals are actually collected by a single channel, one may be tempted to apply dual source estimators such as the 2S-MLE. It is known that the 2S-MLE for the joint time-delay and Doppler frequency estimation of two signals has an important computational cost. This is the reason why variants of this estimator have been derived, such as the CRE whose performance has been studied in the previous section. However these variants do not perform very well when the path separation is very small. However it is possible to build another variant of the 2S-MLE with the knowledge of the path separation shortness. The idea of the Approximate Maximum Likelihood Estimator (AMLE) presented in the coming sections comes from the assumption of a very small path separation which naturally lead to a Taylor approximation. Indeed, by approximating the likelihood criterion knowing that the path separation is small, it will be possible to find a closed form expression of the path separation estimate and, this way, to reduce the complexity of the maximization problem.

3.4.1 Close-to-Ground Assumptions

Based on Guissan experiment, the receiver R being close to the ground (tens of meters above the reflecting surface), the expected relative path difference $\Delta\tau = \tau_1 - \tau_0$ is of the same order. Based on the equation that links the height with the path separation: $c\Delta\tau = 2h \sin(e)$, the variation of the path separation with the transmitting satellite can be found in Figure 3.26 for the case $h = 25\text{m}$. From Figure 3.26, it is clear that both the direct and the reflected

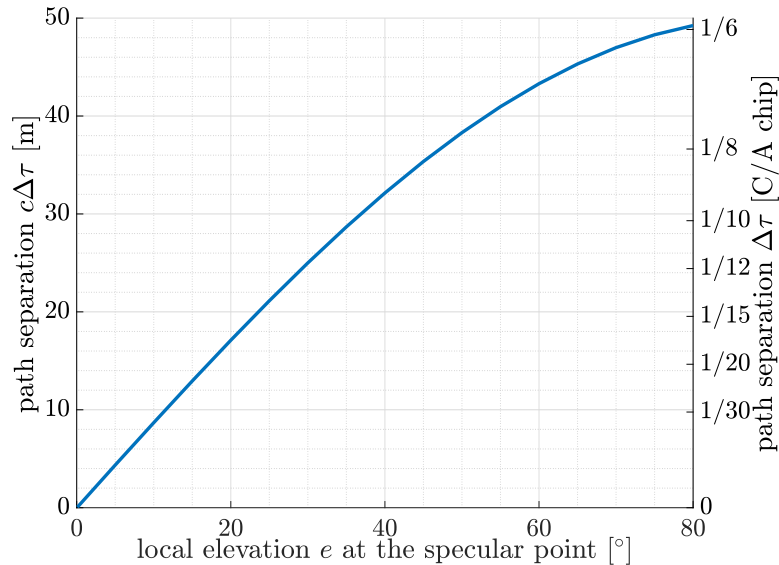


Figure 3.26: Path separation evolution with regard to the local elevation e of the transmitting satellite for a receiver height $h = 25\text{m}$.

path are very close in time. For very large band GNSS signals such as GALILEO E5, these

signals may sometimes be separable but for most of the GNSS signals a strong interference will exist.

On the other hand, given the geometry and the motionless nature of the reflecting surface, the Doppler frequencies of both the direct and the reflected signal do not differ from more than a fraction of Hertz. It can be shown that in a static geometry, the Doppler frequency difference between the direct signal and its reflection is only due to the receiver height and the elevation of the satellite: indeed, for very low altitude scenarios, the phase difference between the direct and the reflected path can be expressed as follows [GK88]:

$$\Delta\phi = \phi_1 - \phi_0 = \frac{2\omega_c h}{c} \sin(e). \quad (3.14)$$

Then, as the satellite elevation e varies, the relative phase varies and the first derivative corresponds to the relative Doppler frequency:

$$\Delta F_d = (b_1 - b_0)f_c = \frac{2f_c h}{c} \cos(e) \frac{de}{dt}. \quad (3.15)$$

This expression is often used to do altimetry based on the SNR observations [Rib14; Lar08] in GNSS-IR. A worst-case numerical application yields, for GPS L1 satellites with elevation rate $de/dt = 0.14$ mrad/s, $e = 0$ rad, $f_c = 1575.42$ MHz and a receiver at altitude $h = 25$ m: $\Delta F_d \approx 0.04$ Hz. Such a small difference will not be observable for coherent integration time considered in this study.

In short, two main assumptions are made due to the considered low altitude geometry:

- the Doppler frequencies of the direct and reflected paths are considered equal: $b_0 = b_1 = b$,
- the reflected path delay is very close to the direct delay $\tau_1 = \tau_0 + \Delta\tau$, $\Delta\tau$ small.

Consequently, $\boldsymbol{\eta}_0 = (\tau_0, b)^T$ and $\boldsymbol{\eta}_1 = (\tau_0 + \Delta\tau, b)^T$. And the final dual source CSM is given by:

$$\mathbf{x} = \mathbf{A}(\tau_0, \Delta\tau, b)\boldsymbol{\alpha} + \mathbf{w}, \quad \mathbf{w} \sim \mathcal{CN}(0, \sigma_n^2 \mathbf{I}_N), \quad (3.16)$$

with, for $n \in [N_1, N_2]$, $\mathbf{A}(\tau_0, \Delta\tau, b) = [\mathbf{a}_0, \mathbf{a}_1]$, \mathbf{a}_0 is defined in the the general case for $i = 0$ in Section 3.1.2 and $\mathbf{a}_1^T = (\dots, s(nT_s - \tau_0 - \Delta\tau)e^{-j\omega_c b(nT_s - \tau_0 - \Delta\tau)}, \dots)$.

3.4.2 Approximation of the Maximum Likelihood Criterion

Given the dual source signal model provided in (3.16), the corresponding 2S-MLE of $\boldsymbol{\xi} \triangleq [\tau_0, \Delta\tau, b, \rho_0, \phi_0, \rho_1, \phi_1]^T$ is given by [SN89; Ott93]:

$$\left(\widehat{\tau}_0, \widehat{\Delta\tau}, \widehat{b}\right) = \arg \max_{\tau_0, \Delta\tau, b} \|\mathbf{P}_A \mathbf{x}\|^2 \quad (3.17)$$

and, for $(\tau_0, \Delta\tau, b) = (\widehat{\tau}_0, \widehat{\Delta\tau}, \widehat{b})$ and $i \in \{0, 1\}$,

$$\widehat{\rho}_i = \left| \left[\left(\mathbf{A}^H \mathbf{A} \right)^{-1} \mathbf{A}^H \mathbf{x} \right]_i \right|, \quad \widehat{\phi}_i = \arg \left\{ \left[\left(\mathbf{A}^H \right)^{-1} \mathbf{A}^H \mathbf{x} \right]_i \right\}, \quad \widehat{\sigma}_n^2 = \frac{1}{N} \left\| \mathbf{P}_{\mathbf{A}}^\perp \mathbf{x} \right\|^2 \quad (3.18)$$

where $\mathbf{P}_{\mathbf{A}} = \mathbf{A} \left(\mathbf{A}^H \mathbf{A} \right)^{-1} \mathbf{A}^H$ is the projection onto the subspace spanned by the columns of \mathbf{A} (signal subspace) and $\mathbf{P}_{\mathbf{A}}^\perp = \mathbf{I} - \mathbf{P}_{\mathbf{A}}$ is the projection onto the noise subspace.

The aim of this section is to adapt the AMLE presented in [VBC14] to the problem of time-delay estimation of closely spaced sources which is motivated by the ground-based GNSS-R application.

Suppose the signal model described in (3.16). The likelihood criterion, noted $L(\tau_0, \Delta\tau, b)$ to be maximized is defined by (3.17). It can be written as follows:

$$L(\tau_0, \Delta\tau, b) \triangleq \left\| \mathbf{P}_{\mathbf{A}} \mathbf{x} \right\|^2 = \mathbf{x}^H \mathbf{P}_{\mathbf{A}} \mathbf{x} = \left(\mathbf{A}^H \mathbf{x} \right)^H \left(\mathbf{A}^H \mathbf{A} \right)^{-1} \mathbf{A}^H \mathbf{x} \quad (3.19)$$

where the inverse matrix can be explicitly written with regard to the path separation $\Delta\tau$:

$$\left(\mathbf{A}^H \mathbf{A} \right)^{-1} \propto \frac{1}{1 - |c(\Delta\tau)|^2} \begin{bmatrix} 1 & -c(\Delta\tau) \\ -c(\Delta\tau)^* & 1 \end{bmatrix} \quad (3.20)$$

where $c(\Delta\tau) \propto \mathbf{a}_0^H \mathbf{a}_1$ is the auto-correlation of the signal expressed in $\Delta\tau$.

Now if one expands the matrices product, the projector $\mathbf{P}_{\mathbf{A}}$ results in a finite sum of similar terms:

$$\mathbf{P}_{\mathbf{A}} = \frac{\mathbf{a}_0 \mathbf{a}_0^H + \mathbf{a}_1 \mathbf{a}_1^H - c(\Delta\tau)^* \mathbf{a}_0 \mathbf{a}_1^H - c(\Delta\tau) \mathbf{a}_1 \mathbf{a}_0^H}{1 - |c(\Delta\tau)|^2}, \quad (3.21)$$

and, with, for $i \in \{0, 1\}$, $\beta_i = \mathbf{a}_i^H \mathbf{x}$, the likelihood criterion can be expressed as

$$L(\tau_0, \Delta\tau, b) = \frac{\beta_0^* \beta_0 + \beta_1^* \beta_1 - c(\Delta\tau)^* \beta_0^* \beta_1 - c(\Delta\tau) \beta_1^* \beta_0}{1 - |c(\Delta\tau)|^2}. \quad (3.22)$$

Expression (3.22) can be further simplified by exploiting the fact that $\Delta\tau$ is very small. In that case both $c(\Delta\tau)$ and β_1 can be approximated with a truncation of their Taylor series:

$$c(\Delta\tau) = 1 + \sum_{n \in \mathbb{N}^*} c_n \Delta\tau^n, \quad (3.23)$$

$$|c(\Delta\tau)|^2 = 1 + \sum_{n \in \mathbb{N}^*} d_n \Delta\tau^n, \quad (3.24)$$

$$\beta_1 = \beta_0 + \sum_{n \in \mathbb{N}^*} \beta_{1,n} \Delta\tau^n, \quad (3.25)$$

where c_n , d_n and $\beta_{1,n}$ are the n -th Taylor coefficients of $c(\Delta\tau)$, $|c(\Delta\tau)|^2$ and β_1 , respectively.

Proof. see Appendix E.1. □

By truncating and expanding these series, it is possible to obtain a 3rd order Taylor development of the likelihood criterion:

$$L(\tau_0, \Delta\tau, b) \approx L^{\text{Taylor}}(\tau_0, \Delta\tau, b) = \sum_{n=0}^3 L_n(\tau_0, b) \Delta\tau^n \quad (3.26)$$

with

$$L_0(\tau_0, b) = -\frac{B_2}{d_2}, \quad L_1(\tau_0, b) = -\frac{B_3}{d_2}, \quad (3.27)$$

$$L_2(\tau_0, b) = -\frac{1}{d_2} \left(B_4 - \frac{d_4}{d_2} B_2 \right), \quad (3.28)$$

$$L_3(\tau_0, b) = -\frac{1}{d_2} \left(B_5 - \frac{d_4}{d_2} B_3 \right). \quad (3.29)$$

and B_n and d_n can be expressed with regard to the baseband signal samples thanks to (E.8), (E.9) and (E.13).

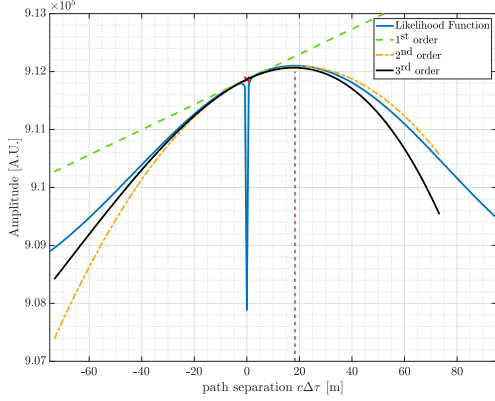
Proof. see Appendix E.2. □

3.4.3 Description of the Algorithm

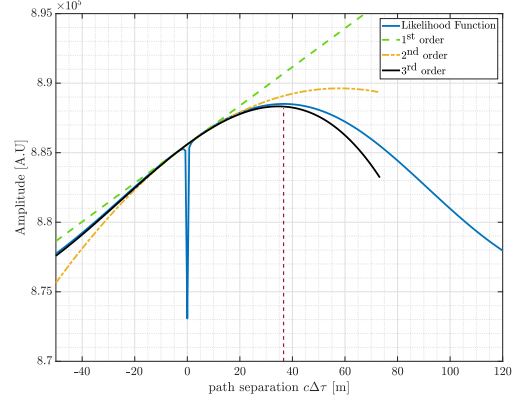
3.4.3.1 Intuition

In expression (3.26), the dependency on the relative delay $\Delta\tau$ is simplified. To better illustrate the meaning of this approximation, one can plot the real likelihood criterion $L(\tau_0, \Delta\tau, b)$ and compare it to its different order Taylor approximations. In Figure 3.27, A cut at the true values of τ_0 and b of the exact likelihood function is displayed along with the corresponding Taylor approximations (from order 0 to order 3). These figures are two illustrations without noise, for a signal GPS L1 C/A with $F_s = 4$ MHz, $b = 0$, $\rho_1/\rho_0 = 0.5$ and $\Delta\phi = \phi_1 - \phi_0 = 0$. The only difference between the two figures is the relative delay which is small in Figure 3.27a and large in Figure 3.27b.

From these figures, it is clear that the order of the Taylor approximation is important: for very small $\Delta\tau$ (Figure 3.27a), the likelihood is well represented at the 2nd order around the extremum area, which is of interest since the criterion is maximized for the correct value of $\Delta\tau$. In the case of a larger $\Delta\tau$ (Figure 3.27b), the 2nd order is not fitting the true likelihood function around the extremum anymore. On the other hand, the 3rd order provides a good approximation. The true likelihood function maximum being approximated by one of the two extrema of the 3rd order polynomial.



(a) $\Delta\tau = 1/16$ L1 C/A chips ($\sim 18.31\text{m}$).



(b) $\Delta\tau = 1/8$ L1 C/A chips ($\sim 32.63\text{m}$).

Figure 3.27: Illustration of the likelihood criterion Taylor approximations at different orders and relative delay $\Delta\tau$.

3.4.3.2 Resolution of the 3rd order polynomial

To obtain an estimation of $\Delta\tau$, one wants then to maximize the likelihood criterion. The observations made from Figure 3.27 suggest to relate the maximum of the likelihood function to one of the extrema of the 3rd order Taylor approximation. These extrema can be obtained by zeroing the first derivative of expression (3.26). Then the correct extremum is the one that has a negative curvature, in other words, the second derivative evaluated at this extremum is negative. Consequently, to estimate the relative $\widehat{\Delta\tau}$ from the expression (3.26), one can do as follows:

- Find the two candidates $\Delta\tau_1$ and $\Delta\tau_2$ by zeroing the first derivative of (3.26):

$$\frac{\partial L^{\text{Taylor}}(\tau_0, \Delta\tau, b)}{\partial \Delta\tau} = 0. \quad (3.30)$$

Using the reduced discriminant $\delta = L_2^2 - 3L_1L_3$, the two candidates can be written as:

$$\Delta\tau_{1/2} = \frac{-L_2 \pm \sqrt{\delta}}{3L_3}, \quad (3.31)$$

where the dependency on τ_0 and b has been omitted to lighten the notation.

- Evaluate the second derivative of (3.26) for both candidate and pick the one that has the minimum curvature:

$$\frac{\partial^2 L^{\text{Taylor}}(\tau_0, \Delta\tau, b)}{\partial \Delta\tau^2} < 0. \quad (3.32)$$

- The estimated relative delay is obtained by solving the straightforward minimization problem:

$$\widehat{\Delta\tau} = \arg \min_{\Delta\tau_1, \Delta\tau_2} (2L_2 + 6L_3\Delta\tau). \quad (3.33)$$

This estimated $\widehat{\Delta\tau}$ can be evaluated for all values of τ_0 and b .

To sum up, the 3rd order Taylor approximation of the likelihood function allows to find a closed-form solution for the estimated relative delay $\widehat{\Delta\tau}$ for all τ_0 and b . Once the procedure presented above is done, one can inject $\widehat{\Delta\tau}$ in the Taylor approximation of the likelihood function (3.26). The maximum likelihood estimation (3.17) turns to an approximate maximum likelihood estimation defined by

$$\begin{aligned} \widehat{\Delta\tau}(\tau_0, b) &= \arg \min_{\Delta\tau} (2L_2 + 6L_3\Delta\tau) \\ \text{so that } \begin{cases} \frac{\partial L^{\text{Taylor}}(\tau_0, \Delta\tau, b)}{\partial \Delta\tau} = 0, \\ (\widehat{\tau}_0, \widehat{b}) = \arg \min_{\tau_0, b} (L^{\text{Taylor}}(\tau_0, \widehat{\Delta\tau}(\tau_0, b), b)). \end{cases} \end{aligned} \quad (3.34)$$

The reduction to a two-dimensional expression of the AMLE makes it faster to solve than the original three-dimensional expression presented in (3.17).

3.4.4 Discussion on the Approximation Validity

Based on Appendix E.1, the AMLE cannot be expected to perform well when the path separation is too important. Consequently, it is necessary to study the goodness-of-fit between the ACF $c(\tau)$ and its 4th order Taylor approximation involved in the approximation of the likelihood function. Figure 3.28 presents the exact ACF and its 4th order Taylor approximation for a GPS L1 C/A signal sampled at different values of the sampling frequency F_s . Comparing different values of F_s here is similar to comparing different qualities of receivers where the baseband signal has been sampled at a frequency equal to the RF front-end bandwidth. In this figure, the effect of F_s on the resulting shape of the exact ACF is clearly visible: the larger the RF front-end bandwidth, the more oscillations one will observe. If one could take an infinite bandwidth, they would obtain a perfect triangular shape. It is not surprising that the Taylor approximation is sensitive to these oscillations since they are impossible to model with a 4th order polynomial. Consequently, the Taylor approximation will be valid for a larger range of time delays around 0 when the signal will have a smaller bandwidth.

In order to explicit this dependency between F_s and the goodness of fit of the Taylor approximation, the relative error in percentage between the approximation and the exact function is defined:

$$e(\tau) \triangleq 100 \frac{c^{\text{Taylor}}(\tau) - c(\tau)}{c(\tau)}. \quad (3.35)$$

Now if one fixes the relative error to a maximum value e_{\max} , it is possible to draw an abacus that gives the relation between F_s and the maximum time delay or path separation below which the Taylor approximation is fitting the exact auto-correlation with a relative error smaller than e_{\max} . Figure 3.29 is an example of such an abacus. There are two ways to use Figure 3.29. First, for a given existing hardware, the RF front-end bandwidth is fixed for instance, to $F_s = 4F_0$. In that case, the ACF will be correctly approximated ($e_{\max} = 0.01\%$) by the 4th order Taylor approximation for $\Delta\tau$ values smaller than about 0.1 C/A chips. Above

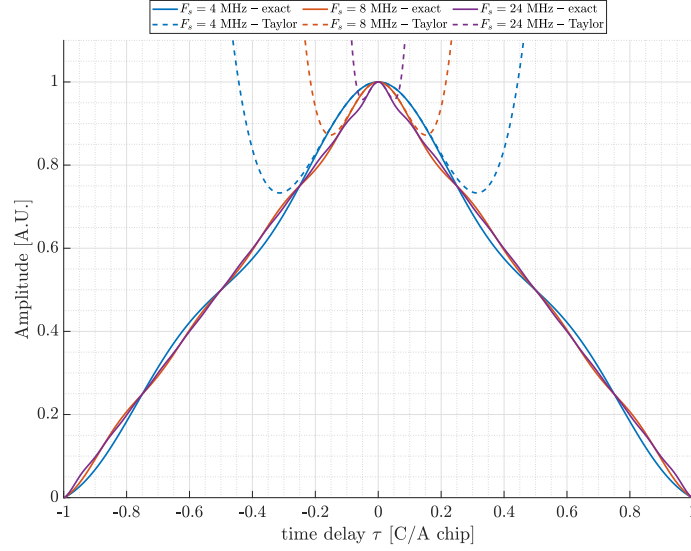


Figure 3.28: Exact (plain lines) and 4th order Taylor approximation (dashed lines) auto-correlation function for different sampling frequencies $F_s \in \{4, 8, 24\}$ MHz.

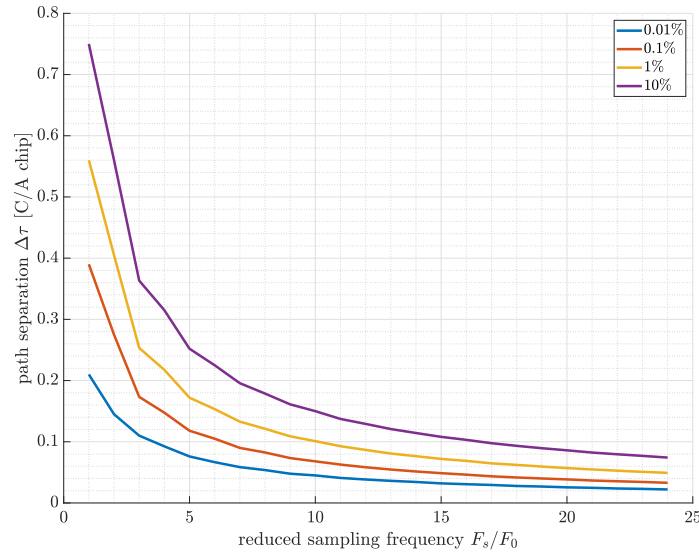


Figure 3.29: Relation between the path separation $\Delta\tau$, the sampling frequency F_s (expressed in number of $F_0 = 1.023$ MHz) and the relative error between the exact auto-correlation function and its 4th Taylor approximation.

this value, the AMLE cannot be expected to work properly since there is a significant error induced by the approximation. Secondly, if the geometry is fixed: say the receiver is at about 10 meters above a target reflection surface. From the equation that links the height with the path separation seen in Section 3.4.1, the largest path separation to be expected is two times

the actual height: 20m which is about 0.068 C/A chips. From Figure 3.29, the maximum signal bandwidth to allow a correct approximation of the auto-correlation function for the AMLE is about $F_s = 5F_0$. If the RF front-end has a larger bandwidth, a numerical filtering may be necessary to be able to apply the AMLE for this scenario.

As a take-away remark, Figure 3.28 highlights the fact that the AMLE will not perform well for too large path separation, it is important to be aware of it when electing the application.

3.5 Performance on Simulated Data

3.5.1 Simulation Set-Up

To look at the performance of the AMLE, the MSE of the estimated path separation $\Delta\tau$ is compared to the MSE of the exact 2S-MLE recalled in (3.17). Similarly the AMLE MSE of the estimated direct signal time-delay τ_0 is compared to the MSE of the 2S-MLE and the MSE of a standard single source processing 1S-MLE. A GPS L1 C/A signal is considered with RF front-end bandwidth set to 4 MHz. The path separation considered is set to 0.09 C/A chips, two phase differences are considered: $\Delta\phi = \pi/3$ and $\Delta\phi = 2\pi/3$ and relative amplitude is set to 0.5. Considering the remark done in Section 3.4.4, the AMLE does not look at $\Delta\tau$ candidates greater than 0.25 C/A chips. In order to fairly compare the AMLE and the 2S-MLE performance, the same restriction has been applied to the latter. Each point is estimated with 2000 Monte Carlo runs.

3.5.2 Cramér-Rao Bounds

Considering the assumptions and starting from the joint delay-Doppler estimation problem presented in chapter 2 for the estimation of $\epsilon = (\sigma_n^2, \boldsymbol{\eta}_0, \rho_0, \phi_0, \boldsymbol{\eta}_1, \rho_1, \phi_1)^T$ and its corresponding FIM $\mathbf{F}_{\epsilon|\epsilon}$, it is straightforward to obtain an expression of the FIM for the estimation of the vector of parameters under study $\boldsymbol{\xi} = (\sigma_n^2, \tau_0, \Delta\tau, b, \rho_0, \phi_0, \rho_1, \phi_1)^T$ using the following reparameterization:

$$\mathbf{F}_{\boldsymbol{\xi}|\boldsymbol{\xi}} = \left(\frac{\partial \epsilon}{\partial \boldsymbol{\xi}^T} \right)^T \mathbf{F}_{\epsilon|\epsilon} \frac{\partial \epsilon}{\partial \boldsymbol{\xi}^T} \quad (3.36)$$

where $\frac{\partial \epsilon}{\partial \boldsymbol{\xi}^T}$ is the jacobian of the application for which the image of ϵ is $\boldsymbol{\xi}$ defined by the constraints derived from the close-to-ground assumptions enumerated in Section 3.4.1: $b_0 = b_1 = b$ and $\Delta\tau = \tau_1 - \tau_0$. The Cramér-Rao Bound for the estimation of $\boldsymbol{\xi}$ is the inverse of the resulting FIM.

3.5.3 Numerical Results

Figure 3.30 presents the RMSE of both the AMLE and the 2S-MLE for the estimation of the path separation for considered scenarios. For both relative phase $\Delta\phi$, the performance of the proposed algorithm AMLE and the 2S-MLE are similar over a wide range of SNR. This is true up to a certain SNR point (about 42 dB) where the bias induced by the Taylor approximation becomes larger than the standard deviation. The AMLE approach seems a promising solution for scenarios with a SNR that ranges from 30 dB to 42 dB.

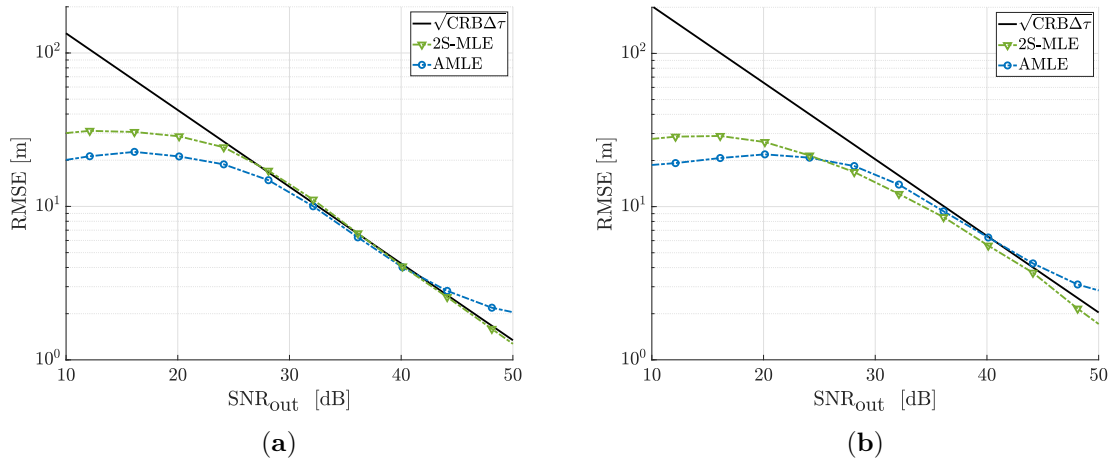


Figure 3.30: RMSE for the estimation of the path separation $c\Delta\tau$. (a) is with $\Delta\phi = \pi/3$ and (b) is with $\Delta\phi = 2\pi/3$. $\Delta\tau = 0.09$ C/A chips and relative amplitude is 0.5.

Another results from these simulations is proposed in Figure 3.31 where the RMSE of the AMLE, the 2S-MLE and the 1S-MLE for the estimation of the main signal time-delay are compared. As expected for the single source processing, the bias induced by the misspecification appears at a given SNR level as seen in Section 2.5. Again the the AMLE and the 2S-MLE present very similar performance and one can notice that the bias induced by the Taylor approximation visible in Figure 3.30 does not appear for the estimation of the direct signal time-delay. This suggests that the AMLE could be used as a multipath mitigation technique for robust navigation applications.

3.5.4 Wrap-Up on the AMLE

In this section, the AMLE has been introduced to tackle ground-based GNSS-R scenarios in which there is signal crosstalk. This reduces to a dual source estimation problem but with very small path separation. By exploiting the smallness of this path separation and resorting to a third order Taylor approximation of the likelihood criterion, it is possible to obtain an estimate of both the path separation and the direct signal time-delay. This promising algorithm seems a valuable solution for very close-to-ground GNSS-R scenarios even if it requires very good SNR levels.

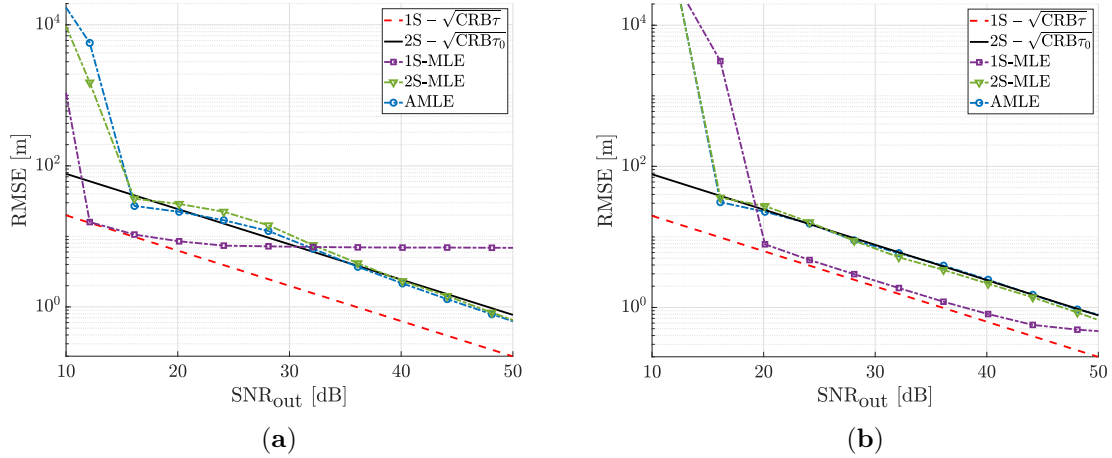


Figure 3.31: RMSE for the estimation of the main signal time delay $c\tau_0$ with AMLE, 2S-MLE and 1S-MLE. (a) is with $\Delta\phi = \pi/3$ and (b) is with $\Delta\phi = 2\pi/3$.

Now that the case where crosstalk could not be avoided is covered, there is still the case where crosstalk can actually be avoided by resorting to larger bandwidth signals.

3.6 Altimetry Using Wideband GNSS Signals

In this last part, the crosstalk is still assumed present but the GNSS signals considered are no longer GPS L1 C/A whose ACF width was of about 300 meters but GPS L5 and GALILEO E5A or E5B whose ACF width is only 30 meters. With this signals, as suggested in Section 3.3 it is actually possible to apply dual source algorithms such as the CRE on both channels (direct and reflected) in order to filter out the interfering signal due to crosstalk.

This section proposes a operational illustration of ground-based GNSS-R altimetry based on the Gruissan data set. The GPS PRN 27 signal of recording #6 is processed here as an example. Figure 3.32 presents the satellite elevation during the recording with corresponding expected path separation assuming a true height h of 25 meters.

3.6.1 Crosstalk and Multipath

In order to complete the second order statistics study of crosstalk done in Section 3.3, one can draw an analogy with GNSS multipath phenomenon as presented in Section 1.4 and studied in Chapter 2, and resort to metrics that provide insights on such phenomenon. In particular, by looking, in Figure 3.33, at the MPEE of a GPS L5Q signal sampled at $F_s = 20$ MHz, in presence of a secondary source with an amplitude ratio between the interfering source and the main source set to 0.3 when applying a 1S-MLE and a CRE, all the possible values of the bias induced by crosstalk can be read. From Figure 3.33a, one can see that applying a

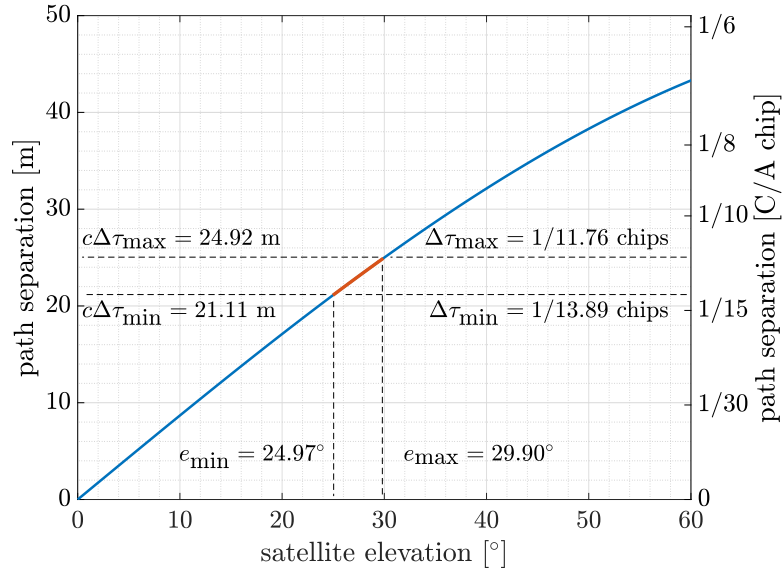


Figure 3.32: GPS PRN 27 elevation evolution during recording #6 of Gruissan data set.

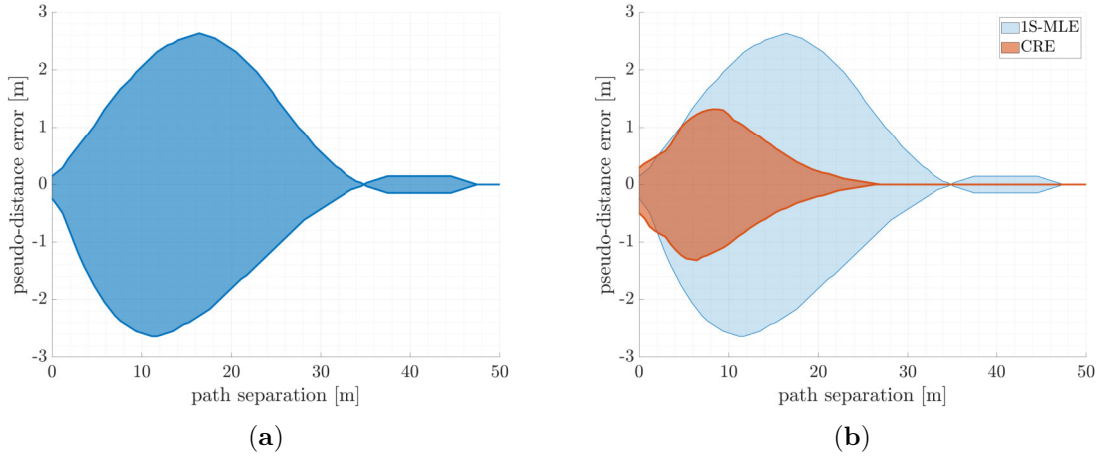


Figure 3.33: MPEE of a 1S-MLE (a) and a CRE (b) in presence of crosstalk for GPS L5Q signal sampled at $F_s = 20$ MHz.

1S-MLE in presence of crosstalk, even with large bandwidth GNSS signals, exposes the user to varying biases. In particular at a path separation of 25 meters, which corresponds, for instance, to the end of Gruissan recording #6 for GPS PRN 27, the bias on the estimated delay of the main signal, converted in meters can vary from -1 to 1 meter. If one wants to apply a single source processing algorithm has to wait that the satellite elevation gets large enough to see a path separation of more that 45 meters, which was not possible in the case of the Gruissan experiment. An alternative is then to apply a dual source processing algorithm such as the CRE. In Figure 3.33b, the corresponding MPEE is superimposed to the 1S-MLE one. The area of this new MPEE is smaller and its boundaries reach zero at smaller path

separation (about 26 meters). Consequently, one should not be too much affected by crosstalk by applying the CRE. This coherently supports the results presented in Section 3.3 on CRE applied to GPS L5Q signals.

The next two sections provide illustrations of the effect of crosstalk on the altimetry product based on the Gruissan data set.

3.6.2 Single Source Processing

Considering a single source processing (1S-MLE) on each channel of the recording #6 for GPS L5Q filtered at 20 MHz and coherently integrated during 20 ms. The results can be found in Figure 3.34 for the measured SNR and Figure 3.35 for the estimated path separation and corresponding height. Figure 3.34 shows that in each channels the signals are quite powerful.

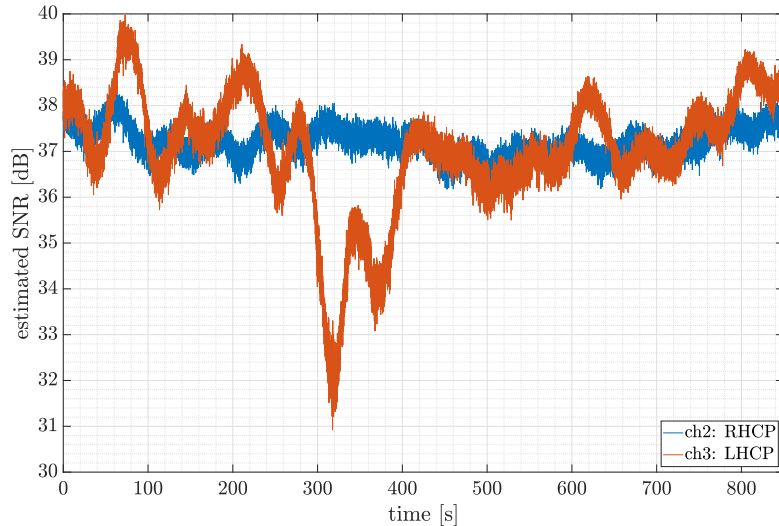
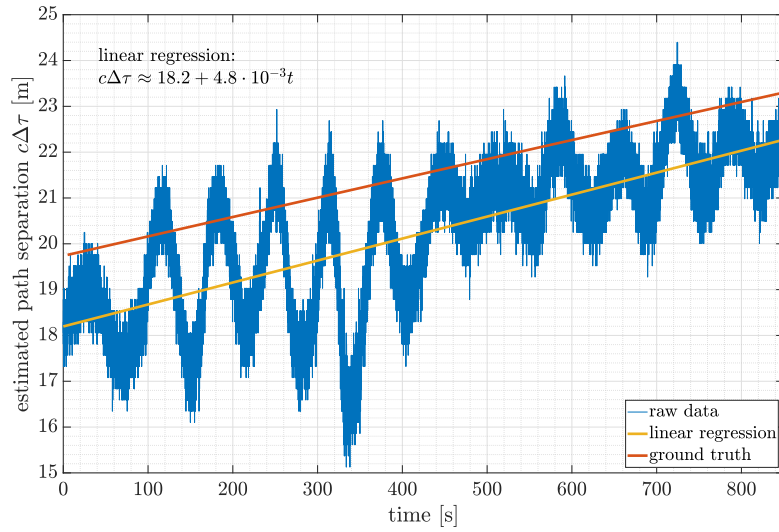
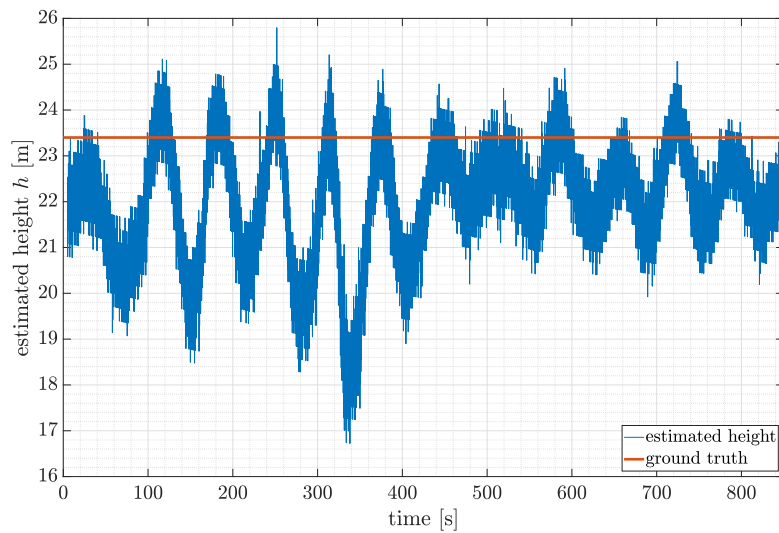


Figure 3.34: Estimated SNR at the output of the single matched filter processed with a 1S-MLE for channel ch2 (RHCP) and ch3 (LHCP) of recording #6.

At such low elevation, the LHCP component of the reflected signal is indeed dominant. Regarding the path separation estimate in Figure 3.35a, one can clearly observe oscillations of the estimate around a slowly varying mean. A linear regression of these estimates is also displayed, along with the true value. There is a significant gap between the regression and the true value which is a consequence of the crosstalk, as expected. Figure 3.35b is the same data converted into height estimation using (3.1). It is clear that ignoring the presence of the crosstalk lead to biased height estimation with oscillations as the satellite elevation changes. As a side note, the oscillations observed on the estimated path separation of the order of 2 meters around the mean value are in accordance with the short MPEE analysis done in Section 3.6.1, where an oscillation of ± 1 meter was predicted on one channel. The path separation being a combination of two channels, the effect has been amplified by a factor two.



(a)



(b)

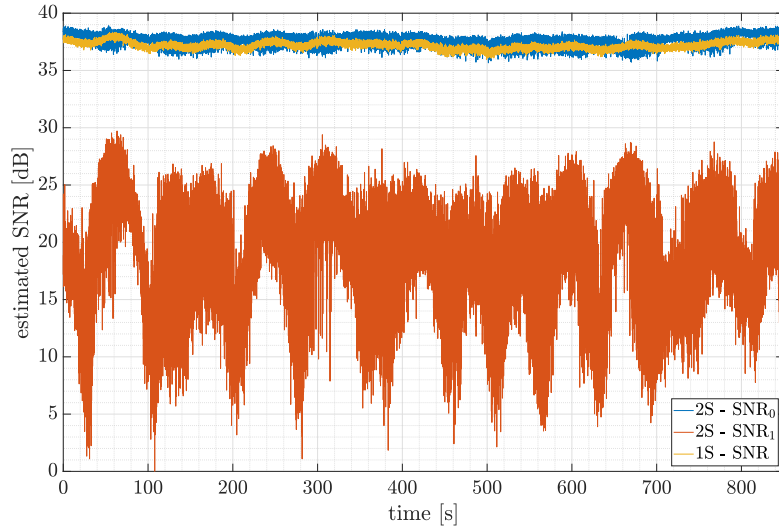
Figure 3.35: Estimated path separation (a) and correspond height (b) between the reflected channel ch3 (LHCP) and the direct channel ch2 (RHCP) using a 1S-MLE.

3.6.3 Dual Source Processing

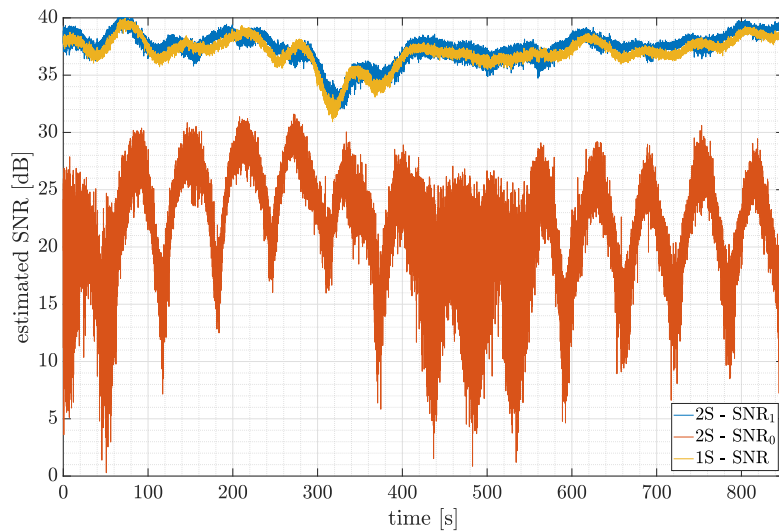
If one applies a dual source estimator to each channel would get the estimated parameters of the main or strongest signal on one hand, and noisy estimated parameters of the interfering signal due to crosstalk on the other hand. By doing this and only keeping the strongest estimated parameters, one would then simply filter out the crosstalk contribution.

Figure 3.36 presents the measured SNR for each channel and for each signal estimate (the

strongest and the interfering one). Figure 3.37 presents the estimated path separation and corresponding height when applying this dual source processing. The estimated height is



(a)



(b)

Figure 3.36: Estimated SNR of the dual source matched filter using a dual source CRE on the RHCP ch2 channel (a) and the LHCP ch3 channel (b). Results with the 1S-MLE approach are also displayed for comparison.

closer to the ground truth and the oscillations observed in the single source processing have been suppressed. This partly supports the dual source processing as a solution for ground-based altimetry. During the recording, small unidentified events have occurred and have significantly affected the received power as one can notice in Figure 3.36b between second 400 and second 600 for the orange curves. The consequence of these events is that the estimated

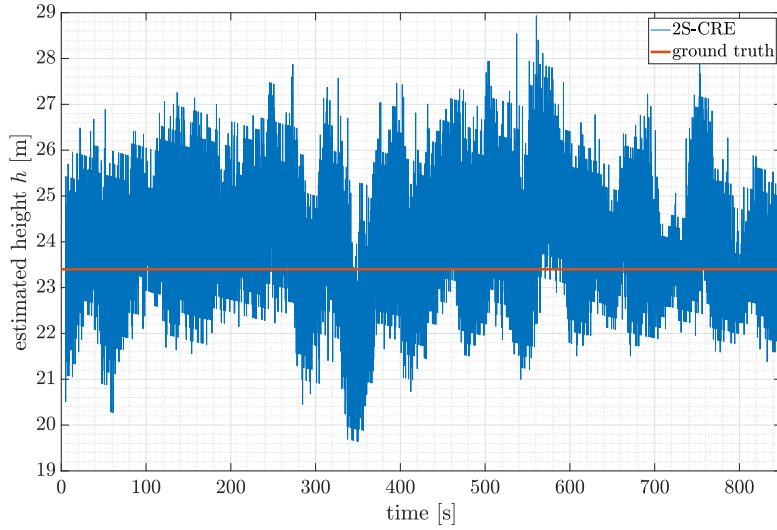


Figure 3.37: Estimated height between the reflected channel ch3 (LHCP) and the direct channel ch2 (RHCP) using a CRE.

height has some variations difficult to interpret. However it is possible to identify a subset during which the estimates are consistent. In particular, this is true during the time window between second 710 and second 730 summarized in Figure 3.38. During this window, all the

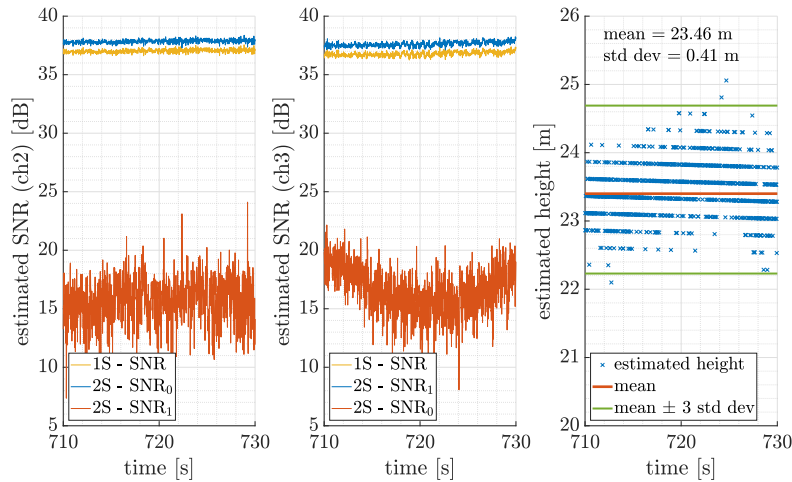


Figure 3.38: Overview of a subsection of recording #6. (**Left**) is the estimated SNR on ch2, (**Middle**) the estimated SNR on ch3 and (**Right**) the estimated height using a CRE.

estimated parameters are stable and their values are collected in Table 3.2. The parameters values in this table were used to compute the Cramér-Rao bound for the estimation of the height based on the expression derived in Section 2.3. To obtain them, the CRB for the estimation of the main signal in a dual source context for each channel $CRB_{\tau_0}^{\text{ch2}}$ and $CRB_{\tau_1}^{\text{ch3}}$ was evaluated and then recombined to obtain the corresponding bound for the estimation of

Table 3.2: Overview of a subsection of recording #6.

ch2	ch3	height
SNR ₀ = 38 dB	SNR ₀ = 16 dB	mean = 23.46 m
SNR ₁ = 15 dB	SNR ₁ = 37.5 dB	std dev = 0.41 m

the height:

$$\sqrt{\text{CRB}_h} = \frac{c\sqrt{\text{CRB}_{\tau_0}^{\text{ch2}} + \text{CRB}_{\tau_1}^{\text{ch3}}}}{2\sin(e)} \approx 0.27\text{m}. \quad (3.37)$$

The observed standard deviation, recorded in Table 3.2, is larger than this optimal performance. Reasons to this can be enumerated as follows: i) at this path separation (ground truth predicted a path separation of about 22 meters at second 700), there is still a small crosstalk that affects the performance of the CRE as intuited by Figure 3.33b, ii) unidentified events may have corrupted the data as it was the case at other moments of the recording and iii) the implementation of the CRE may affect the final performance, in particular the choice of the grid search resolution might have brought an additional quantization error.

3.6.4 Wrap-Up on Wideband Signals Processing

In this last part, crosstalk issue was tackled exploiting wideband GNSS signals. As suggested in Section 3.3, a dual source estimator improve significantly conventional GNSS-R processing in presence of crosstalk. In particular it does reduce the bias and oscillation induced by crosstalk. This was supported by the Gruissan data set using the CRE. It is clear that more sophisticated estimators could be applied in order to reduce the bias induced by the crosstalk for small path separation values. For instance, one may look at existing multipath estimating techniques to pick an estimator with the smallest MPEE area.

3.7 Conclusion

In this chapter, the multipath is no longer seen as a nuisance but as a source of information. The study of reflected GNSS signals upon the Earth’s surface is known as GNSS-R. The scope of the chapter only focuses on ground-based scenarios where the direct and reflected signals interfere with one another.

This specific ground-based scenario was the object of a data collection campaign near Gruissan, which has been fully presented and taken as a reference for the rest of the chapter in terms of geometry, receiver parameters and received signals.

In standard GNSS-R, two antennas are usually used to decouple the direct and the reflected paths. The problem in ground-based scenarios is that the direct antenna also collects

part of the reflected signal and vice-versa. This phenomenon, called signal crosstalk, induces a bias on the altimetry product similarly to multipath in GNSS. A thorough study of the impact of crosstalk was first done to identify situations where crosstalk can or cannot be avoided. One can play on the receiver algorithm or on the processed signal to minimize the crosstalk effect.

For the cases where crosstalk cannot be avoided because the induced path separation between the signal of interest and the interfering one is too small, a high resolution AMLE was proposed. It is based on a third order Taylor approximation of the likelihood ratio to be maximized and it shows a promising performance for GNSS-R altimetry as well as for multipath mitigation.

However by processing wideband GNSS signals, applying more classic dual source estimating solutions such as the CRE may get rid of the crosstalk effect. This was illustrated with the Gruissan data set.

Towards Diffuse Scattering

Contents

4.1	Introduction	132
4.2	Coherence Analysis	135
4.2.1	Mallorca Experiment	136
4.2.2	Coherence Transition <i>à l'œil</i>	137
4.2.3	Coherence Indicators	138
4.2.4	Wrap-Up on Coherence Detection	145
4.3	Impulse Response Estimation	145
4.3.1	Motivation	145
4.3.2	Signal Model	146
4.3.3	Compact CRB for the Joint Delay-Doppler Estimation with a Discrete Impulse Response	149
4.3.4	Validation and Discussion	152
4.3.5	Wrap-Up on Impulse Response Estimation	154
4.4	Impulse Response Size Determination: A Detection Problem	155
4.4.1	Theoretical Analysis	156
4.4.2	Iterative Procedure: $P + \text{next}$ Test	158
4.4.3	Overshoot-and-Decimate Procedures	159
4.4.4	Wrap-Up on Impulse Response Size Determination	161
4.5	Conclusion	162

Résumé

Dans ce chapitre, la géométrie et la nature de la surface de réflexion ne permettent plus de modéliser le signal réfléchi comme une simple copie retardée et atténuée du signal émis. En effet, dans le cas où la surface de réflexion est plus rugueuse au sens du critère de Rayleigh (qui dépend de la rugosité de la surface mais aussi de la longueur d'onde et de l'angle d'incidence du signal), le signal réfléchi perd en cohérence. Cela s'observe en particulier sur la phase porteuse du signal réfléchi dont la variation, régulière dans le cas cohérent, devient imprévisible dans le cas incohérent. L'étude de série temporelle de la mesure de la phase du trajet réfléchi

donne donc les clés pour comprendre le passage de réflexion cohérente à réflexion incohérente. En observant cette série temporelle, deux indicateurs de cohérence sont étudiés, l'un testant la régularité de la variation de la phase et l'autre testant la gaussianité des mesures. Ces indicateurs sont testés sur des données collectées en haut du Puig Major de Majorque par l'*Institut d'Estudis Espacials de Catalunya* (IEEC). Dans le cas d'une réflexion tout à fait diffuse, l'énergie réfléchie ne provient plus d'une petite surface déterminée par la première zone de Fresnel mais d'une surface éclairante bien plus étendue qui peut s'étendre à des dizaines de kilomètres autour du point de réflexion spéculaire. Dans de telles conditions, le signal reçu est la somme de toutes les contributions de cette surface éclairante, ce qui résulte en un signal potentiellement très déformé. Un modèle plus adapté pour tenir compte de cette surface étendue est de considérer le signal reçu comme la convolution entre le signal émis et la réponse impulsionnelle de la surface de réflexion. Il est alors possible d'estimer les paramètres de cette réponse impulsionnelle à l'aide d'un estimateur comme celui du maximum de vraisemblance. Les performances associées à cette estimation sont bornées par la borne de Cramér-Rao qui doivent être calculées. Reste alors le problème de la détermination de la taille de réponse impulsionnelle. Ce problème revient à déterminer le nombre de coefficients qui composent la réponse impulsionnelle, ce qui peut se faire à l'aide de tests d'hypothèses de deux manières différentes : la première en sous-estimant le nombre de coefficients puis en l'augmentant de manière itérative, la seconde en surestimant ce nombre et en sélectionnant uniquement les coefficients les plus pertinents. Chacune de ces approches affecte la précision de la mesure des coefficients.

Ce dernier chapitre commence donc, avec la Section 4.2, par l'étude de la cohérence du signal réfléchi lorsque la géométrie est proche du critère de Rayleigh. Le réflexion est ensuite considérée diffuse et le modèle convolutif est introduit dans la Section 4.3 avec le calcul de la borne de Cramér-Rao et sa validation par les propriétés asymptotiques de l'estimateur du maximum de vraisemblance. Enfin, le problème de la détermination du nombre de coefficients qui décrivent la réponse impulsionnelle de la surface de réflexion est étudié dans la Section 4.4 où deux approches sont proposées pour obtenir le nombre correct de coefficients.

4.1 Introduction

So far the reflection was assumed coherent and specular: the reflected signal was seen as a simple additional source with different time-delay, attenuation and sometimes different Doppler frequency. This assumption can usually be done for smooth enough surfaces.

Surface roughness is a relative feature that depends on the signal wavelength λ , the variation of height of the surface Δh , and the elevation angle e . In Figure 4.1a, the elevation angle is very small and the path separation $c\Delta\tau$ between a trajectory with a reflection at the trough of the wave and the trajectory with a reflection at the top of a wave is very small. In this case, the range of delays received by all the possible scatterers is concentrated and one can say that the reflecting surface is almost mirror-like. On the other hand, in Figure 4.1b, the elevation angle is much larger. In this case, the path separation $c\Delta\tau$ between both trajectories (one

through the trough, the other through the top of a wave), is larger as well. Consequently, the range of delays received by all possible scatterers is more spread. The reflecting surface cannot be seen as a mirror anymore.

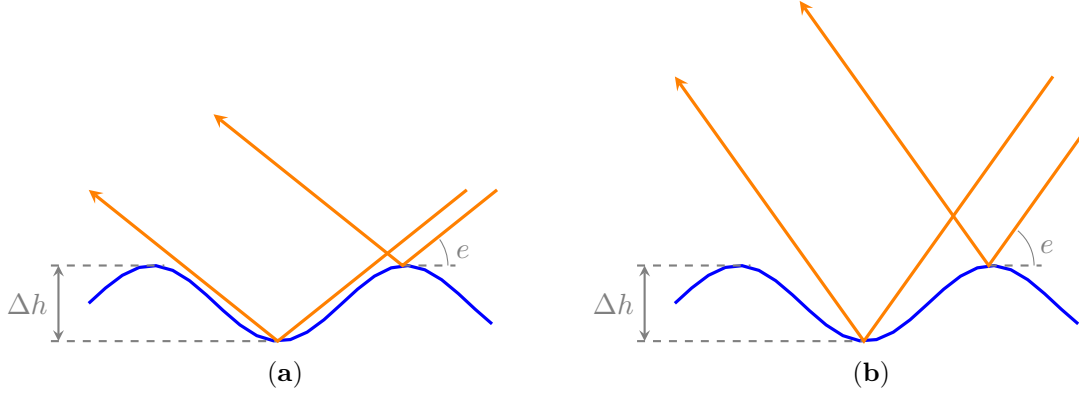


Figure 4.1: Derivation of the Rayleigh criterion. (a) for low elevation angle and (b) for large elevation angle.

This intuition was captured by Rayleigh with the following relation:

$$\Delta\phi = \frac{2\pi}{\lambda} c\Delta\tau = \frac{4\pi\Delta h}{\lambda} \sin(e). \quad (4.1)$$

If the phase difference $\Delta\phi$ is very small as in Figure 4.1a, the two rays are almost in phase which results in a coherent reflection. Then if $\Delta\phi$ increases, the two rays will interfere until the worst case $\Delta\phi = \pi$ where they cancel. In this case, the surface scatters and is considered rough. Usually, $\Delta\phi = \pi/2$ is arbitrary to separate rough from smooth surfaces. The so-called Rayleigh criterion tells that a surface is considered smooth if

$$\Delta h < \frac{\lambda}{8 \sin(e)}. \quad (4.2)$$

Consequently, by observing a time series of the carrier phase of the reflected path, as the elevation angle varies, and with different sea state, a transition from a coherent reflection to a non-coherent reflection should be observable.

For rough surfaces, the energy reflected comes from an extended zone usually called *glistening zone*. In [BS87], the glistening zone is defined as *that part of the Earth's surface which can participate in the reflection of waves for a given position of the transmitter and the receiver*. As an illustration, Figure 4.2 presents the diffuse reflection of sun rays over a moderately rough sea surface.

To get an idea of the dimensions of this glistening zone, let \mathbf{q} denote the scattering vector, being the difference between the scattered unit vector \mathbf{n}_s that goes from a reflection point P to the receiver R , and the incident unit vector \mathbf{n}_i that goes from the transmitter T to the reflection point P :

$$\mathbf{q} \triangleq \frac{2\pi}{\lambda} (\mathbf{n}_s - \mathbf{n}_i). \quad (4.3)$$



Figure 4.2: Sunset Reflection over the sea surface (credit: Xavier Lubeigt).

This scattering vector can also be seen graphically in Figure 4.3. The angle between the vertical axis (noted z) and the scattering vector is the scattering angle noted β . Considering

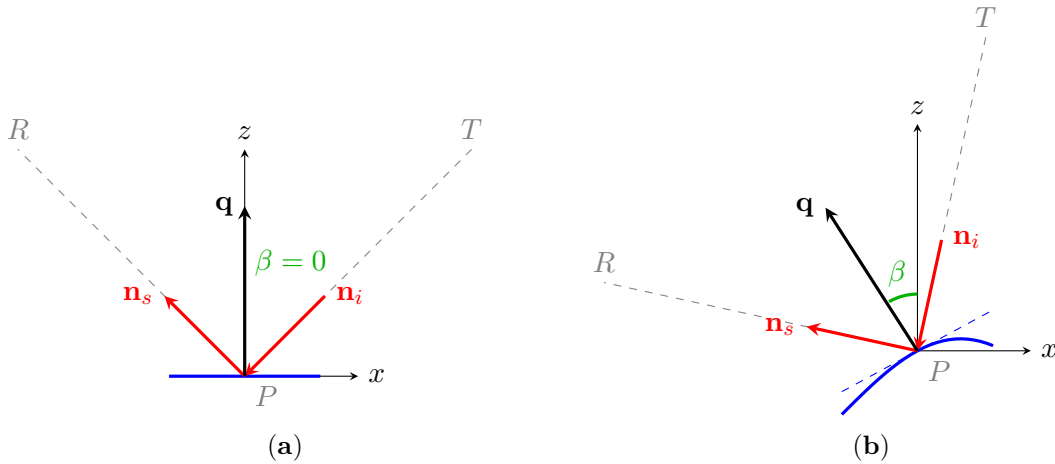


Figure 4.3: Definition of the scattering vector \mathbf{q} along with the scattering angle β .

a surface as a random object with a vertical root mean square height noted σ_v , and with an horizontal auto-correlation length l_h , it was shown in [BS87] that the energy reflected from a point P with corresponding scattering angle β was attenuated by a coefficient $G(\beta, \beta_0)$ of the form

$$G(\beta, \beta_0) = \cot^2(\beta_0) e^{-\frac{\tan^2(\beta)}{\tan^2(\beta_0)}}, \quad (4.4)$$

where $\tan(\cdot)$ and $\cot(\cdot)$ denote the tangent and cotangent functions, respectively and β_0 is the mean value of the ratio of the vertical and the horizontal dimensions of the irregularities:

$$\tan(\beta_0) \triangleq 2\sigma_v/l_h. \quad (4.5)$$

As an example, from [Car02], $\beta_0 = 5^\circ$ correspond to calm sea conditions (wind speed around 4 m/s) and $\beta_0 = 8^\circ$ to rough sea conditions (wind speed around 10 m/s). Other models such as the one described in [Elf97] could be used to link the sea state to the surface wind speeds.

Based on the shape of $G(\beta, \beta_0)$ in (4.4), the edge of the glistening zone can be defined as the set of points on the surface for which $\beta = \beta_0$.

As suggested by Figure 4.2, the glistening zone can be very large. The reflected signal, which can be seen as the convolution of the transmitted signal with the impulse response of the reflecting surface can then be significantly distorted. The study of these distorted signals requires a more appropriate signal model where the impulse response of the reflecting surface should appear. With this signal model goes the corresponding MLE and CRB to know the best achievable performance on the estimation of the impulse response coefficients.

Naturally, the size of the glistening zone, in other words, the number of pulses required to describe the reflecting surface impulse response, is unknown. The problem of determining this number, also referred to as the detection problem as introduced in Section 1.2.3, should then be addressed for the impulse response model at hand.

In this chapter, a deeper look at the nature of the reflection is proposed. First, in Section 4.2, the question of the transition from a coherent to a non-coherent reflection is addressed for grazing angle reflections. This study, supported by a Mallorca experiment proposes two coherence indicators meant to automatically detect coherent reflections. In the case of a non-coherent reflection, the energy reflected may come from an extended surface called glistening zone. In Section 4.3 the glistening zone that corresponds to the Mallorca experiment is presented to justify a new signal model that take into account the size of the reflecting surface. This signal model consists of the convolution between the transmitted signal and the impulse response of the reflecting surface. Closed form expressions of the CRB for the estimation of the parameters of this signal model are derived and validated using the asymptotic properties of the MLE. Finally the question of the impulse response size determination is tackled in Section 4.4.

The work presented in Section 4.2 and at the beginning of Section 4.3 was done in collaboration with the IEEC during a four month visit in their facilities near Barcelona, Spain.

4.2 Coherence Analysis

The question of the coherence of a reflection in GNSS-R is fundamental when high-accuracy carrier phase-based altimetry is intended. As mentioned before, when the reflection is not coherent, the reflected path's carrier phase varies randomly and cannot be tracked. Based on an experiment done at the Puig Major on Mallorca Island, Spain, reflected path carrier phase time series are studied in order to highlight the transition from coherent to non-coherent reflections, as the satellite elevation varies. From the observation of this transition, two coherence indicators or detectors will be proposed with their associated statistics.

4.2.1 Mallorca Experiment

This coherence analysis is based on an experiment campaign partially organized by the IEEC from April to July 2021. One of the objectives of this experiment was to perform GNSS-R altimetry with the carrier phase measurement.

4.2.1.1 Experimental Set-Up

For this experiment a receiver was placed at the top of the Puig Major which towers the island at 1436 meters above the sea level (see Figure 4.4). Since it is located at about 4 km from the nearest shore, only reflections with satellite elevations smaller than 19.74° could be collected by the receiver.



Figure 4.4: Site location at the Puig Major on Mallorca Island, Spain (credit: www.stepmap.de).

The receiver was the SPIR instrument presented in [Rib17]. It was configured with four synchronized RF channels with the following settings:

- ch0 (L1-UP): center frequency $f_c = 1575$ MHz (intermediate frequency IF = 420 kHz), RHCP antenna,
- ch1 (L5-UP): $f_c = 1176.25$ MHz (IF = 200 kHz), RHCP antenna,
- ch2 (L1-DN): $f_c = 1575$ MHz (IF = 420 kHz), LHCP antenna,
- ch3 (L5-DN): $f_c = 1176.25$ MHz (IF = 200 kHz), LHCP antenna.

Each channel is sampled at 80 Msps and each sample is described with its in-phase and quadrature components over 4 bits.

4.2.1.2 IEEC Processing

During the experiment, a hundred of satellite tracks were recorded. The satellites tracked were from GPS, GALILEO and BeiDou constellations with elevations that vary from almost zero up to 15° . Since the receiver was installed over months, many different sea states were observed with different significant wave heights, wind speeds and wind directions.

All the tracks were processed in a similar way at IEEC: the direct path was processed using a standard GNSS architecture with tracking loops as introduced in Section 1.3.3. Then, the expected delay of the reflected path was computed based on geometry (position of the transmitting satellite, the receiver and the assumed reflecting surface), and based on models to compensate tropospheric extra delay that can be significant at such low elevation angles [GL03]. The reflected path was then computed at the compute time location using a simple cross-correlation with a local replica. This is a typical cGNSS-R processing. The output of this processing is a time series of the successive complex CCF or waveforms, centered on the direct on one hand and on the assumed reflected delay on the other hand. These waveforms are computed with an integration time set to 1 ms. Figure 4.5 summarizes a computed track, which corresponds to a GPS satellite, during about thirty minutes (an averaging over one second was done to obtain these figures).

4.2.2 Coherence Transition *à l'œil*

From the complex waveforms obtained by the IEEC processing, one can then obtain time series of the complex amplitude at the peak for the reflected path. These time series are usually averaged over a few seconds to smooth them. In particular, if one looks at the carrier phase time series, Figure 4.6a is obtained. For the processing presented in the previous section, if all the contributions that affect the path separation, i.e., geometric delay and tropospheric delay, were perfectly known, the carrier phase for the reflected path should be equal to zero at all times. However, the location of the reflecting surface, its roughness and the model simplifications cannot be fully modeled, and this can be observed in either Figure 4.6a or Figure 4.6b, where a residual phase variation is visible at the beginning of the recording. For the GPS track, the phase variation turns messy starting from minute 5 and onward. In the case of the GALILEO E5A, its carrier phase variations are first a little erratic, then smoother and finally erratic again. In the literature [Roe21], this transition starting at minute 5 is an expression of the transition from coherent to non-coherent reflections. It can be observed in different tracks and the transition moments occur at different elevation angles depending on the sea state and the GNSS signal used (either L1/E1 or L5/E5A signals), which was expected given the fact that the Rayleigh criterion (4.2) also depends on the elevation angle, the surface roughness and the signal wavelength.

So far this transition is more or less spotted by looking at the time series and a indicator could be built in order to automatically detect the transition, or at least provide an opinion on whether the current reflection is coherent or not. In the next section, two indicators are proposed to detect or indicate the coherence of the reflected signal.

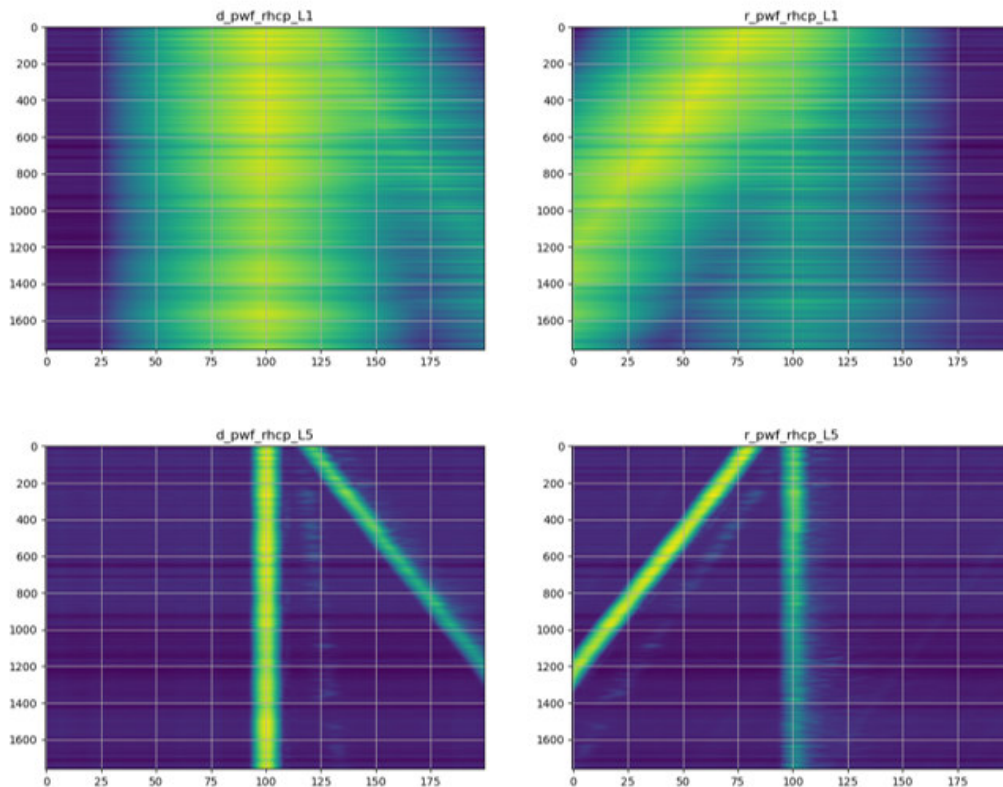


Figure 4.5: Example of Mallorca experiment processed data. (**Left**) are the direct paths, (**Right**) are the reflected paths, (**Top**) are the L1 channels and (**Bottom**) are the L5 channels. Horizontal axis is in samples and vertical axis is in seconds (credit: IEEC).

4.2.3 Coherence Indicators

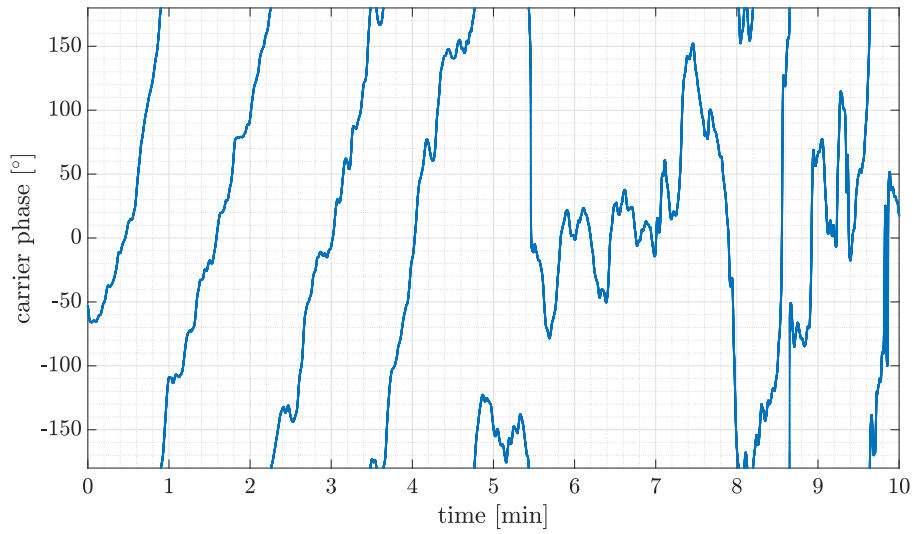
In this section the detection of the coherence of a reflection is addressed. It is set as an hypothesis test with the following hypothesis:

- null hypothesis H_0 : the reflection is coherent,
- alternative hypothesis H_1 : the reflection is non-coherent.

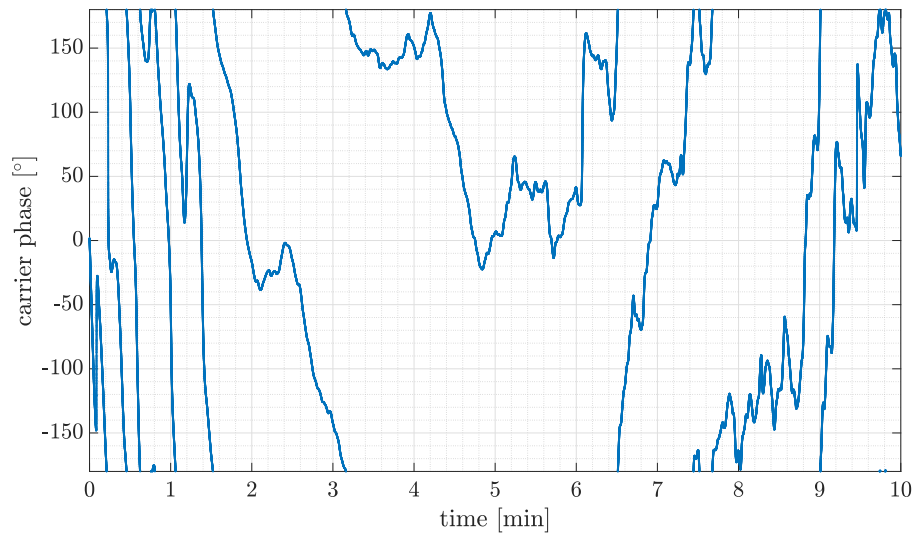
To deal with hypothesis tests, the probability of false alarm (PFA) and probability of detection (PD) are also used, which are defined as:

$$\text{PFA} = P[\text{reject } H_0 | H_0 \text{ true}], \quad (4.6)$$

$$\text{PD} = P[\text{reject } H_0 | H_1 \text{ true}]. \quad (4.7)$$



(a)



(b)

Figure 4.6: Example of GPS L5 (a) and GALILEO E5A (b) reflected path carrier phase time series from complex waveforms averaged over 10 seconds.

4.2.3.1 Simple Difference Indicator

Based on Figure 4.6, the time series of the observed carrier phase $\{\phi_k\}$ for $k = 1..N$, N the number of points, is smooth and regular when the reflection is coherent and erratic when the reflection is non-coherent. This suggests that evaluating the regularity of the time series may help determining whether the reflection is coherent or not. As initially proposed by IEEC, a way to do this is to look at the phase difference between two consecutive points $\Delta\phi_k = \phi_{k+1} - \phi_k$, and then look at its cosine. Consequently, a test statistic T^{SD} is built as

follows:

$$T_k^{\text{SD}} = \cos(\phi_{k+1} - \phi_k) \geq \text{thresh.} \quad (4.8)$$

If the reflection is coherent, the phase difference should be locally constant and the cosine should be equal to 1. Then, if the reflection is not coherent, random variations on the residual phase difference will decrease the resulting test statistic T^{SD} .

In order to fix the threshold, one needs to consider what happens when the reflection is fully coherent: in this case, the residual carrier phase difference can be seen as a random variable with a normal distribution, with a mean equal to a constant μ_ϕ , and a variance equal to the thermal noise variance, noted σ_ϕ^2 . The threshold determination is usually done by fixing the PFA, which is defined by:

$$\begin{aligned} \text{PFA} &= P \left[T_k^{\text{SD}} < \text{thresh.} | H_0 \right] \\ &= P \left[\cos(\phi_{k+1} - \phi_k) < \text{thresh.} | \phi_k \sim \mathcal{N}(\mu_\phi, \sigma_\phi^2) \right] \\ &= P \left[|\phi_{k+1} - \phi_k| > \arccos(\text{thresh.}) | \phi_k \sim \mathcal{N}(\mu_\phi, \sigma_\phi^2) \right] \end{aligned} \quad (4.9)$$

Now if $\phi_k \sim \mathcal{N}(0, \sigma_\phi^2)$, then the difference of two independent terms is also normally distributed with the same mean but twice the variance: $\phi_{k+1} - \phi_k \sim \mathcal{N}(0, 2\sigma_\phi^2)$; and by defining the variable $U = (\phi_{k+1} - \phi_k) / \sqrt{2}\sigma_\phi$ such that $U \sim \mathcal{N}(0, 1)$, the PFA defined in (4.9) can be written as:

$$\begin{aligned} \text{PFA} &= P \left[|U| > \frac{\arccos(\text{thresh.})}{\sqrt{2}\sigma_\phi} | U \sim \mathcal{N}(0, 1) \right] \\ &= P \left[U > \frac{\arccos(\text{thresh.})}{\sqrt{2}\sigma_\phi} | U \sim \mathcal{N}(0, 1) \right] + P \left[U < -\frac{\arccos(\text{thresh.})}{\sqrt{2}\sigma_\phi} | U \sim \mathcal{N}(0, 1) \right] \\ &= 1 - \Phi \left(\frac{\arccos(\text{thresh.})}{\sqrt{2}\sigma_\phi} \right) + \Phi \left(-\frac{\arccos(\text{thresh.})}{\sqrt{2}\sigma_\phi} \right) \end{aligned}$$

with $\Phi(\cdot)$ the CDF of the standard normal distribution. Then, exploiting the symmetry of such a distribution,

$$\text{PFA} = 2 \left(1 - \Phi \left(\frac{\arccos(\text{thresh.})}{\sqrt{2}\sigma_\phi} \right) \right). \quad (4.10)$$

By inverting (4.10), the threshold is a simple expression of the desired PFA and the noise level of the measured phase difference:

$$\text{thresh.} = \cos \left(\sqrt{2}\sigma_\phi \Phi^{-1} \left(1 - \frac{\text{PFA}}{2} \right) \right). \quad (4.11)$$

As a remark, the distribution of the carrier phase is usually better described by a Von Mises distribution, also known as wrapped normal distribution [CGH07] but for small enough σ_ϕ , the wrapped normal and the normal distributions are equivalent.

Now, in the case of a non-coherent reflection, the phase distribution becomes uniformly random, that is, for non-coherent reflections, $\phi_k \sim \mathcal{U}([-\pi, \pi])$. It is then possible to evaluate

the PD defined by:

$$\text{PD} = P \left[T_k^{\text{SD}} < \text{thresh.} | H_1 \right] \quad (4.12)$$

$$= P \left[\cos(\Delta\phi_k) < \text{thresh.} | \Delta\phi_k \sim \mathcal{U}([- \pi, \pi]) \right] \quad (4.13)$$

$$= P \left[|\Delta\phi_k| > \arccos(\text{thresh.}) | \Delta\phi_k \sim \mathcal{U}([- \pi, \pi]) \right] \quad (4.14)$$

$$= 2P \left[\arccos(\text{thresh.}) < |\Delta\phi_k| < \pi | \Delta\phi_k \sim \mathcal{U}([- \pi, \pi]) \right] \quad (4.15)$$

$$= \frac{2}{2\pi} (\pi - \arccos(\text{thresh.})) \quad (4.16)$$

Using the expression of the threshold (4.11), the PD can be written as:

$$\text{PD} = 1 - \frac{\sqrt{2}\sigma_\phi}{\pi} \Phi^{-1} \left(1 - \frac{\text{PFA}}{2} \right). \quad (4.17)$$

This equation allows to draw Receiver Operator Characteristic (ROC) curves to see the global performance of the simple difference test, and the impact of the noise parameter σ_ϕ . Based on Figure 4.6, the observed variance of the data in the coherent regime is always less than 10 degrees. Figure 4.7 presents ROC curves for different values of σ_ϕ . Provided that the

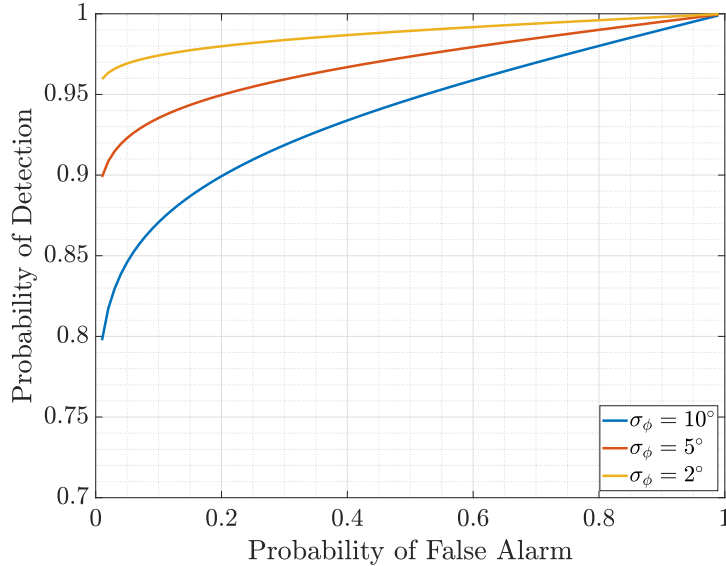


Figure 4.7: ROC curves for the simple difference coherence test.

assumptions made hold for the considered carrier phase time series, this simple difference test seems a good candidate as a coherence indicator.

4.2.3.2 Lilliefors Test

Another way to test the coherence based on the carrier phase observation is to look at histograms of subsets of the time series. Figure 4.8 presents three histograms built with 3000 samples, that is, over 3 seconds, at four instants of the GPS L5 time series displayed in Figure 4.6a. This figure suggests that the distribution of the carrier phase is strongly affected by

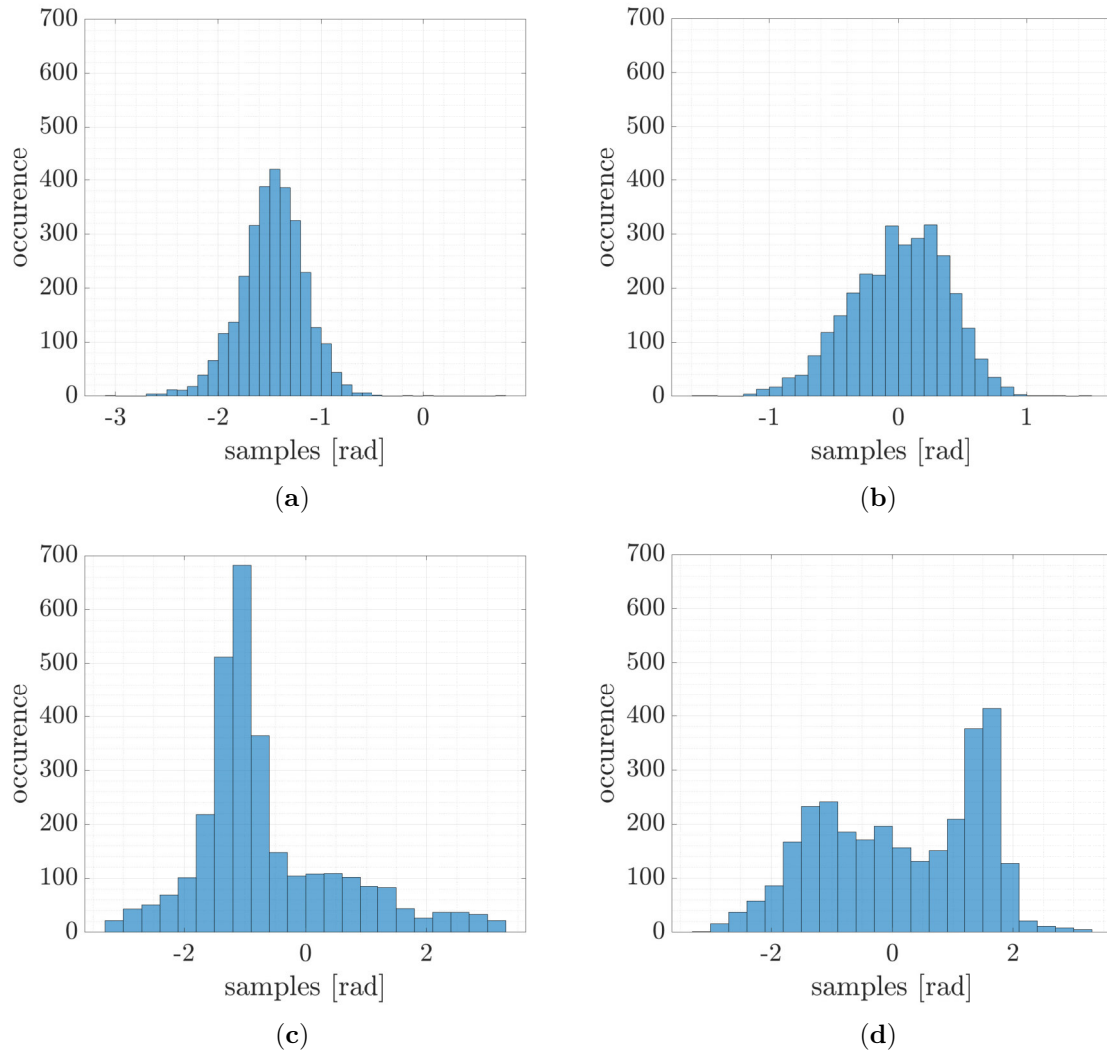


Figure 4.8: Histograms based on 3000 samples in the coherent regime (a) at minute 1, (b) at minute 3 and in the non-coherent regime (c) at minute 6 and (d) at minute 9.

the nature of the reflection: in the coherent regime, distributions look Gaussian and in the non-coherent regime they do not look Gaussian anymore. Based on this a goodness-of-fit test, such as the Lilliefors test [Lil67], that checks the Gaussianity of a distribution, could be applied to the subsets of the time series. This test evaluates the hypothesis that the carrier phase samples have a normal distribution, with unspecified mean and variance, against the alternative hypothesis that the sample does not have a normal distribution. This test is a

Kolmogorov–Smirnov test adapted to Gaussian distributions.

The Lilliefors test statistic is the maximum vertical distance between the empirical CDF built from the samples, and a theoretical normal CDF defined by the mean and the variance of the tested data set. An illustration of this test statistic can be found in Figure 4.9. For the Lilliefors test, the Gaussianity hypothesis (therefore the coherence hypothesis) is

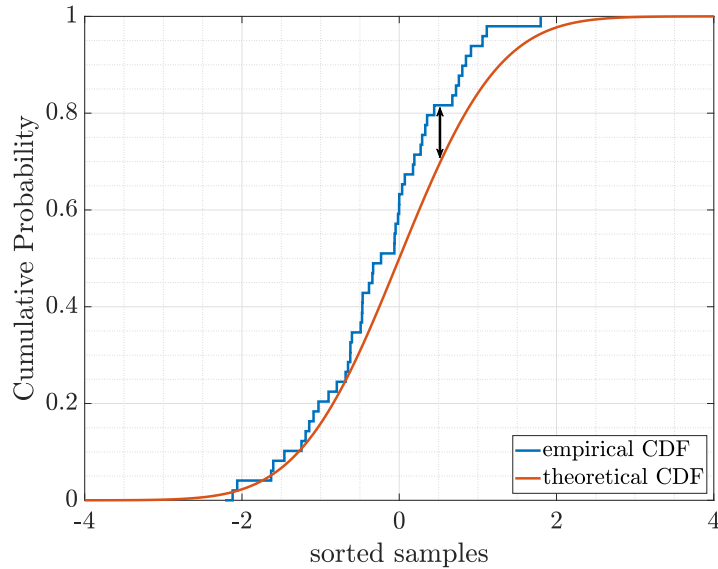


Figure 4.9: Example of a comparison between empirical and theoretical CDF.

rejected at the significance level that corresponds to the PFA. It can be set arbitrarily in the implementation of the test.

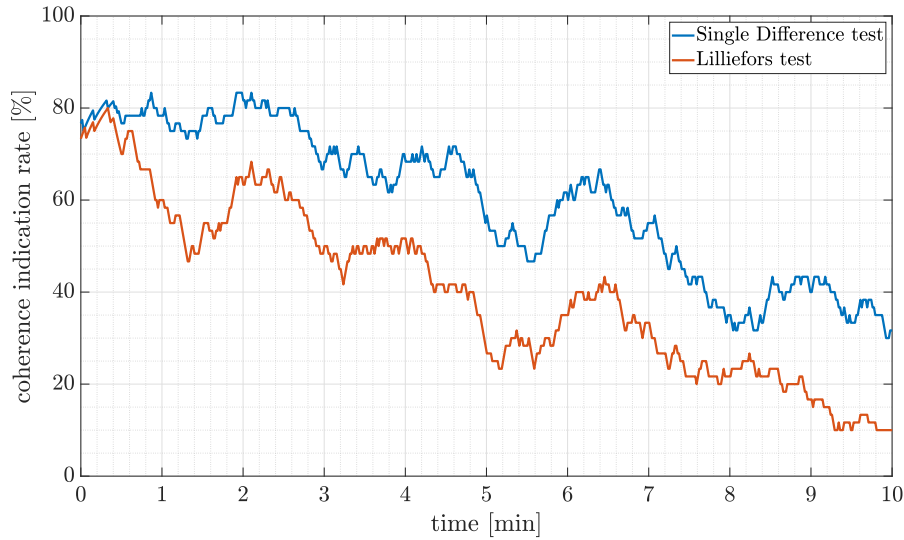
4.2.3.3 Results on Mallorca Data

In this section, the tests previously introduced are applied to the two carrier phase sets shown in Figure 4.6. The implementation of the tests was as follows:

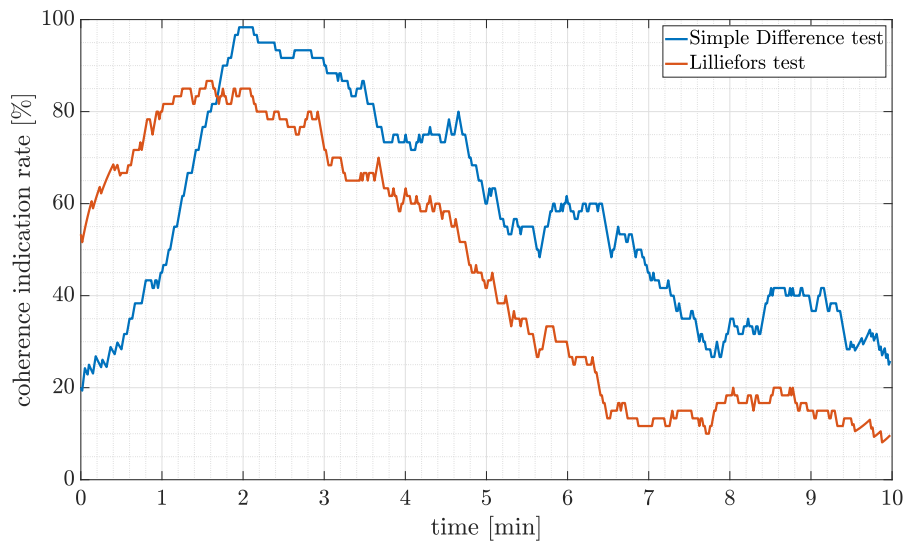
- For the simple difference test,
 - the initial carrier phase set, with a sample every 1ms, was first averaged over 1000 points to get a set with samples every second,
 - the test statistic was built for every sample-to-sample phase difference and compared to the threshold that corresponds to PFA=0.1 with $\sigma_\phi = 10^\circ$,
 - an average of the outputs of the test was done over a 1 minute sliding window.
- For the Lilliefors test,
 - the initial carrier phase set was divided into subsets of 1000 samples, representing 1 second,

- the Lilliefors test was applied to these subsets with a set $PFA=0.1$,
- an average of the outputs of the test was done over a 1 minute sliding window.

Figure 4.10 presents the results of these procedures. For both tracks, the tests' global



(a)



(b)

Figure 4.10: Example of GPS L5 (a) and GALILEO E5A (b) reflected path carrier phase time series from complex waveforms averaged over 10 seconds.

behavior coincide with one another, and with what was expected: in Figure 4.10a, the coherence indication rate, slowly decreases, and in Figure 4.10b, there is a first step where the coherence indication rate is rather small, then quite large and finally it slowly decreases. This corresponds to the observation done in Figure 4.6b. For the first two minutes of this last track,

the Lilliefors test indicator is larger than the simple difference test. The score obtained by the simple difference test might be affected by the important phase variation at the beginning of this track. Originally, the simple difference test assumes the phase with a constant mean. This is not true at the very beginning of the track depicted in Figure 4.6b which may be the reason why this test score is so low.

4.2.4 Wrap-Up on Coherence Detection

The nature of a reflection is a key feature that needs to be properly determined in order to perform carrier phase-based GNSS-R altimetry. By looking at carrier phase time series, it is sometimes possible to determine the transition from a coherent to a non-coherent regime. From these observations, coherence indicators can be thought of as in [Roe21]. In this section, two indicators, the simple difference test and the Lilliefors test, have been presented along with theoretical elements. They have then been applied to real data from the Mallorca experiment, to show how consistent they are with one another.

The next section considers a diffuse reflection that comes from a large glistening zone, as mentioned in Section 4.1. The reflecting surface considered here significantly distorts the reflected signal, and a new signal model is required to address this problem.

4.3 Impulse Response Estimation

4.3.1 Motivation

As mentioned before, when the reflection is diffuse, the energy reflected comes from an extended surface called glistening zone. Figure 4.11 presents a view of the Mallorca experiment presented in Section 4.2.1, for a scenario where the satellite elevation is set to 8° . In this figure, two sets of contour lines are displayed:

- iso- β_0 lines in degrees, which correspond to the edge of the glistening zone for a given sea state,
- iso-delay lines in meters, which correspond to sets of points that lead to the same excess delay at the receiver.

From this figure, the shape of the glistening zone delimited by the iso- β_0 lines matches the shape for the sun rays reflection previously shown in Figure 4.2. As a consequence, it is clear that this zone extends to tens of kilometers. By intersecting the glistening zone with the iso-delay lines, the receiver will receive signals with excess delay that exceeds 300 meters. The specular signal model is therefore too simplistic to describe such scenario. The rest of this section proposes a signal model adapted to a surface with an extended impulse response.

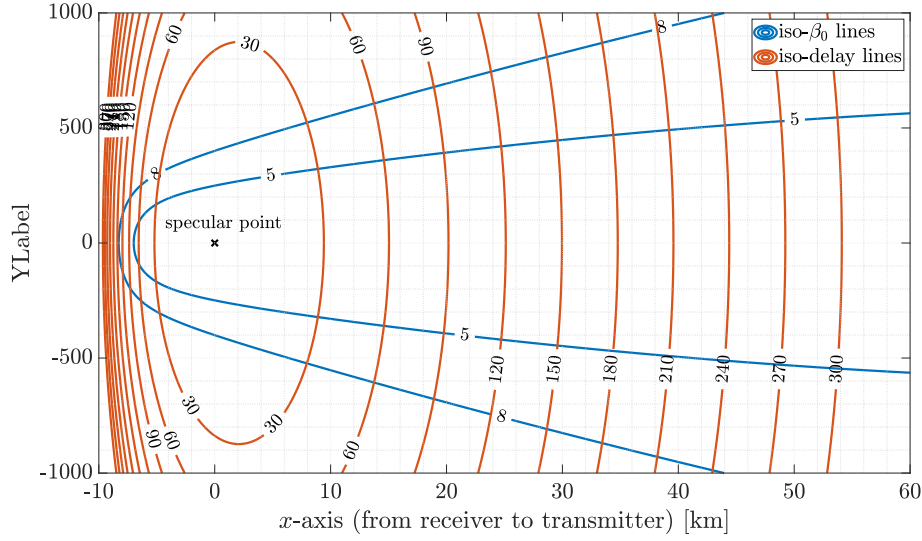


Figure 4.11: Mallorca experiment centered on the specular point with iso- β_0 and iso-delay lines.

4.3.2 Signal Model

In this study, a transmitter T is emitting a band-limited signal $s(t)$ with bandwidth B , over a carrier frequency f_c . This band-limited signal can be expressed as follows,

$$s(t) = \sum_{n=N'_1}^{N'_2} s\left(\frac{n}{F_s}\right) \text{sinc}\left(\pi F_s \left(t - \frac{n}{F_s}\right)\right) \quad (4.18)$$

$$\Leftrightarrow \text{FT}\{s(t)\}(f) \triangleq S(f) = \frac{1}{F_s} \sum_{n=N'_1}^{N'_2} s\left(\frac{n}{F_s}\right) e^{-j2\pi n \frac{f}{F_s}}, \quad -\frac{B}{2} \leq f \leq \frac{B}{2}, \quad (4.19)$$

where $\text{sinc}(\cdot)$ is the sine cardinal function, f the frequency, $F_s \geq B$ is the sampling frequency, N'_1, N'_2 are in \mathbb{Z} with $N'_1 < N'_2$ and \Leftrightarrow refers to the time-frequency pair. The signal travels from T to a reflecting surface and then to the receiver R . An illustration of this scenario is presented in Figure 4.12.

Let S be the specular point of the reflecting surface, the transmitter T and S have motions assumed linear and uniform during the duration of observations T_I so that the positions can be described as $\mathbf{p}_{T/S}(t) = \mathbf{p}_{T/S} + \mathbf{v}_{T/S} \cdot t$ where \mathbf{p} and \mathbf{v} are the position and velocity vectors, respectively, and t is the time variable. With this assumption, the distance between T and S is classically approximated by a first order distance-velocity model [Ric03],

$$\|\mathbf{p}_{TS}(t)\|^2 \triangleq \|\mathbf{p}_S(t) - \mathbf{p}_T(t - \tilde{\tau}(t))\|^2 = c\tilde{\tau} \approx d + vt \quad (4.20)$$

$$\tilde{\tau}(t) \approx \tau_S + bt, \quad \tau_S = \frac{d}{c}, \quad b = \frac{v}{c}, \quad (4.21)$$

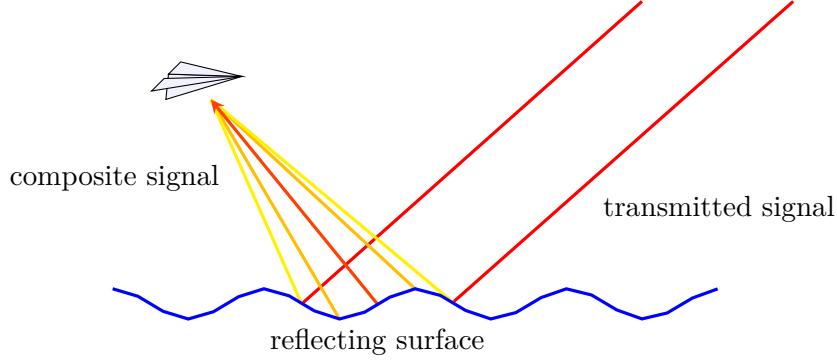


Figure 4.12: Illustration of the diffuse reflection.

where d is the absolute distance between T and S at instant $t = 0$, v is the radial velocity between T and S , τ is the time delay due to the propagation path, $(1 - b)$ is the dilatation induced by the Doppler effect and c is the speed of light in vacuum. From (4.21), the complex analytic signal at the point S can be written as,

$$x_S(t) = \rho_S e^{j\tilde{\phi}_S} s((1 - b_S)(t - \tau_S)) e^{j\omega_c(1-b_S)(t-\tau_S)}, \quad (4.22)$$

where $\omega_c = 2\pi f_c$, $\boldsymbol{\eta}_S^T = (\tau_S, b_S)$, ρ_S and $\tilde{\phi}_S$, the amplitude (strictly positive) and the phase of the complex coefficient induced by propagation characteristics (fading, scintillation, etc). A simplification of the model can be obtained with the narrowband hypothesis [Ric03]. If one considers that the product $B \cdot T_I$ (where T_I is also called the coherent integration time for the considered observation model) is smaller than the inverse Doppler term c/v , then the Doppler effect on the baseband signal $s(t)$ can be neglected: $s((1 - b)(t - \tau)) \approx s(t - \tau)$ [Van01b, ch.9]. The complex analytic signal at the point S is then written as (with $\phi_S = \tilde{\phi}_S - \omega_c(1 + b_S)\tau_S$),

$$x_S(t) \approx x(t) e^{j\omega_c t} = \left(\rho_S e^{j\phi_S} s(t - \tau_S) e^{-j\omega_c b_S(t-\tau_S)} \right) e^{j\omega_c t}. \quad (4.23)$$

The reflecting surface is a complex object that distorts the signal $x_S(t)$, and that can be characterized by its impulse response $h(t)$, as illustrated in Figure 4.13.

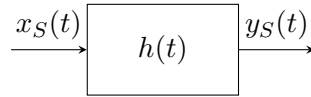


Figure 4.13: Equivalent block diagram of the reflecting surface.

The output of such a reflection, expressed at the specular point S , is the convolution product $(*)$ between the input and $h(t)$,

$$y_S(t) = h(t) * x_S(t). \quad (4.24)$$

Similarly to [ZH16], the impulse response is modeled as a series of echoes regularly separated by a fixed time interval which is the sampling period $T_s = 1/F_s$ (which simply results from the

Fourier Series of the surface frequency transfer function). Consequently, the impulse response can be written as a sum of delayed and attenuated Dirac functions,

$$h(t) = \sum_{p=1}^P \tilde{\rho}_p e^{j\tilde{\phi}_p} \delta(t - (p-1)T_s), \quad (4.25)$$

where P is the number of consecutive echoes in the impulse response of the reflecting surface. The resulting signal expressed at the receiver R after the reflection is then written as follows,

$$y_R(t) = \sum_{p=1}^P \tilde{\rho}_p e^{j\tilde{\phi}_p} d(t - (p-1)T_s; \boldsymbol{\eta}, \rho, \phi) e^{j\omega_c(t - (p-1)T_s)} \quad (4.26)$$

$$= \left(\sum_{p=1}^P \rho_p e^{j\phi_p} s_p(t; \boldsymbol{\eta}) \right) e^{j\omega_c t}, \quad (4.27)$$

with $\boldsymbol{\eta} = [\tau, b]^T$, τ is the sum of the time delay due to the propagation from T to S and the one due to the propagation from S to R , b is the resulting Doppler stretch after the reflection, $\rho_p \triangleq \rho \tilde{\rho}_p$ and $\phi_p \triangleq \phi + \tilde{\phi}_p - \omega_c(p-1)T_s$, $\rho e^{j\phi}$ being the complex amplitude associated to the transmission from T to R via a perfect specular reflection in S , and with $\tau_p = \tau + (p-1)T_s$ yielding,

$$s_p(t; \boldsymbol{\eta}) \triangleq s(t - \tau_p) e^{-j\omega_c b(t - \tau_p)}. \quad (4.28)$$

The baseband signal sampled at sampling frequency F_s containing the reflected signal is then given by,

$$y(t) = y_R(t) e^{-j\omega_c t} = \sum_{p=1}^P d_p(t; \boldsymbol{\eta}, \rho_p, \phi_p) + w(t), \quad (4.29)$$

$$d_p(t; \boldsymbol{\eta}, \rho_p, \phi_p) \triangleq \rho_p e^{j\phi_p} s_p(t; \boldsymbol{\eta}), \quad (4.30)$$

where $w(t)$ is a zero-mean additive complex Gaussian noise with variance σ_n^2 . Now if one considers the acquisition of $N = N_2 - N_1 + 1$ ($N_1 \ll N'_1$, $N_2 \gg N'_2$) samples at a sampling frequency F_s , the resulting discrete signal appears as a CSM, as introduced in Section 1.2,

$$\mathbf{y} = \mathbf{A}_P(\boldsymbol{\eta})\boldsymbol{\alpha} + \mathbf{w}, \quad \mathbf{w} \sim \mathcal{CN}(0, \sigma_n^2 \mathbf{I}_N), \quad (4.31)$$

with, for $n \in [N_1, N_2]$ and $p \in [1, P]$,

$$\begin{aligned} \mathbf{y}^T &= (\dots, y(nT_s), \dots), \\ \mathbf{A}_P(\boldsymbol{\eta}) &= [\dots, \mathbf{s}_p(\boldsymbol{\eta}), \dots], \\ \mathbf{s}_p(\boldsymbol{\eta})^T &= (\dots, s(nT_s - \tau_p) e^{-j\omega_c b(nT_s - \tau_p)}, \dots), \\ \boldsymbol{\alpha}^T &\triangleq (\dots, \alpha_p, \dots) = (\dots, \rho_p e^{j\phi_p}, \dots), \\ \mathbf{w}^T &= (\dots, w(nT_s), \dots). \end{aligned}$$

4.3.3 Compact CRB for the Joint Delay-Doppler Estimation with a Discrete Impulse Response

4.3.3.1 Evaluation of the Fisher Information Matrix

The purpose of this section is to present a new compact CRB for the estimation of the parameters of the CSM (4.31). These parameters can be presented under the form of a vector $\boldsymbol{\epsilon}^T \triangleq (\sigma_n^2, \bar{\boldsymbol{\epsilon}}^T)$ with $\bar{\boldsymbol{\epsilon}}^T \triangleq (\boldsymbol{\eta}^T, \alpha_1^r, \alpha_1^i, \dots, \alpha_P^r, \alpha_P^i)$ with, for $p \in [1, P]$, $\alpha_p = \alpha_p^r + j\alpha_p^i$. From its expression in (4.31) and from the assumption of a zero-mean complex Gaussian white noise, the distribution of the sampled received signal is also Gaussian: $\mathbf{y} \sim \mathcal{CN}(\mathbf{A}_P(\boldsymbol{\eta})\boldsymbol{\alpha}, \sigma_n^2 \mathbf{I}_N)$ and one can apply the Slepian-Bangs formula [YB92] to evaluate the FIM, which is defined as the inverse of the CRB,

$$\mathbf{CRB}_{\boldsymbol{\epsilon}|\boldsymbol{\epsilon}} \triangleq \left(\mathbf{F}_{\boldsymbol{\epsilon}|\boldsymbol{\epsilon}} \right)^{-1}, \quad (4.32)$$

and,

$$\left[\mathbf{F}_{\boldsymbol{\epsilon}|\boldsymbol{\epsilon}} \right]_{k,l} \triangleq F_{\epsilon_k, \epsilon_l | \boldsymbol{\epsilon}} = \frac{2}{\sigma_n^2} \operatorname{Re} \left\{ \left(\frac{\partial \mathbf{A}_P(\boldsymbol{\eta})\boldsymbol{\alpha}}{\partial \epsilon_k} \right)^H \left(\frac{\partial \mathbf{A}_P(\boldsymbol{\eta})\boldsymbol{\alpha}}{\partial \epsilon_l} \right) \right\} + \frac{N}{\sigma_n^4} \frac{\partial \sigma_n^2}{\partial \epsilon_k} \frac{\partial \sigma_n^2}{\partial \epsilon_l}, \quad (4.33)$$

where k and l denotes the row and column index. The noise variance being independent from the other parameters [Ott93], the FIM is simply,

$$\mathbf{F}_{\boldsymbol{\epsilon}|\boldsymbol{\epsilon}} = \begin{bmatrix} F_{\sigma_n^2|\boldsymbol{\epsilon}} & \mathbf{0}_{1,2P+2} \\ \mathbf{0}_{2P+2,1} & \mathbf{F}_{\bar{\boldsymbol{\epsilon}}|\boldsymbol{\epsilon}} \end{bmatrix}, \quad (4.34)$$

where $F_{\sigma_n^2|\boldsymbol{\epsilon}} = N/\sigma_n^4$, which is a known result, and $\mathbf{F}_{\bar{\boldsymbol{\epsilon}}|\boldsymbol{\epsilon}}$ is the FIM for the estimation of the delay-Doppler along with the P echoes of the discrete impulse response. This FIM can be written as follows,

$$\mathbf{F}_{\bar{\boldsymbol{\epsilon}}|\boldsymbol{\epsilon}}(\boldsymbol{\epsilon}) = \frac{2F_s}{\sigma_n^2} \operatorname{Re} \left\{ \mathbf{Q}\mathbf{W}^\delta \mathbf{Q}^H \right\}, \quad (4.35)$$

with \mathbf{Q} defined in (F.3) and \mathbf{W}^δ defined as,

$$\mathbf{W}^\delta \triangleq \begin{bmatrix} \mathbf{W}_1^\delta & \mathbf{W}_2^{\delta H} & \mathbf{W}_3^{\delta H} \\ \mathbf{W}_2^\delta & \mathbf{W}_{2,2}^\delta & \mathbf{W}_4^{\delta H} \\ \mathbf{W}_3^\delta & \mathbf{W}_4^\delta & \mathbf{W}_{3,3}^\delta \end{bmatrix}, \quad (4.36)$$

where the different components are $P \times P$ hermitian matrices computed through the baseband signal samples, for p the row index and q the column index in $[1, P]$,

$$\begin{aligned} \left[\mathbf{W}_1^\delta \right]_{p,q} &= \frac{1}{F_s} \mathbf{s}^H \mathbf{V}^{\Delta,0} (p-q) \mathbf{s}, & \left[\mathbf{W}_2^\delta \right]_{p,q} &= \frac{1}{F_s^2} \mathbf{s}^H \mathbf{V}^{\Delta,0} (p-q) \mathbf{D} \mathbf{s}, \\ \left[\mathbf{W}_3^\delta \right]_{p,q} &= \mathbf{s}^H \mathbf{V}^{\Delta,1} (p-q) \mathbf{s}, & \left[\mathbf{W}_4^\delta \right]_{p,q} &= \frac{1}{F_s} \mathbf{s}^H \mathbf{D} \mathbf{V}^{\Delta,1} (p-q) \mathbf{s}, \\ \left[\mathbf{W}_{2,2}^\delta \right]_{p,q} &= \mathbf{s}^H \mathbf{D} \mathbf{V}^{\Delta,0} (p-q) \mathbf{D} \mathbf{s}, & \left[\mathbf{W}_{3,3}^\delta \right]_{p,q} &= F_s \mathbf{s}^H \mathbf{V}^{\Delta,2} (p-q), \end{aligned} \quad (4.37)$$

with \mathbf{s} the baseband sample vector defined in (F.26), \mathbf{D} in (F.29), $\mathbf{V}^{\Delta,0}(\cdot)$ in (F.30), $\mathbf{V}^{\Delta,1}(\cdot)$ in (F.33) and $\mathbf{V}^{\Delta,2}(\cdot)$ in (F.36).

Proof. see Appendix F.1 □

Remark that an equivalent expression can be found by considering the vector of unknown parameters $\boldsymbol{\zeta}^T \triangleq (\sigma_n^2, \bar{\boldsymbol{\zeta}}^T)$ and $\bar{\boldsymbol{\zeta}}^T \triangleq (\boldsymbol{\eta}^T, \boldsymbol{\rho}^T, \boldsymbol{\phi}^T)$ where for $p \in [1, P]$, $\boldsymbol{\rho}^T = (\dots, \rho_p, \dots)$ and $\boldsymbol{\phi}^T = (\dots, \phi_p, \dots)$. The only change in the computation is in the matrix \mathbf{Q} but the FIM can be written as in (4.35) (see Appendix F.2). For the rest of this work, the vector of unknown parameters may change from $\boldsymbol{\epsilon}$ to $\boldsymbol{\zeta}$ depending on the need.

4.3.3.2 Comparison with Existing Results

The obtained FIM can be compared to existing formulations for similar problems. First, if $P = 1$, then, remarking that $\mathbf{V}^{\Delta,0}(0) = \mathbf{I}_N$,

$$\begin{aligned} W_1^\delta &= \frac{1}{F_s} \mathbf{s}^H \mathbf{s}, \quad W_2^\delta = \frac{1}{F_s^2} \mathbf{s}^H \mathbf{D} \mathbf{s}, \quad W_3^\delta = \mathbf{s}^H \mathbf{V}^{\Delta,1}(0) \mathbf{s}, \\ W_4^\delta &= \frac{1}{F_s} \mathbf{s}^H \mathbf{D} \mathbf{V}^{\Delta,1}(0) \mathbf{s}, \quad W_{2,2}^\delta = \mathbf{s}^H \mathbf{D}^2 \mathbf{s}, \quad W_{3,3}^\delta = F_s \mathbf{s}^H \mathbf{V}^{\Delta,2}(0) \mathbf{s}, \end{aligned} \quad (4.38)$$

and the resulting FIM characterizes the estimation of the joint delay-Doppler and complex amplitude of a signal, for instance, when no multipath is present. This has been studied in [Das20a; Med20] for the GNSS case.

Secondly, if $P = 2$, the resulting FIM represents a two-ray model such as the one studied in Section 2.3. As a reminder, in Chapter 2, the general expression of the dual source CRB was evaluated for the estimation of following vector of unknowns $\boldsymbol{\xi}$ defined as

$$\boldsymbol{\xi}^T = (\sigma_n^2, \tau_1, b_1, \rho_1, \phi_1, \tau_2, b_2, \rho_2, \phi_2), \quad (4.39)$$

where there is no relation between τ_1 and τ_2 , or between b_1 and b_2 . In that case one can evaluate the general expression of this dual source CRB for a range $\Delta\tau = \tau_2 - \tau_1$, known as the path separation, and apply a reparameterization to constrain the general CRB to the model used in the this contribution, that is,

$$\tau_1 = \tau = \tau_2 - \Delta\tau \text{ and } b_1 = b_2 = b. \quad (4.40)$$

Note that when $\Delta\tau = 1/F_s$, the resulting reparameterized FIM should match the FIM evaluated in (4.35) when considering the vector of unknown parameters $\boldsymbol{\zeta}$ as mentioned at the end of Section 4.3.3.1. For $P = 2$, this vector is defined as

$$\boldsymbol{\zeta}^T = (\sigma_n^2, \tau, b, \rho_1, \rho_2, \phi_1, \phi_2), \quad (4.41)$$

With the relations in (4.40), the jacobian corresponding to this reparameterization is,

$$\frac{\partial \boldsymbol{\xi}(\boldsymbol{\zeta})}{\partial \boldsymbol{\zeta}^T} = \begin{bmatrix} \mathbf{e}_1 & \mathbf{e}_2 + \mathbf{e}_6 & \mathbf{e}_3 + \mathbf{e}_7 & \mathbf{e}_4 & \mathbf{e}_8 & \mathbf{e}_5 & \mathbf{e}_9 \end{bmatrix}, \quad (4.42)$$

where \mathbf{e}_i is the 9-element column unitary vector with zeros everywhere except at the i -th index. Then,

$$\mathbf{F}_{\boldsymbol{\zeta}|\boldsymbol{\zeta}}^r(\boldsymbol{\zeta}) = \left(\frac{\partial \boldsymbol{\xi}(\boldsymbol{\zeta})}{\partial \boldsymbol{\zeta}^T} \right)^T \mathbf{F}_{\boldsymbol{\xi}|\boldsymbol{\xi}}(\boldsymbol{\xi}) \frac{\partial \boldsymbol{\xi}(\boldsymbol{\zeta})}{\partial \boldsymbol{\zeta}^T}, \quad (4.43)$$

where $\mathbf{F}_{\boldsymbol{\zeta}|\boldsymbol{\zeta}}^r(\boldsymbol{\zeta})$ is the reparameterized FIM, from the CRB expression derived in Section 2.3 and the relations (4.40). To visually validate the consistency between the reparameterized FIM (4.43) and the work presented in this section, a numerical application is proposed using a simple GNSS signal: the GPS L1 C/A signal. In the sequel, the C/A chip which is about $1\mu\text{s}$ will be used as a time unit. Figure 4.14 presents the τ term of the square root of the inverse of $\mathbf{F}_{\boldsymbol{\zeta}|\boldsymbol{\zeta}}^r$, when $\Delta\tau$ varies, for three values of F_s . The three points at $1/8$, $1/4$ and $1/2$ C/A chips correspond to the τ term of the square root inverse of the FIM defined in (4.35). These points are located on their corresponding curves which demonstrates that the CRB expressions derived in this contribution for $P = 2$ are consistent with the existing expressions when applying the constraints defined in (4.40).

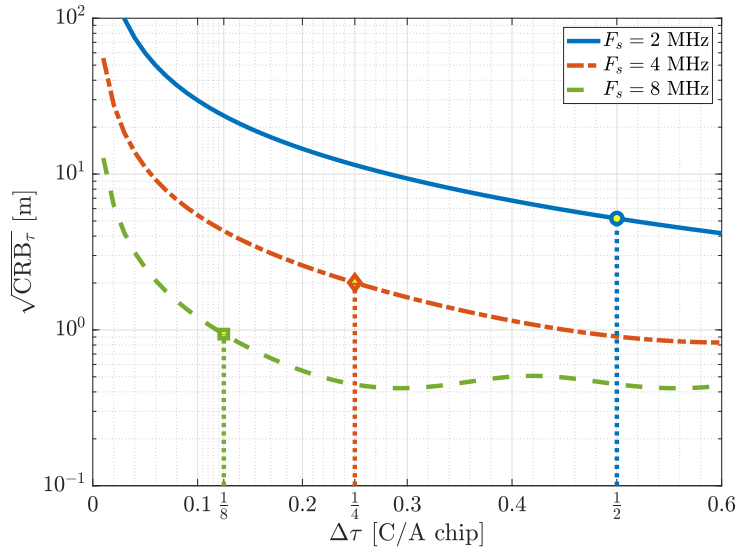


Figure 4.14: Evolution of the constrained CRB obtained after reparameterization of the general dual source CRB for $F_s = \{2, 4, 8\}$ MHz as a function of the path separation $\Delta\tau$ expressed in GPS L1 C/A chips. The three points are the evaluation of the CRB derived in this contribution. This figure was obtained for a GPS L1 C/A signal with a noise level $\text{SNR}_{\text{out}}=33\text{dB}$, amplitudes $\boldsymbol{\rho}^T = (1, 0.5)$ and phases $\boldsymbol{\phi}^T = (0, 0)$. The vertical axis is multiplied by the speed of light to be converted to meters.

Finally, in order to connect this work to other existing CRB expressions as in [ZH16], recall that in this reference, the authors had to use a Taylor approximation to obtain tractable

expressions. Here the expression proposed in (4.35) is easy to handle thanks to its matrix form and it does not rely on any assumption; it only exploits the Shannon-Nyquist theorem on the representation of band-limited signals. As a final comment on the existing expressions proposed in [ZH16], even if the authors proposed a series of simulation in order to compare the CRB derived in this reference with different estimators performance, they were not relevant to validate the correctness of the expressions since the estimator used were not adapted to the signal model, either assuming a single echo whereas many were actually present, or assuming the amplitudes known. The question of the validation of the CRB expression proposed in this contribution beyond existing results, is tackled in the next section where it is compared to the MSE of the MLE that matches the signal model (4.31).

4.3.4 Validation and Discussion

4.3.4.1 Methodology and Considered Scenarios

A way to ensure the validity of the CRB expression derived in Section 4.3.3 is to find an efficient estimator for the signal model under study and to evaluate its MSE. Indeed, an efficient estimator is unbiased and with a MSE equal to the CRB. Unfortunately, such an estimator cannot be found for the nonlinear problem under study, and one can only find an estimator with an asymptotic efficiency, for instance the conditional MLE. The purpose of this section is first to present an implementation of the MLE, and then to apply it to two scenarios in order to obtain an estimate of the MSE, and compare it to the corresponding CRB. In short, if the MLE MSE fits with the CRB, this implies that the derived expression is correct.

The two scenarios considered for this validation are presented in Figure 4.15a and Figure 4.15b under the form of amplitude-delay-profiles, similarly to multipath power-delay-profiles that can be found in [Kap, Fig. 9.14]. Scenario (a) is a simple set of four consecutive decreasing echoes. Scenario (b) is also a set of four consecutive echoes, but with the second being of amplitude zero.

4.3.4.2 Maximum Likelihood Estimator

The MLE is a common sense estimator, that is, it consists of selecting the parameters that are the most likely with respect to the samples available. Knowing the probability density function of the signal (4.31),

$$p(\mathbf{y}; \boldsymbol{\epsilon}) = \frac{1}{(\pi\sigma_n^2)^N} e^{-\frac{1}{\sigma_n^2} \|\mathbf{y} - \mathbf{A}_P \boldsymbol{\alpha}\|^2}, \quad (4.44)$$

maximizing (4.44) is equivalent to minimizing the norm in the exponential function, which can be split into two orthogonal terms with the introduction of the projector over the space

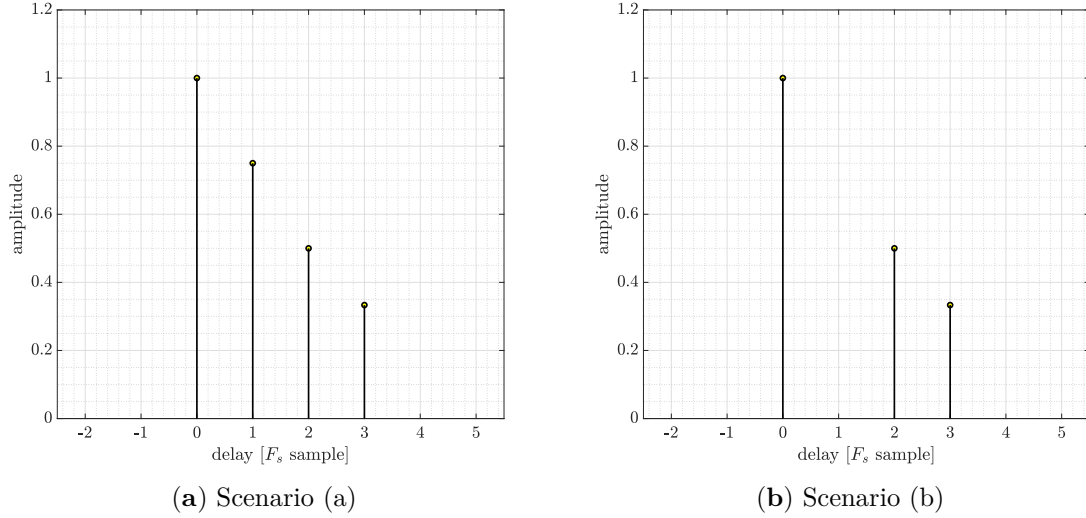


Figure 4.15: Amplitude-delay-profiles of the scenarios considered. It consists of **(a)** a set of four consecutive echoes with $\boldsymbol{\rho}_1^T = (1, 3/4, 1/2, 1/3)$ for scenario (a) and **(b)** $\boldsymbol{\rho}_2^T = (1, 0, 1/2, 1/3)$ for scenario (b). For these scenarios, the sampling frequency is set to $F_s = 4$ MHz.

formed by the columns of the matrix \mathbf{A}_P : $\mathbf{P}_{\mathbf{A}_P} = \mathbf{A}_P (\mathbf{A}_P^H \mathbf{A}_P)^{-1} \mathbf{A}_P^H$, $\mathbf{P}_{\mathbf{A}_P}^\perp = \mathbf{I} - \mathbf{P}_{\mathbf{A}_P}$.

$$\begin{aligned} \|\mathbf{y} - \mathbf{A}_P \boldsymbol{\alpha}\|^2 &= \|\mathbf{P}_{\mathbf{A}_P} (\mathbf{y} - \mathbf{A}_P \boldsymbol{\alpha})\|^2 + \|\mathbf{P}_{\mathbf{A}_P}^\perp (\mathbf{y} - \mathbf{A}_P \boldsymbol{\alpha})\|^2 \\ &= \left\| \mathbf{A}_P \left((\mathbf{A}_P^H \mathbf{A}_P)^{-1} \mathbf{A}_P^H \mathbf{y} - \boldsymbol{\alpha} \right) \right\|^2 + \|\mathbf{P}_{\mathbf{A}_P}^\perp \mathbf{y}\|^2. \end{aligned} \quad (4.45)$$

From the decomposition (4.45), the expression of the estimated vector $\hat{\boldsymbol{\epsilon}}$ is simplified; the estimation of the delay-Doppler vector $\hat{\boldsymbol{\eta}}$ is decoupled from the estimation of the complex amplitudes,

$$\hat{\boldsymbol{\eta}} = \arg \max_{\boldsymbol{\eta}} \left\| \mathbf{P}_{\mathbf{A}_P(\boldsymbol{\eta})} \mathbf{y} \right\|^2, \quad \hat{\alpha}_p = \left[\left(\mathbf{A}_P^H(\hat{\boldsymbol{\eta}}) \mathbf{A}_P(\hat{\boldsymbol{\eta}}) \right)^{-1} \mathbf{A}_P^H(\hat{\boldsymbol{\eta}}) \mathbf{y} \right]_p, \quad (4.46)$$

$$\hat{\alpha}_p^r = \text{Re}\{\hat{\alpha}_p\}, \quad \hat{\alpha}_p^i = \text{Im}\{\hat{\alpha}_p\}, \quad \hat{\rho}_p = |\hat{\alpha}_p|, \quad \hat{\phi}_p^i = \arg\{\hat{\alpha}_p\}, \quad (4.47)$$

$$\hat{\sigma}_n^2 = \frac{1}{N} \left\| \mathbf{P}_{\mathbf{A}_P(\hat{\boldsymbol{\eta}})}^\perp \mathbf{y} \right\|^2. \quad (4.48)$$

For the rest of this section, the MLE of an impulse response, parameterized by the number of pulses P and the regular interval between each pulse $\Delta\tau_p$, will be denoted IR-MLE($P, \Delta\tau_p$). In this work, the input of the estimator is the number of consecutive sources to estimate P , which is assumed to be known in this section, each sources being separated by T_s as it is presented in the signal model (4.31), that is, the implemented estimator will be IR-MLE(P, T_s).

4.3.4.3 Numerical Results

The following figures show the root CRB and the root MSE (RMSE) of the MLE for 1000 Monte Carlo realizations, as a function of the SNR at the output of the matched filter. The deterministic parameters are set as follows: $\tau = 0$, $F_d = bf_c = 200$ Hz, α depends on the scenario under consideration (see Figure 4.15a and 4.15b for the amplitudes), the phase of the echoes, ϕ , is a set of four random phases. The SNR_{out} is defined with respect to the first echo ρ_1 ,

$$\text{SNR}_{\text{out}} \triangleq \frac{\rho_1^2 \mathbf{s}^H \mathbf{s}}{\sigma_n^2}. \quad (4.49)$$

For all the simulations, a GPS L1 C/A signal, coherently integrated for $T_I = 1$ ms at a sampling frequency $F_s = 4$ MHz was considered.

Scenario (a) For this first scenario, the true values of the phases were randomly fixed to $\phi_1^T = (334^\circ, 37^\circ, 114^\circ, 355^\circ)$. Figure 4.16a and Figure 4.16b present the RMSE for the estimation of the delay τ and the Doppler frequency F_d of the IR-MLE(4, T_s). In Figure 4.16a, one can observe the threshold region (where the RMSE reaches the root CRB) at $\text{SNR}_{\text{out}} = 27$ dB. For the Doppler frequency, its RMSE is equal to the corresponding bounds for the range of SNR_{out} considered here. Figure 4.16c presents the RMSE for the four echoes complex amplitudes estimations along with their corresponding bounds. From this figure, one can see that the RMSE follows the root CRB, which validates the proposed CRB expression.

Scenario (b) In this second scenario, the true values of the phases are set to $\phi_2^T = (45^\circ, \text{N/A}, 184^\circ, 328^\circ)$, the second phase being not applicable because the second amplitude is equal to 0. Figure 4.17a and Figure 4.17b correspond to the RMSE of the IR-MLE(4, T_s) for the estimation of the delay and Doppler frequency. For both parameters the RMSE does reach the root CRB, which, again, is in accordance with theory. Figure 4.17c, presents the RMSE for the estimation of the four amplitudes. In this figure, one can see a good fit of the RMSE on the corresponding CRB.

4.3.5 Wrap-Up on Impulse Response Estimation

The strong distortion induced by diffuse scattering of a signal can be modeled as a convolution between the transmitted signal and the impulse response of the reflecting surface. This impulse response is band-limited and its coefficients can be estimated using a MLE. A closed form expression of the CRB has been derived and validated using the asymptotic properties of the MLE. So far, the number of pulses that describe the impulse response was assumed known. However this number is often unknown and can vary in time. Next section provides elements to tackle the question of number of pulses determination.

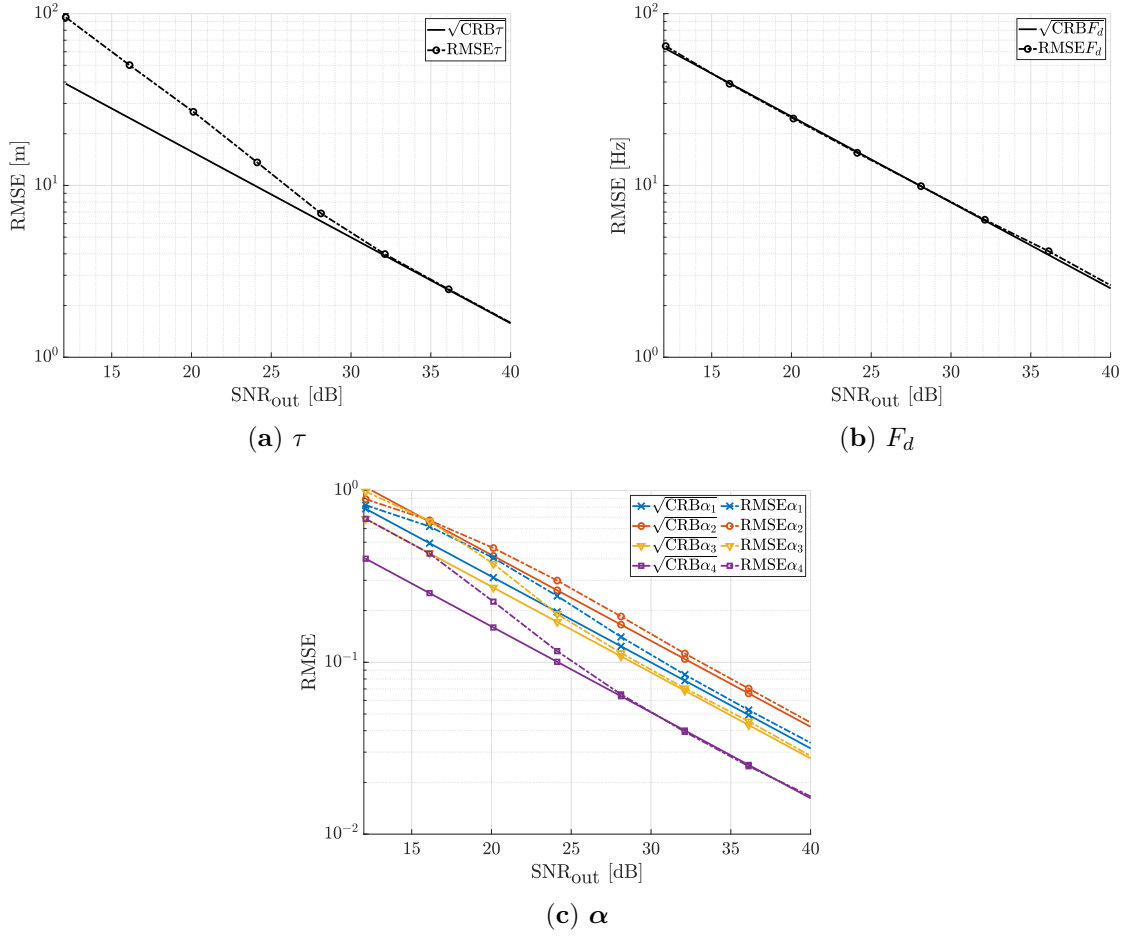


Figure 4.16: Scenario (a): RMSE for the estimation of the parameters with IR-MLE(4, T_s).

4.4 Impulse Response Size Determination: A Detection Problem

In this section the question of determining the number of pulses that describe the reflecting surface impulse response introduced in the signal model (4.31) is addressed. First, a theoretical analysis of the impact of under- and overestimating the number of pulses is proposed. This study suggests two different strategies to determine the number of pulses. These strategies are then further developed.

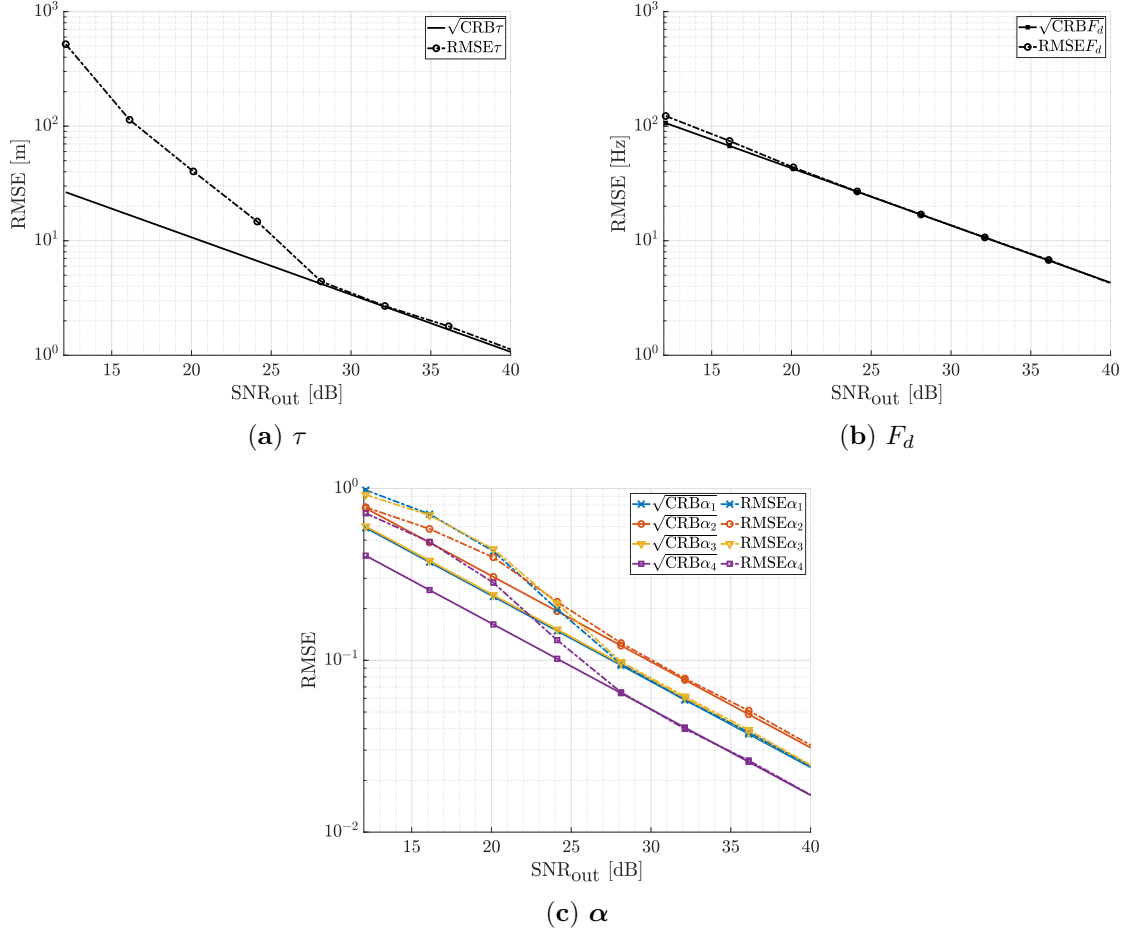


Figure 4.17: Scenario (b): RMSE for the estimation of the parameters with IR-MLE(4, T_s).

4.4.1 Theoretical Analysis

Let $h(t)$ be a band-limited causal impulse response with a finite number of pulses P . This impulse response can be written as,

$$h(t) = \sum_{p=1}^P \alpha_p \delta(t - (p-1)T_s) + \sum_{q=1}^{\infty} \alpha_{P+q} \delta(t - (P+q-1)T_s), \quad \begin{cases} \alpha_1 \neq 0 \\ \alpha_P \neq 0 \\ \alpha_{P+q} = 0 \end{cases}, \quad (4.50)$$

and its corresponding transfer function,

$$H(f) = \sum_{p=1}^P \alpha_p e^{-j2\pi f(p-1)T_s} + \sum_{q=1}^{\infty} \alpha_{P+q} e^{-j2\pi f(P+q-1)T_s} = \sum_{p=1}^P \alpha_p e^{-j2\pi f(p-1)T_s}, \quad (4.51)$$

which is fully described with the samples $\boldsymbol{\alpha}^T = (\alpha_1, \dots, \alpha_P)$. One can then distinguish:

- the intermediate zero coefficients, $\alpha_p = 0$, $2 \leq p \leq P-1$ which are part of the transfer

function definition,

- the trailing zero coefficients, $\alpha_{P+q} = 0$, $1 \leq q$ which are not part of the transfer function.

In order to better understand the impact of under- and overshooting, the global MSE of the impulse response is considered.

$$\text{MSE}_H \triangleq E \left\{ \frac{1}{F_s} \int_{-\frac{F_s}{2}}^{\frac{F_s}{2}} |H(f) - \hat{H}(f)|^2 df \right\} = E \left\{ \frac{1}{F_s} \int_{-\infty}^{\infty} |h(t) - \hat{h}(t)|^2 dt \right\} \quad (4.52)$$

Three cases can be thought of to evaluate (4.52).

- Undershooting case:

$$\hat{H}(f) = \sum_{q=1}^{P-\Delta P} \hat{\alpha}_q e^{-j2\pi f(q-1)T_s}, \quad 1 \leq \Delta P \leq P-1, \quad (4.53)$$

In this case, it can be shown that

$$\text{MSE}_H = \sum_{p=1}^{P-\Delta P} E \left\{ |\alpha_p - \hat{\alpha}_p|^2 \right\} + \sum_{q=P-\Delta P+1}^P |\alpha_q|^2, \quad (4.54)$$

This is a case of misspecification which has been studied in [For17; RH15] and in Section 2.5. In misspecified cases, the MSE does not tend to zero because of the second term of (4.54). Besides the estimates are also affected and biased.

- Overshooting case:

$$\hat{H}(f) = \sum_{q=1}^{P+\Delta P} \hat{\alpha}_q e^{-j2\pi f(q-1)T_s}, \quad 1 \leq \Delta P, \quad (4.55)$$

Again, it can be shown that

$$\text{MSE}_H = \underbrace{\sum_{p=1}^P E \left\{ |\alpha_p - \hat{\alpha}_p|^2 \right\}}_{\text{asymptotically: } Tr\{\text{CRB}_{\alpha|\epsilon}\}} + \sum_{q=P+1}^{P+\Delta P} E \left\{ |0 - \hat{\alpha}_q|^2 \right\}, \quad (4.56)$$

Here the case is correctly specified but the estimation of the trailing zero coefficients is detrimental for two reasons

- the estimation of the trailing zero coefficients degrade the CRB for α_p , $1 \leq p \leq P$ because increasing the number of unknown parameters increases the CRB [MCL12].
- the estimation of the trailing zero coefficients increases the MSE_H through the second term of (4.56).

However the MSE_H converges to 0.

- Correct length case:

$$\hat{H}(f) = \sum_{q=1}^P \hat{\alpha}_q e^{-j2\pi f(q-1)T_s}, \quad \Delta P \geq 1. \quad (4.57)$$

This case corresponds to the overshooting case (4.56) with $\Delta P = 0$:

$$\text{MSE}_H = \underbrace{\sum_{p=1}^P E \left\{ |\alpha_p - \hat{\alpha}_p|^2 \right\}}_{\text{asymptotically: } Tr\{\text{CRB}_{\alpha|\epsilon}\}}. \quad (4.58)$$

Details on the previous results can be found in G.1

From this analysis, the best estimation strategy seems to be by overshooting rather than undershooting since the MSE asymptotically reduces to 0. The ideal case being having the correct impulse response length, for which the MSE_H has no additional term and the corresponding CRB is minimal.

For these reasons, test mechanisms could be thought of to either iteratively estimate the impulse response with a growing number of pulses, that is by undershooting, or to estimate it with an excessive number of pulses, or overshooting, and then evaluate the relevance of each one of the estimates, in order to see if they carry information or if they are just noise.

In the next two sections two families of procedures are presented to tackle the issue of an unknown number of pulses. The first category is iterative: it assumes a number of estimated pulses and tests if there is another pulse in the residue. The second proposed category is based on first overshooting the number of pulses, and then test how likely each estimated pulse is to be part of the impulse response.

4.4.2 Iterative Procedure: $P + \text{next Test}$

This first category of test assumes that P consecutive pulses have already been estimated. Then, the procedure proposed hereafter tests if there is a signal in the residual noise that results from the difference between the received signal and the estimated impulse response convolved with a clean replica. In $P + \text{next}$, the test controls the next candidate, that is, $P + 1$ whose time location is constrained at T_s after the current estimated impulse response. This test is then a simple evaluation of the likelihood that there is another source at time $\hat{\tau} + (P + 1)T_s$,

$$T_{P+\text{next}} = \left| \left(\mathbf{P}_{\mathbf{A}_P(\hat{\boldsymbol{\eta}})}^\perp \mathbf{y} \right)^H \mathbf{s}_{P+1}(\hat{\boldsymbol{\eta}}) \right|^2 \geq \text{threshold } h. \quad (4.59)$$

Under the null hypothesis H_0 , there is no sources except the P sources already detected. Under the alternative hypothesis H_1 , there is an extra source at $P + 1$. Consequently, under H_0 , the orthogonal projection of the data vector over the noise subspace, $\mathbf{P}_{\mathbf{A}_P(\hat{\boldsymbol{\eta}})}^\perp \mathbf{y}$, is simply

noise. However, $\mathbf{s}_{P+1}(\hat{\boldsymbol{\eta}})$ being a deterministic series of 1 and -1 of average 0 very close to the P previous signals, the test statistic $T_{P+\text{next}}$ is a combination of complex Gaussian random variables that are *dependent*. It results that this dependency reduces the variance of the orthogonal projection of \mathbf{s}_{P+1} over the space of the P previous pulses, defined by \mathbf{A}_P . This variance is decreased by a coefficient k_σ that depends on the distance between each pulse (fixed by F_s) and the number of pulses already estimated. See G.2 for more details to evaluate this coefficient. With k_σ evaluated, it is possible to normalize the test statistic $T_{P+\text{next}}$ to obtain a χ_2^2 distribution,

$$\left(\mathbf{P}_{\mathbf{A}_P(\hat{\boldsymbol{\eta}})}^\perp \mathbf{y}\right)^H \mathbf{s}_{P+1}(\hat{\boldsymbol{\eta}}) \xrightarrow{H_0} \left(\mathbf{P}_{\mathbf{A}_P(\hat{\boldsymbol{\eta}})}^\perp \mathbf{n}\right)^H \mathbf{s}_{P+1}(\hat{\boldsymbol{\eta}}) \sim \mathcal{CN}(0, Nk_\sigma\sigma_n^2) \quad (4.60)$$

$$\frac{2}{Nk_\sigma\sigma_n^2} T_{P+\text{next}} \sim \chi_2^2. \quad (4.61)$$

From this, one can fix the PFA and determine the corresponding threshold h of this test,

$$\text{PFA} = P \left[\frac{2}{Nk_\sigma\sigma_n^2} T_{P+\text{next}} > h \mid H_0 \right] = 1 - \left(1 - e^{-h/2}\right) \Leftrightarrow h = -2 \log(\text{PFA}). \quad (4.62)$$

If the test statistic is smaller than this threshold, the user will decide that there is no signal at the next time location with a given PFA. This first test is quite simple, however, it has a few limitations: i) it focuses on one single time location, that is, if there is no energy at the next three time locations but there is one at the fourth (this is the case of intermediate zeros coefficient mentioned in Section 4.4.1), the user might not be able to see it, ii) if the threshold is reached, there is a possibility that the detected item is actually further, and iii) even if the test itself is simple, the overall procedure results quite time consuming because one has to re-evaluate the IR-MLE with an increasing number of sources, which can be quite large.

4.4.3 Overshoot-and-Decimate Procedures

As mentioned in the previous section, iterative approaches to determine the number of sources are known to be time consuming: the user would potentially need to run consecutive and increasingly complex estimators until reaching a satisfying number of pulses. An alternative approach is to deliberately overestimate the number of sources and try to differentiate the estimated pulses to see whether they are actual pulses or simply trailing zero coefficients. The idea is to fix a maximum number of pulses M and to apply a IR-MLE(M, T_s) for M pulses. Suppose now that there are only K actual pulses among the M estimated ones, it was shown in Section 4.4.1 and [CM08] that asymptotically, the K true values are among the M estimates. Consequently, one only needs to test each of the M pulses and discard the least relevant with an appropriate criterion.

4.4.3.1 Overshooting Example

First, the aim is to highlight the presence of the true values in the output of the overshooting IR-MLE(M, T_s). Figure 4.18 presents the output of the IR-MLE(M, T_s) looking for $M = 6$ pulses for the two scenarios presented in Figure 4.15a and 4.15b where $K = 4$. These figures were obtained by running 1000 Monte Carlo simulations and estimating systematically 6 pulses, the SNR_{out} as defined in (4.49) was set to 39dB. The estimated amplitudes located at their estimated delay are plotted. In these figures, one can see that for any scenario, the estimator spots the true pulses among a number of lower amplitude estimates. It then sounds reasonable to think that an adequate test on the estimated vector would filter out the non-relevant estimates.

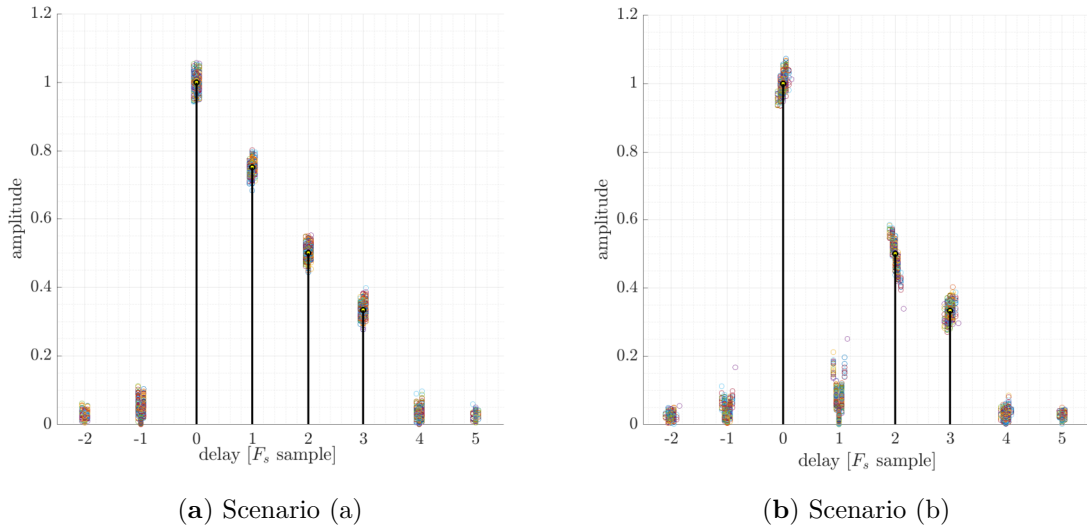


Figure 4.18: Output of the misspecified IR-MLE(M, T_s) ($M = 6$) : (a) Scenario (a) and (b) Scenario (b), $K = 4$.

4.4.3.2 Chung and Mecklenbräuker Test

In order to test the relevance of each estimate with the resulting vector of estimated parameters: $\hat{\zeta}_M = [\hat{\tau}, \hat{F}_d, \hat{\rho}_M^T, \hat{\phi}_M^T]^T$, one may consider the following hypothesis to be tested, as done in [CM08],

- H_m : the m -th pulse is null: $\rho_m = 0 \rightarrow \mathbf{y} = \sum_{p=1, p \neq m}^M \rho_p e^{j\phi_p} \mathbf{s}_p + \mathbf{n}$
- A_m : the m -th pulse is not null: $\rho_m \neq 0 \rightarrow \mathbf{y} = \sum_{p=1}^M \rho_p e^{j\phi_p} \mathbf{s}_p + \mathbf{n}$

Consequently, one can think of a likelihood ratio (LR) that would compare both hypoth-

esis,

$$\text{LR}_m = \frac{\|\mathbf{P}_{\mathbf{A}_M}^\perp \mathbf{y}\|^2}{\|\mathbf{P}_{\mathbf{A}_{M-1,m}}^\perp \mathbf{y}\|^2} \geq \text{threshold } h, \quad (4.63)$$

where $\mathbf{A}_{M-1,m} = \mathbf{A}_{M-1,m}(\hat{\boldsymbol{\eta}})$ denotes the matrix $\mathbf{A}_M = \mathbf{A}_M(\hat{\boldsymbol{\eta}})$ without the m -th column. It can be shown that, under the null hypothesis H_m , LR has a β distribution with shape parameters 1 and $N - 1$. See G.3 for more details on the distribution derivation.

Consequently, from the cumulative distribution function of a β distribution, one can link the threshold h to a given PFA,

$$\text{PFA} = P[\text{LR} > h \mid \text{LR} \sim \beta_{1,N-1}] = 1 - \frac{B_h(1, N-1)}{B(1, N-1)} = (1-h)^{N-1} \Leftrightarrow h = 1 - \text{PFA}^{\frac{1}{N-1}} \quad (4.64)$$

where B is the beta function and B_h is the incomplete beta function.

4.4.3.3 Variant: Sorted Amplitudes Decimation

An intuitive extension of the Chung and Mecklenbräuker test is to order the vector of estimated pulses according to their corresponding amplitudes $\tilde{\rho}$, where $\tilde{\rho}_1 < \tilde{\rho}_2 < \dots < \tilde{\rho}_M$. The idea is then to test each consecutive pulse from the weakest to the strongest. If the m -th is tested and tagged non-relevant, it is then removed from the vector of amplitudes $\tilde{\rho}$. Consequently, as long as the pulses are removed, it is always the first element of the vector whose relevance is tested and the size of the projector $\mathbf{P}_{\mathbf{A}}$ is reduced. The test stops whenever there is a pulse that is considered relevant because this one is strong enough to be an actual pulse. Because the test is going from the weakest to the strongest pulse, this implies that the remaining ones will be relevant as well. This might be interesting to limit the number of tests done.

4.4.4 Wrap-Up on Impulse Response Size Determination

The question of determining the number of received pulses is a detection problem that can be tackled following two strategies. A first strategy consists of undershooting the true number, and iteratively increment this number to find the correct value. This strategy exposes the user to obtain intermediate biased estimates, since the undershooting model used is misspecified. It can also be quite long if the number of sources is very large. The second strategy overshoots the number of sources, and potentially filters out the least relevant estimates that are unlikely part of the impulse response. This approach provides unbiased estimates in the asymptotic regime, and requires only one iteration, for this reason, this last approach seems more adapted to the problem at hand.

4.5 Conclusion

In this last chapter, the nature of the reflection has been called into question. In previous chapters, the reflection was always assumed to be coherent and specular. This assumption held for the considered scenarios (urban environment, ground-based stations, reflections over a pond), but when the surface roughness cannot be neglected anymore, the reflection slowly turns non-coherent, as predicted by the Rayleigh criterion.

In a first approach, the coherence of the reflection was investigated at the carrier phase level: based on the IEEC Mallorca experiment data sets, the transition from a coherent to a non-coherent reflection was observed, and hypothesis tests were proposed to automatically detect this transition. The proposed tests, namely the Simple Difference test and the Lilliefors test, showed results in accordance to the expectation. A further step down this road would be to test them on many other tracks, and on different surfaces. This could help detecting in-land water bodies or frozen land in future GNSS-R missions.

Then, a diffuse reflection was considered. Depending on the surface roughness, the area that may reflect energy towards the receiver can be very large. As an illustration, this area, also known as glistening zone, was computed for the Mallorca experiment example. Results show that the receiver may receive a composite signal from points at tens of kilometers from the specular point, then the received signal in the case of diffuse reflections cannot be modeled as a simple ray anymore. A way to describe it is to see it as the convolution of the simple ray transmitted signal, and the reflecting surface impulse response. The impulse response carries the information of the surface roughness, and by estimating its coefficients, it would be possible to know the sea state just by looking at the composite signal. To this adapted signal model, the corresponding CRB was derived in a closed form expression and validated using the MLE.

The question of the impulse response size determination was then addressed, since it is an unknown to be estimated. Determining the number of pulses that describe the impulse response is a detection problem that can be tackled with hypothesis tests in two different ways: the first is by underestimating the number of pulses and iteratively increment it until finding the correct number. The main drawback of this approach is that as long as the number is underestimated, the processing will always be misspecified, and the output of the estimator may be biased. Another issue is that the number of iterations can be large if the surface size is large as well. The second approach is by overestimating the number of pulses. In this case, the estimated value will be asymptotically unbiased, although the overall performance in the MSE sense will not be optimal. A possible second step is then to discard the trailing zeros measured and re-run a last MLE with the correct number of pulses, to get an optimal solution.

Conclusion and Perspectives

Conclusion

The main objective of this thesis was to give comprehensive tools to assess the achievable performance of existing and proposed GNSS-R techniques. This was motivated by the recent commissioning of GNSS satellites: GPS Block III and GALILEO, and the interest shown by the ESA in GNSS-R, for instance through the HydroGNSS satellite mission.

For this purpose, an overview of the tools and concepts was proposed in Chapter 1, to provide the fundamental tools of estimation theory with, in particular, the introduction of a theoretical lower bound in the MSE sense, the CRB. Moreover, an introduction to GNSS principles, signals and standard processing techniques was provided to better understand how rich these systems are. The main challenge of GNSS, namely the multipath, was also presented as it is still an open issue for navigation applications, and it shares a number of similarities with ground-based GNSS-R. Finally, the main results in GNSS-R along with existing processing techniques were also presented to give a starting point to this thesis work.

As just mentioned, GNSS multipath presents similarities with ground-based GNSS-R, and it has been widely studied ever since the first GNSS constellation was commissioned. For these reasons, Chapter 2 focused on the multipath problem and how the estimation theory tools can serve to assess the multipath effect on the ranging performance. It started with the comparison of different multipath mitigation strategies using the MPEE, a widely used first order metric, and showed how the CRB for the signal model at hand can add information on the multipath effect. A closed form expression of the CRB for the dual source signal model was derived and validated using the asymptotic performance of the MLE. Such lower bounds were then used to build a second order metric, called CCB, that indicates how much a single multipath affects the achievable performance of an efficient estimator in terms of MSE. Such insight completes the information provided by the MPEE. Finally, since low-cost receivers are not equipped with multipath mitigating architectures, it was worth looking at the effect of multipath on the MSE for misspecified estimators, that is, for estimators that do not take into account the potential presence of multipath. This last study led to the derivation of the MCRB for multipath scenarios, and provided a better understanding of the multipath effect on both bias and variance of the final range estimate.

In Chapter 3, ground-based GNSS-R was studied based on the results obtained for multipath. This chapter was supported by a Gruissan data campaign organized by the CNES. First, this campaign along with the recorded data sets was presented, in order to give a framework for the rest of the chapter. Then, one of the main challenges in ground-based GNSS-R, namely signal crosstalk, was studied based on the CRB for the dual source signal model derived in the previous chapter. This crosstalk study showed that two scenarios may occur in ground-based GNSS-R. First, there is a crosstalk that cannot be avoided (e.g., for GNSS

legacy signals such as GPS L1 C/A, or for very low altitude and/or elevation angles): in this first case the path separation is very short, and a possible solution is to exploit this shortness to approximate optimal but computationally expensive algorithms such as the 2S-MLE. For this scenario, the AMLE algorithm was proposed to deal with a very short path separation using a third order Taylor approximation. Such algorithm presents good performance in simulations, and seems a promising multipath mitigation strategy. In a second scenario, there is a crosstalk but sub-optimal dual source algorithms are able to reduce or even cancel its effect. This is the case for wideband signals such as GPS L5 and GALILEO E5 signals. This was demonstrated on the Gruissan data set using a CRE. Based on a theoretical study of the crosstalk effect, in this chapter, dual antenna unbiased GNSS-R altimetry was proved to be doable thanks to recent GNSS signals.

So far, the reflection was assumed coherent and specular. This may apply to a range of ground-based scenarios but it is generally not true when the elevation angle gets larger and when the reflecting surface is rough. In Chapter 4, the transition from coherent to non-coherent reflections was investigated by looking at time series of estimated carrier phase. The coherence of the reflection can be linked to the regularity of this time series and, using hypothesis tests on either this regularity or the Gaussianity of the measured points, coherence indicators were proposed and tested on Mallorca data sets. Part of this work was done in collaboration with the IEEC. Finally, when the reflection is non-coherent and diffuse as it is the case for rough surfaces at large enough elevation angle, the reflected energy comes from an extended reflecting surface called glistening surface and the reflected signal, result of the convolution between the transmitted signal and the impulse response of the reflecting surface, can be significantly distorted. A signal model, adapted to this convolution product was then proposed, and a closed form expression of the corresponding CRB was derived and validated based on the asymptotic properties of the MLE. With this proposed model raised the question of the determination of the number of pulses that define the impulse response. This detection problem was addressed first theoretically and then from a more practical perspective, with two proposed strategies to converge to the correct number of pulses: i) underestimation and iterative increase of the number of pulses, and ii) overestimation and decimation of the least relevant estimates.

Perspectives

The work presented in this thesis can naturally be branched out. Some of the more promising ideas are detailed hereafter.

Regarding the multipath impact analysis, the last contribution presented in the thesis was based on the theory of misspecified estimation. In that perspective, the MCRB obtained in this work seemed to be the good way to characterize most of the receivers. This result could be extended to build a comprehensive metric that would extend the information provided by the proposed CCBR. In the case where it is difficult to model the multipath phenomenon, another approach could be to use semiparametric signal models as in [For19]. Such approaches

can then be extended to other misspecified signal models of particular interest for the GNSS community. For instance, in the case of a GNSS signal affected by an interference (e.g., jammer), as proposed in [Ort] (under review, Navigation journal), but also in the case of spoofing. The multipath effect being also the convolution with a channel impulse response, the detection tests developed in the last chapter of this thesis could also be exploited to determine the relevant number of multipath contributors. This would allow to adapt the current multipath mitigation strategies to more complex scenarios, or to develop new multi-source estimation techniques dedicated to such problem.

In this thesis, only CSMs were studied: both the dual source and the impulse response signal models were assuming all the unknown parameters being deterministic. This is an assumption that may be discussed, especially for the impulse response problem where the object to be estimated is random. A natural extension to the work presented in this thesis is to formulate an Unconditional Signal Model (USM), and see how this affects the final estimation performance based on the unconditional CRB and adapted estimators [SN90]. Besides, the prior information on the amplitudes of the impulse response taps could be linked to the surface properties. This can be of great interest to classify different reflecting surfaces based on GNSS-R observations. As a matter of fact, the CNES recently did an airborne data collection campaign over different water surfaces (lakes and sea). The data collected could help to understand how the reflecting surface nature is captured by the corresponding impulse response estimate.

For the ground-based GNSS-R case study, the work presented could be better illustrated with other data sets to cover all possible path separation scenarios and GNSS signals. In particular, the AltBOC modulation (e.g., GALILEO E5 band signal) with its very wide bandwidth is expected to provide precise altimetry products based on the time-delay estimation, then maybe avoiding the problems related to carrier phase-based measurements for non-coherent reflections. In addition, the study of GNSS meta-signals, which are the combination of two GNSS signals at different frequency bands as a single signal [Ort20], could be extended to a dual source context in order to assess the potential performance of such signals for GNSS-R applications.

The proposed approaches focused on time-delay estimation, but another promising technique is to do altimetry based on the carrier phase. This was mentioned in the last chapter as a motivation for the coherence analysis, but directly exploiting these observables may lead to centimeter-level precision on the altimetry product. This is very challenging because the carrier phase estimation needs to solve a phase ambiguity that is non-trivial. In terms of performance bounds, the recent work in [Med20] could be extended to the GNSS-R problem.

Finally, the GNSS Direct Positioning Estimation (DPE), an alternative to the standard two-step approach (i.e., estimation of pseudo-ranges and then PVT solution), that consists of estimating the receiver position directly from the I/Q samples [CG17] could be applied to process all the reflected signals at a time, and this way, to characterize a larger reflecting surface.

Fourier Transform Relations

In order to deal with most of the derivations of this thesis (mostly FIM components), the Fourier transform of a set of functions needs to be evaluated. First, remembering that the signal is band-limited of band $B \leq F_s$, one has,

$$s(t) \Leftrightarrow \text{FT} \{s(t)\} (f) \triangleq S(f) = \left(\frac{1}{F_s} \sum_{n=N_1}^{N_2} s(nT_s) e^{-j2\pi f n T_s} \right) \mathbf{1}_{[-\frac{F_s}{2}, \frac{F_s}{2}]}. \quad (\text{A.1})$$

To tackle the issue that may come from the spectral shift due to the Doppler effect, one simply needs to take F_s large enough so that $\frac{F_s}{2} \geq \frac{B}{2} + f_c \max\{|b_0|, |b_1|, |\Delta b|\}$ ($\Delta b = b_1 - b_0$).

A first expression is a simple application of the frequency shift relation when using the Fourier transform of a signal multiplied by a complex time-varying exponential.

$$s(t) e^{j2\pi f_c b t} \Leftrightarrow \text{FT} \{s(t) e^{j2\pi f_c b t}\} (f) \triangleq S(f - f_c b) \quad (\text{A.2})$$

Let s_0 be defined by $s_0(t; \tau) = s(t - \tau)$, then we have that,

$$(t - \tau) s_0(t; \tau) = t s_0(t; \tau) - \tau s_0(t; \tau), \quad (\text{A.3})$$

and

$$\begin{aligned} (t - \tau) s(t - \tau) &\Leftrightarrow \frac{j}{2\pi} \frac{d}{df} \left(S(f) e^{-j2\pi f \tau} \right) - \tau S(f) e^{-j2\pi f \tau} \\ &\Leftrightarrow \frac{j}{2\pi} \frac{d}{df} (S(f)) e^{-j2\pi f \tau}. \end{aligned} \quad (\text{A.4})$$

Now let s_1 be defined by $s_1(t; b) = s(t) e^{j2\pi f_c b t}$, it is known that

$$t s_1(t; b) \Leftrightarrow \frac{j}{2\pi} \frac{d}{df} \underbrace{(\text{FT} \{s_1(t; b)\} (f))}_{(\text{A.2})} \quad (\text{A.5})$$

therefore

$$t s(t) e^{j2\pi f_c b t} \Leftrightarrow \frac{j}{2\pi} \frac{d}{df} (S(f - f_c b)) \quad (\text{A.6})$$

Similarly

$$t^2 s(t) e^{j2\pi f_c b t} \Leftrightarrow \left(\frac{j}{2\pi}\right)^2 \frac{d^2}{df^2} (S(f - f_c b)). \quad (\text{A.7})$$

Besides, with the superscript ⁽¹⁾ referring to the first time derivative,

$$\begin{aligned} s_1^{(1)}(t; b) &\triangleq \frac{d}{dt}(s_1(t; b)) = s^{(1)}(t) e^{j2\pi f_c b t} + (j2\pi f_c b) s_1(t; b) \\ \Leftrightarrow s^{(1)}(t) e^{j2\pi f_c b t} &= s_1^{(1)}(t; b) - (j2\pi f_c b) s_1(t; b) \end{aligned}$$

Then, knowing the Fourier transform of the k -th time derivative of a function

$$\text{FT} \{s^{(k)}(t)\}(f) = (j2\pi f)^k S(f) \quad (\text{A.8})$$

one directly gets

$$s^{(1)}(t) e^{j2\pi f_c b t} \Leftrightarrow j2\pi (f - f_c b) S(f - f_c b) \quad (\text{A.9})$$

Now, if s_2 is defined as $s_2(t; b) = ts(t) e^{j2\pi f_c b t}$,

$$\begin{aligned} s_2^{(1)}(t; b) &= s_1(t; b) + ts^{(1)}(t) e^{j2\pi f_c b t} + (j2\pi f_c b) s_2(t; b) \\ \Leftrightarrow ts^{(1)}(t) e^{j2\pi f_c b t} &= \underbrace{-s_1(t; b)}_{(\text{A.2})} + \underbrace{s_2^{(1)}(t; b)}_{(\text{A.8})} - (j2\pi f_c b) \underbrace{s_2(t; b)}_{(\text{A.10})} \end{aligned}$$

therefore,

$$ts^{(1)}(t) e^{j2\pi f_c b t} \Leftrightarrow -S(f - f_c b) - (f - f_c b) \frac{d}{df} (S(f - f_c b)) \quad (\text{A.10})$$

Finally, by taking again s_1 as $s_1(t; b) = s(t) e^{j2\pi f_c b t}$,

$$\begin{aligned} s_1^{(2)}(t; b) &= s^{(2)}(t) e^{j2\pi f_c b t} + 2(j2\pi f_c b) s^{(1)}(t) e^{j2\pi f_c b t} + (j2\pi f_c b)^2 s_1(t; b) \\ \Leftrightarrow s^{(2)}(t) e^{j2\pi f_c b t} &= \underbrace{s_1^{(2)}(t; b)}_{(\text{A.8})} - (j4\pi f_c b) \underbrace{s^{(1)}(t) e^{j2\pi f_c b t}}_{(\text{A.9})} + 4\pi^2 (f_c b)^2 \underbrace{s_1(t; b)}_{(\text{A.2})} \end{aligned}$$

one obtains,

$$\begin{aligned} s^{(2)}(t) e^{j2\pi f_c b t} &\Leftrightarrow (j2\pi f)^2 S(f - f_c b) + 8\pi^2 f_c b (f - f_c b) S(f - f_c b) + 4\pi^2 (f_c b)^2 S(f - f_c b) \\ &\Leftrightarrow -4\pi^2 (f - f_c b)^2 S(f - f_c b) \end{aligned} \quad (\text{A.11})$$

Matrices Relations

B.1 Block Matrix inversion Lemma

From [PP12, Sec. 9.1],

$$\begin{bmatrix} \mathbf{A}_{1,1} & \mathbf{A}_{1,2} \\ \mathbf{A}_{2,1} & \mathbf{A}_{2,2} \end{bmatrix}^{-1} = \begin{bmatrix} \mathbf{C}_1^{-1} & -\mathbf{A}_{1,1}^{-1}\mathbf{A}_{1,2}\mathbf{C}_2^{-1} \\ -\mathbf{C}_2^{-1}\mathbf{A}_{2,1}\mathbf{A}_{1,1}^{-1} & \mathbf{C}_2^{-1} \end{bmatrix} \quad (\text{B.1})$$

with

$$\mathbf{C}_1 = \mathbf{A}_{1,1} - \mathbf{A}_{1,2}\mathbf{A}_{2,2}^{-1}\mathbf{A}_{2,1}, \quad (\text{B.2})$$

$$\mathbf{C}_2 = \mathbf{A}_{2,2} - \mathbf{A}_{2,1}\mathbf{A}_{1,1}^{-1}\mathbf{A}_{1,2}. \quad (\text{B.3})$$

B.2 Details on Orthogonal Projectors Upon Subspaces of a Vector Subspace

Let $\mathbf{A}_M = [\dots, \mathbf{a}_m, \dots]$ for $m \in [1, M]$ a full-rank matrix of M vectors. The projector upon the vector subspace defined by the column of \mathbf{A}_M is defined by $\mathbf{P}_{\mathbf{A}_M} = \mathbf{A}_M (\mathbf{A}_M^H \mathbf{A}_M)^{-1} \mathbf{A}_M^H$. Considering $\mathbf{A}_M = [\mathbf{A}_{M-1}, \mathbf{a}_m]$ where \mathbf{A}_{M-1} is the matrix \mathbf{A}_M without the m -th column, the aim of the following developments is to decompose this projector into two projectors: one over \mathbf{A}_{M-1} and the other over \mathbf{a}_m . A first approach is to simply separate the two components:

$$\mathbf{P}_{\mathbf{A}_M} = [\mathbf{A}_{M-1}, \mathbf{a}_m] \left([\mathbf{A}_{M-1}, \mathbf{a}_m]^H [\mathbf{A}_{M-1}, \mathbf{a}_m] \right)^{-1} [\mathbf{A}_{M-1}, \mathbf{a}_m]^H \quad (\text{B.4})$$

Developing the inverse term,

$$\left([\mathbf{A}_{M-1}, \mathbf{a}_m]^H [\mathbf{A}_{M-1}, \mathbf{a}_m] \right)^{-1} = \begin{bmatrix} \mathbf{A}_{M-1}^H \mathbf{A}_{M-1} & \mathbf{A}_{M-1}^H \mathbf{a}_m \\ \mathbf{a}_m^H \mathbf{A}_{M-1} & \mathbf{a}_m^H \mathbf{a}_m \end{bmatrix}^{-1} = \begin{bmatrix} \mathbf{B}_{11} & \mathbf{B}_{12} \\ \mathbf{B}_{21} & \mathbf{B}_{22} \end{bmatrix} \quad (\text{B.5})$$

By resorting to the block matrix inversion lemma (B.1), one gets the submatrices, defined in (B.5):

$$\begin{aligned}
\mathbf{B}_{11} &= \left(\mathbf{A}_{M-1}^H \mathbf{A}_{M-1} - \mathbf{A}_{M-1}^H \mathbf{a}_m \left(\mathbf{a}_m^H \mathbf{a}_m \right)^{-1} \mathbf{a}_m^H \mathbf{A}_{M-1} \right)^{-1} \\
&= \left(\mathbf{A}_{M-1}^H \left(\mathbf{I} - \mathbf{a}_m \left(\mathbf{a}_m^H \mathbf{a}_m \right)^{-1} \mathbf{a}_m^H \right) \mathbf{A}_{M-1} \right)^{-1} \\
&= \left(\mathbf{A}_{M-1}^H \mathbf{P}_{\mathbf{a}_m}^\perp \mathbf{A}_{M-1} \right)^{-1}, \tag{B.6}
\end{aligned}$$

$$\begin{aligned}
\mathbf{B}_{21} &= - \left(\mathbf{a}_m^H \mathbf{a}_m - \mathbf{a}_m^H \mathbf{A}_{M-1} \left(\mathbf{A}_{M-1}^H \mathbf{A}_{M-1} \right)^{-1} \mathbf{A}_{M-1}^H \mathbf{a}_m \right)^{-1} \mathbf{a}_m^H \mathbf{A}_{M-1} \left(\mathbf{A}_{M-1}^H \mathbf{A}_{M-1} \right)^{-1} \\
&= - \left(\mathbf{a}_m^H \left(\mathbf{I} - \mathbf{A}_{M-1} \left(\mathbf{A}_{M-1}^H \mathbf{A}_{M-1} \right)^{-1} \mathbf{A}_{M-1}^H \right) \mathbf{a}_m \right)^{-1} \mathbf{a}_m^H \mathbf{A}_{M-1} \left(\mathbf{A}_{M-1}^H \mathbf{A}_{M-1} \right)^{-1} \\
&= - \left(\mathbf{a}_m^H \mathbf{P}_{\mathbf{A}_{M-1}}^\perp \mathbf{a}_m \right)^{-1} \mathbf{a}_m^H \mathbf{A}_{M-1} \left(\mathbf{A}_{M-1}^H \mathbf{A}_{M-1} \right)^{-1}, \tag{B.7}
\end{aligned}$$

$$\mathbf{B}_{12} = - \left(\mathbf{A}_{M-1}^H \mathbf{A}_{M-1} \right)^{-1} \mathbf{A}_{M-1}^H \mathbf{a}_m \left(\mathbf{a}_m^H \mathbf{a}_m - \mathbf{a}_m^H \mathbf{A}_{M-1} \left(\mathbf{A}_{M-1}^H \mathbf{A}_{M-1} \right)^{-1} \mathbf{A}_{M-1}^H \mathbf{a}_m \right)^{-1}, \tag{B.8}$$

$$\begin{aligned}
\mathbf{B}_{22} &= \left(\mathbf{a}_m^H \mathbf{a}_m - \mathbf{a}_m^H \mathbf{A}_{M-1} \left(\mathbf{A}_{M-1}^H \mathbf{A}_{M-1} \right)^{-1} \mathbf{A}_{M-1}^H \mathbf{a}_m \right)^{-1} \\
&= \left(\mathbf{a}_m^H \left(\mathbf{I} - \mathbf{A}_{M-1} \left(\mathbf{A}_{M-1}^H \mathbf{A}_{M-1} \right)^{-1} \mathbf{A}_{M-1}^H \right) \mathbf{a}_m \right)^{-1} \\
&= \left(\mathbf{a}_m^H \mathbf{P}_{\mathbf{A}_{M-1}}^\perp \mathbf{a}_m \right)^{-1}. \tag{B.9}
\end{aligned}$$

Using the PosDef identity [PP12, eq. (185)] for \mathbf{P} and \mathbf{R} invertible, definite positive matrices and \mathbf{B} :

$$\left(\mathbf{P}^{-1} + \mathbf{B}^H \mathbf{R}^{-1} \mathbf{B} \right)^{-1} \mathbf{B}^H \mathbf{R}^{-1} = \mathbf{P} \mathbf{B}^H \left(\mathbf{B} \mathbf{P} \mathbf{B}^H + \mathbf{R} \right)^{-1} \tag{B.10}$$

$$\Leftrightarrow - \left(\mathbf{P}^{-1} - \mathbf{B}^H \mathbf{R}^{-1} \mathbf{B} \right)^{-1} \mathbf{B}^H \mathbf{R}^{-1} = - \mathbf{P} \mathbf{B}^H \left(\mathbf{R} - \mathbf{B} \mathbf{P} \mathbf{B}^H \right)^{-1}, \tag{B.11}$$

for $\mathbf{P} = \left(\mathbf{A}_{M-1}^H \mathbf{A}_{M-1} \right)^{-1}$, $\mathbf{R} = \mathbf{a}_m^H \mathbf{a}_m$ and $\mathbf{B} = \mathbf{a}_m^H \mathbf{A}_{M-1}$, (B.11) allows to rewrite \mathbf{B}_{12} as:

$$\mathbf{B}_{12} = - \left(\mathbf{A}_{M-1}^H \mathbf{P}_{\mathbf{a}_m}^\perp \mathbf{A}_{M-1} \right)^{-1} \mathbf{A}_{M-1}^H \mathbf{a}_m \left(\mathbf{a}_m^H \mathbf{a}_m \right)^{-1}. \tag{B.12}$$

Hence, the computation goes on,

$$\begin{aligned}
& \left([\mathbf{A}_{M-1}, \mathbf{a}_m]^H [\mathbf{A}_{M-1}, \mathbf{a}_m] \right)^{-1} [\mathbf{A}_{M-1}, \mathbf{a}_m]^H \\
&= \left[\begin{array}{l} \left(\mathbf{A}_{M-1}^H \mathbf{P}_{\mathbf{a}_m}^\perp \mathbf{A}_{M-1} \right)^{-1} \mathbf{A}_{M-1}^H - \left(\mathbf{A}_{M-1}^H \mathbf{P}_{\mathbf{a}_m}^\perp \mathbf{A}_{M-1} \right)^{-1} \mathbf{A}_{M-1}^H \mathbf{a}_m \left(\mathbf{a}_m^H \mathbf{a}_m \right)^{-1} \mathbf{a}_m^H \\ - \left(\mathbf{a}_m^H \mathbf{P}_{\mathbf{A}_{M-1}}^\perp \mathbf{a}_m \right)^{-1} \mathbf{a}_m^H \mathbf{A}_{M-1} \left(\mathbf{A}_{M-1}^H \mathbf{A}_{M-1} \right)^{-1} \mathbf{A}_{M-1}^H + \left(\mathbf{a}_m^H \mathbf{P}_{\mathbf{A}_{M-1}}^\perp \mathbf{a}_m \right)^{-1} \mathbf{a}_m^H \end{array} \right] \tag{B.13}
\end{aligned}$$

and

$$\begin{aligned}\mathbf{P}_{\mathbf{A}_M} &= \mathbf{A}_{M-1} \left(\left(\mathbf{A}_{M-1}^H \mathbf{P}_{\mathbf{a}_m}^\perp \mathbf{A}_{M-1} \right)^{-1} \mathbf{A}_{M-1}^H - \left(\mathbf{A}_{M-1}^H \mathbf{P}_{\mathbf{a}_m}^\perp \mathbf{A}_{M-1} \right)^{-1} \mathbf{A}_{M-1}^H \mathbf{a}_m \left(\mathbf{a}_m^H \mathbf{a}_m \right)^{-1} \mathbf{a}_m^H \right) \\ &\quad + \mathbf{a}_m \left(- \left(\mathbf{a}_m^H \mathbf{P}_{\mathbf{A}_{M-1}}^\perp \mathbf{a}_m \right)^{-1} \mathbf{a}_m^H \mathbf{A}_{M-1} \left(\mathbf{A}_{M-1}^H \mathbf{A}_{M-1} \right)^{-1} \mathbf{A}_{M-1}^H + \left(\mathbf{a}_m^H \mathbf{P}_{\mathbf{A}_{M-1}}^\perp \mathbf{a}_m \right)^{-1} \mathbf{a}_m^H \right),\end{aligned}\tag{B.14}$$

that is, $\mathbf{P}_{\mathbf{A}_M} = \tilde{\mathbf{P}}_{\mathbf{A}_{M-1}} + \tilde{\mathbf{P}}_{\mathbf{a}_m}$ where,

$$\begin{aligned}\tilde{\mathbf{P}}_{\mathbf{A}_{M-1}} &= \mathbf{A}_{M-1} \left(\mathbf{A}_{M-1}^H \mathbf{P}_{\mathbf{a}_m}^\perp \mathbf{A}_{M-1} \right)^{-1} \mathbf{A}_{M-1}^H - \mathbf{A}_{M-1} \left(\mathbf{A}_{M-1}^H \mathbf{P}_{\mathbf{a}_m}^\perp \mathbf{A}_{M-1} \right)^{-1} \mathbf{A}_{M-1}^H \mathbf{a}_m \left(\mathbf{a}_m^H \mathbf{a}_m \right)^{-1} \mathbf{a}_m^H \\ &= \mathbf{A}_{M-1} \left(\mathbf{A}_{M-1}^H \mathbf{P}_{\mathbf{a}_m}^\perp \mathbf{A}_{M-1} \right)^{-1} \mathbf{A}_{M-1}^H \left(\mathbf{I} - \mathbf{a}_m \left(\mathbf{a}_m^H \mathbf{a}_m \right)^{-1} \mathbf{a}_m^H \right) \\ &= \mathbf{A}_{M-1} \left(\mathbf{A}_{M-1}^H \mathbf{P}_{\mathbf{a}_m}^\perp \mathbf{A}_{M-1} \right)^{-1} \mathbf{A}_{M-1}^H \mathbf{P}_{\mathbf{a}_m}^\perp,\end{aligned}\tag{B.15}$$

$$\begin{aligned}\tilde{\mathbf{P}}_{\mathbf{a}_m} &= -\mathbf{a}_m \left(\mathbf{a}_m^H \mathbf{P}_{\mathbf{A}_{M-1}}^\perp \mathbf{a}_m \right)^{-1} \mathbf{a}_m^H \mathbf{A}_{M-1} \left(\mathbf{A}_{M-1}^H \mathbf{A}_{M-1} \right)^{-1} \mathbf{A}_{M-1}^H + \mathbf{a}_m \left(\mathbf{a}_m^H \mathbf{P}_{\mathbf{A}_{M-1}}^\perp \mathbf{a}_m \right)^{-1} \mathbf{a}_m^H \\ &= \mathbf{a}_m \left(\mathbf{a}_m^H \mathbf{P}_{\mathbf{A}_{M-1}}^\perp \mathbf{a}_m \right)^{-1} \mathbf{a}_m^H \left(\mathbf{I} - \mathbf{A}_{M-1} \left(\mathbf{A}_{M-1}^H \mathbf{A}_{M-1} \right)^{-1} \mathbf{A}_{M-1}^H \right) \\ &= \mathbf{a}_m \left(\mathbf{a}_m^H \mathbf{P}_{\mathbf{A}_{M-1}}^\perp \mathbf{a}_m \right)^{-1} \mathbf{a}_m^H \mathbf{P}_{\mathbf{A}_{M-1}}^\perp.\end{aligned}\tag{B.16}$$

This decomposition is not orthogonal, one cannot show that $\tilde{\mathbf{P}}_{\mathbf{A}_{M-1}} \tilde{\mathbf{P}}_{\mathbf{a}_m} = \mathbf{0}$. Here, the aim is to obtain a decomposition including $\mathbf{P}_{\mathbf{A}_{M-1}}$, a first step is to project $\tilde{\mathbf{P}}_{\mathbf{a}_m}$ over this subspace:

$$\begin{aligned}\tilde{\mathbf{P}}_{\mathbf{a}_m} &= \left(\mathbf{P}_{\mathbf{A}_{M-1}} + \mathbf{P}_{\mathbf{A}_{M-1}}^\perp \right) \tilde{\mathbf{P}}_{\mathbf{a}_m} \\ &= \mathbf{P}_{\mathbf{A}_{M-1}} \tilde{\mathbf{P}}_{\mathbf{a}_m} + \mathbf{P}_{\mathbf{A}_{M-1}}^\perp \mathbf{a}_m \left(\mathbf{a}_m^H \mathbf{P}_{\mathbf{A}_{M-1}}^\perp \mathbf{a}_m \right)^{-1} \mathbf{a}_m^H \mathbf{P}_{\mathbf{A}_{M-1}}^\perp \\ &= \mathbf{P}_{\mathbf{A}_{M-1}} \tilde{\mathbf{P}}_{\mathbf{a}_m} + \left(\mathbf{P}_{\mathbf{A}_{M-1}}^\perp \mathbf{a}_m \right) \left(\left(\mathbf{P}_{\mathbf{A}_{M-1}}^\perp \mathbf{a}_m \right)^H \left(\mathbf{P}_{\mathbf{A}_{M-1}}^\perp \mathbf{a}_m \right) \right)^{-1} \left(\mathbf{P}_{\mathbf{A}_{M-1}}^\perp \mathbf{a}_m \right)^H \\ &= \mathbf{P}_{\mathbf{A}_{M-1}} \tilde{\mathbf{P}}_{\mathbf{a}_m} + \mathbf{P}_{\left(\mathbf{P}_{\mathbf{A}_{M-1}}^\perp \mathbf{a}_m \right)}.\end{aligned}\tag{B.17}$$

Hence, $\mathbf{P}_{\left(\mathbf{P}_{\mathbf{A}_{M-1}}^\perp \mathbf{a}_m \right)}$ is orthogonal to the subspace defined by \mathbf{A}_{M-1} , the rest (underbraced in the following expression) should reduce to $\mathbf{P}_{\mathbf{A}_{M-1}}$,

$$\mathbf{P}_{\mathbf{A}_M} = \tilde{\mathbf{P}}_{\mathbf{A}_{M-1}} + \tilde{\mathbf{P}}_{\mathbf{a}_m} = \underbrace{\tilde{\mathbf{P}}_{\mathbf{A}_{M-1}} + \mathbf{P}_{\mathbf{A}_{M-1}} \tilde{\mathbf{P}}_{\mathbf{a}_m}}_{\mathbf{P}_{\mathbf{A}_{M-1}}} + \mathbf{P}_{\left(\mathbf{P}_{\mathbf{A}_{M-1}}^\perp \mathbf{a}_m \right)}.\tag{B.18}$$

One can verify this:

$$\begin{aligned}
& \tilde{\mathbf{P}}_{\mathbf{A}_{M-1}} + \mathbf{P}_{\mathbf{A}_{M-1}} \tilde{\mathbf{P}}_{\mathbf{a}_m} \\
&= \mathbf{A}_{M-1} \left(\left(\mathbf{A}_{M-1}^H \mathbf{P}_{\mathbf{a}_m}^\perp \mathbf{A}_{M-1} \right)^{-1} \mathbf{A}_{M-1}^H \mathbf{P}_{\mathbf{a}_m}^\perp + \underbrace{\left(\mathbf{A}_{M-1}^H \mathbf{A}_{M-1} \right)^{-1} \mathbf{A}_{M-1}^H \mathbf{a}_m \left(\mathbf{a}_m^H \mathbf{P}_{\mathbf{A}_{M-1}}^\perp \mathbf{a}_m \right)^{-1} \mathbf{a}_m^H \mathbf{P}_{\mathbf{A}_{M-1}}^\perp}_{(B.11)} \right) \\
&= \mathbf{A}_{M-1} \left(\left(\mathbf{A}_{M-1}^H \mathbf{P}_{\mathbf{a}_m}^\perp \mathbf{A}_{M-1} \right)^{-1} \mathbf{A}_{M-1}^H \mathbf{P}_{\mathbf{a}_m}^\perp + \underbrace{\left(\mathbf{A}_{M-1}^H \mathbf{P}_{\mathbf{a}_m}^\perp \mathbf{A}_{M-1} \right)^{-1} \mathbf{A}_{M-1}^H \mathbf{a}_m \left(\mathbf{a}_m^H \mathbf{a}_m \right)^{-1} \mathbf{a}_m^H \mathbf{P}_{\mathbf{A}_{M-1}}^\perp}_{(B.11)} \right) \\
&= \mathbf{A}_{M-1} \left(\mathbf{A}_{M-1}^H \mathbf{P}_{\mathbf{a}_m}^\perp \mathbf{A}_{M-1} \right)^{-1} \mathbf{A}_{M-1}^H \underbrace{\left(\mathbf{P}_{\mathbf{a}_m}^\perp + \mathbf{P}_{\mathbf{a}_m} \mathbf{P}_{\mathbf{A}_{M-1}}^\perp \right)}_{(B.19)}. \tag{B.19}
\end{aligned}$$

This last underbraced term can be written as

$$\begin{aligned}
\mathbf{P}_{\mathbf{a}_m}^\perp + \mathbf{P}_{\mathbf{a}_m} \mathbf{P}_{\mathbf{A}_{M-1}}^\perp &= \mathbf{I} - \mathbf{P}_{\mathbf{a}_m} + \mathbf{P}_{\mathbf{a}_m} (\mathbf{I} - \mathbf{P}_{\mathbf{A}_{M-1}}) \\
&= \mathbf{I} - \mathbf{P}_{\mathbf{a}_m} \mathbf{P}_{\mathbf{A}_{M-1}} \\
&= \mathbf{I} - \mathbf{P}_{\mathbf{A}_{M-1}} + \mathbf{P}_{\mathbf{A}_{M-1}} - \mathbf{P}_{\mathbf{a}_m} \mathbf{P}_{\mathbf{A}_{M-1}} \\
&= \mathbf{P}_{\mathbf{A}_{M-1}}^\perp + \mathbf{P}_{\mathbf{a}_m}^\perp \mathbf{P}_{\mathbf{A}_{M-1}}, \tag{B.20}
\end{aligned}$$

which leads to

$$\begin{aligned}
& \tilde{\mathbf{P}}_{\mathbf{A}_{M-1}} + \mathbf{P}_{\mathbf{A}_{M-1}} \tilde{\mathbf{P}}_{\mathbf{a}_m} \\
&= \mathbf{A}_{M-1} \left(\mathbf{A}_{M-1}^H \mathbf{P}_{\mathbf{a}_m}^\perp \mathbf{A}_{M-1} \right)^{-1} \mathbf{A}_{M-1}^H \left(\mathbf{P}_{\mathbf{a}_m}^\perp + \mathbf{P}_{\mathbf{a}_m} \mathbf{P}_{\mathbf{A}_{M-1}}^\perp \right) \\
&= \mathbf{A}_{M-1} \left(\mathbf{A}_{M-1}^H \mathbf{P}_{\mathbf{a}_m}^\perp \mathbf{A}_{M-1} \right)^{-1} \mathbf{A}_{M-1}^H \left(\mathbf{P}_{\mathbf{A}_{M-1}}^\perp + \mathbf{P}_{\mathbf{a}_m}^\perp \mathbf{P}_{\mathbf{A}_{M-1}} \right) \\
&= \mathbf{A}_{M-1} \left(\mathbf{A}_{M-1}^H \mathbf{P}_{\mathbf{a}_m}^\perp \mathbf{A}_{M-1} \right)^{-1} \underbrace{\mathbf{A}_{M-1}^H \mathbf{P}_{\mathbf{A}_{M-1}}^\perp}_{=0} + \mathbf{A}_{M-1} \left(\mathbf{A}_{M-1}^H \mathbf{P}_{\mathbf{a}_m}^\perp \mathbf{A}_{M-1} \right)^{-1} \mathbf{A}_{M-1}^H \mathbf{P}_{\mathbf{a}_m}^\perp \mathbf{P}_{\mathbf{A}_{M-1}} \\
&= \mathbf{A}_{M-1} \left(\mathbf{A}_{M-1}^H \mathbf{P}_{\mathbf{a}_m}^\perp \mathbf{A}_{M-1} \right)^{-1} \mathbf{A}_{M-1}^H \mathbf{P}_{\mathbf{a}_m}^\perp \mathbf{A}_{M-1} \left(\mathbf{A}_{M-1}^H \mathbf{A}_{M-1} \right)^{-1} \mathbf{A}_{M-1}^H \\
&= \mathbf{A}_{M-1} \left(\mathbf{A}_{M-1}^H \mathbf{A}_{M-1} \right)^{-1} \mathbf{A}_{M-1}^H = \mathbf{P}_{\mathbf{A}_{M-1}}. \tag{B.21}
\end{aligned}$$

Finally, one gets the desired orthogonal decomposition,

$$\mathbf{P}_{\mathbf{A}_M} = \mathbf{P}_{\mathbf{A}_{M-1}} + \mathbf{P} \left(\mathbf{P}_{\mathbf{A}_{M-1}}^\perp \mathbf{a}_m \right). \tag{B.22}$$

Details on the Derivation of the Dual Source Model Fisher Information Matrix

C.1 Derivation Based on the Slepian-Bangs Formulas

Hereafter can be found details on the derivation of the FIM (2.23). Given the signal model (2.12), the derivatives of the parameters vector excluding the noise variance σ_n^2 , $\bar{\epsilon}$, can be expressed in a matrix form as

$$\frac{\partial}{\partial \bar{\epsilon}} (\mathbf{d}(t; \boldsymbol{\theta}_0) + \mathbf{d}(t; \boldsymbol{\theta}_1)) = \mathbf{Q}(\bar{\epsilon}) \mathcal{D}(t; \bar{\epsilon}) \mathbf{e}(t; \bar{\epsilon}), \quad (\text{C.1})$$

where

$$\mathbf{Q}(\bar{\epsilon}) = \begin{bmatrix} \mathbf{Q}_0 & \mathbf{0} \\ \mathbf{0} & \mathbf{Q}_1 \end{bmatrix}, \quad \mathbf{Q}_i = \begin{bmatrix} j\rho_i w_c b_i & 0 & -\rho_i \\ 0 & -j\rho_i w_c & 0 \\ 1 & 0 & 0 \\ j\rho_i & 0 & 0 \end{bmatrix}, \quad (\text{C.2})$$

$$\mathcal{D}(t; \bar{\epsilon}) = \begin{bmatrix} s(t - \tau_0) & 0 \\ (t - \tau_0)s(t - \tau_0) & 0 \\ s^{(1)}(t - \tau_0) & 0 \\ 0 & s(t - \tau_1) \\ 0 & (t - \tau_1)s(t - \tau_1) \\ 0 & s^{(1)}(t - \tau_1) \end{bmatrix}, \quad (\text{C.3})$$

$$\mathbf{e}(t; \bar{\epsilon}) = \begin{pmatrix} e^{j\psi_0} e^{-j\omega_c b_0 t} \\ e^{j\psi_1} e^{-j\omega_c b_1 t} \end{pmatrix}, \quad \text{with } \psi_i = \phi_i + \omega_c b_i \tau_i \quad (\text{C.4})$$

Therefore, the derivative of the vector $\mathbf{A}\boldsymbol{\alpha}$ (when $t = nT_s$) with regard to $\bar{\epsilon}$ is

$$\left(\frac{\partial \mathbf{A}\boldsymbol{\alpha}}{\partial \bar{\epsilon}} \right)^T = \mathbf{Q}(\bar{\epsilon}) [\dots, \mathcal{D}(nT_s; \bar{\epsilon}) \mathbf{e}(nT_s; \bar{\epsilon}), \dots]_{N_1 \leq n \leq N_2}. \quad (\text{C.5})$$

From this result one can write that

$$\begin{aligned} & \left(\frac{\partial \mathbf{A}\boldsymbol{\alpha}}{\partial \bar{\boldsymbol{\epsilon}}^T} \right)^H \left(\frac{\partial \mathbf{A}\boldsymbol{\alpha}}{\partial \bar{\boldsymbol{\epsilon}}^T} \right) = \\ & \mathbf{Q}(\bar{\boldsymbol{\epsilon}})^* \left(\sum_{n=N_1}^{N_2} \mathcal{D}(nT_s; \bar{\boldsymbol{\epsilon}})^* (\mathbf{I}_2 + \boldsymbol{\Delta}_\theta(nT_s; \bar{\boldsymbol{\epsilon}})^*) \mathcal{D}(nT_s; \bar{\boldsymbol{\epsilon}})^T \right) \mathbf{Q}(\bar{\boldsymbol{\epsilon}})^T, \end{aligned} \quad (\text{C.6})$$

with $\boldsymbol{\Delta}_\theta$ induced by the difference of delay, Doppler shifts and phase between the two signals,

$$\begin{aligned} \boldsymbol{\Delta}_\theta(nT_s; \bar{\boldsymbol{\epsilon}}) & \triangleq \mathbf{e}(nT_s; \bar{\boldsymbol{\epsilon}}) \mathbf{e}(nT_s; \bar{\boldsymbol{\epsilon}})^H - \mathbf{I}_2 \\ & = \begin{bmatrix} 0 & e^{-j\Delta\psi} e^{j2\pi f_c \Delta b n T_s} \\ e^{j\Delta\psi} e^{-j2\pi f_c \Delta b n T_s} & 0 \end{bmatrix}, \end{aligned} \quad (\text{C.7})$$

with

$$\Delta\psi = \psi_1 - \psi_0 = \Delta\phi + \omega_c(b_1\tau_1 - b_0\tau_0), \quad \Delta b = b_1 - b_0, \quad \Delta\phi = \phi_1 - \phi_0. \quad (\text{C.8})$$

Similarly to [Das19], taking the limit of (C.6) when N'_1 and N'_2 are very large leads to an integral form

$$\begin{aligned} & \lim_{(N_1, N_2) \rightarrow (-\infty, +\infty)} \left(\frac{\partial \mathbf{A}\boldsymbol{\alpha}}{\partial \bar{\boldsymbol{\epsilon}}^T} \right)^H \left(\frac{\partial \mathbf{A}\boldsymbol{\alpha}}{\partial \bar{\boldsymbol{\epsilon}}^T} \right) \\ & = F_s \left(\mathbf{Q}(\bar{\boldsymbol{\epsilon}}) \begin{bmatrix} \mathbf{W}_0 & (\mathbf{W}^\Delta)^H \\ \mathbf{W}^\Delta & \mathbf{W}_1 \end{bmatrix} \mathbf{Q}(\bar{\boldsymbol{\epsilon}})^H \right)^*, \end{aligned} \quad (\text{C.9})$$

where \mathbf{W}_0 and \mathbf{W}_1 are derived and studied in the single source case in [Med20] and [Das20a] and

$$\mathbf{W}^\Delta \triangleq \begin{bmatrix} W_{1,1}^\Delta & W_{1,2}^\Delta & W_{1,3}^\Delta \\ W_{2,1}^\Delta & W_{2,2}^\Delta & W_{2,3}^\Delta \\ W_{3,1}^\Delta & W_{3,2}^\Delta & W_{3,3}^\Delta \end{bmatrix} e^{j\Delta\psi} e^{-j\omega_c \Delta b \tau_0}, \quad (\text{C.10})$$

with

$$W_{1,1}^\Delta = e^{j\omega_c \Delta b \tau_0} \int_{\mathbb{R}} s(t - \tau_1) s(t - \tau_0)^* e^{-j\omega_c \Delta b t} dt, \quad (\text{C.11})$$

$$W_{1,2}^\Delta = e^{j\omega_c \Delta b \tau_0} \int_{\mathbb{R}} (t - \tau_0) s(t - \tau_1) s(t - \tau_0)^* e^{-j\omega_c \Delta b t} dt, \quad (\text{C.12})$$

$$W_{1,3}^\Delta = e^{j\omega_c \Delta b \tau_0} \int_{\mathbb{R}} s(t - \tau_1) s^{(1)}(t - \tau_0)^* e^{-j\omega_c \Delta b t} dt, \quad (\text{C.13})$$

$$W_{2,1}^\Delta = e^{j\omega_c \Delta b \tau_0} \int_{\mathbb{R}} (t - \tau_1) s(t - \tau_1) s(t - \tau_0)^* e^{-j\omega_c \Delta b t} dt, \quad (\text{C.14})$$

$$W_{2,2}^\Delta = e^{j\omega_c \Delta b \tau_0} \int_{\mathbb{R}} (t - \tau_1)(t - \tau_0) s(t - \tau_1) s(t - \tau_0)^* e^{-j\omega_c \Delta b t} dt, \quad (\text{C.15})$$

$$W_{2,3}^\Delta = e^{j\omega_c \Delta b \tau_0} \int_{\mathbb{R}} (t - \tau_1) s(t - \tau_1) s^{(1)}(t - \tau_0)^* e^{-j\omega_c \Delta b t} dt, \quad (\text{C.16})$$

$$W_{3,1}^\Delta = e^{j\omega_c \Delta b \tau_0} \int_{\mathbb{R}} s^{(1)}(t - \tau_1) s(t - \tau_0)^* e^{-j\omega_c \Delta b t} dt, \quad (\text{C.17})$$

$$W_{3,2}^\Delta = e^{j\omega_c \Delta b \tau_0} \int_{\mathbb{R}} (t - \tau_0) s^{(1)}(t - \tau_1) s(t - \tau_0)^* e^{-j\omega_c \Delta b t} dt, \quad (\text{C.18})$$

$$W_{3,3}^\Delta = e^{j\omega_c \Delta b \tau_0} \int_{\mathbb{R}} s^{(1)}(t - \tau_1) s^{(1)}(t - \tau_0)^* e^{-j\omega_c \Delta b t} dt. \quad (\text{C.19})$$

Exploiting the Fourier transform properties over the hermitian product and the relations recalled in Appendix A, one can work these integral expressions as follows:

$$\begin{aligned} W_{1,1}^\Delta &= e^{j\omega_c \Delta b \tau_0} \int_{\mathbb{R}} s(t - \tau_1) s(t - \tau_0)^* e^{-j2\pi f_c \Delta b t} dt = \int_{\mathbb{R}} s(u - \Delta\tau) s(u)^* e^{-j2\pi f_c \Delta b u} du, \\ &= \int_{\mathbb{R}} s(u - \Delta\tau) \underbrace{\left(s(u) e^{j2\pi f_c \Delta b u} \right)^*}_{(\text{A.2})} du = \int_{-\frac{F_s}{2}}^{\frac{F_s}{2}} S(f) e^{-j2\pi f \Delta\tau} S(f - f_c \Delta b)^* df, \end{aligned}$$

and using the sum definition of the Fourier transform (A.1),

$$\begin{aligned} W_{1,1}^\Delta &= \frac{1}{F_s} \int_{-\frac{1}{2}}^{\frac{1}{2}} \left(\mathbf{s}^T \boldsymbol{\nu}(f)^* \right) e^{-j2\pi f \frac{\Delta\tau}{T_s}} \left(\mathbf{s}^H \mathbf{U} \left(\frac{f_c \Delta b}{F_s} \right) \boldsymbol{\nu}(f) \right) df \\ &= \frac{1}{F_s} \mathbf{s}^H \mathbf{U} \left(\frac{f_c \Delta b}{F_s} \right) \mathbf{V}^{\Delta,0} \left(\frac{\Delta\tau}{T_s} \right) \mathbf{s}. \end{aligned} \quad (\text{C.20})$$

Following the same procedure,

$$\begin{aligned}
W_{1,2}^\Delta &= e^{j\omega_c \Delta b \tau_0} \int_{\mathbb{R}} (t - \tau_0) s(t - \tau_1) s(t - \tau_0)^* e^{-j2\pi f_c \Delta b t} dt = \int_{\mathbb{R}} u s(u - \Delta\tau) s(u)^* e^{-j2\pi f_c \Delta b u} du \\
&= \int_{\mathbb{R}} s(u - \Delta\tau) \underbrace{(u s(u) e^{j2\pi f_c \Delta b u})^*}_{(A.6)} du = \int_{-\frac{F_s}{2}}^{\frac{F_s}{2}} S(f) e^{-j2\pi f \Delta\tau} \left(\frac{j}{2\pi} \frac{d}{df} (S(f - f_c \Delta b)) \right)^* df \\
&= \frac{1}{F_s^2} \int_{-\frac{1}{2}}^{\frac{1}{2}} (\mathbf{s}^T \boldsymbol{\nu}(f)^*) e^{-j2\pi f \frac{\Delta\tau}{T_s}} \left(\mathbf{s}^H \mathbf{D} \mathbf{U} \left(\frac{f_c \Delta b}{F_s} \right) \boldsymbol{\nu}(f) \right) df \\
&= \frac{1}{F_s^2} \mathbf{s}^H \mathbf{D} \mathbf{U} \left(\frac{f_c \Delta b}{F_s} \right) \mathbf{V}^{\Delta,0} \left(\frac{\Delta\tau}{T_s} \right) \mathbf{s}, \tag{C.21}
\end{aligned}$$

$$\begin{aligned}
W_{1,3}^\Delta &= e^{j\omega_c \Delta b \tau_0} \int_{\mathbb{R}} s(t - \tau_1) s^{(1)}(t - \tau_0)^* e^{-j2\pi f_c \Delta b t} dt = \int_{\mathbb{R}} s(u - \Delta\tau) s^{(1)}(u)^* e^{-j2\pi f_c \Delta b u} du, \\
&= \int_{\mathbb{R}} s(u - \Delta\tau) \underbrace{(s^{(1)}(u) e^{j2\pi f_c \Delta b u})^*}_{(A.9)} du \\
&= \int_{-\frac{F_s}{2}}^{\frac{F_s}{2}} (S(f) e^{-j2\pi f \Delta\tau}) (j2\pi(f - f_c \Delta b) S(f - f_c \Delta b))^* df \\
&= \frac{1}{F_s} \int_{-\frac{1}{2}}^{\frac{1}{2}} (\mathbf{s}^T \boldsymbol{\nu}(f)^*) e^{-j2\pi f \frac{\Delta\tau}{T_s}} \left(-j2\pi F_s f \mathbf{s}^H \mathbf{U} \left(\frac{f_c \Delta b}{F_s} \right) \boldsymbol{\nu}(f) + j2\pi f_c \Delta b \mathbf{s}^H \mathbf{U} \left(\frac{f_c \Delta b}{F_s} \right) \boldsymbol{\nu}(f) \right) df \\
&= -\mathbf{s}^H \mathbf{U} \left(\frac{f_c \Delta b}{F_s} \right) \mathbf{V}^{\Delta,1} \left(\frac{\Delta\tau}{T_s} \right) \mathbf{s} + \frac{j\omega_c \Delta b}{F_s} \mathbf{s}^H \mathbf{U} \left(\frac{f_c \Delta b}{F_s} \right) \mathbf{V}^{\Delta,0} \left(\frac{\Delta\tau}{T_s} \right) \mathbf{s}, \tag{C.22}
\end{aligned}$$

$$\begin{aligned}
W_{2,1}^\Delta &= e^{j\omega_c \Delta b \tau_0} \int_{\mathbb{R}} (t - \tau_1) s(t - \tau_1) s(t - \tau_0)^* e^{-j2\pi f_c \Delta b t} dt \\
&= \int_{\mathbb{R}} (u - \Delta\tau) s(u - \Delta\tau) s(u)^* e^{-j2\pi f_c \Delta b u} du \\
&= \int_{\mathbb{R}} \underbrace{(u - \Delta\tau) s(u - \Delta\tau)}_{(A.4)} \underbrace{(s(u) e^{j2\pi f_c \Delta b u})^*}_{(A.2)} du \\
&= \int_{-\frac{F_s}{2}}^{\frac{F_s}{2}} \left(\frac{j}{2\pi} \frac{d}{df} (S(f)) e^{-j2\pi f \Delta\tau} \right) S(f - f_c \Delta b)^* df \\
&= \frac{1}{F_s^2} \int_{-\frac{1}{2}}^{\frac{1}{2}} (\mathbf{s}^T \mathbf{D} \boldsymbol{\nu}(f)^*) e^{-j2\pi f \frac{\Delta\tau}{T_s}} \left(\mathbf{s}^H \mathbf{U} \left(\frac{f_c \Delta b}{F_s} \right) \boldsymbol{\nu}(f) \right) df \\
&= \frac{1}{F_s^2} \mathbf{s}^H \mathbf{U} \left(\frac{f_c \Delta b}{F_s} \right) \mathbf{V}^{\Delta,0} \left(\frac{\Delta\tau}{T_s} \right) \mathbf{D} \mathbf{s}, \tag{C.23}
\end{aligned}$$

$$\begin{aligned}
W_{2,2}^{\Delta} &= e^{j\omega_c \Delta b \tau_0} \int_{\mathbb{R}} (t - \tau_1)(t - \tau_0) s(t - \tau_1) s(t - \tau_0)^* e^{-j2\pi f_c \Delta b t} dt \\
&= \int_{\mathbb{R}} u(u - \Delta\tau) s(u - \Delta\tau) s(u)^* e^{-j2\pi f_c \Delta b u} du \\
&= \int_{\mathbb{R}} \underbrace{((u - \Delta\tau) s(u - \Delta\tau))}_{(A.4)} \underbrace{(u s(u) e^{j2\pi f_c \Delta b u})^*}_{(A.6)} du \\
&= \int_{-\frac{F_s}{2}}^{\frac{F_s}{2}} \left(\frac{j}{2\pi} \frac{d}{df} (S(f)) e^{-j2\pi f \Delta\tau} \right) \left(\frac{j}{2\pi} \frac{d}{df} (S(f - f_c \Delta b)) \right)^* df \\
&= \frac{1}{F_s^3} \int_{-\frac{1}{2}}^{\frac{1}{2}} (\mathbf{s}^T \mathbf{D} \boldsymbol{\nu}(f)^*) e^{-j2\pi f \frac{\Delta\tau}{T_s}} \left(\mathbf{s}^H \mathbf{D} \mathbf{U} \left(\frac{f_c \Delta b}{F_s} \right) \boldsymbol{\nu}(f) \right) df \\
&= \frac{1}{F_s^3} \mathbf{s}^H \mathbf{D} \mathbf{U} \left(\frac{f_c \Delta b}{F_s} \right) \mathbf{V}^{\Delta,0} \left(\frac{\Delta\tau}{T_s} \right) \mathbf{D} \mathbf{s}, \tag{C.24}
\end{aligned}$$

$$\begin{aligned}
W_{2,3}^{\Delta} &= e^{j\omega_c \Delta b \tau_0} \int_{\mathbb{R}} (t - \tau_1) s(t - \tau_1) s^{(1)}(t - \tau_0)^* e^{-j2\pi f_c \Delta b t} dt \\
&= \int_{\mathbb{R}} (u - \Delta\tau) s(u - \Delta\tau) s^{(1)}(u)^* e^{-j2\pi f_c \Delta b u} du \\
&= \int_{\mathbb{R}} \underbrace{((u - \Delta\tau) s(u - \Delta\tau))}_{(A.4)} \underbrace{(s^{(1)}(u) e^{j2\pi f_c \Delta b u})^*}_{(A.9)} du \\
&= \int_{-\frac{F_s}{2}}^{\frac{F_s}{2}} \left(\frac{j}{2\pi} \frac{d}{df} (S(f)) e^{-j2\pi f \Delta\tau} \right) (j2\pi(f - f_c \Delta b) S(f - f_c \Delta b))^* df \\
&= \frac{1}{F_s^2} \int_{-\frac{1}{2}}^{\frac{1}{2}} (\mathbf{s}^T \mathbf{D} \boldsymbol{\nu}(f)^*) e^{-j2\pi f \frac{\Delta\tau}{T_s}} \left(-j2\pi F_s f \mathbf{s}^H \mathbf{U} \left(\frac{f_c \Delta b}{F_s} \right) \boldsymbol{\nu}(f) + j2\pi f_c \Delta b \mathbf{s}^H \mathbf{U} \left(\frac{f_c \Delta b}{F_s} \right) \boldsymbol{\nu}(f) \right) df \\
&= -\frac{1}{F_s} \mathbf{s}^H \mathbf{U} \left(\frac{f_c \Delta b}{F_s} \right) \mathbf{V}^{\Delta,1} \left(\frac{\Delta\tau}{T_s} \right) \mathbf{D} \mathbf{s} + \frac{j\omega_c \Delta b}{F_s^2} \mathbf{s}^H \mathbf{U} \left(\frac{f_c \Delta b}{F_s} \right) \mathbf{V}^{\Delta,0} \left(\frac{\Delta\tau}{T_s} \right) \mathbf{D} \mathbf{s}, \tag{C.25}
\end{aligned}$$

$$\begin{aligned}
W_{3,1}^{\Delta} &= e^{j\omega_c \Delta b \tau_0} \int_{\mathbb{R}} s^{(1)}(t - \tau_1) s(t - \tau_0)^* e^{-j2\pi f_c \Delta b t} dt = \int_{\mathbb{R}} s^{(1)}(u - \Delta\tau) s(u)^* e^{-j2\pi f_c \Delta b u} du, \\
&= \int_{\mathbb{R}} s^{(1)}(u - \Delta\tau) \underbrace{(s(u) e^{j2\pi f_c \Delta b u})^*}_{(A.2)} du = \int_{-\frac{F_s}{2}}^{\frac{F_s}{2}} (j2\pi f S(f) e^{-j2\pi f \Delta\tau}) (S(f - f_c \Delta b))^* df \\
&= \int_{-\frac{1}{2}}^{\frac{1}{2}} (j2\pi f \mathbf{s}^T \boldsymbol{\nu}(f)^*) e^{-j2\pi f \frac{\Delta\tau}{T_s}} \left(\mathbf{s}^H \mathbf{U} \left(\frac{f_c \Delta b}{F_s} \right) \boldsymbol{\nu}(f) \right) df \\
&= \mathbf{s}^H \mathbf{U} \left(\frac{f_c \Delta b}{F_s} \right) \mathbf{V}^{\Delta,1} \left(\frac{\Delta\tau}{T_s} \right) \mathbf{s}, \tag{C.26}
\end{aligned}$$

$$\begin{aligned}
W_{3,2}^\Delta &= e^{j\omega_c \Delta b \tau_0} \int_{\mathbb{R}} (t - \tau_0) s^{(1)}(t - \tau_1) s(t - \tau_0)^* e^{-j2\pi f_c \Delta b t} dt \\
&= \int_{\mathbb{R}} s^{(1)}(u - \Delta\tau) s(u)^* e^{-j2\pi f_c \Delta b u} du \\
&= \int_{\mathbb{R}} s^{(1)}(u - \Delta\tau) \underbrace{\left(u s(u) e^{j2\pi f_c \Delta b u} \right)^*}_{(A.6)} du \\
&= \int_{-\frac{F_s}{2}}^{\frac{F_s}{2}} \left(j2\pi f S(f) e^{-j2\pi f \Delta\tau} \right) \left(\frac{j}{2\pi} \frac{d}{df} (S(f - f_c \Delta b)) \right)^* df \\
&= \frac{1}{F_s} \int_{-\frac{1}{2}}^{\frac{1}{2}} \left(j2\pi f \mathbf{s}^T \boldsymbol{\nu}(f)^* \right) e^{-j2\pi f \frac{\Delta\tau}{T_s}} \left(\mathbf{s}^H \mathbf{D}\mathbf{U} \left(\frac{f_c \Delta b}{F_s} \right) \boldsymbol{\nu}(f) \right) df \\
&= \frac{1}{F_s} \mathbf{s}^H \mathbf{D}\mathbf{U} \left(\frac{f_c \Delta b}{F_s} \right) \mathbf{V}^{\Delta,1} \left(\frac{\Delta\tau}{T_s} \right) \mathbf{s}, \tag{C.27}
\end{aligned}$$

$$\begin{aligned}
W_{3,3}^\Delta &= e^{j\omega_c \Delta b \tau_0} \int_{\mathbb{R}} s^{(1)}(t - \tau_1) s^{(1)}(t - \tau_0)^* e^{-j2\pi f_c \Delta b t} dt = \int_{\mathbb{R}} s^{(1)}(u - \Delta\tau) s^{(1)}(u)^* e^{-j2\pi f_c \Delta b u} du, \\
&= \int_{\mathbb{R}} s^{(1)}(u - \Delta\tau) \underbrace{\left(s^{(1)}(u) e^{j2\pi f_c \Delta b u} \right)^*}_{(A.9)} du \\
&= \int_{-\frac{F_s}{2}}^{\frac{F_s}{2}} \left(j2\pi f S(f) e^{-j2\pi f \Delta\tau} \right) (j2\pi(f - f_c \Delta b) S(f - f_c \Delta b))^* df \\
&= \int_{-\frac{1}{2}}^{\frac{1}{2}} \left(j2\pi f \mathbf{s}^T \boldsymbol{\nu}(f)^* \right) e^{-j2\pi f \frac{\Delta\tau}{T_s}} \left(-j2\pi F_s f \mathbf{s}^H \mathbf{U} \left(\frac{f_c \Delta b}{F_s} \right) \boldsymbol{\nu}(f) + j2\pi f_c \Delta b \mathbf{s}^H \mathbf{U} \left(\frac{f_c \Delta b}{F_s} \right) \boldsymbol{\nu}(f) \right) df \\
&= F_s \mathbf{s}^H \mathbf{U} \left(\frac{f_c \Delta b}{F_s} \right) \mathbf{V}^{\Delta,2} \left(\frac{\Delta\tau}{T_s} \right) \mathbf{s} + j\omega_c \Delta b \mathbf{s}^H \mathbf{U} \left(\frac{f_c \Delta b}{F_s} \right) \mathbf{V}^{\Delta,1} \left(\frac{\Delta\tau}{T_s} \right) \mathbf{s}, \tag{C.28}
\end{aligned}$$

where

$$\mathbf{s} = \left(\dots \quad s(nT_s) \quad \dots \right)_{N_1 \leq n \leq N_2}^T, \quad (\text{C.29})$$

$$\boldsymbol{\nu}(f) = \left(\dots \quad e^{j2\pi f n} \quad \dots \right)_{N_1 \leq n \leq N_2}^T, \quad (\text{C.30})$$

$$\mathbf{U}(p) = \text{diag} \left(\dots \quad e^{-j2\pi p n} \quad \dots \right)_{N_1 \leq n \leq N_2}, \quad (\text{C.31})$$

$$\mathbf{D} = \left(\dots \quad n \quad \dots \right)_{N_1 \leq n \leq N_2}^T, \quad (\text{C.32})$$

$$\mathbf{V}^{\Delta,0}(q) = \int_{-\frac{1}{2}}^{\frac{1}{2}} \boldsymbol{\nu}(f) \boldsymbol{\nu}^H(f) e^{-j2\pi f q} \mathrm{d}f, \quad (\text{C.33})$$

$$\begin{aligned} [\mathbf{V}^{\Delta,0}(q)]_{k,l} &= \int_{-\frac{1}{2}}^{\frac{1}{2}} e^{j2\pi f(k-l-q)} \mathrm{d}f = \left[\frac{e^{j2\pi f(k-l-q)}}{j2\pi(k-l-q)} \right]_{-\frac{1}{2}}^{\frac{1}{2}} \\ &= \frac{\sin(\pi(k-l-q))}{\pi(k-l-q)} = \text{sinc}(k-l-q) \end{aligned} \quad (\text{C.34})$$

$$\mathbf{V}^{\Delta,1}(q) = j2\pi \int_{-\frac{1}{2}}^{\frac{1}{2}} f \boldsymbol{\nu}(f) \boldsymbol{\nu}^H(f) e^{-j2\pi f q} \mathrm{d}f, \quad (\text{C.35})$$

$$\begin{aligned} [\mathbf{V}^{\Delta,1}(q)]_{k,l} &= j2\pi \int_{-\frac{1}{2}}^{\frac{1}{2}} f e^{j2\pi f(k-l-q)} \mathrm{d}f \\ &= j2\pi \left(\left[\frac{f e^{j2\pi f(k-l-q)}}{j2\pi(k-l-q)} \right]_{-\frac{1}{2}}^{\frac{1}{2}} - \int_{-\frac{1}{2}}^{\frac{1}{2}} \frac{e^{j2\pi f(k-l-q)}}{j2\pi(k-l-q)} \mathrm{d}f \right) \\ &= \frac{1}{k-l-q} (\cos(\pi(k-l-q)) - \text{sinc}(k-l-q)) \end{aligned} \quad (\text{C.36})$$

$$\mathbf{V}^{\Delta,2}(q) = 4\pi^2 \int_{-\frac{1}{2}}^{\frac{1}{2}} f^2 \boldsymbol{\nu}(f) \boldsymbol{\nu}^H(f) e^{-j2\pi f q} \mathrm{d}f, \quad (\text{C.37})$$

$$\begin{aligned} [\mathbf{V}^{\Delta,2}(q)]_{k,l} &= 4\pi^2 \int_{-\frac{1}{2}}^{\frac{1}{2}} f^2 e^{j2\pi f(k-l-q)} \mathrm{d}f \\ &= 4\pi^2 \left(\left[\frac{f^2 e^{j2\pi f(k-l-q)}}{j2\pi(k-l-q)} \right]_{-\frac{1}{2}}^{\frac{1}{2}} - \int_{-\frac{1}{2}}^{\frac{1}{2}} \frac{2f e^{j2\pi f(k-l-q)}}{j2\pi(k-l-q)} \mathrm{d}f \right) \\ &= \frac{4\pi^2}{j2\pi(k-l-q)} \frac{1}{4} \left[e^{j\pi(k-l-q)} - e^{-j\pi(k-l-q)} \right] \\ &\quad - \frac{8\pi^2}{j2\pi(k-l-q)} \left(\left[\frac{f e^{j2\pi f(k-l-q)}}{j2\pi(k-l-q)} \right]_{-\frac{1}{2}}^{\frac{1}{2}} - \int_{-\frac{1}{2}}^{\frac{1}{2}} \frac{e^{j2\pi f(k-l-q)}}{j2\pi(k-l-q)} \mathrm{d}f \right) \\ &= \pi^2 \text{sinc}(k-l-q) + 2 \frac{\cos(\pi(k-l-q)) - \text{sinc}(k-l-q)}{(k-l-q)^2} \end{aligned} \quad (\text{C.38})$$

C.2 Derivation Based on Orthogonal Projection

From (2.48), and omitting the dependency on $\bar{\boldsymbol{\eta}}_2$ for the sake of clarity, the matrix $\boldsymbol{\Phi}$ is defined using the projector $\mathbf{P}_{\mathbf{A}}$:

$$\begin{aligned} \boldsymbol{\Phi} &= \begin{bmatrix} \frac{\partial \mathbf{a}^H(\boldsymbol{\eta}_0)}{\partial \boldsymbol{\eta}_0} \\ \frac{\partial \mathbf{a}^H(\boldsymbol{\eta}_1)}{\partial \boldsymbol{\eta}_1} \end{bmatrix} \mathbf{P}_{\mathbf{A}}^\perp \begin{bmatrix} \frac{\partial \mathbf{a}^H(\boldsymbol{\eta}_0)}{\partial \boldsymbol{\eta}_0} \\ \frac{\partial \mathbf{a}^H(\boldsymbol{\eta}_1)}{\partial \boldsymbol{\eta}_1} \end{bmatrix}^H \\ &= \underbrace{\begin{bmatrix} \frac{\partial \mathbf{a}^H(\boldsymbol{\eta}_0)}{\partial \boldsymbol{\eta}_0} \\ \frac{\partial \mathbf{a}^H(\boldsymbol{\eta}_1)}{\partial \boldsymbol{\eta}_1} \end{bmatrix}}_{\text{Appendix C.2.1}} \underbrace{\begin{bmatrix} \frac{\partial \mathbf{a}^H(\boldsymbol{\eta}_0)}{\partial \boldsymbol{\eta}_0} \\ \frac{\partial \mathbf{a}^H(\boldsymbol{\eta}_1)}{\partial \boldsymbol{\eta}_1} \end{bmatrix}^H}_{\text{Appendix C.2.1}} - \underbrace{\begin{bmatrix} \frac{\partial \mathbf{a}^H(\boldsymbol{\eta}_0)}{\partial \boldsymbol{\eta}_0} \\ \frac{\partial \mathbf{a}^H(\boldsymbol{\eta}_1)}{\partial \boldsymbol{\eta}_1} \end{bmatrix}}_{\text{Appendix C.2.3}} \underbrace{\left(\mathbf{A}^H \mathbf{A} \right)^{-1}}_{\text{Appendix C.2.2}} \mathbf{A}^H \underbrace{\begin{bmatrix} \frac{\partial \mathbf{a}^H(\boldsymbol{\eta}_0)}{\partial \boldsymbol{\eta}_0} \\ \frac{\partial \mathbf{a}^H(\boldsymbol{\eta}_1)}{\partial \boldsymbol{\eta}_1} \end{bmatrix}^H}_{\text{Appendix C.2.3}}. \end{aligned} \quad (\text{C.39})$$

C.2.1 First Term of (C.39)

Similarly to the approach in C, the derivative of $a(t; \boldsymbol{\eta}_i)$ with regard to the parameters of interest is

$$\frac{\partial a(t; \boldsymbol{\eta}_i)}{\partial \boldsymbol{\eta}_i} = \mathbf{Q}_i \mathcal{D}(t - \tau_i) e^{-j\omega_c b_i(t - \tau_i)} \quad (\text{C.40})$$

where

$$\mathbf{Q}_i = \begin{bmatrix} j\omega_c b_i & 0 & -1 \\ 0 & -j\omega_c & 0 \end{bmatrix}, \mathcal{D}(t) = \begin{pmatrix} s(t) \\ ts(t) \\ s^{(1)}(t) \end{pmatrix}, \quad (\text{C.41})$$

with $s^{(1)}(t) = \frac{ds(t)}{dt}$. Therefore, when $t = nT_s$, one can write

$$\begin{bmatrix} \frac{\partial \mathbf{a}^H(\boldsymbol{\eta}_0)}{\partial \boldsymbol{\eta}_0} \\ \frac{\partial \mathbf{a}^H(\boldsymbol{\eta}_1)}{\partial \boldsymbol{\eta}_1} \end{bmatrix} = \mathbf{Q}^* \left[\dots, \bar{\mathcal{D}}(nT_s; \bar{\boldsymbol{\eta}}_2) \mathbf{e}(nT_s; \bar{\boldsymbol{\eta}}_2), \dots \right]_{N_1 \leq n \leq N_2}^* \quad (\text{C.42})$$

where

$$\mathbf{Q} = \begin{bmatrix} \mathbf{Q}_0 & \mathbf{0} \\ \mathbf{0} & \mathbf{Q}_1 \end{bmatrix}, \bar{\mathcal{D}}(t; \bar{\boldsymbol{\eta}}_2) = \begin{bmatrix} \mathcal{D}(t - \tau_0) & \mathbf{0} \\ \mathbf{0} & \mathcal{D}(t - \tau_1) \end{bmatrix} \quad (\text{C.43})$$

and $\mathbf{e}(t; \bar{\boldsymbol{\eta}}_2) = \begin{pmatrix} e^{-j\omega_c b_0(t - \tau_0)} \\ e^{-j\omega_c b_1(t - \tau_1)} \end{pmatrix}$. From this result one can write that

$$\begin{bmatrix} \frac{\partial \mathbf{a}^H(\boldsymbol{\eta}_0)}{\partial \boldsymbol{\eta}_0} \\ \frac{\partial \mathbf{a}^H(\boldsymbol{\eta}_1)}{\partial \boldsymbol{\eta}_1} \end{bmatrix} \begin{bmatrix} \frac{\partial \mathbf{a}^H(\boldsymbol{\eta}_0)}{\partial \boldsymbol{\eta}_0} \\ \frac{\partial \mathbf{a}^H(\boldsymbol{\eta}_1)}{\partial \boldsymbol{\eta}_1} \end{bmatrix}^H = \left(\mathbf{Q} \left(\sum_{n=N_1}^{N_2} \bar{\mathcal{D}}(nT_s; \bar{\boldsymbol{\eta}}_2) (\mathbf{I}_2 + \boldsymbol{\Delta}_\theta(nT_s; \bar{\boldsymbol{\eta}}_2)) \bar{\mathcal{D}}(nT_s; \bar{\boldsymbol{\eta}}_2)^H \right) \mathbf{Q}^H \right)^* \quad (\text{C.44})$$

with $\boldsymbol{\Delta}_\theta$ induced by the difference of delay, Doppler shifts between the two signals,

$$\boldsymbol{\Delta}_\theta(nT_s; \bar{\boldsymbol{\eta}}_2) \triangleq \mathbf{e}(nT_s; \bar{\boldsymbol{\eta}}_2) \mathbf{e}(nT_s; \bar{\boldsymbol{\eta}}_2)^H - \mathbf{I}_2. \quad (\text{C.45})$$

Then, taking the limit of (C.44) when N_1 and N_2 are very large, it leads to an integral form

$$\lim_{(N_1, N_2) \rightarrow (-\infty, +\infty)} \begin{bmatrix} \frac{\partial \mathbf{a}^H(\boldsymbol{\eta}_0)}{\partial \boldsymbol{\eta}_0} \\ \frac{\partial \mathbf{a}^H(\boldsymbol{\eta}_1)}{\partial \boldsymbol{\eta}_1} \end{bmatrix} \begin{bmatrix} \frac{\partial \mathbf{a}^H(\boldsymbol{\eta}_0)}{\partial \boldsymbol{\eta}_0} \\ \frac{\partial \mathbf{a}^H(\boldsymbol{\eta}_1)}{\partial \boldsymbol{\eta}_1} \end{bmatrix}^H = F_s \left(\mathbf{Q} \begin{bmatrix} (\cdot)_{1,1} & (\cdot)_{1,2} \\ (\cdot)_{2,1} & (\cdot)_{2,2} \end{bmatrix} \mathbf{Q}^H \right)^* \quad (\text{C.46})$$

where $(\cdot)_{1,1} = (\cdot)_{2,2} = \mathbf{W}$ is derived and studied in the single source case in [Med20] and [Das20a] and reminded in (2.26) and $(\cdot)_{2,1} = (\cdot)_{1,2}^H = \mathbf{W}^\Delta$ is derived in the dual source case in C and is defined in (2.28). For the computation of \mathbf{W}^Δ no phase difference in the multiplicative complex exponential (2.28) is considered since it appears in the \mathbf{R}_α matrix defined in (2.47).

C.2.2 Inverse in the Second Term of (C.39)

In a similar way, it is possible to evaluate the matrix $\mathbf{A}^H \mathbf{A}$ as follows:

$$\mathbf{A}^H \mathbf{A} = \begin{bmatrix} a(t; \boldsymbol{\eta}_0)^H a(t; \boldsymbol{\eta}_0) & a(t; \boldsymbol{\eta}_0)^H a(t; \boldsymbol{\eta}_1) \\ a(t; \boldsymbol{\eta}_1)^H a(t; \boldsymbol{\eta}_0) & a(t; \boldsymbol{\eta}_1)^H a(t; \boldsymbol{\eta}_1) \end{bmatrix}, \quad (\text{C.47})$$

and, when $t = nT_s$ and both N_1 and N_2 are very large, it leads to an integral form:

$$\lim_{(N_1, N_2) \rightarrow (-\infty, +\infty)} \mathbf{A}^H \mathbf{A} = F_s \begin{bmatrix} w_1 & (W_{1,1}^\Delta e^{j\omega_c b_1 \Delta \tau})^* \\ W_{1,1}^\Delta e^{j\omega_c b_1 \Delta \tau} & w_1 \end{bmatrix}^*, \quad (\text{C.48})$$

and then,

$$\lim_{(N_1, N_2) \rightarrow (-\infty, +\infty)} (\mathbf{A}^H \mathbf{A})^{-1} = \frac{w_1}{F_s(w_1^2 - |W_{1,1}^\Delta|^2)} \begin{bmatrix} 1 & -\frac{(W_{1,1}^\Delta e^{j\omega_c b_1 \Delta \tau})^*}{w_1} \\ -\frac{W_{1,1}^\Delta e^{j\omega_c b_1 \Delta \tau}}{w_1} & 1 \end{bmatrix}^*. \quad (\text{C.49})$$

C.2.3 Second Term of (C.39)

Again, from (C.42), one can write that

$$\begin{bmatrix} \frac{\partial \mathbf{a}^H(\boldsymbol{\eta}_0)}{\partial \boldsymbol{\eta}_0} \\ \frac{\partial \mathbf{a}^H(\boldsymbol{\eta}_1)}{\partial \boldsymbol{\eta}_1} \end{bmatrix} \mathbf{A} = \mathbf{Q}^* \left(\sum_{n=N_1}^{N_2} \bar{\mathcal{D}}(nT_s; \bar{\boldsymbol{\eta}}_2) (\mathbf{I}_2 + \boldsymbol{\Delta}_\theta(nT_s; \bar{\boldsymbol{\eta}}_2)) \begin{bmatrix} s(nT_s - \tau_0)^* & 0 \\ 0 & s(nT_s - \tau_1)^* \end{bmatrix} \right)^* \quad (\text{C.50})$$

Then, when N_1 and N_2 are very large, it leads to an integral form

$$\lim_{(N_1, N_2) \rightarrow (-\infty, +\infty)} \begin{bmatrix} \frac{\partial \mathbf{a}^H(\boldsymbol{\eta}_0)}{\partial \boldsymbol{\eta}_0} \\ \frac{\partial \mathbf{a}^H(\boldsymbol{\eta}_1)}{\partial \boldsymbol{\eta}_1} \end{bmatrix} \mathbf{A} = F_s \left(\mathbf{Q} \begin{bmatrix} \mathbf{w} & (\mathbf{w}_{1,\cdot}^\Delta)^H \\ \mathbf{w}_{\cdot,1}^\Delta & \mathbf{w} \end{bmatrix} \right)^* \quad (\text{C.51})$$

where \mathbf{w} is the first column of \mathbf{W} recalled in (2.25), $\mathbf{w}_{:,1}^\Delta$ is the first column of \mathbf{W}^Δ recalled in (2.28) and $\mathbf{w}_{1,\cdot}^\Delta$ is the first row of \mathbf{W}^Δ . Then, combining (C.51) with (C.49), the second term of (C.39) can be written:

$$\begin{aligned}
& \begin{bmatrix} \frac{\partial \mathbf{a}^H(\boldsymbol{\eta}_0)}{\partial \boldsymbol{\eta}_0} \\ \frac{\partial \mathbf{a}^H(\boldsymbol{\eta}_1)}{\partial \boldsymbol{\eta}_1} \end{bmatrix} \mathbf{A} (\mathbf{A}^H \mathbf{A})^{-1} \mathbf{A}^H \begin{bmatrix} \frac{\partial \mathbf{a}^H(\boldsymbol{\eta}_0)}{\partial \boldsymbol{\eta}_0} \\ \frac{\partial \mathbf{a}^H(\boldsymbol{\eta}_1)}{\partial \boldsymbol{\eta}_1} \end{bmatrix}^H \\
&= \frac{F_s w_1}{w_1^2 - |W_{1,1}^\Delta|^2} \left(\mathbf{Q} \begin{bmatrix} \mathbf{w} & (\mathbf{w}_{1,\cdot}^\Delta)^H \\ \mathbf{w}_{:,1}^\Delta & \mathbf{w} \end{bmatrix} \right. \\
&\quad \times \begin{bmatrix} 1 & -\frac{(W_{1,1}^\Delta)^*}{w_1} e^{-j\omega_c b_1 \Delta \tau} \\ -\frac{W_{1,1}^\Delta}{w_1} e^{j\omega_c b_1 \Delta \tau} & 1 \end{bmatrix} \\
&\quad \times \left. \begin{bmatrix} \mathbf{w}^H & (\mathbf{w}_{:,1}^\Delta)^H \\ \mathbf{w}_{1,\cdot}^\Delta & \mathbf{w}^H \end{bmatrix} \mathbf{Q}^H \right)^* \\
&= \frac{F_s w_1}{w_1^2 - |W_{1,1}^\Delta|^2} \left(\mathbf{Q} \begin{bmatrix} (\cdot)_{1,1} & (\cdot)_{1,2} \\ (\cdot)_{2,1} & (\cdot)_{2,2} \end{bmatrix} \mathbf{Q}^H \right)^* \tag{C.52}
\end{aligned}$$

with

$$(\cdot)_{1,1} = \mathbf{w} \mathbf{w}^H + (\mathbf{w}_{1,\cdot}^\Delta)^H \mathbf{w}_{1,\cdot}^\Delta - 2\text{Re} \left\{ \mathbf{w} \mathbf{w}_{1,\cdot}^\Delta \left(\frac{W_{1,1}^\Delta}{w_1} e^{j\omega_c b_1 \Delta \tau} \right)^* \right\}, \tag{C.53}$$

$$(\cdot)_{2,1} = (\cdot)_{1,2}^H = \mathbf{w} \mathbf{w}_{1,\cdot}^\Delta + \mathbf{w}_{:,1}^\Delta \mathbf{w}^H - \mathbf{w} \mathbf{w}^H \frac{W_{1,1}^\Delta}{w_1} e^{j\omega_c b_1 \Delta \tau} - \mathbf{w}_{:,1}^\Delta \mathbf{w}_{1,\cdot}^\Delta \left(\frac{W_{1,1}^\Delta}{w_1} e^{j\omega_c b_1 \Delta \tau} \right)^*, \tag{C.54}$$

$$(\cdot)_{2,2} = \mathbf{w} \mathbf{w}^H + \mathbf{w}_{:,1}^\Delta (\mathbf{w}_{:,1}^\Delta)^H - 2\text{Re} \left\{ \mathbf{w}_{:,1}^\Delta \mathbf{w}^H \left(\frac{W_{1,1}^\Delta}{w_1} e^{j\omega_c b_1 \Delta \tau} \right)^* \right\}. \tag{C.55}$$

If one subtracts (C.52) to (C.46), the matrix $\boldsymbol{\Phi}$ is obtained and $\boldsymbol{\Phi}_{i,j}$ with $i, j = \{1, 2\}$ are the corresponding submatrices when only the terms $(\cdot)_{i,j}$ are used in (C.46) and (C.52).

Details on the Derivation of the Misspecified Cramér Rao Bounds

Here are the details on the derivation of the matrix $\mathbf{A}(\boldsymbol{\theta}_{pt})$ defined in (2.84). The term to be derived is

$$(\delta \mathbf{a})^H \left(\frac{\partial^2 \alpha_{pt} \mathbf{a}_{pt}}{\partial \theta_p \partial \theta_q} \right) \quad (\text{D.1})$$

To compute the MCRB, the terms are first considered under their continuous time expression. If $a(t; \boldsymbol{\eta}) = s(t - \tau) e^{-j\omega_c b(t - \tau)}$, then

$$\delta a(t) = \alpha_0 a(t; \boldsymbol{\eta}_0) + \alpha_1 a(t; \boldsymbol{\eta}_1) - \alpha_{pt} a(t; \boldsymbol{\eta}_{pt}) = \tilde{\mathbf{A}}(t) \tilde{\boldsymbol{\alpha}}, \quad (\text{D.2})$$

$$\tilde{\mathbf{A}}(t) = \left[a(t; \boldsymbol{\eta}_0), a(t; \boldsymbol{\eta}_1), a(t; \boldsymbol{\eta}_{pt}) \right], \quad \tilde{\boldsymbol{\alpha}} = \left(\rho_0 e^{j\phi_0}, \rho_1 e^{j\phi_1}, -\rho_{pt} e^{j\phi_{pt}} \right)^T. \quad (\text{D.3})$$

Therefore, the discrete expression of this model mismatch term is

$$\delta \mathbf{a} = \tilde{\mathbf{A}} \tilde{\boldsymbol{\alpha}} = [\mathbf{a}_0, \mathbf{a}_1, \mathbf{a}_{pt}] \tilde{\boldsymbol{\alpha}}. \quad (\text{D.4})$$

Then, keeping the continuous time expression for the computation of the successive derivatives, one can easily obtain the first derivative, which was already used in Appendix C,

$$\frac{\partial \alpha a(t; \boldsymbol{\eta})}{\partial \boldsymbol{\theta}} = \mathbf{Q} \mathcal{D}^{(1)}(t, \tau) e^{-j\omega_c b(t - \tau)} \quad (\text{D.5})$$

with

$$\mathbf{Q} = \begin{bmatrix} j\alpha\omega_c b & 0 & -\alpha \\ 0 & -j\alpha\omega_c & 0 \\ e^{j\phi} & 0 & 0 \\ \alpha & 0 & 0 \end{bmatrix}, \quad \mathcal{D}^{(1)}(t; \tau) = \begin{bmatrix} s(t - \tau) \\ (t - \tau)s(t - \tau) \\ s^{(1)}(t - \tau) \end{bmatrix}. \quad (\text{D.6})$$

Similarly the second derivative can be written in a matrix form as,

$$\frac{\partial^2 \alpha a(t; \boldsymbol{\eta})}{\partial \boldsymbol{\theta} \partial \boldsymbol{\theta}^T} = \begin{bmatrix} \mathbf{Q}_1 & \mathbf{Q}_2 & \mathbf{Q}_3 & \mathbf{Q}_4 \end{bmatrix} \left(\mathcal{D}^{(2)}(t; \boldsymbol{\eta}) \otimes \mathbf{I}_4 \right) e^{-j\omega_c b(t - \tau)}, \quad (\text{D.7})$$

with

$$\mathbf{Q}_1 = \begin{bmatrix} -\alpha\omega_c^2 b^2 & 0 & 0 & -j2\alpha\omega_c b & 0 & \alpha \\ j\alpha\omega_c & \alpha\omega_c^2 b & 0 & 0 & j\alpha\omega_c & 0 \\ je^{j\phi}\omega_c b & 0 & 0 & -e^{j\phi} & 0 & 0 \\ -\alpha\omega_c b & 0 & 0 & -j\alpha & 0 & 0 \end{bmatrix}, \quad (\text{D.8})$$

$$\mathbf{Q}_2 = \begin{bmatrix} j\alpha\omega_c & \alpha\omega_c^2 b & 0 & 0 & j\alpha\omega_c & 0 \\ 0 & 0 & -\alpha\omega_c^2 & 0 & 0 & 0 \\ 0 & -je^{j\phi}\omega_c & 0 & 0 & 0 & 0 \\ 0 & \alpha\omega_c & 0 & 0 & 0 & 0 \end{bmatrix}, \quad (\text{D.9})$$

$$\mathbf{Q}_3 = \begin{bmatrix} je^{j\phi}\omega_c b & 0 & 0 & -e^{j\phi} & 0 & 0 \\ 0 & -je^{j\phi}\omega_c & 0 & 0 & 0 & 0 \\ 0 & 0 & 0 & 0 & 0 & 0 \\ je^{j\phi} & 0 & 0 & 0 & 0 & 0 \end{bmatrix}, \quad (\text{D.10})$$

$$\mathbf{Q}_4 = \begin{bmatrix} -\alpha\omega_c b & 0 & 0 & -j\alpha & 0 & 0 \\ 0 & \alpha\omega_c & 0 & 0 & 0 & 0 \\ je^{j\phi} & 0 & 0 & 0 & 0 & 0 \\ -\alpha & 0 & 0 & 0 & 0 & 0 \end{bmatrix}, \quad (\text{D.11})$$

$$\mathcal{D}^{(2)}(t; \tau) = \begin{bmatrix} s(t - \tau) \\ (t - \tau)s(t - \tau) \\ (t - \tau)^2 s(t - \tau) \\ s^{(1)}(t - \tau) \\ (t - \tau)s^{(1)}(t - \tau) \\ s^{(2)}(t - \tau) \end{bmatrix} \triangleq \begin{bmatrix} d_1(t) \\ d_2(t) \\ d_3(t) \\ d_4(t) \\ d_5(t) \\ d_6(t) \end{bmatrix}. \quad (\text{D.12})$$

A way to write the Hessian matrix components under its discrete form is,

$$\left[\frac{\partial^2 \alpha \mathbf{a}^T}{\partial \boldsymbol{\theta} \partial \boldsymbol{\theta}^T} \right]_{p,q} = \frac{\partial^2 \alpha \mathbf{a}^T}{\partial \theta_p \partial \theta_q} = [\mathbf{Q}_q]_{p,\cdot} \left[\dots, \mathcal{D}^{(2)}(nT_s; \boldsymbol{\eta}) e^{-j\omega_c b(nT_s - \tau)}, \dots \right]_{N_1 \leq n \leq N_2}, \quad (\text{D.13})$$

where $[\mathbf{Q}_q]_{p,\cdot}$ is the p -th row of the matrix \mathbf{Q}_q .

The first term of the information matrix $\mathbf{A}(\boldsymbol{\theta}_{pt})$ is simply the product of the model means difference term and the Hessian matrix, which can be expressed element-wise as

$$\delta \mathbf{a}^H \left[\frac{\partial^2 \alpha \mathbf{a}}{\partial \boldsymbol{\theta} \partial \boldsymbol{\theta}^T} \right]_{p,q} = (\tilde{\mathbf{A}} \tilde{\boldsymbol{\alpha}})^H \left([\mathbf{Q}_q]_{p,\cdot} \left[\dots, \mathcal{D}^{(2)}(nT_s; \boldsymbol{\eta}) e^{-j\omega_c b(nT_s - \tau)}, \dots \right]_{N_1 \leq n \leq N_2} \right)^T \quad (\text{D.14})$$

$$= [\mathbf{Q}_q]_{p,\cdot} \sum_{k \in \{0,1,pt\}} \tilde{\alpha}_k^* \sum_{n=N_1}^{N_2} \begin{pmatrix} a(nT_s; \boldsymbol{\eta}_k)^* d_1(nT_s) e^{-j\omega_c b(nT_s - \tau)} \\ a(nT_s; \boldsymbol{\eta}_k)^* d_2(nT_s) e^{-j\omega_c b(nT_s - \tau)} \\ a(nT_s; \boldsymbol{\eta}_k)^* d_3(nT_s) e^{-j\omega_c b(nT_s - \tau)} \\ a(nT_s; \boldsymbol{\eta}_k)^* d_4(nT_s) e^{-j\omega_c b(nT_s - \tau)} \\ a(nT_s; \boldsymbol{\eta}_k)^* d_5(nT_s) e^{-j\omega_c b(nT_s - \tau)} \\ a(nT_s; \boldsymbol{\eta}_k)^* d_6(nT_s) e^{-j\omega_c b(nT_s - \tau)} \end{pmatrix}. \quad (\text{D.15})$$

Each term of the column vector is then a sum that can be seen as an integral when the number

of samples tends to infinity. For $i \in \{1, 6\}$,

$$\lim_{(N_1, N_2) \rightarrow (-\infty, +\infty)} T_s \sum_{n=N_1}^{N_2} a(nT_s; \boldsymbol{\eta}_k)^* d_i(nT_s) e^{-j\omega_c b(nT_s - \tau)} = \int_{\mathbb{R}} a(t; \boldsymbol{\eta}_k)^* d_i(t) e^{-j\omega_c b(t - \tau)} dt, \quad (\text{D.16})$$

therefore,

$$\lim_{(N_1, N_2) \rightarrow (-\infty, +\infty)} \delta \mathbf{a}^H \left[\frac{\partial^2 \alpha \mathbf{a}}{\partial \boldsymbol{\theta} \partial \boldsymbol{\theta}^T} \right]_{p,q} = F_s [\mathbf{Q}_q]_{p,\cdot} \sum_{k \in \{0, 1, pt\}} \alpha_k^* \mathbf{w}^{\mathbf{A}}(\boldsymbol{\eta}_k). \quad (\text{D.17})$$

Finally, thanks to the Shannon Theorem for band-limited signals, the computation of the matrix $\mathbf{A}(\boldsymbol{\theta}_{pt})$ and then of the MCRB reduces to the six following integrals which are the six components of the vector $\mathbf{w}^{\mathbf{A}}(\boldsymbol{\eta}_k)$, for $k \in \{0, 1, pt\}$,

$$w_1^{\mathbf{A}}(\boldsymbol{\eta}_k) = \int_{\mathbb{R}} s(t - \tau_{pt}) s(t - \tau_k)^* e^{-j\omega_c (b_{pt}(t - \tau_{pt}) - b_k(t - \tau_k))} dt, \quad (\text{D.18})$$

$$w_2^{\mathbf{A}}(\boldsymbol{\eta}_k) = \int_{\mathbb{R}} (t - \tau_{pt}) s(t - \tau_{pt}) s(t - \tau_k)^* e^{-j\omega_c (b_{pt}(t - \tau_{pt}) - b_k(t - \tau_k))} dt, \quad (\text{D.19})$$

$$w_3^{\mathbf{A}}(\boldsymbol{\eta}_k) = \int_{\mathbb{R}} (t - \tau_{pt})^2 s(t - \tau_{pt}) s(t - \tau_k)^* e^{-j\omega_c (b_{pt}(t - \tau_{pt}) - b_k(t - \tau_k))} dt, \quad (\text{D.20})$$

$$w_4^{\mathbf{A}}(\boldsymbol{\eta}_k) = \int_{\mathbb{R}} s^{(1)}(t - \tau_{pt}) s(t - \tau_k)^* e^{-j\omega_c (b_{pt}(t - \tau_{pt}) - b_k(t - \tau_k))} dt, \quad (\text{D.21})$$

$$w_5^{\mathbf{A}}(\boldsymbol{\eta}_k) = \int_{\mathbb{R}} (t - \tau_{pt}) s^{(1)}(t - \tau_{pt}) s(t - \tau_k)^* e^{-j\omega_c (b_{pt}(t - \tau_{pt}) - b_k(t - \tau_k))} dt, \quad (\text{D.22})$$

$$w_6^{\mathbf{A}}(\boldsymbol{\eta}_k) = \int_{\mathbb{R}} s^{(2)}(t - \tau_{pt}) s(t - \tau_k)^* e^{-j\omega_c (b_{pt}(t - \tau_{pt}) - b_k(t - \tau_k))} dt, \quad (\text{D.23})$$

One can work these integral expressions as follows:

$$\begin{aligned} w_1^{\mathbf{A}}(\boldsymbol{\eta}_k) &= \int_{\mathbb{R}} s(t - \tau_{pt}) s(t - \tau_k)^* e^{-j\omega_c (b_{pt}(t - \tau_{pt}) - b_k(t - \tau_k))} dt \\ &= e^{-j\omega_c b_k \Delta \tau_k} \int_{\mathbb{R}} s(u) s(u - \Delta \tau_k)^* e^{j\omega_c \Delta b_k u} du \end{aligned}$$

with $\Delta \tau_k \triangleq \tau_k - \tau_{pt}$ and $\Delta b_k \triangleq b_k - b_{pt}$. Then, using the Fourier transform properties over the hermitian product and the relations recalled in Appendix A,

$$\begin{aligned} w_1^{\mathbf{A}}(\boldsymbol{\eta}_k) e^{j\omega_c b_k \Delta \tau_k} &= \int_{\mathbb{R}} \underbrace{s(u) e^{j\omega_c \Delta b_k u}}_{(\text{A.2})} (s(u - \Delta \tau_k))^* du \\ &= \int_{-\frac{F_s}{2}}^{\frac{F_s}{2}} S(f - f_c \Delta b_k) \left(S(f) e^{-j2\pi f \Delta \tau_k} \right)^* df \\ &= \frac{1}{F_s} \int_{-\frac{1}{2}}^{\frac{1}{2}} \left(\mathbf{s}^T \mathbf{U} \left(-\frac{f_c \Delta b_k}{F_s} \right) \boldsymbol{\nu}(f)^* \right) e^{j2\pi f \frac{\Delta \tau_k}{T_s}} \left(\mathbf{s}^H \boldsymbol{\nu}(f) \right) df \\ &= \frac{1}{F_s} \mathbf{s}^H \mathbf{V}^{\Delta, 0} \left(-\frac{\Delta \tau_k}{T_s} \right) \mathbf{U} \left(-\frac{f_c \Delta b_k}{F_s} \right) \mathbf{s} \end{aligned}$$

Hence

$$w_1^{\mathbf{A}}(\boldsymbol{\eta}_k) = \frac{1}{F_s} \mathbf{s}^H \mathbf{V}^{\Delta,0} \left(-\frac{\Delta\tau_k}{T_s} \right) \mathbf{U} \left(-\frac{f_c \Delta b_k}{F_s} \right) \mathbf{s} e^{-j\omega_c b_k \Delta\tau_k}, \quad (\text{D.24})$$

with $\boldsymbol{\nu}(\cdot)$ defined in (C.30), $\mathbf{U}(\cdot)$ defined in (C.31) and $\mathbf{V}^{\Delta,0}(\cdot)$ defined in (C.33).

Similarly,

$$\begin{aligned} w_2^{\mathbf{A}}(\boldsymbol{\eta}_k) &= \int_{\mathbb{R}} (t - \tau_{pt}) s(t - \tau_{pt}) s(t - \tau_k)^* e^{-j\omega_c (b_{pt}(t - \tau_{pt}) - b_k(t - \tau_k))} dt \\ &= e^{-j\omega_c b_k \Delta\tau_k} \int_{\mathbb{R}} u s(u) s(u - \Delta\tau_k)^* e^{j\omega_c \Delta b_k u} du \end{aligned}$$

Therefore,

$$\begin{aligned} w_2^{\mathbf{A}}(\boldsymbol{\eta}_k) e^{j\omega_c b_k \Delta\tau_k} &= \int_{\mathbb{R}} \underbrace{u s(u) e^{j\omega_c \Delta b_k u}}_{(\text{A.6})} (s(u - \Delta\tau_k))^* du \\ &= \int_{-\frac{F_s}{2}}^{\frac{F_s}{2}} \left(\frac{j}{2\pi} \frac{d}{df} (S(f - f_c \Delta b_k)) \right) (S(f) e^{-j2\pi f \Delta\tau_k})^* df \\ &= \frac{1}{F_s^2} \int_{-\frac{1}{2}}^{\frac{1}{2}} \left(\mathbf{s}^T \mathbf{D} \mathbf{U} \left(-\frac{f_c \Delta b_k}{F_s} \right) \boldsymbol{\nu}(f)^* \right) e^{j2\pi f \frac{\Delta\tau_k}{T_s}} (\mathbf{s}^H \boldsymbol{\nu}(f)) df \\ &= \frac{1}{F_s^2} \mathbf{s}^H \mathbf{V}^{\Delta,0} \left(-\frac{\Delta\tau_k}{T_s} \right) \mathbf{U} \left(-\frac{f_c \Delta b_k}{F_s} \right) \mathbf{D} \mathbf{s} \end{aligned}$$

Hence

$$w_2^{\mathbf{A}}(\boldsymbol{\eta}_k) = \frac{1}{F_s^2} \mathbf{s}^H \mathbf{V}^{\Delta,0} \left(-\frac{\Delta\tau_k}{T_s} \right) \mathbf{U} \left(-\frac{f_c \Delta b_k}{F_s} \right) \mathbf{D} \mathbf{s} e^{-j\omega_c b_k \Delta\tau_k}, \quad (\text{D.25})$$

with $\mathbf{U}(\cdot)$ defined in (C.31), $\mathbf{V}^{\Delta,0}(\cdot)$ defined in (C.33) and \mathbf{D} defined in (C.32).

And this goes on...

$$\begin{aligned} w_3^{\mathbf{A}}(\boldsymbol{\eta}_k) &= \int_{\mathbb{R}} (t - \tau_{pt})^2 s(t - \tau_{pt}) s(t - \tau_k)^* e^{-j\omega_c (b_{pt}(t - \tau_{pt}) - b_k(t - \tau_k))} dt \\ &= e^{-j\omega_c b_k \Delta\tau_k} \int_{\mathbb{R}} u^2 s(u) s(u - \Delta\tau_k)^* e^{j\omega_c \Delta b_k u} du \end{aligned}$$

Therefore,

$$\begin{aligned} w_3^{\mathbf{A}}(\boldsymbol{\eta}_k) e^{j\omega_c b_k \Delta\tau_k} &= \int_{\mathbb{R}} \underbrace{u^2 s(u) e^{j\omega_c \Delta b_k u}}_{(\text{A.7})} (s(u - \Delta\tau_k))^* du \\ &= \int_{-\frac{F_s}{2}}^{\frac{F_s}{2}} \left(\left(\frac{j}{2\pi} \right)^2 \frac{d^2}{df^2} (S(f - f_c \Delta b_k)) \right) (S(f) e^{-j2\pi f \Delta\tau_k})^* df \\ &= \frac{1}{F_s^3} \int_{-\frac{1}{2}}^{\frac{1}{2}} \left(\mathbf{s}^T \mathbf{D}^2 \mathbf{U} \left(-\frac{f_c \Delta b_k}{F_s} \right) \boldsymbol{\nu}(f)^* \right) e^{j2\pi f \frac{\Delta\tau_k}{T_s}} (\mathbf{s}^H \boldsymbol{\nu}(f)) df \\ &= \frac{1}{F_s^3} \mathbf{s}^H \mathbf{V}^{\Delta,0} \left(-\frac{\Delta\tau_k}{T_s} \right) \mathbf{U} \left(-\frac{f_c \Delta b_k}{F_s} \right) \mathbf{D}^2 \mathbf{s} \end{aligned}$$

Hence

$$w_3^{\mathbf{A}}(\boldsymbol{\eta}_k) = \frac{1}{F_s^3} \mathbf{s}^H \mathbf{V}^{\Delta,0} \left(-\frac{\Delta\tau_k}{T_s} \right) \mathbf{U} \left(-\frac{f_c \Delta b_k}{F_s} \right) \mathbf{D}^2 \mathbf{s} e^{-j\omega_c b_k \Delta\tau_k}, \quad (\text{D.26})$$

with $\mathbf{U}(\cdot)$ defined in (C.31), $\mathbf{V}^{\Delta,0}(\cdot)$ defined in (C.33) and \mathbf{D} defined in (C.32).

... and on...

$$\begin{aligned} w_4^{\mathbf{A}}(\boldsymbol{\eta}_k) &= \int_{\mathbb{R}} s^{(1)}(t - \tau_{pt}) s(t - \tau_k)^* e^{-j\omega_c (b_{pt}(t - \tau_{pt}) - b_k(t - \tau_k))} dt \\ &= e^{-j\omega_c b_k \Delta\tau_k} \int_{\mathbb{R}} s^{(1)}(u) s(u - \Delta\tau_k)^* e^{j\omega_c \Delta b_k u} du \end{aligned}$$

Therefore,

$$\begin{aligned} w_4^{\mathbf{A}}(\boldsymbol{\eta}_k) e^{j\omega_c b_k \Delta\tau_k} &= \int_{\mathbb{R}} \underbrace{s^{(1)}(u) e^{j\omega_c \Delta b_k u}}_{(\text{A.9})} (s(u - \Delta\tau_k))^* du \\ &= \int_{-\frac{F_s}{2}}^{\frac{F_s}{2}} (j2\pi(f - f_c \Delta b_k) S(f - f_c \Delta b_k)) (S(f) e^{-j2\pi f \Delta\tau_k})^* df \\ &= \frac{1}{F_s} \int_{-\frac{1}{2}}^{\frac{1}{2}} \left(j2\pi(f F_s - f_c \Delta b_k) \mathbf{s}^T \mathbf{U} \left(-\frac{f_c \Delta b_k}{F_s} \right) \boldsymbol{\nu}(f)^* \right) e^{j2\pi f \frac{\Delta\tau_k}{T_s}} (\mathbf{s}^H \boldsymbol{\nu}(f)) df \\ &= \mathbf{s}^H \mathbf{V}^{\Delta,1} \left(-\frac{\Delta\tau_k}{T_s} \right) \mathbf{U} \left(-\frac{f_c \Delta b_k}{F_s} \right) \mathbf{s} - \frac{j2\pi f_c \Delta b_k}{F_s} \mathbf{s}^H \mathbf{V}^{\Delta,0} \left(-\frac{\Delta\tau_k}{T_s} \right) \mathbf{U} \left(-\frac{f_c \Delta b_k}{F_s} \right) \mathbf{s} \end{aligned}$$

Hence

$$\begin{aligned} w_4^{\mathbf{A}}(\boldsymbol{\eta}_k) &= \left(\mathbf{s}^H \mathbf{V}^{\Delta,1} \left(-\frac{\Delta\tau_k}{T_s} \right) \mathbf{U} \left(-\frac{f_c \Delta b_k}{F_s} \right) \mathbf{s} - \frac{j\omega_c \Delta b_k}{F_s} \mathbf{s}^H \mathbf{V}^{\Delta,0} \left(-\frac{\Delta\tau_k}{T_s} \right) \right. \\ &\quad \left. \times \mathbf{U} \left(-\frac{f_c \Delta b_k}{F_s} \right) \mathbf{s} \right) e^{-j\omega_c b_k \Delta\tau_k} \end{aligned} \quad (\text{D.27})$$

with $\mathbf{U}(\cdot)$ defined in (C.32), $\mathbf{V}^{\Delta,0}(\cdot)$ defined in (C.33) and $\mathbf{V}^{\Delta,1}(\cdot)$ defined in (C.35).

... and on...

$$\begin{aligned} w_5^{\mathbf{A}}(\boldsymbol{\eta}_k) &= \int_{\mathbb{R}} (t - \tau_{pt}) s^{(1)}(t - \tau_{pt}) s(t - \tau_k)^* e^{-j\omega_c (b_{pt}(t - \tau_{pt}) - b_k(t - \tau_k))} dt \\ &= e^{-j\omega_c b_k \Delta\tau_k} \int_{\mathbb{R}} u s^{(1)}(u) s(u - \Delta\tau_k)^* e^{j\omega_c \Delta b_k u} du \end{aligned}$$

Therefore,

$$\begin{aligned}
w_5^{\mathbf{A}}(\boldsymbol{\eta}_k) e^{j\omega_c b_k \Delta\tau_k} &= \int_{\mathbb{R}} \underbrace{u s^{(1)}(u) e^{j\omega_c \Delta b_k u}}_{\text{(A.10)}} (s(u - \Delta\tau_k))^* \mathrm{d}u \\
&= \int_{-\frac{F_s}{2}}^{\frac{F_s}{2}} \left(-S(f - f_c \Delta b_k) - (f - f_c \Delta b_k) \frac{\mathrm{d}}{\mathrm{d}f} (S(f - f_c \Delta b_k)) \right) (S(f) e^{-j2\pi f \Delta\tau_k})^* \mathrm{d}f \\
&= -\frac{1}{F_s} \int_{-\frac{1}{2}}^{\frac{1}{2}} \left(\mathbf{s}^T \mathbf{U} \left(-\frac{f_c \Delta b_k}{F_s} \right) \boldsymbol{\nu}(f)^* \right) e^{j2\pi f \frac{\Delta\tau_k}{T_s}} (\mathbf{s}^H \boldsymbol{\nu}(f)) \mathrm{d}f \\
&\quad + \frac{1}{F_s} \int_{-\frac{1}{2}}^{\frac{1}{2}} j2\pi f \left(\mathbf{s}^T \mathbf{D} \mathbf{U} \left(-\frac{f_c \Delta b_k}{F_s} \right) \boldsymbol{\nu}(f)^* \right) e^{j2\pi f \frac{\Delta\tau_k}{T_s}} (\mathbf{s}^H \boldsymbol{\nu}(f)) \mathrm{d}f \\
&\quad - j2\pi \frac{f_c \Delta b_k}{F_s^2} \int_{-\frac{1}{2}}^{\frac{1}{2}} \left(\mathbf{s}^T \mathbf{D} \mathbf{U} \left(-\frac{f_c \Delta b_k}{F_s} \right) \boldsymbol{\nu}(f)^* \right) e^{j2\pi f \frac{\Delta\tau_k}{T_s}} (\mathbf{s}^H \boldsymbol{\nu}(f)) \mathrm{d}f \\
&= -\frac{1}{F_s} \mathbf{s}^H \mathbf{V}^{\Delta,0} \left(-\frac{\Delta\tau_k}{T_s} \right) \mathbf{U} \left(-\frac{f_c \Delta b_k}{F_s} \right) \mathbf{s} + \frac{1}{F_s} \mathbf{s}^H \mathbf{V}^{\Delta,1} \left(-\frac{\Delta\tau_k}{T_s} \right) \mathbf{U} \left(-\frac{f_c \Delta b_k}{F_s} \right) \mathbf{D} \mathbf{s} \\
&\quad - j2\pi \frac{f_c \Delta b_k}{F_s^2} \mathbf{s}^H \mathbf{V}^{\Delta,0} \left(-\frac{\Delta\tau_k}{T_s} \right) \mathbf{U} \left(-\frac{f_c \Delta b_k}{F_s} \right) \mathbf{D} \mathbf{s}
\end{aligned}$$

Hence

$$\begin{aligned}
w_5^{\mathbf{A}}(\boldsymbol{\eta}_k) &= \left(-\frac{1}{F_s} \mathbf{s}^H \mathbf{V}^{\Delta,0} \left(-\frac{\Delta\tau_k}{T_s} \right) \mathbf{U} \left(-\frac{f_c \Delta b_k}{F_s} \right) \mathbf{s} + \frac{1}{F_s} \mathbf{s}^H \mathbf{V}^{\Delta,1} \left(-\frac{\Delta\tau_k}{T_s} \right) \mathbf{U} \left(-\frac{f_c \Delta b_k}{F_s} \right) \mathbf{D} \mathbf{s} \right. \\
&\quad \left. - j \frac{\omega_c \Delta b_k}{F_s^2} \mathbf{s}^H \mathbf{V}^{\Delta,0} \left(-\frac{\Delta\tau_k}{T_s} \right) \mathbf{U} \left(-\frac{f_c \Delta b_k}{F_s} \right) \mathbf{D} \mathbf{s} \right) e^{-j\omega_c b_k \Delta\tau_k}
\end{aligned} \tag{D.28}$$

with $\mathbf{U}(\cdot)$ defined in (C.31), $\mathbf{V}^{\Delta,0}(\cdot)$ defined in (C.33), $\mathbf{V}^{\Delta,1}(\cdot)$ defined in (C.35) and \mathbf{D} defined in (C.32).

and the last term being derived in a very similar way,

$$\begin{aligned}
w_6^{\mathbf{A}}(\boldsymbol{\eta}_k) &= \int_{\mathbb{R}} s^{(2)}(t - \tau_{pt}) s(t - \tau_k)^* e^{-j\omega_c (b_{pt}(t - \tau_{pt}) - b_k(t - \tau_k))} \mathrm{d}t \\
&= e^{-j\omega_c b_k \Delta\tau_k} \int_{\mathbb{R}} s^{(2)}(u) s(u - \Delta\tau_k)^* e^{j\omega_c \Delta b_k u} \mathrm{d}u
\end{aligned}$$

Therefore,

$$\begin{aligned}
w_6^{\mathbf{A}}(\boldsymbol{\eta}_k) e^{j\omega_c b_k \Delta\tau_k} &= \int_{\mathbb{R}} \underbrace{s^{(2)}(u) e^{j\omega_c \Delta b_k u}}_{\text{(A.11)}} (s(u - \Delta\tau_k))^* du \\
&= \int_{-\frac{F_s}{2}}^{\frac{F_s}{2}} \left(-4\pi^2 (f - f_c \Delta b_k)^2 S(f - f_c \Delta b_k) \right) \left(S(f) e^{-j2\pi f \Delta\tau_k} \right)^* df \\
&= \int_{-\frac{1}{2}}^{\frac{1}{2}} \left(\left(-F_s (4\pi^2 f^2) - j4\pi f_c \Delta b_k (j2\pi f) - 4\pi^2 \frac{(f_c \Delta b_k)^2}{F_s} \right) \left(\mathbf{s}^T \mathbf{U} \left(-\frac{f_c \Delta b_k}{F_s} \right) \boldsymbol{\nu}(f)^* \right) \right) \\
&\quad \times e^{j2\pi f \frac{\Delta\tau_k}{T_s}} \left(\mathbf{s}^H \boldsymbol{\nu}(f) \right) df \\
&= -F_s \mathbf{s}^H \mathbf{V}^{\Delta,2} \left(-\frac{\Delta\tau_k}{T_s} \right) \mathbf{U} \left(-\frac{f_c \Delta b_k}{F_s} \right) \mathbf{s} - j4\pi f_c \Delta b_k \mathbf{s}^H \mathbf{V}^{\Delta,1} \left(-\frac{\Delta\tau_k}{T_s} \right) \mathbf{U} \left(-\frac{f_c \Delta b_k}{F_s} \right) \mathbf{s} \\
&\quad - 4\pi^2 \frac{(f_c \Delta b_k)^2}{F_s} \mathbf{s}^H \mathbf{V}^{\Delta,0} \left(-\frac{\Delta\tau_k}{T_s} \right) \mathbf{U} \left(-\frac{f_c \Delta b_k}{F_s} \right) \mathbf{s}
\end{aligned}$$

Hence

$$\begin{aligned}
w_6^{\mathbf{A}}(\boldsymbol{\eta}_k) &= \left(-F_s \mathbf{s}^H \mathbf{V}^{\Delta,2} \left(-\frac{\Delta\tau_k}{T_s} \right) \mathbf{U} \left(-\frac{f_c \Delta b_k}{F_s} \right) \mathbf{s} - j2\omega_c \Delta b_k \mathbf{s}^H \mathbf{V}^{\Delta,1} \left(-\frac{\Delta\tau_k}{T_s} \right) \mathbf{U} \left(-\frac{f_c \Delta b_k}{F_s} \right) \mathbf{s} \right. \\
&\quad \left. - \frac{(\omega_c \Delta b_k)^2}{F_s} \mathbf{s}^H \mathbf{V}^{\Delta,0} \left(-\frac{\Delta\tau_k}{T_s} \right) \mathbf{U} \left(-\frac{f_c \Delta b_k}{F_s} \right) \mathbf{s} \right) e^{-j\omega_c b_k \Delta\tau_k}
\end{aligned} \tag{D.29}$$

with $\mathbf{U}(\cdot)$ defined in (C.31), $\mathbf{V}^{\Delta,0}(\cdot)$ defined in (C.33), $\mathbf{V}^{\Delta,1}$ defined in (C.35) and $\mathbf{V}^{\Delta,2}(\cdot)$ defined in (C.37).

Based on the definitions of matrices $\mathbf{V}^{\Delta,0}$, $\mathbf{V}^{\Delta,1}$, $\mathbf{V}^{\Delta,2}$ and \mathbf{U} , one can do the following remarks:

- $(\mathbf{V}^{\Delta,0}(q))^H = \mathbf{V}^{\Delta,0}(-q)$,
- $(\mathbf{V}^{\Delta,1}(q))^H = -\mathbf{V}^{\Delta,1}(-q)$,
- $(\mathbf{V}^{\Delta,2}(q))^H = \mathbf{V}^{\Delta,2}(-q)$,
- $(\mathbf{U}(p))^H = \mathbf{U}(-p)$.

This can simplify the expressions of the components of $\mathbf{w}^{\mathbf{A}}$ by taking the conjugate and removing all the minus sign in the matrices parenthesis.

Details on the Computation of the Approximate Maximum Likelihood Estimator

E.1 Details on the Taylor Approximation of c and β_1 Functions

In this appendix, the Taylor series of the auto-correlation term $c(\Delta\tau)$ and the cross-correlation term β_1 are derived.

First recall that a band-limited signal $s(t)$ with bandwidth B equal to the sampling frequency F_s , is considered in this work. The baseband signal can be expressed as follows:

$$s(t) = \sum_{n=N_1}^{N_2} s\left(\frac{n}{B}\right) \text{sinc}\left(\pi B\left(t - \frac{n}{B}\right)\right) \Leftrightarrow \text{TF}\{s(t)\}(f) \triangleq S(f) = \frac{1}{B} \sum_{n=N_1}^{N_2} s\left(\frac{n}{B}\right) e^{-j2\pi n \frac{f}{B}}, \quad -\frac{B}{2} \leq f \leq \frac{B}{2}, \quad (\text{E.1})$$

E.1.1 Auto-correlation Function

From the signal discrete signal model (E.1), if the number of elements $N_2 - N_1$ is very large, the ACF $c(\Delta\tau)$ can be written as an integral:

$$c(\Delta\tau) = \mathbf{a}_0^H \mathbf{a}_1 = F_s \int_{\mathbb{R}} s(t - \tau_0)^* s(t - \tau_0 - \Delta\tau) e^{j\omega_c b \Delta\tau} dt \quad (\text{E.2})$$

$$= F_s e^{j\omega_c b \Delta\tau} \int_{\mathbb{R}} s(u)^* s(u - \Delta\tau) du. \quad (\text{E.3})$$

Then using the Fourier transform properties over the hermitian product and the sum definition of the Fourier transform recalled in (E.1):

$$c(\Delta\tau) = F_s e^{j\omega_c b \Delta\tau} \times \int_{-F_s/2}^{F_s/2} \left(\frac{1}{F_s} \sum_{n=N_1}^{N_2} s(nT_s) e^{-j2\pi f n T_s} \right)^* \left(\frac{1}{F_s} \sum_{n=N_1}^{N_2} s(nT_s) e^{-j2\pi f n T_s} \right) e^{-j2\pi f \Delta\tau} df \quad (\text{E.4})$$

$$= \mathbf{s}^H \left(\int_{-1/2}^{1/2} \boldsymbol{\nu}(f) \boldsymbol{\nu}(f)^H e^{-j2\pi f F_s \Delta\tau} df \right) \mathbf{s} e^{j\omega_c b \Delta\tau} \quad (\text{E.5})$$

where, for $n \in [N_1, N_2]$, $\mathbf{s} = (\dots, s(nT_s), \dots)^T$, $\boldsymbol{\nu}(f) = (\dots, e^{j2\pi f n}, \dots)^T$.

Consequently, the Fourier coefficients for the ACF are simply the successive derivatives of (E.5) evaluated when $\Delta\tau = 0$:

$$c_n = \frac{1}{n!} \left. \frac{\partial^n c(\Delta\tau)}{\partial \Delta\tau^n} \right|_{\Delta\tau=0} = \frac{1}{n!} \sum_{k=0}^n \mathbf{s}^H \mathbf{D}_k(0) \mathbf{s} (j\omega_c b)^{n-k}, \quad (\text{E.6})$$

where

$$\mathbf{D}_k(\tau) = (-j2\pi F_s)^k \int_{-1/2}^{1/2} f^k \boldsymbol{\nu}(f) \boldsymbol{\nu}(f)^H e^{-j2\pi f \tau} df. \quad (\text{E.7})$$

When expressed with $\tau = 0$, $\mathbf{D}_k(0)$ is the k^{th} derivative of a sine cardinal function which can be iteratively computed (see Appendix E.1.3). Then when $\Delta\tau$ is very small, the Taylor series for the auto-correlation term is:

$$c(\Delta\tau) = \sum_{n \in \mathbb{N}} c_n \Delta\tau^n = 1 + \sum_{n \in \mathbb{N}^*} c_n \Delta\tau^n \quad (\text{E.8})$$

$$|c(\Delta\tau)|^2 = \sum_{n \in \mathbb{N}} \left(\sum_{k=0}^n c_k c_{n-k}^* \right) \Delta\tau^n = 1 + \sum_{n \in \mathbb{N}^*} d_n \Delta\tau^n \quad (\text{E.9})$$

E.1.2 Cross-Correlation Function

Similarly when the number of element is large enough, the cross-correlation between \mathbf{a}_1 and the data \mathbf{x} can be expressed in as

$$\beta_1 = \mathbf{a}_1^H \mathbf{x} = F_s \int_{\mathbb{R}} \left(s(t - \tau_0 - \Delta\tau) e^{-j2\pi f_c b(t - \tau_0 - \Delta\tau)} \right)^* x(t) dt \quad (\text{E.10})$$

Again, switching to the frequency domain,

$$\beta_1 = F_s \int_{-F_s/2}^{F_s/2} \left(\frac{1}{F_s} \sum_{n=N_1}^{N_2} s(nT_s) e^{-j2\pi(f+f_c)nT_s} \right)^* \left(\frac{1}{F_s} \sum_{n=N_1}^{N_2} x(nT_s) e^{-j2\pi f n T_s} \right) e^{j2\pi f(\tau_0 + \Delta\tau)} \mathrm{d}f \quad (\text{E.11})$$

$$= \mathbf{s}^H \mathbf{U}^H \left(\frac{f_c b}{F_s} \right) \left(\int_{-1/2}^{1/2} \boldsymbol{\nu}(f) \boldsymbol{\nu}(f)^H e^{j2\pi f F_s(\tau_0 + \Delta\tau)} \mathrm{d}f \right) \mathbf{x} \quad (\text{E.12})$$

where $\mathbf{U}(b) = \text{diag}(\dots, e^{-j2\pi b n}, \dots)_{N_1 \leq n \leq N_2}$.

Then the Taylor series for the cross-correlation term is deduced from the successive derivatives of (E.12):

$$\beta_{1,k} = \frac{1}{k!} \left. \frac{\partial^k \beta_1}{\partial \Delta\tau^k} \right|_{\Delta\tau=0} = \frac{1}{k!} \left(\mathbf{D}_k \left(\frac{\tau_0}{T_s} \right) \mathbf{U} \left(\frac{f_c b}{F_s} \right) \mathbf{s} \right)^H \mathbf{x} = \frac{1}{k!} R_{\mathbf{x}, \mathbf{D}\mathbf{s}}^{(k)}(\tau_0, b f_c). \quad (\text{E.13})$$

The term $R_{\mathbf{x}, \mathbf{D}\mathbf{s}}^{(k)}(\tau_0, b f_c)$ is actually the cross-correlation between the data \mathbf{x} and the k^{th} derivative of the signal \mathbf{s} . Similarly to the auto-correlation term, it is expressed with regard to the successive derivatives of a sine cardinal which can be iteratively computed as detailed in Appendix E.1.3. Therefore, for small value of $\Delta\tau$, the Taylor series for the cross-correlation term is:

$$\beta_1 = \sum_{n \in \mathbb{N}} \beta_{1,n} \Delta\tau^n = \beta_0 + \sum_{n \in \mathbb{N}^*} \beta_{1,n} \Delta\tau^n \quad (\text{E.14})$$

E.1.3 Note on the Sine Cardinal Derivatives

The Taylor coefficients derived in the previous section all depend on the successive derivatives of a sine cardinal of the form:

$$\text{sinc}(u - \delta u) = \int_{-1/2}^{1/2} e^{j2\pi f(u - \delta u)} \mathrm{d}f \quad (\text{E.15})$$

If one calculates the k^{th} derivative of (E.15)

$$\frac{\partial^k \text{sinc}(u - \delta u)}{\partial \delta u^k} = (-j2\pi)^k \int_{-1/2}^{1/2} f^k e^{j2\pi f(u - \delta u)} \mathrm{d}f, \quad (\text{E.16})$$

a first integration by parts yields

$$\frac{\partial^k \text{sinc}(u - \delta u)}{\partial \delta u^k} = (-j2\pi)^k \left[\frac{f^k e^{j2\pi f(u-\delta u)}}{j2\pi(u-\delta u)} \right]_{-1/2}^{1/2} - \frac{k(-j2\pi)^k}{j2\pi(u-\delta u)} \int_{-1/2}^{1/2} f^{k-1} e^{j2\pi f(u-\delta u)} df \quad (\text{E.17})$$

$$= \frac{(-j2\pi)^k}{j2\pi(u-\delta u)} \left(\left(\frac{1}{2} \right)^k e^{j\pi(u-\delta u)} - \left(-\frac{1}{2} \right)^k e^{-j\pi(u-\delta u)} \right) + \frac{k}{u-\delta u} \frac{\partial^{k-1} \text{sinc}(u-\delta u)}{\partial \delta u^{k-1}} \quad (\text{E.18})$$

Then, depending on the parity of k , an iterative expression of the sine cardinal derivatives can be obtained for $k = 2n$:

$$\frac{\partial^{2n} \text{sinc}(u - \delta u)}{\partial \delta u^{2n}} = \frac{2n}{u - \delta u} \frac{\partial^{2n-1} \text{sinc}(u - \delta u)}{\partial \delta u^{2n-1}} + (-1)^n \pi^{2n} \text{sinc}(u - \delta u), \quad (\text{E.19})$$

and for $k = 2n + 1$:

$$\frac{\partial^{2n+1} \text{sinc}(u - \delta u)}{\partial \delta u^{2n+1}} = \frac{2n + 1}{u - \delta u} \frac{\partial^{2n} \text{sinc}(u - \delta u)}{\partial \delta u^{2n}} + (-1)^{n+1} \pi^{2n+1} \frac{\cos(\pi(u - \delta u))}{\pi(u - \delta u)}. \quad (\text{E.20})$$

E.2 Details on the Taylor Approximation of the Likelihood Criterion

Starting from (3.22), reminded here

$$L(\tau_0, \Delta\tau, b) = \frac{\beta_0^* \beta_0 + \beta_1^* \beta_1 - c(\Delta\tau)^* \beta_0^* \beta_1 - c(\Delta\tau) \beta_1^* \beta_0}{1 - |c(\Delta\tau)|^2} \quad (\text{E.21})$$

each term can be expressed as a Taylor series:

$$\beta_1^* \beta_1 = \beta_0^* \beta_0 + \sum_{n \in \mathbb{N}^*} \left(\sum_{k=0}^n \beta_{1,k}^* \beta_{1,n-k} \right) \Delta\tau^n, \quad (\text{E.22})$$

$$c(\Delta\tau)^* \beta_0^* \beta_1 = \beta_0^* \beta_0 + \sum_{n \in \mathbb{N}^*} \left(\sum_{k=0}^n c_k^* \beta_0^* \beta_{1,n-k} \right) \Delta\tau^n \quad (\text{E.23})$$

$$c(\Delta\tau) \beta_1^* \beta_0 = \beta_0^* \beta_0 + \sum_{n \in \mathbb{N}^*} \left(\sum_{k=0}^n c_k \beta_{1,n-k}^* \beta_0 \right) \Delta\tau^n, \quad (\text{E.24})$$

$$1 - |c(\Delta\tau)|^2 = - \sum_{n \in \mathbb{N}^*} d_n \Delta\tau^n. \quad (\text{E.25})$$

Then, by reordering these terms, the likelihood criterion can be written as follows:

$$L(\tau_0, \Delta\tau, b) = - \frac{\sum_{n \in \mathbb{N}^*} B_n \Delta\tau^{n-1}}{\sum_{n \in \mathbb{N}^*} d_n \Delta\tau^{n-1}} \quad \text{with } B_n \triangleq \sum_{k=0}^n \beta_{1,k}^* \beta_{1,n-k} - c_k^* \beta_0^* \beta_{1,n-k} - c_k \beta_{1,n-k}^* \beta_0 \quad (\text{E.26})$$

The ACF Taylor coefficients, expressed with the derivatives of the sine cardinal present a number of symmetries that simplify the expression of B_n and d_n : with $c_1^* = -c_1$, $c_3^* = -c_3$, one can deduce $d_1 = d_3 = 0$ and similarly $B_1 = 0$. Consequently, if the Taylor series in (E.26) are truncated to the 3rd order, the likelihood criterion reduces to

$$L(\tau_0, \Delta\tau, b) \approx -\frac{B_2 + B_3\Delta\tau + B_4\Delta\tau^2 + B_5\Delta\tau^3}{d_2 + d_4\Delta\tau^2} \quad (\text{E.27})$$

Finally, using the series representation of the denominator, the criterion can be written as a 3rd order Taylor expansion as in

$$\frac{-1}{d_2 + d_4\Delta\tau^2} \approx -\frac{1}{d_2} \left(1 - \frac{d_4}{d_2}\Delta\tau^2\right) \Rightarrow L(\tau_0, \Delta\tau, b) \approx L^{\text{Taylor}}(\tau_0, \Delta\tau, b) = \sum_{n=0}^3 L_n(\tau_0, b)\Delta\tau^n \quad (\text{E.28})$$

with

$$L_0(\tau_0, b) = -\frac{B_2}{d_2}, \quad L_1(\tau_0, b) = -\frac{B_3}{d_2}, \quad (\text{E.29})$$

$$L_2(\tau_0, b) = -\frac{1}{d_2} \left(B_4 - \frac{d_4}{d_2}B_2\right), \quad L_3(\tau_0, b) = -\frac{1}{d_2} \left(B_5 - \frac{d_4}{d_2}B_3\right). \quad (\text{E.30})$$

Details on the Derivation of the Impulse Response Model Fisher Information Matrix

F.1 Real and Imaginary Parts Parameterization

Hereafter can be found details on the derivation of the FIM (4.35). From the signal model (4.26), the derivative of the signal with regard to the vector of unknown parameters excluding the noise variance $\bar{\boldsymbol{\epsilon}}^T = (\boldsymbol{\eta}^T, \alpha_1^r, \alpha_1^i, \dots, \alpha_P^r, \alpha_P^i)$ can be expressed in a matrix form,

$$\frac{\partial}{\partial \bar{\boldsymbol{\epsilon}}} \left(\sum_{p=1}^P d_p(t; \boldsymbol{\eta}, \rho_p, \phi_p) \right) = \mathbf{Q}(\bar{\boldsymbol{\epsilon}}) \mathcal{D}(t; \tau) \mathbf{e}(t; \boldsymbol{\eta}), \quad (\text{F.1})$$

where, with $p \in [1, P]$,

$$\mathbf{Q}(\bar{\boldsymbol{\epsilon}}) = \left[\begin{array}{c|c|c} j\omega_c b \boldsymbol{\alpha}^T & \mathbf{0}_{1,P} & -\boldsymbol{\alpha}^T \\ \mathbf{0}_{1,P} & -j\omega_c \boldsymbol{\alpha}^T & \mathbf{0}_{1,P} \\ \hline \mathbf{I}_P \otimes \begin{pmatrix} 1 \\ j \end{pmatrix} & \mathbf{0}_{2P,P} & \mathbf{0}_{2P,P} \end{array} \right], \quad (\text{F.2})$$

$$\mathbf{e}(t; \boldsymbol{\eta}) = \left[\begin{array}{c|c|c} \boldsymbol{\Psi}_P(t; \boldsymbol{\eta}) & \mathbf{0}_{P,P} & \mathbf{0}_{P,P} \\ \mathbf{0}_{P,P} & \boldsymbol{\Psi}_P(t; \boldsymbol{\eta}) & \mathbf{0}_{P,P} \\ \hline \mathbf{0}_{P,P} & \mathbf{0}_{P,P} & \boldsymbol{\Psi}_P(t; \boldsymbol{\eta}) \end{array} \right], \quad (\text{F.3})$$

$$\mathcal{D}(t; \tau) = \begin{bmatrix} \vdots \\ s(t - \tau_p) \\ \vdots \\ \hline \vdots \\ (t - \tau_p)s(t - \tau_p) \\ \vdots \\ \hline \vdots \\ s^{(1)}(t - \tau_p) \\ \vdots \end{bmatrix}, \quad \Psi_P(t; \boldsymbol{\eta}) = \begin{bmatrix} \ddots & 0 & 0 \\ 0 & e^{-j\omega_c b(t - \tau_p)} & 0 \\ 0 & 0 & \ddots \end{bmatrix}. \quad (\text{F.4})$$

where \otimes denotes the Kronecker product.

Therefore the derivative of the vector $(\mathbf{A}_P \boldsymbol{\alpha})^T$ ($t = nT_s$, with samples $N_1 \leq n \leq N_2$) with regard to $\bar{\boldsymbol{\epsilon}}$ is

$$\frac{\partial (\mathbf{A}_P \boldsymbol{\alpha})^T}{\partial \bar{\boldsymbol{\epsilon}}} = \left[\dots \quad \frac{\partial}{\partial \bar{\boldsymbol{\epsilon}}} \left(\sum_{p=1}^P d_p(nT_s; \boldsymbol{\eta}, \rho_p, \phi_p) \right) \quad \dots \right] \quad (\text{F.5})$$

$$= \left[\dots \quad \mathbf{Q}(\bar{\boldsymbol{\epsilon}}) \mathcal{D}(nT_s; \tau) \mathbf{e}(nT_s; \boldsymbol{\eta}) \quad \dots \right] \quad (\text{F.6})$$

$$= \mathbf{Q}(\bar{\boldsymbol{\epsilon}}) \left[\dots \quad \mathcal{D}(nT_s; \tau) \mathbf{e}(nT_s; \boldsymbol{\eta}) \quad \dots \right]. \quad (\text{F.7})$$

Then, remembering the following properties,

$$\frac{\partial (\mathbf{A}_P \boldsymbol{\alpha})^H}{\partial \bar{\boldsymbol{\epsilon}}^T} = \left(\frac{\partial (\mathbf{A}_P \boldsymbol{\alpha})^T}{\partial \bar{\boldsymbol{\epsilon}}} \right)^*, \quad \frac{\partial (\mathbf{A}_P \boldsymbol{\alpha})}{\partial \bar{\boldsymbol{\epsilon}}^T} = \left(\frac{\partial (\mathbf{A}_P \boldsymbol{\alpha})^T}{\partial \bar{\boldsymbol{\epsilon}}} \right)^T, \quad (\text{F.8})$$

one can write that

$$\frac{\partial (\mathbf{A}_P \boldsymbol{\alpha})^H}{\partial \bar{\boldsymbol{\epsilon}}^T} \frac{\partial (\mathbf{A}_P \boldsymbol{\alpha})}{\partial \bar{\boldsymbol{\epsilon}}^T} = \left(\mathbf{Q}(\bar{\boldsymbol{\epsilon}}) \left(\sum_{n=N_1}^{N_2} \mathcal{D}(nT_s; \tau) \mathcal{D}(nT_s; \tau)^H \right) \mathbf{Q}(\bar{\boldsymbol{\epsilon}})^H \right)^*. \quad (\text{F.9})$$

If one evaluates the limit when N_1 and N_2 tend to infinity:

$$\lim_{(N_1, N_2) \rightarrow (-\infty, +\infty)} T_s \sum_{n=N_1}^{N_2} \mathcal{D}(nT_s; \tau) \mathcal{D}(nT_s; \tau)^H = \int_{-\infty}^{+\infty} \mathcal{D}(t; \tau) \mathcal{D}(t; \tau)^H dt \quad (\text{F.10})$$

$$= \begin{bmatrix} \mathbf{W}_1^\delta & \mathbf{W}_2^{\delta H} & \mathbf{W}_3^{\delta H} \\ \mathbf{W}_2^\delta & \mathbf{W}_{2,2}^\delta & \mathbf{W}_4^{\delta H} \\ \mathbf{W}_3^\delta & \mathbf{W}_4^\delta & \mathbf{W}_{3,3}^\delta \end{bmatrix}, \quad (\text{F.11})$$

where, for p and q in $[1, P]$

$$\left[\mathbf{W}_1^\delta\right]_{p,q} = \int_{\mathbb{R}} s(t - \tau_p) s(t - \tau_q)^* dt \quad (\text{F.12})$$

$$\left[\mathbf{W}_2^\delta\right]_{p,q} = \int_{\mathbb{R}} (t - \tau_p) s(t - \tau_p) s(t - \tau_q)^* dt \quad (\text{F.13})$$

$$\left[\mathbf{W}_3^\delta\right]_{p,q} = \int_{\mathbb{R}} s_p^{(1)}(t - \tau_p) s(t - \tau_q)^* dt \quad (\text{F.14})$$

$$\left[\mathbf{W}_4^\delta\right]_{p,q} = \int_{\mathbb{R}} (t - \tau_q) s^{(1)}(t - \tau_p) s(t - \tau_q)^* dt \quad (\text{F.15})$$

$$\left[\mathbf{W}_{2,2}^\delta\right]_{p,q} = \int_{\mathbb{R}} (t - \tau_p)(t - \tau_q) s(t - \tau_p) s(t - \tau_q) dt \quad (\text{F.16})$$

$$\left[\mathbf{W}_{3,3}^\delta\right]_{p,q} = \int_{\mathbb{R}} s^{(1)}(t - \tau_p) s^{(1)}(t - \tau_q) dt \quad (\text{F.17})$$

These terms are derived in Section F.3.

F.2 Amplitude and Phase Parameterization

In order to obtain the expression of the FIM for the vector of parameters $\bar{\boldsymbol{\zeta}}^T = (\boldsymbol{\eta}^T, \boldsymbol{\rho}^T, \phi^T)$, the only difference is in the derivative of the signal with regard to $\bar{\boldsymbol{\zeta}}$. Again, this derivative can be expressed in a matrix form,

$$\frac{\partial}{\partial \bar{\boldsymbol{\zeta}}} \left(\sum_{p=1}^P d_p(t; \boldsymbol{\eta}, \rho_p, \phi_p) \right) = \mathbf{Q}(\bar{\boldsymbol{\zeta}}) \mathcal{D}(t; \tau) \mathbf{e}(t; \boldsymbol{\eta}), \quad (\text{F.18})$$

where, with $p \in [1, P]$,

$$\mathbf{Q}(\bar{\boldsymbol{\zeta}}) = \left[\begin{array}{c|c|c} j\omega_c b \boldsymbol{\alpha}^T & \mathbf{0}_{1,P} & -\boldsymbol{\alpha}^T \\ \mathbf{0}_{1,P} & -j\omega_c \boldsymbol{\alpha}^T & \mathbf{0}_{1,P} \\ \hline \boldsymbol{\Phi}_P & \mathbf{0}_{P,P} & \mathbf{0}_{P,P} \\ \hline \mathbf{diag}(j\rho) \boldsymbol{\Phi}_P & \mathbf{0}_{P,P} & \mathbf{0}_{P,P} \end{array} \right], \quad \boldsymbol{\Phi}_P = \begin{bmatrix} \ddots & 0 & 0 \\ 0 & e^{j\phi_p} & 0 \\ 0 & 0 & \ddots \end{bmatrix}, \quad (\text{F.19})$$

with $\mathbf{e}(t; \boldsymbol{\eta})$ defined in (F.3), $\mathcal{D}(t; \tau)$ defined in (F.4) and $\mathbf{diag}(j\rho)$ the square diagonal matrix with its diagonal equal to $j\rho$.

F.3 Derivation of the Integral Terms

In this section, the \mathbf{W}^δ terms (F.12)–(F.17) are derived. Exploiting the Fourier transform properties over the hermitian product and the relations recalled in Appendix A, one can work these integral expressions as follows:

$$\begin{aligned}
[\mathbf{W}_1^\delta]_{p,q} &= \int_{\mathbb{R}} s(t - \tau_p) s(t - \tau_q)^* dt = \int_{\mathbb{R}} s(u - (p - q)T_s) s(u)^* du \\
&= \int_{-\frac{F_s}{2}}^{\frac{F_s}{2}} S(f) e^{-j2\pi f(p-q)T_s} S(f)^* df,
\end{aligned}$$

and, using the sum definition of the Fourier transform (A.1) as a matrices product,

$$[\mathbf{W}_1^\delta]_{p,q} = \frac{1}{F_s} \int_{-\frac{1}{2}}^{\frac{1}{2}} (\mathbf{s}^T \boldsymbol{\nu}(f)^*) e^{-j2\pi f(p-q)} (\mathbf{s}^H \boldsymbol{\nu}(f)) df = \frac{1}{F_s} \mathbf{s}^H \mathbf{V}^{\Delta,0}(p-q) \mathbf{s}. \quad (\text{F.20})$$

$$\begin{aligned}
[\mathbf{W}_2^\delta]_{p,q} &= \int_{\mathbb{R}} (t - \tau_p) s(t - \tau_p) s(t - \tau_q)^* dt = \int_{\mathbb{R}} \underbrace{(u - (p - q)T_s) s(u - (p - q)T_s)}_{(\text{A.4})} s(u)^* du \\
&= \int_{-\frac{F_s}{2}}^{\frac{F_s}{2}} \frac{j}{2\pi} \frac{d}{df} (S(f)) e^{-j2\pi f(p-q)T_s} S(f)^* df = \int_{-\frac{1}{2}}^{\frac{1}{2}} (\mathbf{s}^T \mathbf{D} \boldsymbol{\nu}(f)^*) e^{-j2\pi f(p-q)} (\mathbf{s}^H \boldsymbol{\nu}(f)) df \\
&= \frac{1}{F_s^2} \mathbf{s}^H \mathbf{V}^{\Delta,0}(p-q) \mathbf{D} \mathbf{s}. \quad (\text{F.21})
\end{aligned}$$

$$\begin{aligned}
[\mathbf{W}_3^\delta]_{p,q} &= \int_{\mathbb{R}} s^{(1)}(t - \tau_p) s(t - \tau_q)^* dt = \int_{\mathbb{R}} \underbrace{s^{(1)}(u - (p - q)T_s)}_{(\text{A.8})} s(u)^* du \\
&= \int_{-\frac{F_s}{2}}^{\frac{F_s}{2}} j2\pi f S(f) e^{-j2\pi f(p-q)T_s} S(f)^* df = \int_{-\frac{1}{2}}^{\frac{1}{2}} j2\pi f (\mathbf{s}^T \boldsymbol{\nu}(f)^*) e^{-j2\pi f(p-q)} (\mathbf{s}^H \boldsymbol{\nu}(f)) df \\
&= \mathbf{s}^H \mathbf{V}^{\Delta,1}(p-q) \mathbf{s}. \quad (\text{F.22})
\end{aligned}$$

$$\begin{aligned}
[\mathbf{W}_4^\delta]_{p,q} &= \int_{\mathbb{R}} (t - \tau_q) s^{(1)}(t - \tau_p) s(t - \tau_q)^* dt = \int_{\mathbb{R}} \underbrace{s^{(1)}(u - (p - q)T_s)}_{(\text{A.8})} (us(u))^* du \\
&= \int_{-\frac{F_s}{2}}^{\frac{F_s}{2}} j2\pi f S(f) e^{-j2\pi f(p-q)T_s} \left(\frac{j}{2\pi} \frac{d}{df} (S(f)) \right)^* df \\
&= \frac{1}{F_s} \int_{-\frac{1}{2}}^{\frac{1}{2}} j2\pi f (\mathbf{s}^T \boldsymbol{\nu}(f)^*) e^{-j2\pi f(p-q)} (\mathbf{s}^H \mathbf{D} \boldsymbol{\nu}(f)) df \\
&= \frac{1}{F_s} \mathbf{s}^H \mathbf{D} \mathbf{V}^{\Delta,1}(p-q) \mathbf{s}. \quad (\text{F.23})
\end{aligned}$$

$$\begin{aligned}
[\mathbf{W}_{2,2}^\delta]_{p,q} &= \int_{\mathbb{R}} (t - \tau_p)(t - \tau_q)s(t - \tau_p)s(t - \tau_q)dt = \int_{\mathbb{R}} \underbrace{(u - (p - q)T_s)s(u - \Delta\tau)}_{(A.4)} (us(u))^* du \\
&= \int_{-\frac{F_s}{2}}^{\frac{F_s}{2}} \frac{j}{2\pi} \frac{d}{df} (S(f)) e^{-j2\pi f(p-q)T_s} \left(\frac{j}{2\pi} \frac{d}{df} (S(f)) \right)^* df \\
&= \frac{1}{F_s^3} \int_{-\frac{1}{2}}^{\frac{1}{2}} (\mathbf{s}^T \mathbf{D} \boldsymbol{\nu}(f))^* e^{-j2\pi f(p-q)} (\mathbf{s}^H \mathbf{D} \boldsymbol{\nu}(f)) df \\
&= \mathbf{s}^H \mathbf{D} \mathbf{V}^{\Delta,0} (p - q) \mathbf{D} \mathbf{s}.
\end{aligned} \tag{F.24}$$

$$\begin{aligned}
[\mathbf{W}_{3,3}^\delta]_{p,q} &= \int_{\mathbb{R}} s^{(1)}(t - \tau_p)s^{(1)}(t - \tau_q)dt = \int_{\mathbb{R}} \underbrace{s^{(1)}(u - (p - q)T_s)}_{(A.8)} s^{(1)}(u)^* du \\
&= \int_{-\frac{F_s}{2}}^{\frac{F_s}{2}} (j2\pi f S(f) e^{-j2\pi f(p-q)T_s}) (j2\pi f S(f))^* df \\
&= F_s \int_{-\frac{1}{2}}^{\frac{1}{2}} 4\pi^2 f^2 (\mathbf{s}^T \boldsymbol{\nu}(f))^* e^{-j2\pi f(p-q)} (\mathbf{s}^H \boldsymbol{\nu}(f)) df \\
&= F_s \mathbf{s}^H \mathbf{V}^{\Delta,2} (p - q) \mathbf{s}.
\end{aligned} \tag{F.25}$$

where

$$\mathbf{s} = \left(\dots \quad s(nT_s) \quad \dots \right)_{N_1 \leq n \leq N_2}^T, \tag{F.26}$$

$$\boldsymbol{\nu}(f) = \left(\dots \quad e^{j2\pi f n} \quad \dots \right)_{N_1 \leq n \leq N_2}^T, \tag{F.27}$$

$$\mathbf{U}(p) = \text{diag} \left(\dots \quad e^{-j2\pi p n} \quad \dots \right)_{N_1 \leq n \leq N_2}, \tag{F.28}$$

$$\mathbf{D} = \left(\dots \quad n \quad \dots \right)_{N_1 \leq n \leq N_2}^T, \tag{F.29}$$

$$\mathbf{V}^{\Delta,0}(q) = \int_{-\frac{1}{2}}^{\frac{1}{2}} \boldsymbol{\nu}(f) \boldsymbol{\nu}^H(f) e^{-j2\pi f q} df, \tag{F.30}$$

$$\begin{aligned}
[\mathbf{V}^{\Delta,0}(q)]_{k,l} &= \int_{-\frac{1}{2}}^{\frac{1}{2}} e^{j2\pi f(k-l-q)} df = \left[\frac{e^{j2\pi f(k-l-q)}}{j2\pi(k-l-q)} \right]_{-\frac{1}{2}}^{\frac{1}{2}} \\
&= \frac{\sin(\pi(k-l-q))}{\pi(k-l-q)} = \text{sinc}(k-l-q)
\end{aligned} \tag{F.31}$$

$$\tag{F.32}$$

$$\mathbf{V}^{\Delta,1}(q) = j2\pi \int_{-\frac{1}{2}}^{\frac{1}{2}} f \boldsymbol{\nu}(f) \boldsymbol{\nu}^H(f) e^{-j2\pi f q} df, \quad (\text{F.33})$$

$$\begin{aligned} [\mathbf{V}^{\Delta,1}(q)]_{k,l} &= j2\pi \int_{-\frac{1}{2}}^{\frac{1}{2}} f e^{j2\pi f(k-l-q)} df \\ &= j2\pi \left(\left[\frac{f e^{j2\pi f(k-l-q)}}{j2\pi(k-l-q)} \right]_{-\frac{1}{2}}^{\frac{1}{2}} - \int_{-\frac{1}{2}}^{\frac{1}{2}} \frac{e^{j2\pi f(k-l-q)}}{j2\pi(k-l-q)} df \right) \\ &= \frac{1}{k-l-q} (\cos(\pi(k-l-q)) - \text{sinc}(k-l-q)) \end{aligned} \quad (\text{F.34})$$

$$(\text{F.35})$$

$$\mathbf{V}^{\Delta,2}(q) = 4\pi^2 \int_{-\frac{1}{2}}^{\frac{1}{2}} f^2 \boldsymbol{\nu}(f) \boldsymbol{\nu}^H(f) e^{-j2\pi f q} df, \quad (\text{F.36})$$

$$\begin{aligned} [\mathbf{V}^{\Delta,2}(q)]_{k,l} &= 4\pi^2 \int_{-\frac{1}{2}}^{\frac{1}{2}} f^2 e^{j2\pi f(k-l-q)} df \\ &= 4\pi^2 \left(\left[\frac{f^2 e^{j2\pi f(k-l-q)}}{j2\pi(k-l-q)} \right]_{-\frac{1}{2}}^{\frac{1}{2}} - \int_{-\frac{1}{2}}^{+\frac{1}{2}} \frac{2f e^{j2\pi f(k-l-q)}}{j2\pi(k-l-q)} df \right) \\ &= \frac{4\pi^2}{j2\pi(k-l-q)} \frac{1}{4} [e^{j\pi(k-l-q)} - e^{-j\pi(k-l-q)}] \\ &\quad - \frac{8\pi^2}{j2\pi(k-l-q)} \left(\left[\frac{f e^{j2\pi f(k-l-q)}}{j2\pi(k-l-q)} \right]_{-\frac{1}{2}}^{\frac{1}{2}} - \int_{-\frac{1}{2}}^{+\frac{1}{2}} \frac{e^{j2\pi f(k-l-q)}}{j2\pi(k-l-q)} df \right) \\ &= \pi^2 \text{sinc}(k-l-q) + 2 \frac{\cos(\pi(k-l-q)) - \text{sinc}(k-l-q)}{(k-l-q)^2} \end{aligned} \quad (\text{F.37})$$

Details on the Impulse Response Size Determination Problem

G.1 Details on the Global MSE for Under- and Overshooting Cases

This section gives an insight of how the MSE defined in (4.52) varies whether the number of pulses considered is underestimated or overestimated. First recall that

$$\int_{-\frac{F_s}{2}}^{\frac{F_s}{2}} e^{-j2\pi fpT_s} \left(e^{-j2\pi fqT_s} \right)^* df = \delta_p^q F_s. \quad (\text{G.1})$$

For the undershooting case:

$$\int_{-\frac{F_s}{2}}^{\frac{F_s}{2}} \left| H(f) - \hat{H}(f) \right|^2 df = \int_{-\frac{F_s}{2}}^{\frac{F_s}{2}} \left| \sum_{p=1}^P \alpha_p e^{-j2\pi f(p-1)T_s} - \sum_{q=1}^{P-\Delta P} \hat{\alpha}_q e^{-j2\pi f(q-1)T_s} \right|^2 df \quad (\text{G.2})$$

$$= \int_{-\frac{F_s}{2}}^{\frac{F_s}{2}} \left| \sum_{p=1}^{P-\Delta P} (\alpha_p - \hat{\alpha}_p) e^{-j2\pi f(p-1)T_s} + \sum_{q=P-\Delta P+1}^P \alpha_q e^{-j2\pi f(q-1)T_s} \right|^2 df \quad (\text{G.3})$$

$$= \sum_{p=1}^{P-\Delta P} |\alpha_p - \hat{\alpha}_p|^2 + \sum_{q=P-\Delta P+1}^P |\alpha_q|^2 \quad \text{using (G.1),} \quad (\text{G.4})$$

which leads to (4.54).

Now regarding the overshooting case,

$$\int_{-\frac{F_s}{2}}^{\frac{F_s}{2}} \left| H(f) - \hat{H}(f) \right|^2 df = \int_{-\frac{F_s}{2}}^{\frac{F_s}{2}} \left| \sum_{p=1}^P \alpha_p e^{-j2\pi f(p-1)T_s} - \sum_{q=1}^{P+\Delta P} \hat{\alpha}_q e^{-j2\pi f(q-1)T_s} \right|^2 df \quad (\text{G.5})$$

$$= \int_{-\frac{F_s}{2}}^{\frac{F_s}{2}} \left| \sum_{p=1}^P (\alpha_p - \hat{\alpha}_p) e^{-j2\pi f(p-1)T_s} - \sum_{q=P+1}^{P+\Delta P} \hat{\alpha}_q e^{-j2\pi f(q-1)T_s} \right|^2 df \quad (\text{G.6})$$

$$\int_{-\frac{F_s}{2}}^{\frac{F_s}{2}} |H(f) - \widehat{H}(f)|^2 df = \sum_{p=1}^P |\alpha_p - \widehat{\alpha}_p|^2 + \sum_{q=P+1}^{P+\Delta P} |0 - \widehat{\alpha}_q|^2, \quad (\text{G.7})$$

which leads to (4.56).

G.2 $P + \text{next}$ Correlation Coefficient

Let one consider a study case, the GPS L1 C/A. The auto-correlation function is known and can be modeled by a zero-centered triangle. One can then assume that the normalized cross-correlation between \mathbf{s}_P and \mathbf{s}_{P+1} is simply: $\mathbf{s}_P^H \mathbf{s}_{P+1} = 1 - pF_0/F_s$ where F_0 is the GPS L1 C/A chip rate, equal to 1.023 MHz. Then, if one considers the case with $P = 2$ sources already detected and no other remaining source (H_0):

$$\mathbf{P}_{\mathbf{A}_2} \mathbf{s}_3 = \mathbf{A}_2 \left(\mathbf{A}_2^H \mathbf{A}_2 \right)^{-1} \mathbf{A}_2^H \mathbf{s}_3 = \begin{bmatrix} \mathbf{s}_1 & \mathbf{s}_2 \end{bmatrix} \begin{bmatrix} \mathbf{s}_1^H \mathbf{s}_1 & \mathbf{s}_1^H \mathbf{s}_2 \\ \mathbf{s}_2^H \mathbf{s}_1 & \mathbf{s}_2^H \mathbf{s}_2 \end{bmatrix}^{-1} \begin{bmatrix} \mathbf{s}_1^H \mathbf{s}_3 \\ \mathbf{s}_2^H \mathbf{s}_3 \end{bmatrix} \quad (\text{G.8})$$

Then with the approximated triangular shape and assuming that $F_s/F_0 \gg 1$, one can get

$$\mathbf{P}_{\mathbf{A}_2}^\perp \mathbf{s}_3 \approx \mathbf{s}_3 - \left(1 - \frac{F_0}{F_s} \right) \mathbf{s}_2 + \frac{F_0}{2F_s} \mathbf{s}_1. \quad (\text{G.9})$$

And for F_s large enough, this is no longer a series of +1 and -1 because of the cross-correlation between close-in-time signals. Figure G.1 shows an example for $F_s = 8F_0$: the variance of \mathbf{s}_3 is 1 but the variance of its orthogonal projection is now 0.2336. There is then a given

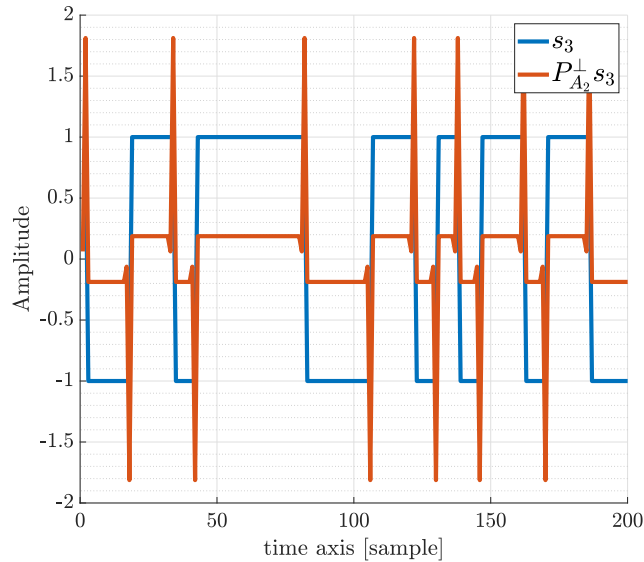


Figure G.1: Projection of \mathbf{s}_{P+1} on the space spanned by the columns of \mathbf{A}_P , $P = 2$, $F_s = 8F_0$.

correlation coefficient k_σ that depends on F_s , the pseudo-random noise code, the number of

signals and the distance between the consecutive pulses considered. This coefficient directly determines the distribution under H_0 and is needed to set the threshold for a given probability of false alarm. However it is difficult to anticipate k_σ , as it can be seen in the following table G.1. Consequently, k_σ needs to be evaluated during the detection test.

Table G.1: Examples of k_σ for GPS L1 C/A with $P = 2$.

F_s/F_0	2	4	8	12
k_σ	0.6673	0.4290	0.2336	0.1596

G.3 Chung and Mecklenbräuker Likelihood Ratio Distribution Derivation

The orthogonal projector over the space defined by the column of \mathbf{A}_M can be separated into two orthogonal projectors. One over the subspace defined by $M - 1$ columns (omitting the m -th component) and the other, which is naturally the projection upon the subspace defined by the m -th column, orthogonalized:

$$\mathbf{P}_{\mathbf{A}_M} = \mathbf{P}_{\mathbf{A}_{M-1,m}} + \mathbf{P}\left(\mathbf{P}_{\mathbf{A}_{M-1,m}}^\perp \mathbf{s}_m\right) \quad (\text{G.10})$$

Proof. See Appendix B.2 for more details. □

Consequently, the likelihood ratio defined in (4.63) can be reorganized using the orthogonal decomposition (G.10):

$$\text{LR}_m = \frac{\left\| \mathbf{P}_{\mathbf{A}_M}^\perp \mathbf{y} \right\|^2}{\left\| \mathbf{P}_{\mathbf{A}_{M-1,m}}^\perp \mathbf{y} \right\|^2} = \frac{\left\| \mathbf{P}_{\mathbf{A}_{M-1,m}}^\perp \mathbf{y} \right\|^2 - \left\| \mathbf{P}\left(\mathbf{P}_{\mathbf{A}_{M-1,m}}^\perp \mathbf{s}_m\right) \mathbf{y} \right\|^2}{\left\| \mathbf{P}_{\mathbf{A}_{M-1,m}}^\perp \mathbf{y} \right\|^2} \quad (\text{G.11})$$

Therefore,

$$\text{LR}_m = 1 - \frac{\left| \mathbf{s}_m^H \mathbf{P}_{\mathbf{A}_{M-1,m}}^\perp \mathbf{y} \right|^2}{\left\| \mathbf{P}_{\mathbf{A}_{M-1,m}}^\perp \mathbf{s}_m \right\|^2 \left\| \mathbf{P}_{\mathbf{A}_{M-1,m}}^\perp \mathbf{y} \right\|^2} \quad (\text{G.12})$$

Under the H_m hypothesis, the m -th component is not relevant. In that case the numerator $\left| \mathbf{s}_m^H \mathbf{P}_{\mathbf{A}_{M-1,m}}^\perp \mathbf{y} \right|^2$ has the same probability density function as in (4.61), the first norm of the denominator $\left\| \mathbf{P}_{\mathbf{A}_{M-1,m}}^\perp \mathbf{s}_m \right\|^2$ is an attenuated version of the vector \mathbf{s}_m as detailed in G.2 and

the last norm is the norm of the residual noise. In short:

$$\text{LR}_m \xrightarrow{H_m} 1 - \frac{\overbrace{\left| \mathbf{s}_m^H \mathbf{P}_{\mathbf{A}_{M-1,m}}^\perp \mathbf{y} \right|^2}^{\sim \chi_2^2(0, Nk_\sigma \sigma_n^2/2)}}{\underbrace{\left\| \mathbf{P}_{\mathbf{A}_{M-1,m}}^\perp \mathbf{s}_m \right\|^2}_{=Nk_\sigma} \underbrace{\left\| \mathbf{P}_{\mathbf{A}_{M-1,m}}^\perp \mathbf{y} \right\|^2}_{\sim \chi_{2N}^2(0, \sigma_n^2/2)}} \quad (\text{G.13})$$

Now, considering the fractional component of this expression:

$$\text{LR}_m \sim \frac{\chi_2^2}{\chi_{2N}^2} = \frac{\chi_2^2}{\chi_2^2 + \chi_{2(N-1)}^2} = \beta_{1,N-1} \quad (\text{G.14})$$

which has a known probability density function and which allows to compute a desired probability of false alarm.

Bibliography

- [Aka74] Hirotugu Akaike. “A New Look at the Statistical Model Identification.” In: *IEEE Transactions on Automatic Control* 19.6 (1974), pp. 716–723 (cit. on pp. 16, 17).
- [And00] Kenneth D. Anderson. “Determination of Water Level and Tides Using Interferometric Observations of GPS Signals.” In: *Journal of Atmospheric and Oceanic Technology* 17.8 (2000), pp. 1118–1127 (cit. on p. 37).
- [Bet01] John W. Betz. “Binary Offset Carrier Modulations for Radionavigation.” In: *Navigation* 48.4 (2001), pp. 227–246 (cit. on p. 22).
- [BH95] Yoav Benjamini and Yosef Hochberg. “Controlling the False Discovery Rate: A Practical and Powerful Approach to Multiple Testing.” In: *Journal of the Royal Statistical Society: Series B (Methodological)* 57.1 (1995), pp. 289–300 (cit. on p. 17).
- [BN12] Nuria Blanco-Delgado and Fernando D. Nunes. “Multipath Estimation in Multicorrelator GNSS Receivers using the Maximum Likelihood Principle.” In: *IEEE Transactions on Aerospace and Electronic Systems* 48.4 (2012), pp. 3222–3233 (cit. on p. 34).
- [BRS98] Mats Brenner, Randy Reuter, and Brian Schipper. “GPS Landing System Multipath Evaluation Techniques and Results.” In: *Proceedings of the 11th International Technical Meeting of the Satellite Division of the Institute of Navigation (ION GPS 1998)*. 1998, pp. 999–1008 (cit. on p. 30).
- [BS87] Petr Beckmann and André Spizzichino. *The Scattering of Electromagnetic Waves From Rough Surfaces*. Artech House, 1987 (cit. on pp. 28, 133, 134).
- [BSK85] Alfred Bruckstein, Tie-Jun Shan, and Thomas Kailath. “The Resolution of Overlapping Echos.” In: *IEEE Transactions on Acoustics, Speech, and Signal Processing* 33.6 (1985), pp. 1357–1367 (cit. on p. 17).
- [BZP02] Ramon F. Brcich, Abdelhak M. Zoubir, and Per Pelin. “Detection of Sources Using Bootstrap Techniques.” In: *IEEE Transactions on Signal Processing* 50.2 (2002), pp. 206–215 (cit. on p. 17).
- [Cam14] Adriano Camps et al. “Optimization and Performance Analysis of Interferometric GNSS-R Altimeters: Application to the PARIS IoD Mission.” In: *IEEE Journal of Selected Topics in Applied Earth Observations and Remote Sensing* 7.5 (2014), pp. 1436–1451 (cit. on p. 42).
- [Cam16] Adriano Camps et al. “Sensitivity of GNSS-R Spaceborne Observations to Soil Moisture and Vegetation.” In: *IEEE Journal of Selected Topics in Applied Earth Observations and Remote Sensing* 9.10 (2016), pp. 4730–4742 (cit. on p. 38).
- [Cam20] Adriano Camps. “Spatial Resolution in GNSS-R Under Coherent Scattering.” In: *IEEE Geoscience and Remote Sensing Letters* 17.1 (2020), pp. 32–36 (cit. on p. 36).

- [Cap69] Jack Capon. “High-Resolution Frequency-Wavenumber Spectrum Analysis.” In: *Proceedings of the IEEE* 57.8 (1969), pp. 1408–1418 (cit. on p. 15).
- [Car02] Estel Cardellach. “Sea Surface Determination Using GNSS Reflected Signals.” PhD thesis. Universitat Politècnica de Catalunya, Barcelona, Spain, 2002 (cit. on p. 135).
- [CD11] Xin Chen and Fabio Dovis. “Enhanced CADLL Structure for Multipath Mitigation in Urban Scenarios.” In: *Proceedings of the 2011 International Technical Meeting of The Institute of Navigation*. 2011, pp. 678–686 (cit. on p. 32).
- [CDP10] Xin Chen, Fabio Dovis, and Marco Pini. “An Innovative Multipath Mitigation Method Using Coupled Amplitude Delay Lock Loops in GNSS Receivers.” In: *IEEE/ION Position, Location and Navigation Symposium*. 2010, pp. 1118–1126 (cit. on p. 32).
- [CG17] Pau Closas and Adria Gusi-Amigo. “Direct Position Estimation of GNSS Receivers: Analyzing Main Results, Architectures, Enhancements, and Challenges.” In: *IEEE Signal Processing Magazine* 34.5 (2017), pp. 72–84 (cit. on p. 165).
- [CGH07] Jianqing Cai, Erik W. Grafarend, and Congwei Hu. “The Statistical Property of the GNSS Carrier Phase Observations and its Effects on the Hypothesis Testing of the Related Estimators.” In: *Proceedings of the 20th International Technical Meeting of the Satellite Division of The Institute of Navigation (ION GNSS 2007)*. 2007, pp. 331–338 (cit. on pp. 40, 140).
- [Che13] Xin Chen et al. “Comparative Studies of GPS Multipath Mitigation Methods Performance.” In: *IEEE Transactions on Aerospace and Electronic Systems* 49.3 (2013), pp. 1555–1568 (cit. on p. 32).
- [Chu07] Pei-Jung Chung et al. “Detection of the Number of Signals Using the Benjamini-Hochberg Procedure.” In: *IEEE Transactions on Signal Processing* 55.6 (2007), pp. 2497–2508 (cit. on p. 17).
- [CM08] Pei-Jung Chung and Christoph F. Mecklenbräuer. “Deterministic ML Estimation for Unknown Numbers of Signals.” In: *EUSIPCO*. 2008, pp. 1–5 (cit. on pp. 159, 160).
- [Das19] Priyanka Das et al. “On the Accuracy Limit of Time-delay Estimation with a Band-limited Signal.” In: *ICASSP 2019 - 2019 IEEE International Conference on Acoustics, Speech and Signal Processing (ICASSP)*. 2019, pp. 5282–5286 (cit. on pp. 10, 53, 174).
- [Das20a] Priyanka Das et al. “A New Compact Delay, Doppler Stretch and Phase Estimation CRB with a Band-Limited Signal for Generic Remote Sensing Applications.” In: *Remote Sensing* 12.18 (2020), p. 2913 (cit. on pp. 27, 53, 54, 57, 150, 174, 181).
- [Das20b] Priyanka Das et al. “Performance Limits of GNSS Code-Based Precise Positioning: GPS, Galileo & Meta-Signals.” In: *Sensors* 20.8 (2020), p. 2196 (cit. on p. 54).
- [DK11] Quan Ding and Steven Kay. “Maximum Likelihood Estimator Under a Misspecified Model With High Signal-to-Noise Ratio.” In: *IEEE Transactions on Signal Processing* 59.8 (2011), pp. 4012–4016 (cit. on p. 79).

- [Dov15] Fabio Dovis. *GNSS interference threats and countermeasures*. Artech House, 2015 (cit. on p. 28).
- [Egi12] Alejandro Egido et al. “Global Navigation Satellite Systems Reflectometry as a Remote Sensing Tool for Agriculture.” In: *Remote Sensing* 4.8 (2012), pp. 2356–2372 (cit. on p. 40).
- [Elf97] Tanos Elfouhaily et al. “A Unified Directional Spectrum for Long and Short Wind-Driven Waves.” In: *Journal of Geophysical Research: Oceans* 102.C7 (1997), pp. 15781–15796 (cit. on pp. 40, 135).
- [Eur] European Space Agencies (ESA). *Navipedia*. https://gssc.esa.int/navipedia/index.php/Main_Page (cit. on pp. 22, 24).
- [Eur21] European Union. *European GNSS (Galileo) Open Service – Signal in Space Interface Control Document*. Tech. rep. Version Issue 2.0. Retrieved on November 17, 2022. 2021 (cit. on p. 22).
- [Fab19] Fran Fabra et al. “Is Accurate Synoptic Altimetry Achievable by Means of Interferometric GNSS-R?” In: *Remote Sensing* 11.5 (2019) (cit. on p. 36).
- [FJ05] Patric C. Fenton and Jason Jones. “The Theory and Performance of NovAtel Inc.’s Vision Correlator.” In: *Proceedings of the 18th International Technical Meeting of the Satellite Division of The Institute of Navigation* (Jan. 2005), pp. 2178–2186 (cit. on p. 32).
- [Fle99] Bernard H. Fleury et al. “Channel parameter estimation in mobile radio environments using the SAGE algorithm.” In: *IEEE Journal on Selected Areas in Communications* 17.3 (1999), pp. 434–450 (cit. on p. 32).
- [For17] Stefano Fortunati et al. “Performance Bounds for Parameter Estimation under Misspecified Models: Fundamental Findings and Applications.” In: *IEEE Signal Processing Magazine* 34.6 (2017), pp. 142–157 (cit. on pp. 16, 75, 76, 81, 157).
- [For19] Stefano Fortunati et al. “Semiparametric CRB and Slepian-Bangs Formulas for Complex Elliptically Symmetric Distributions.” In: *IEEE Transactions on Signal Processing* 67.20 (2019), pp. 5352–5364 (cit. on p. 164).
- [Gar19] Vaibhav Garg et al. “Subspace Averaging and Order Determination for Source Enumeration.” In: *IEEE Transactions on Signal Processing* 67.11 (2019), pp. 3028–3041 (cit. on p. 17).
- [Gar22] Nil Garcia et al. “Cramér-Rao Bound Analysis of Radars for Extended Vehicular Targets With Known and Unknown Shape.” In: *IEEE Transactions on Signal Processing* 70 (2022), pp. 3280–3295 (cit. on p. 10).
- [GK88] Yola Georgiadou and Alfred Kleusberg. “On Carrier Signal Multipath Effects in Relative GPS Positioning.” In: *Manuscripta Geodaetica* 13.3 (1988), pp. 172–179 (cit. on p. 114).
- [GL03] Jiming Guo and Richard B. Langley. “A New Tropospheric Propagation Delay Mapping Function for Elevation Angles Down to 2 \circ .” In: *Proceedings of the 16th International Technical Meeting of the Satellite Division of The Institute of Navigation (ION GPS/GNSS 2003)*. 2003, pp. 368–376 (cit. on p. 137).

- [Gle05] Scott Gleason et al. “Detection and Processing of Bistatically Reflected GPS Signals from Low Earth Orbit for the Purpose of Ocean Remote Sensing.” In: *IEEE Transactions on Geoscience and Remote Sensing* 43.6 (June 2005), pp. 1229–1241 (cit. on p. 38).
- [Gol67] Robert Gold. “Optimal Binary Sequences for Spread Spectrum Multiplexing.” In: *IEEE Transactions on Information Theory* 13.4 (1967), pp. 619–621 (cit. on p. 21).
- [GR06] Olivier Germain and Giulio Ruffini. “A Revisit to the GNSS-R Code Range Precision.” In: (June 2006) (cit. on p. 42).
- [HBS04] Chris Hegarty, John W. Betz, and Ali Saidi. “Binary Coded Symbol Modulations for GNSS.” In: *Proceedings of the 60th Annual Meeting of The Institute of Navigation (2004)*. 2004, pp. 56–64 (cit. on p. 22).
- [HR80] Felix R. Hoots and Ronald L. Roehrich. *Models for Propagation of NORAD Element Sets*. Tech. rep. Package Compiled by TS Kelso (31 December 1988). 1980 (cit. on pp. 91, 92).
- [HTB04] Chris Hegarty, Michael Tran, and John W. Betz. “Multipath Performance of the New GNSS Signals.” In: *Proceedings of the 2004 National Technical Meeting of The Institute of Navigation*. 2004, pp. 333–342 (cit. on p. 33).
- [Hub67] Peter J. Huber. “The Behavior of Maximum Likelihood Estimates Under Non-standard Conditions.” In: *Proc. 5th Berkley Symp. Math. Statist. Probab.* 1967, pp. 221–233 (cit. on pp. 16, 75).
- [IAH05] Markus Irsigler, Jose Angel Avila-Rodriguez, and Guenter W. Hein. “Criteria for GNSS Multipath Performance Assessment.” In: *Proceedings of the 18th International Technical Meeting of the Satellite Division of The Institute of Navigation (ION GNSS 2005)*. 2005, pp. 2166–2177 (cit. on p. 34).
- [JBH96] Axel Jahn, Hermann Bischl, and Günter Heiß. “Channel Characterisation for Spread Spectrum Satellite Communications.” In: *Proceedings of International Symposium on Spread Spectrum Techniques and Applications (ISSSTA '95)*. Vol. 3. 1996, pp. 1221–1226 (cit. on p. 30).
- [JFS04] Jason Jones, Patrick Fenton, and Brian Smith. *Theory and Performance of the Pulse Aperture Correlator*. Tech. rep. NovAtel Inc., 2004 (cit. on p. 32).
- [Jov10] Aleksandar Jovanovic et al. “Multipath Mitigation Techniques for CBOC, TMBOC and AltBOC Signals using Advanced Correlators Architectures.” In: *IEEE/ION Position, Location and Navigation Symposium*. 2010, pp. 1127–1136 (cit. on p. 34).
- [Kap] *Understanding GPS/GNSS: Principle and Applications*. 3rd. Artech House, 2017 (cit. on pp. 17, 24, 26, 28, 29, 33, 46, 152).
- [Kay93] Steven M. Kay. *Fundamentals of Statistical Signal Processing: Estimation Theory*. Englewood Cliffs, New Jersey, USA: Prentice-Hall, 1993 (cit. on p. 12).
- [KG96] Stephen J. Katzberg and James L. Garrison. *Utilizing GPS to Determine Ionospheric Delay Over the Ocean*. Tech. rep. NASA, 1996 (cit. on p. 37).

- [KN09] Shira Kritchman and Boaz Nadler. “Non-Parametric Detection of the Number of Signals: Hypothesis Testing and Random Matrix Theory.” In: *IEEE Transactions on Signal Processing* 57.10 (2009), pp. 3930–3941 (cit. on p. 17).
- [LAI08] Laurent Lestarquit, Géraldine Artaud, and Jean-Luc Issler. “AltBOC for Dummies or Everything You Always Wanted to Know About AltBOC.” In: *Proceedings of the 21st International Technical Meeting of the Satellite Division of The Institute of Navigation (ION GNSS 2008)*. 2008, pp. 961–970 (cit. on p. 22).
- [Lar08] Kristine M. Larson et al. “Use of GPS Receivers as a Soil Moisture Network for Water Cycle Studies.” In: *Geophysical Research Letters* 35.24 (2008) (cit. on p. 114).
- [Les16] Laurent Lestarquit et al. “Reflectometry With an Open-Source Software GNSS Receiver: Use Case With Carrier Phase Altimetry.” In: *IEEE Journal of Selected Topics in Applied Earth Observations and Remote Sensing* 9.10 (2016), pp. 4843–4853 (cit. on p. 37).
- [Li18] Weiqiang Li et al. “Revisiting the GNSS-R waveform statistics and its impact on altimetric retrievals.” In: *IEEE Trans. Geosci. Remote Sens.* 56.5 (May 2018), pp. 2854–2871 (cit. on p. 42).
- [Lil67] Hubert W. Lilliefors. “On the Kolmogorov-Smirnov Test for Normality with Mean and Variance Unknown.” In: *Journal of the American Statistical Association* 62.318 (1967), pp. 399–402 (cit. on p. 142).
- [Liu17] Wei Liu et al. “Coastal Sea-Level Measurements Based on GNSS-R Phase Altimetry: A Case Study at the Onsala Space Observatory, Sweden.” In: *IEEE Transactions on Geoscience and Remote Sensing* 55.10 (2017), pp. 5625–5636 (cit. on p. 40).
- [Low02] Stephen T. Lowe et al. “First Spaceborne Observation of an Earth-reflected GPS Signal.” In: *Radio Science* 37.1 (2002), pp. 1–28 (cit. on p. 42).
- [LS96] Jian Li and Petre Stoica. “Efficient mixed-spectrum estimation with applications to target feature extraction.” In: *IEEE Transactions on Signal Processing* 44.2 (1996), pp. 281–295 (cit. on p. 14).
- [Luba] Corentin Lubeigt et al. “Approximate Maximum Likelihood Time-Delay Estimation for Two Closely Spaced Sources” (cit. on p. 5).
- [Lubb] Corentin Lubeigt et al. “Band-Limited Impulse Response Estimation Performance” (cit. on p. 5).
- [Lub20] Corentin Lubeigt et al. “Joint Delay-Doppler Estimation Performance in a Dual Source Context.” In: *Remote Sensing* 12.23 (2020), p. 3894 (cit. on p. 4).
- [Lub21] Corentin Lubeigt et al. “On the Impact and Mitigation of Signal Crosstalk in Ground-Based and Low Altitude Airborne GNSS-R.” In: *Remote Sensing* 13.6 (2021), p. 1085 (cit. on p. 4).
- [Lub22a] Corentin Lubeigt et al. “Clean-to-Composite Bound Ratio: A Multipath Criterion for GNSS Signal Design and Analysis.” In: *IEEE Transactions on Aerospace and Electronic Systems* 58.6 (2022), pp. 5412–5424 (cit. on p. 4).

- [Lub22b] Corentin Lubeigt et al. “Close-to-Ground Single Antenna GNSS-R.” In: *ESA Workshop on Satellite Navigation Technologies and European Workshop on GNSS Signals and Signal Processing (NAVITEC)*. 2022 (cit. on p. 5).
- [Lub22c] Corentin Lubeigt et al. “Details on Impulse Response Estimation and Size Determination.” 2022 (cit. on p. 5).
- [Lub22d] Corentin Lubeigt et al. “Developments for MCRB Computation in Multipath Scenarios.” 2022 (cit. on p. 5).
- [Lub22e] Corentin Lubeigt et al. “Les Signaux à Bande Large au Service de la Réflectométrie par GNSS à Site Bas.” In: *Groupe de Recherche et d’Etudes de Traitement du Signal et des Images (GRETSI)*. 2022 (cit. on p. 5).
- [Lub22f] Corentin Lubeigt et al. “Multipath Estimating Techniques Performance Analysis.” In: *IEEE Aerospace Conference (AERO)*. 2022, pp. 1–6 (cit. on p. 5).
- [Lub23] Corentin Lubeigt et al. “Untangling First and Second Order Statistics Contributions in Multipath Scenarios.” In: *Signal Processing* 205 (2023), p. 108868 (cit. on p. 4).
- [Mah20] Meysam Mahooti. *SGP4 Propagator*. <https://www.mathworks.com/matlabcentral/fileexchange/62013-sgp4>. MATLAB Central File Exchange. Retrieved March 9, 2020. 2020 (cit. on p. 92).
- [Mar09] Juan Fernando Marchan-Hernandez et al. “An Efficient Algorithm to the Simulation of Delay–Doppler Maps of Reflected Global Navigation Satellite System Signals.” In: *IEEE Transactions on Geoscience and Remote Sensing* 47.8 (2009), pp. 2733–2740 (cit. on p. 39).
- [Mar14a] Francisco Martin et al. “Cross-Correlation Waveform Analysis for Conventional and Interferometric GNSS-R Approaches.” In: *IEEE Journal of Selected Topics in Applied Earth Observations and Remote Sensing* 7.5 (2014), pp. 1560–1572 (cit. on p. 38).
- [Mar14b] Francisco Martin et al. “Mitigation of direct signal cross-talk and study of the coherent component in GNSS-R.” In: *IEEE Geoscience and Remote Sensing Letters* 12.2 (2014), pp. 279–283 (cit. on pp. 38, 110).
- [Mar93] Manuel Martín-Neira. “A Passive Reflectometry and Interferometry System (PARIS): Application to Ocean Altimetry.” In: *ESA Journal* 17 (1993). US Patent 5 546 087, Aug. 13 1996 (cit. on pp. 1, 35, 37, 39).
- [MB99] Gary A. McGraw and Michael S. Braasch. “GNSS multipath Mitigation using Gated and High Resolution Correlator Concepts.” In: *Proceedings of the 1999 National Technical Meeting of The Institute of Navigation*. 1999, pp. 333–342 (cit. on p. 32).
- [MCL12] Tarek Menni, Eric Chaumette, and Pascal Larzabal. “Reparameterization and Constraints for CRB: Duality and a Major Inequality for System Analysis and Design in the Asymptotic Region.” In: *2012 IEEE International Conference on Acoustics, Speech and Signal Processing (ICASSP)*. 2012, pp. 3545–3548 (cit. on p. 157).

- [McP21] Hamish McPhee et al. “On The Accuracy Limit of Joint Time-Delay/Doppler/Acceleration Estimation with a Band-Limited Signal.” In: *ICASSP 2021*. 2021, pp. 5130–5134 (cit. on p. 27).
- [Med20] Daniel Medina et al. “Compact CRB for Delay, Doppler and Phase Estimation - Application to GNSS SPP & RTK Performance Characterisation.” In: *IET Radar, Sonar & Navigation* 14.10 (2020), pp. 1537–1549 (cit. on pp. 27, 53, 54, 66, 67, 71, 77, 103, 150, 165, 174, 181).
- [Men11] Tarek Menni et al. “CRB for Active Radar.” In: *EUSIPCO 2011*. 2011 (cit. on p. 10).
- [Mor21] Yu Jade Morton et al. *Position, Navigation, and Timing Technologies in the 21st Century, Volumes 1 and 2*. John Wiley & Sons, 2021 (cit. on pp. 24, 28, 34).
- [Mun20] Joan Francesc Munoz-Martin et al. “Snow and Ice Thickness Retrievals Using GNSS-R: Preliminary Results of the MOSAiC Experiment.” In: *Remote Sensing* 12.24 (2020), p. 4038 (cit. on p. 37).
- [NK13] Wooseok Nam and Seung-Hyun Kong. “Least-Squares-Based Iterative Multipath Super-Resolution Technique.” In: *IEEE Transactions on Signal Processing* 61.3 (2013), pp. 519–529 (cit. on p. 32).
- [Nog21] Oriol Nogués i Cervelló et al. “Improved GNSS-R Altimetry Methods: Theory and Experimental Demonstration Using Airborne Dual Frequency Data From the Microwave Interferometric Reflectometer (MIR).” In: *Remote Sensing* 13.20 (2021), p. 4186 (cit. on pp. 40, 41).
- [Ort] Lorenzo Ortega et al. “On the GNSS Synchronization Performance Degradation under Interference Scenarios: Bias and Misspecified CRB” (cit. on pp. 5, 165).
- [Ort20] Lorenzo Ortega et al. “Positioning Performance Limits of GNSS Meta-Signals and HO-BOC Signals.” In: *Sensors* 20.12 (2020), p. 3586 (cit. on pp. 54, 165).
- [Ort23] Lorenzo Ortega et al. “GNSS L5/E5 Maximum Likelihood Synchronization Performance Degradation Under DME Interferences.” In: *IEEE/ION Position, Location and Navigation Symposium*. 2023 (cit. on p. 5).
- [Ott93] Björn Ottersten et al. “Exact and Large Sample Maximum Likelihood Techniques for Parameter Estimation and Detection in Array Processing.” In: *Radar Array Processing*. Ed. by Simon Haykin, John Litva, and Terence J. Shepherd. Heidelberg: Springer-Verlag, 1993. Chap. 4, pp. 99–151 (cit. on pp. 12, 56, 64, 75, 114, 149).
- [OVC22] Lorenzo Ortega, Jordi Vilà-Valls, and Eric Chaumette. “Insights on the Estimation Performance of GNSS-R Coherent and Non-Coherent Processing Schemes.” In: *IEEE Geoscience and Remote Sensing Letters* 19 (2022), pp. 1–5 (cit. on pp. 42, 108).
- [Pas14] Daniel Pascual et al. “Precision Bounds in GNSS-R Ocean Altimetry.” In: *IEEE Journal of Selected Topics in Applied Earth Observations and Remote Sensing* 7.5 (May 2014), pp. 1416–1423 (cit. on p. 42).

- [PP12] Kaare B. Petersen and Michael S. Pedersen. *The Matrix Cookbook*. Tech. rep. Version 20121115. Technical Univ. Denmark, Kongens Lyngby, Denmark, 2012 (cit. on pp. 169, 170).
- [PS07] John G. Proakis and Masoud Salehi. *Digital Communications*. 5th. McGraw-Hill, 2007 (cit. on p. 30).
- [QSS] QSS. *GNSSView*. <https://app.qzss.go.jp/GNSSView/gnssview.html> (cit. on p. 91).
- [RBF16] Miguel Angel Ribot, Cyril Botteron, and Pierre-André Farine. “Derivation of the Cramér-Rao Bound in the GNSS-Reflectometry Context for Static, Ground-Based Receivers in Scenarios with Coherent Reflection.” In: *Sensors* 16.12 (2016), p. 2063 (cit. on p. 42).
- [Ren06] Alexandre Renaux et al. “On the High-SNR Conditional Maximum-Likelihood Estimator Full Statistical Characterization.” In: *IEEE Trans. Signal Process.* 54.12 (Dec. 2006), pp. 4840–4843 (cit. on pp. 13, 106).
- [RH15] Christ D. Richmond and Larry L. Horowitz. “Parameter Bounds on Estimation Accuracy Under Model Misspecification.” In: *IEEE Transactions on Signal Processing* 63.9 (2015), pp. 2263–2278 (cit. on pp. 76, 157).
- [Rib14] Miguel Angel Ribot et al. “Normalized GNSS Interference Pattern Technique for Altimetry.” In: *Sensors* 14.6 (2014), pp. 10234–10257 (cit. on pp. 37, 42, 101, 114).
- [Rib17] Serni Ribó et al. “A Software-Defined GNSS Reflectometry Recording Receiver with Wide-Bandwidth, Multi-Band Capability and Digital Beam-Forming.” In: *Remote Sensing* 9.5 (2017) (cit. on p. 136).
- [Ric03] Dennis W. Ricker. *Echo Signal Processing*. Springer, New York, USA: Kluwer Academic, 2003 (cit. on pp. 49, 146, 147).
- [Ris78] Jorma Rissanen. “Modeling by Shortest Data Description.” In: *Automatica* 14.5 (1978), pp. 465–471 (cit. on p. 17).
- [Rod10] Nereida Rodriguez-Alvarez et al. “Land Geophysical Parameters Retrieval Using the Interference Pattern GNSS-R Technique.” In: *IEEE Transactions on Geoscience and Remote Sensing* 49.1 (2010), pp. 71–84 (cit. on p. 35).
- [Roe20] Carolyn R. Roesler et al. “Coherent GPS Reflections Over Ocean Surface.” In: *IGARSS 2020 - 2020 IEEE International Geoscience and Remote Sensing Symposium*. 2020, pp. 6218–6221 (cit. on p. 41).
- [Roe21] Carolyn J. Roesler et al. “Coherent GNSS-Reflections Characterization Over Ocean and Sea Ice Based on Spire Global CubeSat Data.” In: *IEEE Transactions on Geoscience and Remote Sensing* 60 (2021), pp. 1–18 (cit. on pp. 40, 137, 145).
- [Rou15] Nicolas Roussel et al. “Sea Level Monitoring and Sea State Estimate Using a Single Geodetic Receiver.” In: *Remote sensing of Environment* 171 (2015), pp. 261–277 (cit. on p. 37).
- [Rus21] Ilaria M. Russo et al. “Entropy-Based Coherence Metric for Land Applications of GNSS-R.” In: *IEEE Transactions on Geoscience and Remote Sensing* (2021), pp. 1–1 (cit. on p. 40).

- [SA08] Mohamed Sahnouli and Moeness G. Amin. “Fast Iterative Maximum-Likelihood Algorithm (FIMLA) for Multipath Mitigation in the Next Generation of GNSS Receivers.” In: *IEEE Transactions on Wireless Communications* 7.11 (2008), pp. 4362–4374 (cit. on pp. 32, 72).
- [Sch86] Ralph O. Schmidt. “Multiple Emitter Location and Signal Parameter Estimation.” In: *IEEE Transactions on Antennas and Propagation* 34.3 (1986), pp. 276–280 (cit. on p. 15).
- [Sko08] Merrill I. Skolnik. *Radar Handbook*. 3rd. McGraw-Hill Education, 2008 (cit. on p. 35).
- [SM05] Petre Stoica, Randolph L. Moses, et al. *Spectral Analysis of Signals*. Vol. 452. Pearson Prentice Hall Upper Saddle River, NJ, 2005 (cit. on p. 10).
- [SN89] Petre Stoica and Arye Nehorai. “MUSIC, Maximum Likelihood, and Cramér-Rao Bound.” In: *IEEE Transactions on Acoustics, Speech, and Signal Processing* 37.5 (1989), pp. 720–741 (cit. on p. 114).
- [SN90] Petre Stoica and Arye Nehorai. “Performance Study of Conditional and Unconditional Direction of Arrival Estimation.” In: *IEEE Trans. Acoust., Speech, Signal Process.* 38.10 (Oct. 1990), pp. 1783–1795 (cit. on pp. 10, 13, 165).
- [TF94] Bryan R. Townsend and Patrick C. Fenton. “A Practical Approach to the Reduction of Pseudorange Multipath Errors in a L1 GPS Receiver.” In: *Proceedings of the 7th International Technical Meeting of the Satellite Division of the Institute of Navigation*. 1994, pp. 20–23 (cit. on p. 32).
- [TM17] Peter J. G. Teunissen and Oliver Montenbruck, eds. *Handbook of Global Navigation Satellite Systems*. Switzerland: Springer, 2017 (cit. on pp. 22, 24, 26, 28, 34).
- [Tow95] Bryan R. Townsend et al. “Performance Evaluation of the Multipath Estimating Delay Lock Loop.” In: *Navigation* 42.3 (1995), pp. 502–514 (cit. on p. 32).
- [Tre01] Robert Treuhart et al. “2-cm GPS Altimetry over Crater Lake.” In: *Geophysical Research Letters* 22 (Dec. 2001), pp. 4343–4346 (cit. on p. 42).
- [Tri] Trimble Inc. *GNSS Planning Online*. <http://www.gnssplanningonline.com> (cit. on p. 91).
- [Unw21] Martin J. Unwin et al. “An Introduction to the HydroGNSS GNSS Reflectometry Remote Sensing Mission.” In: *IEEE Journal of Selected Topics in Applied Earth Observations and Remote Sensing* 14 (2021), pp. 6987–6999 (cit. on pp. 1, 41).
- [U.S22a] U.S. Government. *Interface Specification IS-GPS-200 Navstar GPS Space / Segment / Navigation User Interface*. Tech. rep. Version Rev N. Retrieved on November 17, 2022. 2022 (cit. on p. 21).
- [U.S22b] U.S. Government. *Interface Specification IS-GPS-705 Navstar GPS Space / Segment / Navigation User Interface*. Tech. rep. Version Rev. J. Retrieved on November 17, 2022. 2022 (cit. on p. 21).
- [Van01a] Harry L. Van Trees. *Part I: Detection Estimation and Linear Modulation Theory*. Detection, Estimation, and Modulation Theory. Wiley, 2001 (cit. on pp. 13, 53).

- [Van01b] Harry L. Van Trees. *Part III: Radar-Sonar Signal Processing and Gaussian Signals in Noise*. Detection, Estimation, and Modulation Theory. Wiley, 2001 (cit. on pp. 10, 147).
- [Van04] Harry L. Van Trees. *Part IV: Optimum Array Processing*. Detection, Estimation, and Modulation Theory. John Wiley & Sons, 2004 (cit. on p. 10).
- [Van92] Richard D.J. Van Nee. “The Multipath Estimating Delay Lock Loop.” In: *IEEE Second International Symposium on Spread Spectrum Techniques and Applications*. 1992, pp. 39–42 (cit. on p. 32).
- [VBC13] François Vincent, Olivier Besson, and Eric Chaumette. “Approximate Maximum Likelihood Direction of Arrival Estimation for Two Closely Spaced Sources.” In: *2013 5th IEEE International Workshop on Computational Advances in Multi-Sensor Adaptive Processing (CAMSAP)*. 2013, pp. 320–323 (cit. on p. 10).
- [VBC14] François Vincent, Olivier Besson, and Eric Chaumette. “Approximate Maximum Likelihood Estimation of Two Closely Spaced Sources.” In: *Signal Processing 97* (2014), pp. 83–90 (cit. on pp. 10, 15, 115).
- [VFF92] A. J. Van Dierendonck, Patrick C. Fenton, and Tom Ford. “Theory and Performance of Narrow Correlator Spacing in a GPS Receiver.” In: *Navigation* 39.3 (1992), pp. 265–283 (cit. on p. 32).
- [WA21] Mati Wax and Amir Adler. “Detection of the Number of Signals by Signal Subspace Matching.” In: *IEEE Transactions on Signal Processing* 69 (2021), pp. 973–985 (cit. on p. 17).
- [Wei02] Lawrence R. Weill. “Multipath Mitigation using Modernized GPS Signals: How Good Can it Get?” In: *Proceedings of the 15th International Technical Meeting of the Satellite Division of The Institute of Navigation (ION GPS 2002)* (Sept. 2002), pp. 493–505 (cit. on pp. 32, 34, 71).
- [Wei95] Lawrence R. Weill. “Achieving Theoretical Accuracy Limits for Pseudorangeing in the Presence of Multipath.” In: *Proceedings of the 8th International Technical Meeting of the Satellite Division of the Institute of Navigation (ION GPS 1995)*. 1995, pp. 1521–1530 (cit. on pp. 32, 72).
- [Wel67] Peter D. Welch. “The Use of Fast Fourier Transform for the Estimation of Power Spectra: A Method Based on Time Averaging Over Short, Modified Periodograms.” In: *IEEE Transactions on Audio and Electroacoustics* 15.2 (1967), pp. 70–73 (cit. on p. 102).
- [Whi82] Halbert White. “Maximum Likelihood Estimation of Misspecified Models.” In: *Econometrica: Journal of the Econometric Society* (1982), pp. 1–25 (cit. on pp. 16, 75).
- [WK85] Mati Wax and Thomas Kailath. “Detection of signals by information theoretic criteria.” In: *IEEE Transactions on Acoustics, Speech, and Signal Processing* 33.2 (1985), pp. 387–392 (cit. on p. 17).

- [Won90] Kon Max Wong et al. “On Information Theoretic Criteria for Determining the Number of Signals in High Resolution Array Processing.” In: *IEEE Transactions on Acoustics, Speech, and Signal Processing* 38.11 (1990), pp. 1959–1971 (cit. on p. 17).
- [WZ89] Mati Wax and Ilan Ziskind. “Detection of the number of coherent signals by the MDL principle.” In: *IEEE Transactions on Acoustics, Speech, and Signal Processing* 37.8 (1989), pp. 1190–1196 (cit. on p. 17).
- [YB92] Sze Fong Yau and Yoram Bresler. “A Compact Cramér-Rao Bound Expression for Parametric Estimation of Superimposed Signals.” In: *IEEE Transactions on Signal Processing* 40.5 (May 1992), pp. 1226–1230 (cit. on pp. 12, 149).
- [Zav14] Valery U. Zavorotny et al. “Tutorial on Remote Sensing Using GNSS Bistatic Radar of Opportunity.” In: *IEEE Geoscience and Remote Sensing Magazine* 2.4 (2014), pp. 8–45 (cit. on pp. 39, 40).
- [ZH16] Tong Zhao and Tianyao Huang. “Cramer-Rao Lower Bounds for the Joint Delay-Doppler Estimation of an Extended Target.” In: *IEEE Transactions on Signal Processing* 64.6 (2016), pp. 1562–1573 (cit. on pp. 10, 147, 151, 152).
- [ZV00] Valery U. Zavorotny and Alexander G. Voronovich. “Scattering of GPS Signals from the Ocean with Wind Remote Sensing Application.” In: *IEEE Transactions on Geoscience and Remote Sensing* 38.2 (Mar. 2000), pp. 951–964 (cit. on pp. 36, 39, 40).
- [ZW88] Ilan Ziskind and Mati Wax. “Maximum Likelihood Localization of Multiple Sources by Alternating Projection.” In: *IEEE Transactions on Acoustics, Speech, and Signal Processing* 36.10 (1988), pp. 1553–1560 (cit. on pp. 10, 14).
- [ZZ01] Cinzia Zuffada and Valery Zavorotny. “Coherence Time and Statistical Properties of the GPS Signal Scattered Off the Ocean Surface and Their Impact on the Accuracy of Remote Sensing of Sea Surface Topography and Winds.” In: *IEEE 2001 International Geoscience and Remote Sensing Symposium (IGARSS 2001)*. Vol. 7. 2001, pp. 3332–3334 (cit. on p. 42).

TéSA – 7, boulevard de la Gare, 3e étage, bureau du fond
Toulouse